Titre: Title:	Analytical Prediction of Shot Peening Effects on Nickel-Based Superalloy Inconel 718 Fatigue Life
Auteur: Author:	Thierry Klotz
Date:	2018
Type:	Mémoire ou thèse / Dissertation or Thesis
Référence: Citation:	Klotz, T. (2018). Analytical Prediction of Shot Peening Effects on Nickel-Based Superalloy Inconel 718 Fatigue Life [Thèse de doctorat, École Polytechnique de Montréal]. PolyPublie. https://publications.polymtl.ca/3017/

URL de PolyPublie: PolyPublie URL:	https://publications.polymtl.ca/3017/
Directeurs de recherche: Advisors:	Myriam Brochu, & Martin Lévesque
Programme: Program:	Génie mécanique

UNIVERSITÉ DE MONTRÉAL

ANALYTICAL PREDICTION OF SHOT PEENING EFFECTS ON NICKEL-BASED SUPERALLOY INCONEL 718 FATIGUE LIFE

THIERRY KLOTZ
DÉPARTEMENT DE GÉNIE MÉCANIQUE
ÉCOLE POLYTECHNIQUE DE MONTRÉAL

THÈSE PRÉSENTÉE EN VUE DE L'OBTENTION
DU DIPLÔME DE PHILOSOPHIÆ DOCTOR
(GÉNIE MÉCANIQUE)
MARS 2018

UNIVERSITÉ DE MONTRÉAL

ÉCOLE POLYTECHNIQUE DE MONTRÉAL

Cette thèse intitulée :

ANALYTICAL PREDICTION OF SHOT PEENING EFFECTS ON NICKEL-BASED SUPERALLOY INCONEL 718 FATIGUE LIFE

présentée par: KLOTZ Thierry
en vue de l'obtention du diplôme de : Philosophiæ Doctor
a été dûment acceptée par le jury d'examen constitué de :

M. BAÏLON Jean-Paul, D.Sc.A., président
Mme BROCHU Myriam, Ph. D., membre et directrice de recherche
M. LÉVESQUE Martin, Ph. D., membre et codirecteur de recherche
M. DEMERS Vincent, Ph. D., membre
M. MOREL Franck, Doctorat, membre externe

DEDICATION

To my goddaughter and godson,
Valentine and Gabin

ACKNOWLEDGEMENTS

I would like to thank Prof. Myriam Brochu and Prof. Martin Lévesque for their guidance throughout this thesis. Four years ago my knowledge in metallic materials fatigue and shot peening were very tenuous but you gave me the chance to acquire expertise in these fields. I gained in scientific maturity thanks to your advice and constructive criticism. I would also like to thank you for giving me the opportunity to teach during these four years.

I owe special gratitude to my coworkers and friends from École Polytechnique and other institutions. Your advice, help and the many animated conversations we had were precious to me and helped me, day after day, to enhance my work and stay positive. I would like to particularly thank Charles Bianchetti, Dorian Delbergue, Sébastien Blas, Antonio Castro Moreno, Fubin Tu and Hong Yan Miao for their contributions and the fruitful discussions all along this project. The technical support of Josée Laviolette, Isabelle Nowlan, Martin Cardonne and Jean-François Daigle is also gratefully acknowledged. I also owe special gratitude to Prof. Philippe Bocher for his guidance and corrections during the redaction of the second article.

I would like to thank Martin Blanchet for his guidance and help during my internship at Pratt & Whitney Canada.

I would like to thank the Consortium of Research and Innovation in Aerospace in Quebec (CRIAQ), Pratt & Whitney Canada, Héroux-Devtek, Bell Helicopter and L3 Communication MAS who financially supported the project. I am grateful to their engineers for their help, technical remarks and challenging questions. I would also like to thank the Natural Sciences and Engineering Research Council of Canada (NSERC) and the Mathematics of Information Technology and Complex Systems (MITACS) for the scholarships I obtained during my PhD.

Finally, last but not least, I would like to thank my parents, Hélène and Daniel, and my whole family for providing an unconditional support during the past four years. I would also like to thank the one who endured my day-to-day mood and always encouraged me, my beloved Jenny.

RÉSUMÉ

Le grenaillage est un procédé de traitement de surface très utilisé dans l'industrie aérospatiale. Il consiste à projeter, à haute vitesse, des grenailles sur la surface d'une pièce métallique. Lors de l'impact, les grenailles déforment plastiquement une faible épaisseur de matière. Ce procédé crée des contraintes résiduelles en compression à la surface de la pièce ainsi qu'un durcissement au sein de la couche plastiquement déformée. Ces contraintes résiduelles compressives, alliées au durcissement, retardent l'amorçage et freinent la propagation des fissures à la surface de la pièce. La surface d'une pièce étant souvent l'endroit le plus critique pour la formation des fissures en fatigue, le grenaillage permet d'augmenter de façon significative la durée de vie des pièces mécaniquement sollicitées en repoussant sous la surface l'amorçage des fissures.

Malgré ses nombreux avantages, le grenaillage n'est pas exempt d'effets négatifs sur la vie en fatigue. Les cratères créés à la surface lors de l'impact des grenailles sont des concentrateurs de contraintes qui favorisent l'amorçage et la propagation des fissures. De plus, en impactant l'arête d'une pièce, les grenailles peuvent déformer plastiquement cette dernière et créer des bavures. Ces bavures sont critiques pour l'amorçage et la propagation des fissures. Le grenaillage est donc un procédé qui doit être optimisé. Un grenaillage trop léger ne créera pas assez de contraintes résiduelles compressives et de durcissement en surface pour améliorer significativement la vie en fatigue tandis qu'un grenaillage exécuté de manière trop sévère réduira la vie en fatigue de la pièce par la création de concentrateurs de contraintes trop prononcés.

Les paramètres de grenaillage optimaux sont déterminés par la méthode essai et erreur et le grenaillage n'est souvent pas pris en compte durant la phase de conception des pièces. Il est plutôt considéré comme un facteur de sécurité. L'objectif de cette thèse est de développer un outil analytique, adapté au superalliage de nickel Inconel 718, permettant de prédire la vie en fatigue ainsi que les mécanismes d'amorçage et de propagation des fissures en fonction des conditions de grenaillage et des chargements imposés sur la pièce. Ce modèle pourra permettre, dans le futur, de réduire le nombre d'essais destinés à optimiser les conditions de grenaillage et de prendre en compte ses effets bénéfiques sur la vie en fatigue lors de la conception des pièces.

Afin de réaliser cet outil de prédiction analytique, la première étape a consisté à mener une campagne expérimentale d'envergure afin de caractériser, aux échelles macroscopique et microscopique, les évolutions des propriétés mécaniques de l'Inconel 718, avec et sans

grenaillage, durant sa vie en fatigue. Les essais et les observations réalisés ont varié du plus simple essai de traction aux techniques les plus pointues telles que l'étude de la relaxation des contraintes résiduelles, l'observation des faciès de rupture au microscope électronique à balayage ou encore le suivi de la propagation de micro-fissures. Il a été montré qu'un grenaillage optimal peut multiplier par vingt la durée de vie de l'échantillon en régime de fatigue endurance. Cependant, en fatigue olygocyclique, le grenaillage n'apporte aucun effet bénéfique. L'analyse des résultats a permis de définir des recommandations sur les conditions de grenaillage à utiliser afin de maximiser la vie en fatigue de l'Inconel 718. La plus importante étant que l'intensité de grenaillage doit être la plus faible possible afin de minimiser la dégradation de l'état de surface de la pièce tout en étant assez élevée pour engendrer des contraintes compressives de surface suffisantes pour repousser l'amorçage des fissures sous la surface.

Les résultats expérimentaux obtenus ont permis le développement d'un modèle analytique se basant sur le modèle de propagation de fissures de Navarro et de los Rios ainsi que sur le modèle d'amorçage de fissures de Chan. Ces deux modèles ont été améliorés afin de prendre en compte la redistribution des contraintes résiduelles et des déformations plastiques en surface qui ont un effet important sur la vie en fatigue. Le couplage de ces deux modèles modifiés, en plus de prédire la vie en fatigue, a permis pour la première fois de prédire avec précision la profondeur à laquelle se produit l'amorçage des fissures.

Une campagne expérimentale destinée à étudier l'effet de la géométrie des arrêtes d'une pièce sur la formation de bavures sous plusieurs conditions de grenaillage ainsi que la vie en fatigue résultante a aussi été menée. Cette étude, qui est la première du genre dans la littérature ouverte, a permis de mettre en évidence les pratiques à éviter concernant le design et les conditions de grenaillage appliquées aux arêtes des pièces, telles que le grenaillage d'arêtes vives, ou l'utilisation d'intensités de grenaillage trop élevées.

Cette thèse présente l'une des caractérisation mécanique la plus exhaustive de la littérature ouverte sur l'Inconel 718 grenaillé. Les données produites et analysées ainsi que le modèle développé sont des outils qui pourront être utilisés dans l'optimisation des conditions de grenaillage visant à la maximisation de la vie en fatigue des pièces en Inconel 718.

ABSTRACT

Shot peening is a surface treatment largely used in the aerospace industry. This cold working process consists in impinging particles, called shots, at high velocity onto a metallic part surface. The shots plastically deform the treated surface. The process induces surface compressive residual stresses and work hardening. Compressive residual stresses and cold work delay crack initiation and retard short crack propagation at the part surface. The surface is a critical location for crack initiation and shot peening increases service life by pushing crack initiation underneath the surface.

Despite its positive effects on fatigue, shot peening also creates dimples that are stress concentration features which promote crack initiation and propagation. Moreover, when impacting edges, the shots induce plastic deformations in the form of burrs. These burrs, called rolled edges, are highly critical for crack initiation and short crack propagation. Shot peening is thus a process that must be optimized. Shot peening at a low intensity will not induce sufficiently compressive residual stresses and cold work to improve the fatigue life and shot peening at a too high intensity will be detrimental to fatigue life due to the formation of severe surface stress concentration features.

Optimal shot peening parameters are usually determined by trial and error and shot peening is often not accounted for during the design stages of a component, but rather considered as a safety factor. This thesis aims at developing an analytical tool to predict fatigue life, and crack initiation and propagation mechanisms on shot peened nickel-based superalloy Inconel 718 by accounting for the shot peening and the loading conditions. Such a model could allow, in the future, to reduce the costs associated with the optimization of the shot peening conditions and to finally account for its beneficial effects on fatigue life during design stages.

The first step consisted in performing an extensive experimental campaign to characterize, at a microscale and a macroscale, the evolution of peened and unpeened Inconel 718 mechanical properties under cyclic loading. The tests varied from the simplest quasi-static tensile test to the most complex techniques such as the measurement of the residual stresses redistribution, the rupture surfaces observations under a scanning electron microscope or the short cracks propagation monitoring. It was shown that the fatigue life can be increased by a factor of twenty in high cycle fatigue under optimal shot peening conditions. On the other hand, it was observed that shot peening is not beneficial, even detrimental, in low cycle fatigue. The results analysis allowed to define a list of shot peening recommendations

to maximize the fatigue life of shot peeneed Inconel 718. The main one is that the shot peening intensity should be as low as possible to minimize the resulting surface roughness but it should be sufficiently high to induce compressive residual stresses that will repel crack initiations underneath the surface.

The experimental results allowed to calibrate and develop an analytical model adapted from the Navarro and de los Rios propagation model and the Chan's crack initiation model. Both models were modified to account for the residual stresses and cold work redistribution, which were found to have significant effects on the fatigue life. These two models, enhanced and coupled, predicted the fatigue life and for the first time, the crack initiation location on unpeened and shot peeened Inconel 718 specimens.

An experimental campaign was also performed to study the effects of edge geometries, under several shot peening and loading conditions, on the formation of rolled edges and the resulting fatigue life. This study, which is the first one of its kind in the open literature, allowed to make recommendations for the design of edge geometries intended to be shot peened, such as the avoidance of sharp edges and high shot peening intensities.

This thesis presents one of the most exhaustive mechanical characterization of shot peened Inconel 718. Its results and the developed model are useful tools that could be used in the optimization of shot peening conditions aiming at maximizing Inconel 718 fatigue life.

TABLE OF CONTENTS

LIST OF TABLES

LIST OF FIGURES

LIST OF SYMBOLS AND ABBREVIATIONS

Latin symbols

A_1	Paris relation fitting constant
A_2	N-R model parameter
B_j ($j = 1$ to 5)	Residual stress profile fitting constants
C_j ($j = 1, 2$)	Back stress fitting constants
$CTOD$	Crack's tip opening displacement
D	Grain size
D_{exp}	Experimental estimated decile
D_{init}	Subsurface crack initiating grain size
D_{theo}	Theoretical decile
$\bar{D}_{theo}$	Average of the theoretical deciles
E	Young modulus
F	Cost function
G	Shear modulus
I_1	First stress invariant
J_2	Second stress invariant
J_3	Third stress invariant
K	Stress intensity factor
K_{max}	Maximum stress intensity factor within a fatigue cycle
K_{min}	Minimum stress intensity factor within a fatigue cycle
K_{to}	Surface stress concentration factor
K_t	Stress concentration factor
M	Taylor factor
N	Number of cycles
$N_{data,i}$	Total number of data point of the i^{th} experiment
N_{exp}	Total number of experiments
N_f	Number of cycles to failure
$N_{f,max}$	Maximum fatigue life
$N_{f,min}$	Minimum fatigue life
$N_{fav,4A}$	Average fatigue life of CW14 and S230 4A specimens
N_{init}	Number of cycles for crack initiation within a grain
N_{NR}	Number of cycles to failure predicted by the N-R model
$Nb(a_{NR})$	Number of N-R model predicted crack length in the range of the

	experimentally observed a_{rep}
P_j ($j = 1$ to 4)	Full width at half minimum versus the plastic strain relationship fitting constants
Q	Elastic field size saturation value
R	Yield surface evolution
R^2	Coefficient of determination
$R_\varepsilon = \frac{\varepsilon_{min}}{\varepsilon_{max}}$	Strain ratio
$R_\sigma = \frac{\sigma_{min}}{\sigma_{max}}$	Stress ratio
$R_{\sigma,RS}$	Stress ratio accounting for the residual stresses
RSm	Mean width of surface roughness profile elements
R_t	Surface roughness profile height between the deepest valley and the highest peak
$\frac{1}{2}S_2$	X-ray elastic constant
Y	Crack geometry factor
Y_j ($j = 1$, 2)	Yield strength profile fitting constants
Z	Notch factor influence on a source of dislocations
a	Crack length
a_j ($j = 1$, 2)	Back stress fitting parameters
a_c	Crack length when the plastic zone is about to spread in the next grain
a_{NR}	N-R model predicted crack length
a_{rep}	Monitored short crack's depth
a_s	Crack length when the plastic zone has just spread in the next grain
a_{th}	Mechanical threshold
b	Burgers vector
b_j ($j = 1$, 2)	Cold work profile fitting constants before fatigue testing
c	Crack plus plastic zone length
$d_{\sigma_{\text{comp,max}}}$	Maximum compressive residual stress depth
$d_{\sigma_{\text{comp=0}}}$	Depth at which the residual stresses becomes tensile
f	Flow plasticity function
h	Slip band width
i	Number of half grains the plastic zone has propagated through
k	Initial yield strength
m	Grain orientation factor
m_1	Paris relation fitting constant
m_2	N-R model parameter
$n = \frac{a}{c}$	Ratio of the crack length on the crack plus plastic zone length

$n_c = \frac{a_c}{c}$	n when the plastic zone is about to spread in the next grain
$n_s = \frac{a_s}{c}$	n when the plastic zone has just spread in the next grain
p	Total accumulated plastic strain
q	Yield surface hardening rate
r_0	Distance between the grain boundary and the source of dislocations
w_j $(j = 1, 2)$	Fitting constants for short crack propagation growth rate
x_{depth}	Crack tip's depth
x_e	Residual stress profile fitting constant
x_d	Residual stress profile fitting constant
x_{init}	Subsurface crack initiation depth

Greek symbols

$\Delta K = K_{max} - K_{min}$	Stress intensity factor range
ΔK_{th}	Long crack stress intensity factor range threshold
$\Delta\varepsilon_{tot}/2 = \frac{\varepsilon_{max} - \varepsilon_{min}}{2}$	Strain amplitude
$\Delta\sigma = \sigma_{max} - \sigma_{min}$	Stress range
$\Delta\sigma/2 = \frac{\sigma_{max} - \sigma_{min}}{2}$	Stress amplitude
$\Delta\sigma_{FL,RS}$	Fatigue endurance (10^8 cycles) stress range accounting for the residual stresses
α	Notch's depth
α_d	Dimple's depth
β	Notch's half width
β_d	Dimple's half width
β_w	Weibull distribution's shape factor
γ_j $(j = 1, 2)$	Elastic field size evolution fitting parameters
λ_w	Weibull distribution's scale factor
λ_{res}	X-ray wavelength
$\dot{\varepsilon}$	Strain rate
ε_{max}	Maximum strain within a cycle
ε_{min}	Minimum strain within a cycle
ε_p	Plastic strain
ν	Poisson's ratio
σ	Applied stress
σ_1	Crack closure stress
σ_2	Stress required to trigger plastification at the crack's tip
σ_3	Resulting stress on the source of dislocations

σ_{arrest}	Minimum σ_3 required to activate a source of dislocation
$\sigma_{arrest,Z}$	σ_{arrest} accounting for Z
$\sigma_{\text{comp,max}}$	Maximum compressive residual stress
σ_{exp}	Experimentally measured stress
σ_{FL}	10^8 cycles fatigue limit
σ_{FL}^{SP}	Shot peened 10^8 cycles fatigue limit
$\sigma_{FL,R_\sigma=-1}$	Maximum fatigue endurance (10^8 cycles) stress at $R_\sigma = -1$
σ_{max}	Maximum stress within a fatigue cycle
σ_{min}	Minimum stress within a fatigue cycle
σ_{num}	Predicted stress
σ_{RS}	Residual stresses
σ_{surf}	Surface residual stress
σ_u	Ultimate tensile strength
σ_y	Yield strength
$\sigma_{y0.2\%}$	0.2 % offset yield strength
$\sigma_{y0.05\%}$	0.05 % offset yield strength
τ_f	Friction shear stress
χ	Back stress
$\zeta = \frac{x}{c+r_0}$	Non-dimensional N-R model coordinate

Abbreviations

1D	One-dimensional
3D	Three-dimensional
AR	Area reduction at failure
Av	Average
ASTM	American society for testing and materials
Bal	Balance
CRIAQ	Consortium for research and innovation in aerospace in Quebec
CT	Compact test
Conf	Confidence
El	Elongation at failure
EPFM	Elastic-plastic fracture mechanics
FE	Finite element
FCC	Face-centered cubic
FWHM	Full width at half-maximum intensity
HCF	High cycle fatigue

LB	Lower bound
LCF	Low cycle fatigue
LEFM	Linear elastic fracture mechanics
MFM	Microstructural fatigue mechanics
Nb	Number
NSERC	Natural sciences and engineering research council of Canada
Prob	Probability
PSB	Persistent slip band
SAE	Societe of automotive engineers
XRD	X-ray diffraction

LIST OF APPENDICES

CHAPTER 1 INTRODUCTION

Nickel-based superalloy Inconel 718 is largely used in gas turbine components, such as shafts or turbine disks and blades. In service, Inconel 718 components are submitted to high frequency low amplitude (vibrations resulting from minor misalignments) and low frequency high amplitude (take off, cruise and landing) cyclic loads. Fatigue prediction for such critical components is therefore of paramount importance in the industry. Fatigue life prediction capabilities are usually limited to the set of parameters (microstructural features, loading conditions, etc...) tested during experimental campaigns. Experimental campaigns are expensive due to the cost of: the base material (more than 50 USD per kg), the machining, the time required for fatigue tests (several hours or days per specimen) and the fatigue results analysis (statistical analysis, fractography, use of scanning electron microscope). In this context, the development of a fatigue life prediction model taking into account microstructural and manufacturing characteristics would provide the aerospace industry with an opportunity to improve the performance of its components and reduce the costs associated with extensive experimental campaigns.

Shot peening is a coldwork process consisting in projecting high velocity particles onto a ductile metallic part to introduce surface compressive residual stresses and hardening, which both retard crack initiation and propagation. However, shot peening may also increase surface roughness and create rolled edges, which have a detrimental effect on fatigue life. Therefore, the fatigue life improvement brought by shot peening is a compromise between its detrimental and its beneficial effects and optimal shot peening conditions have to be determined. The standards used to select shot peening parameters in the industry were established in the 60's and their validity was hardly questioned ever since. As a consequence, shot peening is usually not accounted for at the design stages in the aerospace industry, but seen as a safety margin. Heavier components than what could safely be used are thus produced, which is critical since nickel-based superalloys constitute more than 50 % of the weight of jet engines.

To reduce costly trial and error experimental campaigns, a fatigue life predictive model that accounts for the material's macro and micro-mechanical properties, and their alteration induced by shot peening, would be an important asset.

In that context, four leading aerospace companies (Pratt & Whitney Canada, Bell Helicopter Textron Canada, L3-Communications MAS and Héroux-Devtek) pooled their resources to fund a large scale four-year project aiming at predicting the effects of shot peening on three materials (Inconel 718, Aluminum 7050 T7-451 and Steel 300M). The project in-

volved 1 research associate, 1 MSc student, 5 PhD candidates and 4 post-doctoral fellows enrolled in 3 universities (École Polytechnique de Montréal, McGill University and École de Technologie Supérieure). The project was financially supported by the Consortium for Research and Innovation in Aerospace in Quebec (CRIAQ), the Natural Sciences and Engineering Research Council of Canada (NSERC) and the Mathematics of Information Technology and Complex Systems (MITACS).

This thesis aims at developing a model that analytically predicts fatigue cracks initiation and propagation in shot peened Inconel 718 with the final objective of predicting fatigue life. The model must be applicable, at room temperature, to two stress levels and three different peening conditions.

The thesis is organized as follows: A literature survey is conducted in Chapter 2 to determine, in Chapter 3, the specific objectives. The scientific approach performed to fulfill the specific objectives is described in Chapter 4. Chapters 5 to 9 present the fulfillment of the specific objectives through 2 published and 2 submitted journal articles. The findings of this thesis are discussed in Chapter 10. Finally, the conclusions of this work as well as recommendations for future work are provided.

CHAPTER 2 LITERATURE SURVEY

2.1 Fatigue generalities

2.1.1 Definition

Fatigue can be defined as "*failure due to repeated loading. In general, one or more tiny cracks start in the material, and these grow until complete failure occurs*" (Dowling, 2013). In this context, the study of fatigue encompasses cracks initiation and propagation due to cyclic loading.

2.1.2 Long cracks

Cracks are usually divided in two kinds: 1) the short cracks and 2) the long cracks. The propagation of mechanically long cracks obeys to the linear elastic fracture mechanics (LEFM). LEFM based models are considered applicable when the crack is approximately 8 times longer than the crack's tip plastic zone radius (Dowling, 2013) created by the stress concentration. In LEFM, crack propagation is assumed to occur in a linear-elastic medium and the crack's tip stress and displacement can be characterized independently of the microstructure with only one parameter: the stress intensity factor K. "K *is a measure of the severity of a crack situation as affected by crack size, stress, and geometry*" (Dowling, 2013). Considering a loading cycle with an applied stress range $\Delta\sigma = \sigma_{max} - \sigma_{min}$, the associated stress intensity factor range $\Delta K = K_{max} - K_{min}$ can be calculated from Irwin's model (Irwin, 1957) as

$$\Delta K = Y \Delta\sigma \sqrt{\pi a} \tag{2.1}$$

where Y is a factor depending on the crack and the specimen geometries and a is the crack length. K depends on the crack length and the applied stress. A crack submitted to a low applied stress range can have the same stress intensity factor as a shorter crack submitted to a higher stress range.

The ΔK under which no long crack can propagate is the long crack stress intensity factor range threshold, ΔK_{th}.

The material's toughness K_c, corresponding to the stress intensity factor triggering a brutal rupture, is a material constant in plain strain condition. In other words: brutal rupture occurs when K_{max} reaches K_c . K_c also depends on the crack opening mode. The three crack opening modes are depicted in Figure 2.1: mode I corresponds to an opening

mode while mode II and III are shearing modes.

In the region $\Delta K > \Delta K_{th}$ but for which $K_{max} < K_c$, the crack growth rate $\mathrm{d}a/\mathrm{d}N$ can be approximated by the Paris relation (Paris and Erdogan, 1963) as

$$\frac{\mathrm{d}a}{\mathrm{d}N} = A_1 \Delta K^{m_1} \tag{2.2}$$

where A_1 and m_1 are material dependent fitting constants. Crack closure phenomena are not accounted for in the Paris relation and the constants A_1 and m_1 also depend on the applied stress ratio. The crack growth rate of a long crack as a function of the stress intensity factor range is schematically represented in Figure 2.2.

2.1.3 Short cracks

A crack is said to be short when it satisfies one of the following conditions (Ritchie and Lankford, 1986): 1) microstructurally short: its length is small when compared to the grain size, 2) mechanically short: its length is small when compared to surrounding or crack's tip plastic zone, 3) physically small: its length is inferior to 1 mm and 4) chemically small: the crack evolves in an environment different from the bulk material. The LEFM cannot be used for the microstructurally and mechanically short cracks because of the non-continuity of the medium and the propagation of the crack in an elastic-plastic medium, respectively (Suresh and Ritchie, 1984).

It is commonly accepted in the literature that short cracks behavior can be divided in two stages (illustrated in Figure 2.2), namely:

1. Stage I: Crack initiation and propagation within the first grains. At this point, the crack is microstructurally small and highly dependent on the microstructure. Miller (1993) calls it the regime of microstructural fatigue mechanics (MFM). The crack is fully driven by shear stress. Propagation will not occur if the crack's driving force is not sufficient to overpass the first microstructural barrier. This phenomenon is called the microstructural threshold. This process can be repeated several times.

2. Stage II: The crack monotically grows and obeys to the elastic-plastic fracture mechanics (EPFM), in which significant plasticity occurs at the crack's tip (Miller, 1993). The crack is mechanically short.

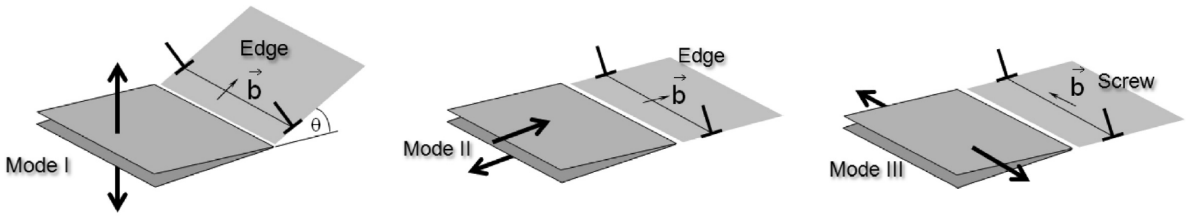

(a) (b) (c)

Figure 2.1 Three rupture modes: (a) opening mode, (b) sliding mode and (c) tearing mode (Chowdhury *et al.*, 2014)

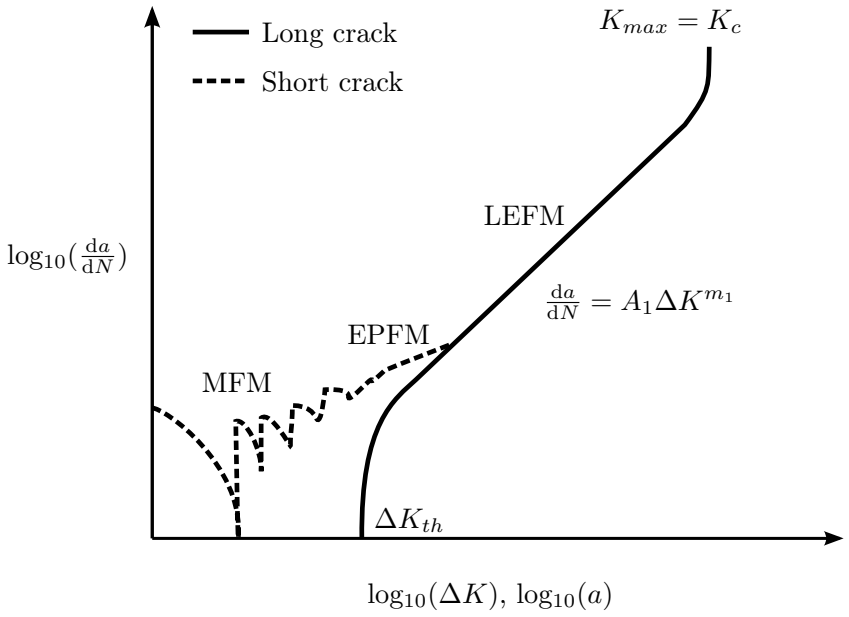

Figure 2.2 Schematic representation of short and long cracks behavior. The full line represents the long crack propagation rate as a function of the stress intensity factor range and the dotted line represents the short cracks behavior as a function of the crack length. The three different mechanical regimes (MFM, EPFM and LEFM) are identified. The Paris relation, the material toughness and the stress intensity factor range threshold are also represented

2.2 Inconel 718 mechanical and fatigue properties

2.2.1 Chemical and monotonic mechanical properties

Chemical properties

Inconel 718 is an austenitic face-centered cubic (FCC) matrix having the chemical composition presented in Table 2.1 (SAE-Aerospace, 2009). The matrix is strengthened with two kinks of γ precipitates: γ' ($Ni_3(Ti-Al)$ and γ'' ($Ni_3(Nb-Ti)$). Inconel 718 also contains second phase δ particles (Ni_3Nb) located along the grain boundaries and within the grains. The presence of NbC and TiN particles has also been reported (Alexandre *et al.*, 2004; Xiao *et al.*, 2008).

Mechanical properties

Inconel 718 minimal monotonic tensile properties (SAE-Aerospace, 2009) are presented in Table 2.2.

2.2.2 Crack initiation in Inconel 718

Initiation at persistent slip bands

When a component is cyclically loaded, slip bands appear in the surface grains having their slip systems oriented in which the maximum shear stress is developed (Sangid, 2013).

Table 2.1 Inconel 718 chemical composition (weight %) (SAE-Aerospace, 2009). Bal.: balance

	Fe	Ni	Cr	Mo	Ti	Al
Minimum	Bal.	50.00	17.00	2.80	0.65	0.20
Maximum	Bal.	55.00	21.00	3.30	1.15	0.80

Table 2.2 Minimal requirements for Inconel 718 monotonic tensile properties (SAE-Aerospace, 2009). EL: elongation at failure and AR: area reduction at failure

σ_u (MPa)	$\sigma_{y0.2\%}$ (MPa)	EL (%)	AR (%)
1276	1034	12	15

In the case of Inconel 718, which is composed of FCC crystals, the slip systems favorable to the maximum shear stress are the {111} planes. Slip bands along the {111} planes have been clearly observed by Xiao *et al.* (2008) with a transmission electron microscope under plastic deformation. Slip bands are constrained within the grain. Dislocations move forward and backward along those slip bands during cyclic loading and create persistent slip bands (PSB). At the component's surface, PSB create intrusion and extrusion features (Maderbacher *et al.*, 2013). According to Sangid (2013), this local plastification leads to a difference of hardness between the slip bands and the rest of the grain. Cracks initiate at the interface between the two zones. The largest grains are more subjected to crack initiation because: 1) the largest grains are less constrained by the surrounding microstructure and are more subjected to deformation (Keller *et al.*, 1989), 2) the dislocation density is initially lower in the largest grains, which results in longer free path for the dislocations (Keller *et al.*, 1989) and 3) the longer PSB result in longer initial cracks (Miao *et al.*, 2009).

Stinville *et al.* (2015) have shown that the maximum strain occurs at twin boundaries favorably oriented in the nickel-based superalloy René 88DT (similar to Inconel 718). Texier *et al.* (2016) observed that, when the crack initiation occurred in a grain, it was near a twin boundary in Inconel 718. Figure 2.3 shows a crack that initiated at a twin boundary in a nickel-based superalloy René 88DT tested under a strain ratio $R_\varepsilon = -0.75$ and a maximum applied strain of $\varepsilon_{max} = 0.40$ %. It suggests that twin boundaries are microstructural weaknesses for crack initiation in nickel-based superalloys.

Initiation at non metallic inclusions

TiN and NbC inclusions are sources of crack initiation in Inconel 718, especially in the presence of fine grains (Alexandre *et al.*, 2004). According to Alexandre *et al.* (2004) and Texier *et al.* (2016), NbC cracking can occur during the first monotonic tensile loading. Figure 2.4 shows a non metallic inclusion that cracked during a tensile test interrupted at 80 % of the yield strength (Texier *et al.*, 2016). Zhou *et al.* (2012) showed that surface NbC carbides can also be damaged during the machining process. Crack initiation near, or at, non metallic inclusions are due to the difference in elasticity between the particles and the material's matrix (Texier *et al.*, 2016).

2.2.3 Short crack propagation

PSB lead to stress concentrations at grain boundaries. These stress concentrations increase with the number of cycles and can trigger PSB in an adjacent grain having a close crystal orientation (Sangid, 2013).

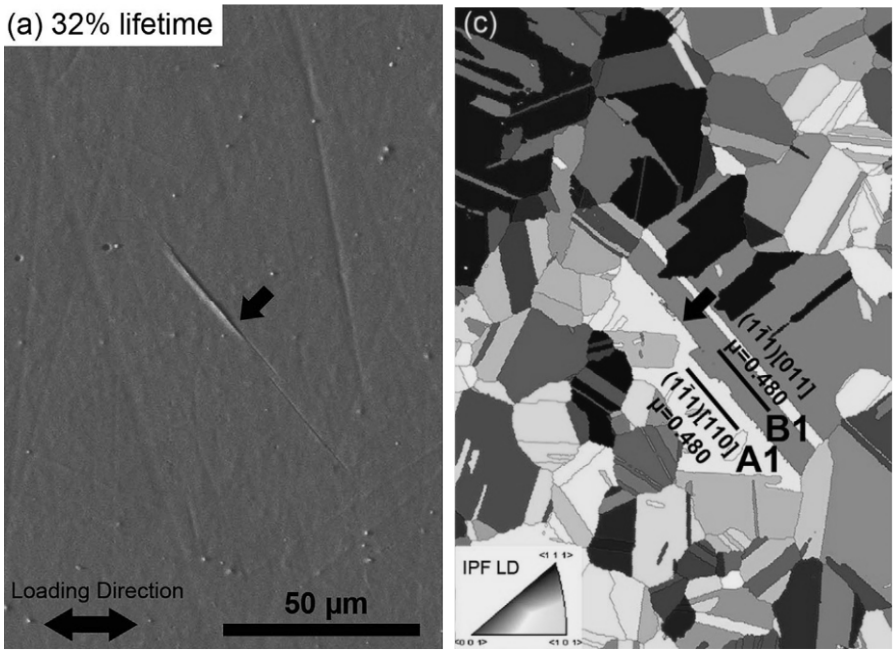

(a) (b)

Figure 2.3 Crack initiation at a twin boundary in René 88DT (Stinville *et al.*, 2016): (a) a crack can be observed on the surface of the specimen at 32 % of the fatigue life and (b) the associated electron backscatter diffraction picture taken prior to fatigue testing. The arrow presents on each picture points toward the same location

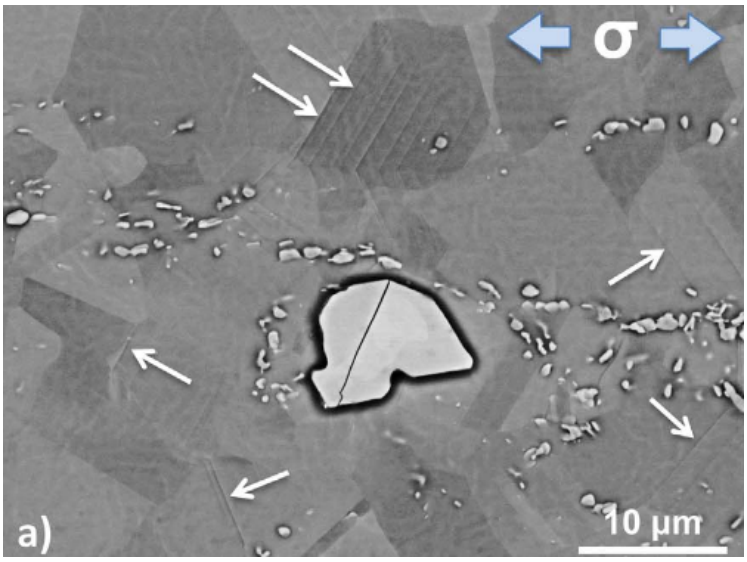

Figure 2.4 Micrograph of a non metallic inclusion cracked during an interrupted tensile test at 80 % of the yield strength (Texier *et al.*, 2016). The arrows show the presence of PSB in favorably oriented grains

A crack typically re-orients when it propagates from a grain to the next due to its crystal orientation dependence. This phenomenon has been observed by Maderbacher *et al.* (2013) in Inconel 718, as shown in Figure 2.5(a), where two short cracks following the PSB of several grains can be observed. This propagation mechanism leads to a faceted failure surface that has been called "*quasi-cleavage feature*" by Mills and Brown (2001) and Ma *et al.* (2010). Figure 2.5(b) shows a crack initiation site and a faceted rupture surface in Inconel 718. These propagation mechanisms are characteristic of the MFM and the beginning of the EPFM regimes and define stages I and II (Miller, 1993).

Most of the fatigue life is spent in the MFM and EPFM regimes. Indeed, Chen *et al.* (2000) observed crack lengths inferior to 0.1 and 1 mm at 80 % of the fatigue life for Inconel 718 specimens tested in rotating bending fatigue under stress amplitudes of 64 % and 42 % of the yield strength, respectively. For higher applied stress levels (shorter fatigue lives), the crack propagation rate is higher and the crack length before brutal rupture is inferior than for lower applied stress due to the higher stress intensity at the crack's tip. This explains why at 80 % of the fatigue life the crack length decreases when the applied load increases. It can be concluded that crack initiation and short crack propagation represents the major part of the total fatigue life. Modelling the propagation kinetic of short cracks is therefore important for fatigue life prediction.

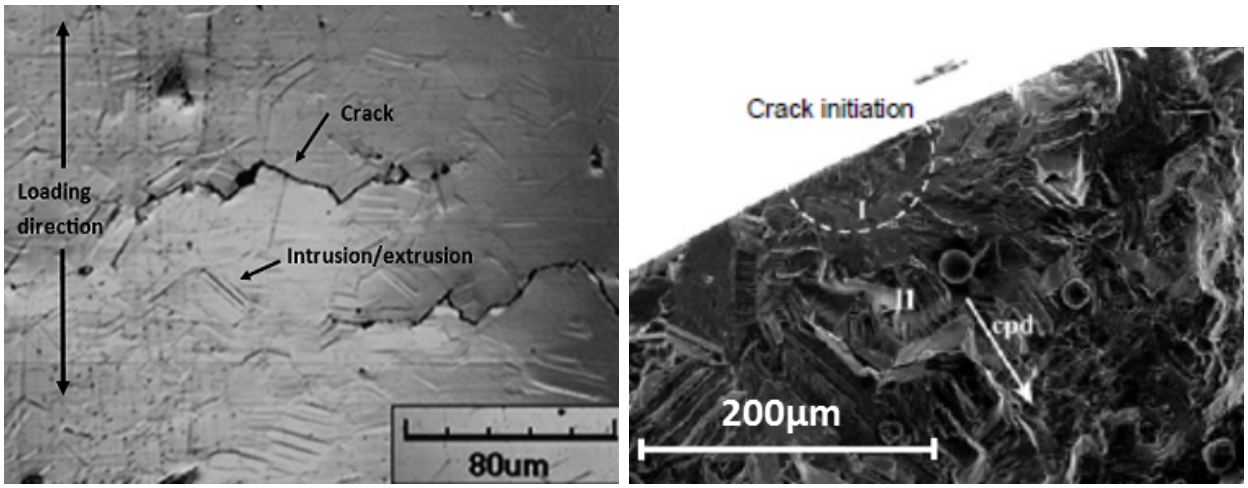

(a) (b)

Figure 2.5 Stage I and II observations: (a) Persistent slip bands causing intrusions and extrusions on the specimen's surface. Crack propagation follows the persistent slip bands (Maderbacher *et al.*, 2013) and (b) Scanning electron microscope picture of crack initiation and short crack propagation on Inconel 718. I is the crack initiation site, II is the faceted site and cpd shows the crack propagation direction (Ma *et al.*, 2010)

2.2.4 Long crack propagation

At the end of stage II (EPFM regime), striations can be observed on Inconel 718 rupture surface and the crack enters in the LEFM regime (Ma *et al.*, 2010). In LEFM, Inconel 718 crack growth rate can be modeled with the Paris relation (Chen *et al.*, 2000). The crack will propagate until the K_c value is reached, leading to the apparition of dimples on the rupture surface due to ductile rupture (Ma *et al.*, 2010). At this point, the specimen is close to brutal rupture.

2.2.5 Cyclic yield properties evolution and predictions

Fournier and Pineau (1977) showed that the plastic strain is homogeneously distributed during the first cycles when Inconel 718 is submitted to low cycle fatigue (LCF) at a strain ratio $R_\varepsilon = -1$. While cycling, the material hardens due to dislocations pileups, PSB are subsequently formed and the material softens due to the γ'' particles shearing (Xiao *et al.*, 2005, 2008). Softening has not been shown to stabilize and its rate increases with the applied strain amplitude (Sudarshan Rao *et al.*, 2012).

Tong *et al.* (2004) and Zhan and Tong (2007) successfully used Chaboche's constitutive equations (Chaboche and Rousselier, 1983) to predict nickel-based alloys mechanical behavior at 650 °C and for $R_\varepsilon = 0$. The authors identified the initial yield strength as 150 MPa, while it is typically of the order of 1000 MPa, which rises questions on the model's validity. Chaboche's constitutive equations, which account for cyclic hardening, ratcheting and Bauschinger effect (Lemaitre *et al.*, 2009) are based on the flow stress evolution expressed with the scalar flow function f as

$$f = J(\sigma - \chi) - R - k \tag{2.3}$$

where σ is the applied stress, R is the isotropic hardening, k is the initial yield strength and J is a stress invariant commonly chosen as the von Mises stress invariant in 1D. The elastic regime is defined as $f < 0$ and the plastic regime as $f = 0$. The back stress χ can be expressed, for a nickel-based superalloy (Zhao *et al.*, 2001), as a Armstrong and Frederick (Armstrong and Frederick, 1966) kinematic hardening rule as

$$\begin{aligned} \chi &= \chi_1 + \chi_2 \\ \chi_i &= a_i(1 - e^{-C_i\varepsilon_p}) \qquad i = 1, 2 \end{aligned} \tag{2.4}$$

where ε_p is the plastic strain within a half cycle and parameters a_i and C_i are material constants.

The isotropic hardening is commonly expressed as

$$R(p) = Q\left(1 - e^{-qp}\right) \tag{2.5}$$

where p is the accumulated plastic strain, q is the elastic field size hardening rate and Q is the elastic field saturation value. Equation (2.5) would not be suitable for Inconel 718 since it cannot represent continuous softening.

2.3 Shot peening

2.3.1 Definitions

Almen intensity: Almen intensity is a measure of the shot peening intensity commonly used in the industry. A flat steel strip, called Almen strip, is shot peened. The Almen strip bends due to the shot peening induced compressive residual stresses on its surface. The Almen strip's arc height is measured and converted into Almen (A) units; 1 A = 25.4 μm. Almen strips are shot peened for different periods of time. Saturation is reached when the shot peening time is doubled and the increase of the Almen strip's arc height is less than 10 %. Almen intensity correspond to the deflection of the Almen strip at saturation.

Coverage: Shot peening creates dimples on a specimen surface. A coverage between 0 % and 100 % is the percentage of the shot peened surface covered by dimples. A coverage beyond 100 % corresponds to a multiple of the shot peening time needed to reach 98 % coverage. For example, 150 % coverage equals 1.5 times the shot peening time needed to reach 98 % coverage.

2.3.2 Optimization of shot peening

Shot peening introduces compressive residual stresses and work hardening on the specimen surface. de los Rios *et al.* (1995) showed that shot peening delays both crack initiation and crack propagation in A316 stainless steel. According to de los Rios *et al.* (1995), in addition to the crack closure effect due to the compressive residual stresses, the work hardening increases the resitance to plastic deformation at the crack's tip. The authors also concluded that the microstructural threshold is not the critical stage for crack propagation in shot peened specimens but it is instead the generation of enough plastic deformation at the crack's tip.

Gao and Wu (2011) also observed that short crack growth rates were significantly reduced in aluminum alloy 7475-T7351 shot peened with S110 steel shots at a peening intensity of 8 A. The authors attributed this beneficial effect to the compressive residual stresses.

Sufficient surface plastic deformation can result in the formation of a nanocrystalline surface layer (Sato *et al.*, 2004). Liu *et al.* (2007) showed that shot peening can also lead to a grain refinement at the shot peened surface. Bagherifard and Guagliano (2012) observed that the hardness and the fatigue strength of low-alloy steel is increased by the presence of a nanocrystalline surface layer.

However, the dimples created at the specimen's surface are stress concentration features (Li *et al.*, 1992). Bagherifard and Guagliano (2012) observed that the roughness increased with the shots impact energy and that the beneficial effects of shot peening on fatigue life (nanocrystalline layer, surface hardening and compressive residual stresses) were masked by the surface defects induced during severe shot peening. Bagherifard *et al.* (2014) reached the same conclusions on shot peened cast iron.

The fatigue life of a shot peened specimen is thus a trade-off between its beneficial (compressive residual stresses, grain refinement and work hardening) and detrimental (surface roughness) effects. Wagner (1999) experimentally showed, in a magnesium AZ 80 alloy, that using a peening intensity below or upon the optimal value resulted in a decrease of the fatigue life.

2.3.3 Shot peening effects on Inconel 718

In Inconel 718, Prevéy (2000) showed that the compressive residual stresses can reach -1000 MPa and that the cold work can be as high as 40 % at the surface after shot peening at an intensity of 8 A and for a coverage of 200 %. For the same shot peening conditions, the depth of the compressive residual stresses is roughly 200 μm. A typical compressive residual stress profile is presented in Figure 2.6(a).

Cammett *et al.* (2005) studied the effect of the coverage on the induced cold work and residual stresses in Inconel 718. The authors shot peened Inconel 718 with CW14 shots at a peening intensity of 9 A. The coverage varied from 61 % to 400 %. The surface compressive residual stresses were between 1000 and 1100 MPa for all the coverages tested. Cammett *et al.* (2005) reported that no specific trend in the depth of compression was observed.

Zaleski *et al.* (2017) studied the effects of shot peening on the surface roughness of Inconel 718. The authors reported that, for a constant impact energy of 180 mJ, a decrease of the shots diameter increased the resulting surface roughness. They also reported that

increasing the impact energy up to 180 mJ reduced the surface roughness when compared to as machined specimens. However, for impact energies higher to 180 mJ, they observed that the roughness increased with the impact energy.

Few papers deal with shot peened Inconel 718 room temperature fatigue performances. Nakamura *et al.* (2011) performed strain controlled low cycle fatigue tests at $R_\varepsilon = 0$ on Inconel 718 shot peened with S110 shots at a peening intensity comprised between 4 and 8 A and a 100 % coverage. The authors observed that, for a 10^4 cycles fatigue life at room temperature, shot peened Inconel 718 can withstand a strain range 1.3 times larger than an unpeened polished specimen. All the crack initiations occurred at the specimens surface.

In high cycle fatigue (HCF), Cammett *et al.* (2005) observed that Inconel 718 fatigue limit (defined at 10^7 cycles) increased from a maximum applied stress of 550 MPa, under a stress ratio of 0.1, for unpeened specimens to 690 MPa (25 % increase) for specimens shot peened with CW14 shots at an intensity of 9 A with a 100 % coverage. All crack initiations on shot peened specimens occurred beneath the surface at a depth corresponding to the depth of compression of the residual stress profile, as shown in Figure 2.6(b). Note that the specimens were exposed to a temperature of 525 °C during 100 hours after peening. The surface compressive residual stresses totally relaxed during the thermal exposure and the maximum compressive residual stresses were around -800 MPa at a depth of 100 μm while they were of -1000 MPa before the thermal exposure. Cammett *et al.* (2005) results suggest

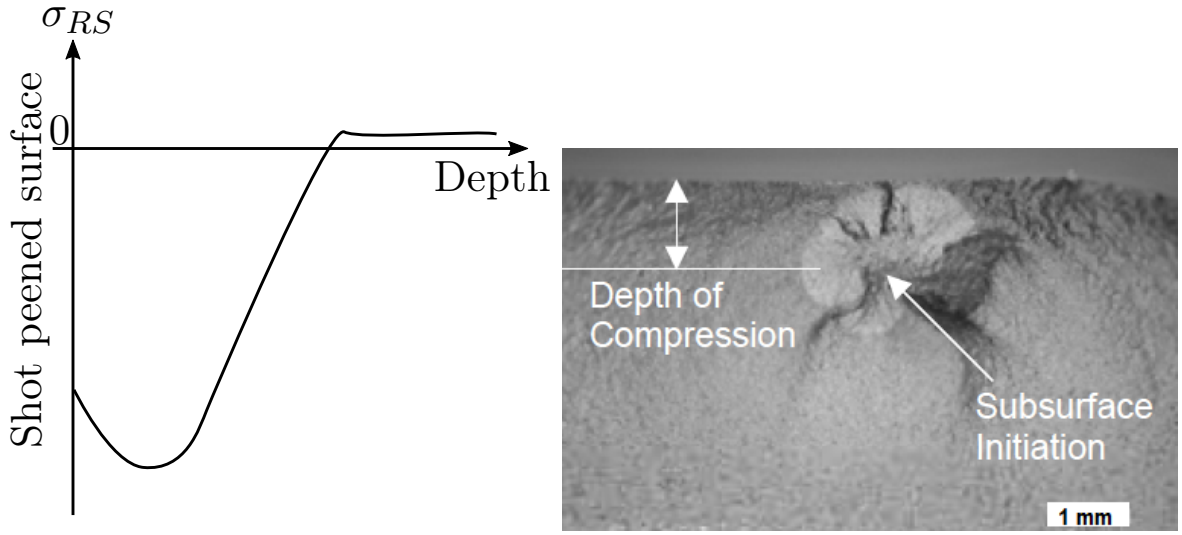

(a) (b)

Figure 2.6 (a) Typical residual stress (σ_{RS}) profile induced by shot peening. (b) Subsurface crack initiation in shot peened Inconel 718 (Cammett *et al.*, 2005)

that Inconel 718 fatigue limit at 10^7 cycles could be increased by more than 25 % when compared to unpeened specimens in the absence of a thermal exposure after shot peening.

2.3.4 Residual stress relaxation

Hoffmeister *et al.* (2012) showed that Inconel 718 residual stresses are mostly redistributed during the first fatigue cycle at a strain ratio of 0. The amplitude of the redistribution mainly depends on the cold work profile and the loading conditions (Prevéy, 2000; Zhuang and Halford, 2001). Kirk (1987) observed that, on several materials including pure nickel, compressive residual stresses introduced by shot peening can redistribute and become tensile at the surface after one monotonic tensile loading higher than the material's yield strength. This compressive to tensile redistribution is due to the difference in yield strength between the shot peened affected surface layer and the bulk material. This phenomenon was also observed by Madariaga *et al.* (2015) for residual stresses induced by machining in Inconel 718. Similar results on Inconel 100 were successfully simulated with a finite element model by Buchanan and John (2014). These results are very important since they show that the compressive residual stresses, which are a beneficial effect of shot peening, can become a drawback when the applied tensile stress overcomes the material's yield strength.

2.3.5 Rolled edges

Edges (chamfers, sharp edges or rounded edges) are present on most industrial parts. During the shot peening process, the shots plastically deform these edges, as depicted in Figure 2.7. The deformation of an edge can create a stress concentration feature commonly called "*rolled edge*" (Figures 2.7(d) and 2.8). Minimizing rolled edges formation is of paramount importance for the industry since they act as stress concentration features and have a detrimental effect on fatigue life (He *et al.*, 2013).

To the best of the author's knowledge, rolled edge effects on fatigue life have only been studied by He *et al.* (2013) and You *et al.* (2017) in the open literature and they were called "*shot peening lips*". He *et al.* (2013) showed that, on a martensitic steel tested in bending fatigue under a strain ratio $R_\varepsilon = 0.1$, the fatigue lives were 10^5, 3×10^5 and 10^7 cycles for an unpeened specimen, a shot peened specimen with rolled edges and a shot peened specimen without rolled edges, respectively. It suggests that the presence of rolled edges reduces the fatigue life improvement potential of the shot peening process. In addition, to the best of the author's knowledge, the impact of the edge geometry, prior to shot peening, on the rolled edges formation has never been studied in the open literature.

Note that similar phenomena can be observed on specimen edges after laser cutting (Pessoa *et al.*, 2016) where burrs in the form of re-solidified drops are formed at the cutting edges. Pessoa *et al.* (2016) showed that these burrs decreased the fatigue life of stainless steel 304.

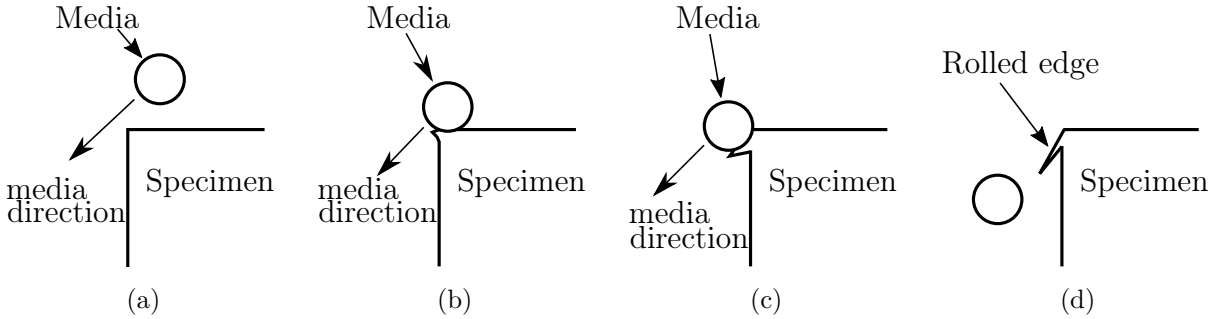

Figure 2.7 Schematic description of a rolled edge formation. (a) The media approaches the edge. (b) The media starts to deform the edge. (c) The media deforms the edge. (d) The created rolled edge acts as a stress concentration feature

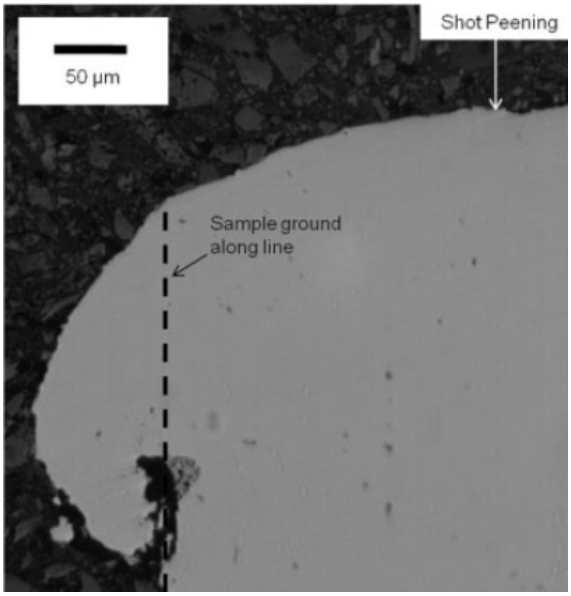

Figure 2.8 Rolled edge formed on a specimen's edge during the shot peening process (He *et al.*, 2013)

2.4 Short crack initiation and growth analytical prediction models

2.4.1 Number of cycles to crack initiation

There is no consensus on the definition of crack initiation. The number of cycles to crack initiation is commonly defined in the literature as the number of cycles at which a crack becomes long enough to be observed. For example, it was 50 μm and 25 μm in de los Rios *et al.* (1995) and Morino *et al.* (2007) studies, respectively.

Several models that predict the number of cycles to crack initiation exist. However, to the best of the author knowledge, the only analytical model able to predict the number of cycles to initiate a crack of a given length is Chan (2003)'s adaptation of Tanaka and Mura (1981) slip bands initiation model. This model was successfully used by Ma *et al.* (2010) to predict the number of cycles for crack initiation in Inconel 718. The number of cycles N_{init} to initiate a crack of length a_0 can be calculated as

$$N_{init} = \frac{8G^2M^2h^2\frac{a_0}{2}}{0.005\pi\left(1-\nu\right)D^3\left(\Delta\sigma - 2M\tau_f\right)^2} \tag{2.6}$$

where D is the grain size, G is the shear modulus, ν is the Poisson's ratio, M is the Taylor factor and τ_f is the frictional shear stress. The slip band width h is challenging to measure and is usually used as a fitting constant (Chan, 2003).

The Taylor factor M is used to compute the resolved shear stress in a grain located in a polycrystal metal as $\sigma = M\tau$. When the preferential slip plane of a grain is favorably oriented (in a 45° direction from the applied stress), $M = 2$ and $\sigma = 2\tau$. Crack initiation is supposed to occur in a favorably oriented grain and $2M\tau_f$ can thus be approximated as the applied stress range under which crack initiation does not occur (Chan, 2003). The model does not account for residual stresses such as the ones induced by shot peening.

2.4.2 Microstructurally short crack growth prediction

Stage I crack propagation is challenging to predict due to the several accelerations and decelerations induced by the crack propagation dependence on the microstructure.

Hobson (1982) proposed a model that accounts for crack growth rate deceleration at the first grain boundary. This model is unable to predict the crack accelerations and decelerations due to the other grain boundaries that the crack will encounter. Chan and Lankford (1983) developed a short crack model based on the reduction of the crack's tip strain near a grain boundary. The orientation of adjacent grains is considered to be the same, which leads to

little to no variation in the crack growth rate predictions. McEvily *et al.* (1991) relied on a modification of LEFM models that account for short cracks. However, the model does not account for crack's accelerations and decelerations. As reported by Hussain (1997) in an extensive literature review, these models do not, or just in certain particular cases "*deal with the usual acceleration and deceleration behavior of short fatigue cracks*".

2.4.3 Mechanically short crack growth rate prediction

In the EPFM regime, Chen *et al.* (2000) and Morino *et al.* (2007) experimentally showed that the crack growth rate of mechanically short cracks in Inconel 718 can be approximated by

$$\frac{\mathrm{d}a}{\mathrm{d}N} = w_1 \left(\frac{\Delta\sigma}{2}\right)^{w_2} a \tag{2.7}$$

where $\Delta\sigma/2$ is the stress amplitude, w_1 and w_2 are material constants.

Other authors proposed a modification of the stress intensity factor range ΔK. For example, El Haddad *et al.* (1979) proposed to use a strain intensity factor range by replacing $\Delta\sigma$ by $E\Delta\varepsilon$ in Equation (2.1). The authors also proposed to add a fictive length to the crack length in order to better predict the higher crack propagation growth rates of mechanically short cracks when compared to those in the LEFM regime (long cracks). This model lacks of physical meaning.

Dowling (1977) proposed a model based on the cyclic J-integral. According to Riemelmoser and Pippan (2002), the physical interpretation of this model rise many difficulties due to its complicated determination using cylic yield stress–strain curves.

None of these models account for microstructural parameters and residual stresses.

2.4.4 An overall crack propagation model

Navarro and de los Rios (1988d) developed a model (referred herein as the "N-R model") able to predict short (microstructurally and mechanically) and long cracks growth rates. This model, based on the crack's tip opening displacement ($CTOD$), accounts for microstructural barriers and residual stresses induced by shot peening. The N-R model, which is the most interesting analytical model for the project due to it's capacity to predict the overall crack propagation process, is described in Section 2.5 in more details.

2.5 N-R model

2.5.1 The original model

The N-R model is based on the Bilby, Cottrell and Swinden's model (Bilby *et al.*, 1963, 1964) which describes the size of the plastic zone at a crack's tip using a distribution function modeling the pile up of dislocations. Based on Tanaka *et al.* (1986) previous work, Navarro and de los Rios (1988a) added the concept of microstructural barrier to the motion of dislocations, which was proposed to be a grain boundary.

Figure 2.9 illustrates the general idea of the N-R model. As shown in Figure 2.9(a), the N-R model assumes that a crack is inherently present in the material. A plastic zone is formed at the crack's tip because of the stress concentration at this location. The plastic zone is constrained at the grain boundary. The crack grows in the plastic zone increasing the local shear stress at the microstructural barrier. As schematized in Figure 2.9(b), it is supposed that a source of dislocations is present in the next grain. The source of dislocations can be

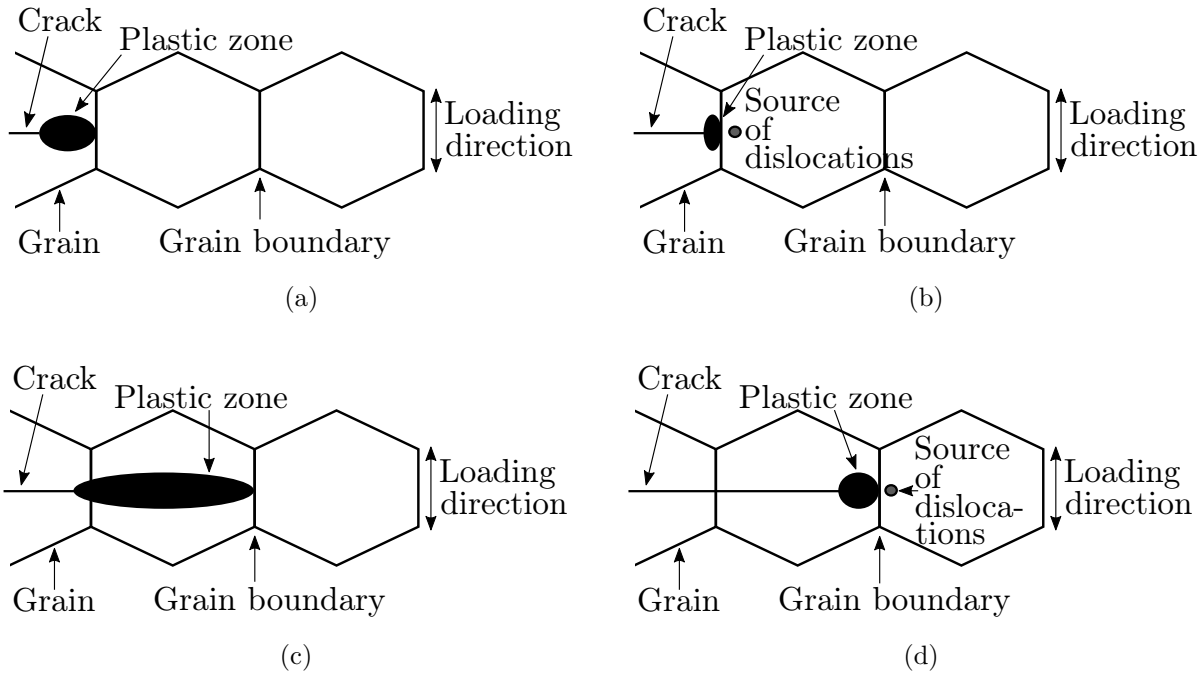

Figure 2.9 Schematic description of the N-R model: (a) The crack is in the 1st grain and the plastic zone is constrained at the grain boundary. (b) The crack grows in the plastic zone, the stress in the plastic zone rises and is felt by the source of dislocations in the next grain. (c) The source of dislocations has been activated and the plastic zone has spread in the second grain. (d) The process starts again

any inclusion or defect in the grain, or even the grain boundary itself. If the stress present in the plastic zone is sufficiently high, it activates the source of dislocations in the second grain. However, if the stress in the plastic zone is not sufficiently high, the source of dislocation is not activated and the crack does not propagate. Navarro and de los Rios called the applied stress under which this condition of non propagating crack is validated the "*true fatigue limit*". If the source of dislocations in the second grain is activated, the plastic zone extends in this latter grain, as depicted in Figure 2.9(c). Then, as shown in Figure 2.9(d), the crack propagates until the stress present in the plastic zone is sufficient to propagate it in the third grain. The repetition of this process is the basis of the N-R model. It is important to note that the model is uni-dimensional, transgranular and that crack propagation is symmetrical, which means that it propagates also in the opposite direction until it meets a free surface.

The principal parameters involved in the model are presented in Figure 2.10. On the x axis, the position of the crack's tip (equivalent to the crack length) is denoted by a, the position of the end of the plastic zone is at half a grain diameter D and the distance between the grain boundary at which the plastic zone is blocked and the source of dislocation is r_0 (considered negligible when compared to the grain size). The crack length plus the plastic zone length is represented by the parameter c. A non-dimensional coordinate system $\zeta(x) = x/(c + r_0)$ is used. $n_1 = a/(c + r_0)$ represents the crack's tip, the end of the plastic zone is at $n_2 = c/(c + r_0)$ and 1 is the location of the source of dislocations. The applied stress σ results in three different stress components, namely:

1. σ_1 represents the crack closure stress. It is the residual stress already present in the material.

2. σ_2 is the stress required to trigger plastification at the crack's tip (friction stress).

3. σ_3 represents the stress acting on the source of dislocations.

In order to activate a source of dislocations, σ_3 must reach a threshold called σ_{arrest} defined as (Curtis *et al.*, 2003a)

$$\sigma^i_{arrest} = \frac{m^i}{m^{i=1}} \frac{\sigma_{FL} - \sigma_1^{i=1}}{\sqrt{i}} + \sigma_1^i \tag{2.8}$$

where i is the number of half grains over which the plastic zone has gone through (i = 1, 3, 5,...), σ_{FL} (the theoretical fatigue limit) represents the σ_{arrest} of the first grain and m^i is the disorientation factor of the i^{th} grain. It should be noted that i is an odd number since it represents the number of half grains the plastic zone has gone through.

If the crack has propagated through the entire plastic zone and $\sigma_3 < \sigma_{arrest}$, the plastic zone cannot propagate in the next grain and the crack propagation stops. When the plastic zone is constrained at the first grain boundary, this condition corresponds to the microstructural threshold. It is also considered that when a source of dislocations in the next grain is activated, the plastic zone immediately extends within this same grain.

Navarro and de los Rios stated that n_1 can reach two critical values: n_s and n_c. Index s refers to the starting position in a grain (the beginning of the computation or when the plastic zone has just spread in the next grain) and index c implies that the plastic zone is just about to spread in the next grain. i is thereafter used as an exponent on the model's variables to mark the number of half grains the plastic zone has expanded through. The model computation is incremental. Each increment represents the computation from n_s^i to n_c^i as schematized in Figure 2.11.

Navarro and de los Rios (1988d) showed that, when the plastic zone has propagated through i half grains, n_c can be calculated as

$$n_c^i = \frac{a_c^i}{c^i + r_0} = \cos\left(\frac{\pi}{2}\frac{\sigma - \sigma_{arrest}^i}{\sigma_2^i - \sigma_1^i}\right) \tag{2.9}$$

Navarro and de los Rios (1987) considered that a crack of length $a_s^{i=1}$ is already present in the material, and obtained as initial conditions

$$\begin{aligned} n_s^{i=1} &= \frac{a_s^{i=1}}{c^{i=1} + r_0} \\ c^{i=1} &= \frac{D}{2} \end{aligned} \tag{2.10}$$

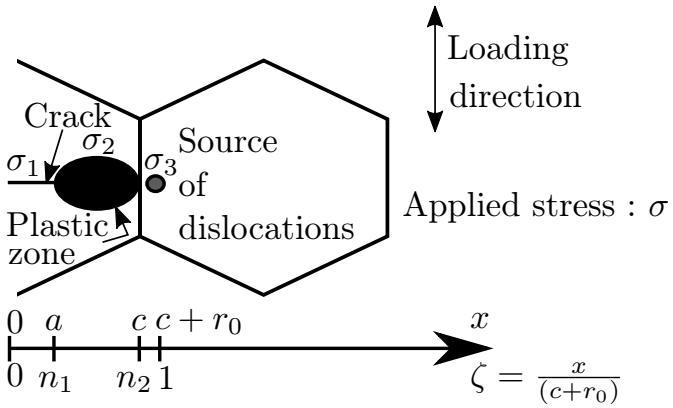

Figure 2.10 Schematic representation of the N-R model parameters

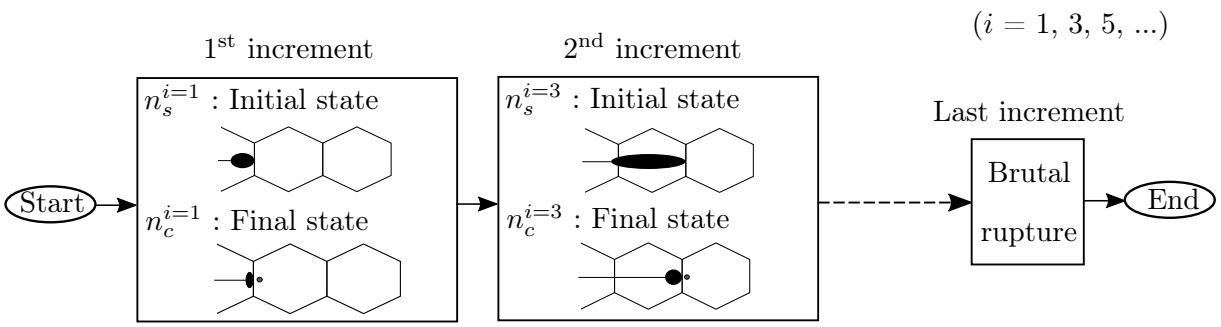

Figure 2.11 Schematic representation of the N-R model computation increments. Each increment is the computation from the initial condition or when the crack's tip has just propagated through the next grain to the situation where the plastic zone is about to propagate in the adjacent grain: from n_s^i to n_c^i. i is an odd number representing the number of half grains the plastic zone has expanded through

When σ_3 reaches σ_{arrest} at the i^{th} step ($n_1 = n_c^i$), the plastic zone suddenly spreads in the next grain and the beginning of the next step ($i+2$) is reached, meaning that

$$\begin{aligned} n_s^{i+2} &= \frac{a_s^{i+2}}{c^{i+2} + r_0} = n_c^i \frac{i}{i+2} \\ c^{i+2} &= \frac{(i+2)\,D}{2} \\ a_s^{i+2} &= a_c^i \end{aligned} \tag{2.11}$$

The N-R model assumes that

$$\frac{\mathrm{d}a}{\mathrm{d}N} = A_2 CTOD^{m_2} \tag{2.12}$$

where A_2 and m_2 are experimentally determined constants and $CTOD$ is the crack's tip opening displacement. The crack's tip opening displacement was defined as the number of dislocations at the crack's tip multiplied by the burger vector's norm b (the distortion due to a dislocation). It was shown that the dislocation distribution S at a coordinate ζ ahead of the crack's tip can be expressed as (Bilby *et al.*, 1963; Navarro and de los Rios, 1988b;

Vallellano, 1999)

$$\begin{aligned} S(\zeta) =& \frac{1}{\pi^2 A}\Bigg\{(\sigma_2^i-\sigma_1^i)\left[\text{arccosh}\left(\left|\frac{1-n_1^i\zeta}{n_1^i-\zeta}\right|\right)-\text{arccosh}\left(\left|\frac{1+n_1^i\zeta}{n_1^i+\zeta}\right|\right)\right] \\ & -(\sigma_3^i-\sigma_2^i)\left[\text{arccosh}\left(\left|\frac{1-n_2^i\zeta}{n_2^i-\zeta}\right|\right)-\text{arccosh}\left(\left|\frac{1+n_2^i\zeta}{n_2^i+\zeta}\right|\right)\right]\Bigg\} \\ & +\frac{2}{\pi^2 A}\frac{\zeta}{\sqrt{(1-\zeta^2)}}\left[(\sigma_2^i-\sigma_1^i)\text{arcsin}(n_1^i)+(\sigma_3^i-\sigma_2^i)\text{arcsin}(n_2^i)+\frac{\pi}{2}(\sigma-\sigma_3^i)\right] \end{aligned} \tag{2.13}$$

with $A = Gb/(2\pi(1-\nu))$ for edge dislocations and $A = Gb/(2\pi)$ for screw dislocations. ν is the Poisson's ratio and G is the shear modulus. Vallellano (1999) showed that the $CTOD$ can be expressed as

$$\begin{aligned} CTOD^i = \frac{bc^i}{\pi^2 A}\Bigg\{2(\sigma_2^i-\sigma_1^i)n_1^i\ln\left(\frac{1}{n_1^i}\right)+(\sigma_3^i-\sigma_2^i)\Bigg[(n_1^i+n_2^i)\text{arccosh}\left(\left|\frac{1+n_2^i n_1^i}{n_2^i+n_1^i}\right|\right) \\ +(n_2^i-n_1^i)\text{arccosh}\left(\left|\frac{1-n_2^i n_1^i}{n_2^i-n_1^i}\right|\right)\Bigg]\Bigg\} \end{aligned} \tag{2.14}$$

From Equation (2.12), the number of cycles can be computed as the integration of

$$\mathrm{d}N = \frac{\mathrm{d}a}{A_2 CTOD^{m_2}} \tag{2.15}$$

$a = cn_1$, c remains constant during an increment and n_1 evolves from n_s to n_c. Thus, the number of cycles for each increment i can be calculated as

$$N^i = \frac{1}{A_2}\int_{n_s^i}^{n_c^i}\frac{c^i \mathrm{d}n}{CTOD^{m_2}} \tag{2.16}$$

Finally, the total number of cycles to rupture N_f can be calculated as the sum of the cycles needed to complete each increment:

$$N_f = \frac{1}{A_2}\sum_i\int_{n_s^i}^{n_c^i}\frac{c^i \mathrm{d}n}{CTOD^{m_2}} \tag{2.17}$$

When the crack becomes sufficiently long to assume confined plasticity at the crack's tip (LEFM), the parameters A_2 and m_2 can be determined by fitting Equation (2.12) with the Paris relation (Equation(2.2)) (de los Rios *et al.*, 2000).

2.5.2 Introduction of residual stresses induced by shot peening

Curtis *et al.* (2003a) and Solis *et al.* (2009) considered that the crack closure stress is equal to the average of the residual stresses σ_{RS} induced by shot peening along the crack, according to

$$\sigma_1^i = \frac{1}{a^i} \int_0^{a^i} \sigma_{RS}(x)\, \mathrm{d}x \tag{2.18}$$

where x is the crack's tip depth (distance from the shot peened surface). To the best of the author's knowledge, the residual stresses redistribution due to cyclic loads has never been accounted for in the N-R model.

2.5.3 Introduction of work hardening

In shot peened samples, σ_2 (friction stress) near the surface can be different from the bulk material's yield strength due to local work hardening. de los Rios *et al.* (2000) experimentally showed that, in aluminum, the yield strength is linearly proportional to the hardness. Based on this assumption, the authors measured the through-thickness hardness profile of the shot peened layer and estimated the value of σ_2 as a function of depth and implemented it in the N-R model. However, this method only accounts for the work hardening due to shot peening prior to cyclic loading and an eventual redistribution of the cold work profile has never been accounted for.

The crack's tip zone is submitted to cyclic yielding during fatigue. This phenomenon can lead to hardening or softening, depending on the material. Xin *et al.* (1990) proposed a strain hardening model based on the mechanics of dislocations. However, this model does not allow the introduction of residual stresses and is only applicable on materials characterized by a cyclic hardening behavior (de los Rios *et al.*, 2000), which is not suitable for Inconel 718. Curtis *et al.* (2003a) considered that strain hardening evolution was not significant in aluminum and used the cyclic yield strength as σ_2 value.

Vallellano *et al.* (2009) and Vallellano *et al.* (2013) divided the plastic zone into two parts: A monotonic plastic zone encompassing a cyclic plastic zone. The monotonic plastic zone represents the plastic zone that will only suffer yielding during the loading phase. On the other hand, the cyclic plastic zone will also be submitted to yielding during the unloading phase. Figure 2.12 depicts the cyclic and the monotonic plastic zones. Both can be blocked at microstructural barriers and both need to expand for the crack to continue its propagation. This approach seems to be more realistic than considering only one monotonic plastic zone since cyclic yielding at the crack's tip is responsible for the local damage accumulation that leads to crack propagation. The crack propagation is driven by the cyclic plastic zone and

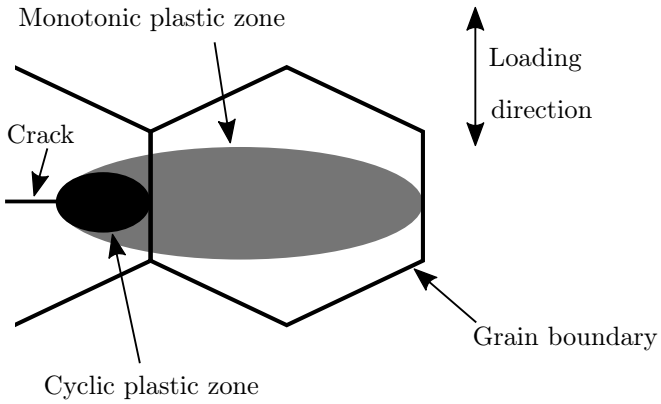

Figure 2.12 Schematic representation of the cyclic plastic zone encompassed by the monotonic plastic zone

its prediction is achieved with the N-R model in which Vallellano *et al.* (2009) considered the parameters ranges: $\Delta\sigma, \Delta\sigma_2$, $\Delta CTOD$, $\Delta\sigma_{FL}$, etc... The propagation of the monotonic plastic zone is predicted with Equation (2.9). Note that his approach would be challenging to apply on Inconel 718 due to its continuous softening behavior under cyclic yielding.

2.5.4 True fatigue limit of shot peened specimens

Curtis *et al.* (2003a) assumed that the theoretical fatigue limit is directly influenced by the residual stress at the surface, according to

$$\sigma_{FL}^{SP} = \sigma_{FL} + \sigma_1^{i=1} \tag{2.19}$$

where σ_{FL}^{SP} is the true theoretical fatigue limit of the shot peened material. Based on this hypothesis, Equation (2.8) can be rewritten as

$$\sigma_{arrest} = \frac{m_i}{m_1}\frac{\sigma_{FL}}{\sqrt{i}} + \sigma_1 \tag{2.20}$$

which now accounts for residual stresses induced by shot peening.

2.5.5 Introduction of roughness

Surface roughness creates stress concentrations that reduce the stress required to trigger plastification in a grain located near the surface. Using conformal mapping techniques and the dislocations distribution, it was shown that the effect of a notch of depth α and half

width β on a source of dislocation located at a depth $iD/2$ can be applied on σ^i_{arrest} with a stress concentration factor Z^i expressed as (Vallellano, 1999; Navarro *et al.*, 1999; Vallellano *et al.*, 2000a,b)

$$Z^i = \frac{\sqrt{i\frac{D}{2}}}{\alpha+\beta}\left[\frac{\beta}{\eta\left(i\frac{D}{2}\right)} + \frac{\alpha}{\sqrt{1+\eta\left(i\frac{D}{2}\right)^2}}\right]^{\frac{1}{2}}$$
$$\eta(x) = \frac{1}{\alpha^2-\beta^2}\left[\alpha\sqrt{(\alpha+x)^2-\alpha^2+\beta^2} - \beta\,(\alpha+x)\right] \tag{2.21}$$

The stress required to activate the next source of dislocations is then computed as

$$\sigma^i_{arrest,Z} = \sigma^i_{arrest} Z^i \tag{2.22}$$

Li *et al.* (1992) showed, using a finite element model, that the stress concentration factor at a shot peened specimen's surface can be expressed as

$$\begin{aligned} K_{t0} &= 1 + 2.1\left(\frac{\alpha_d}{2\beta_d}\right) \qquad \text{for } \frac{\alpha_d}{2\beta_d} \leq 0.30 \\ K_{t0} &= 1 + 4.0\left(\frac{\alpha_d}{2\beta_d}\right)^{1.3} \qquad \text{for } \frac{\alpha_d}{2\beta_d} < 0.15 \end{aligned} \tag{2.23}$$

considering that the dimples introduced by shot peening have a depth of α_d and a half width of β_d. The couples α–α_d and β–β_d can be replaced by the roughness parameters R_t and $RSm/2$, respectively (Solis, 2002). The stress concentration factor K_t on a crack that has propagated from the surface to a depth x can be expressed as (de los Rios *et al.*, 1996; Solis, 2002)

$$K_t(x) = (K_{t0}-1)\left(\frac{R_t}{x}\right)^2 + 1 \qquad \text{for } x > R_t \tag{2.24}$$

These latter relations have been succesfully used by Solis (2002) on shot peened aluminum alloys.

2.5.6 Modeling capacities of the N-R model

Solis *et al.* (2009) successfully generated Kitagawa-Takahashi diagrams (diagrams showing the stress needed to propagate a crack depending on its length) of the peened and unpeened aluminum 2024-T351, as shown in Figure 2.13(a). The full and the dotted lines in Figure 2.13(a) represent σ_{arrest} for unpeened and peened aluminum, respectively. The triangles

and rounds represent the experimental results on peened and unpeened aluminum, respectively. It can be seen that the results are reported for cracks longer than 0.1 mm. This is due to the impossibility for the authors to observe smaller cracks. The results given by the model seem reliable (maximal error of 50 MPa), even if an underestimation of σ_{arrest} is observed for the peened material. The fatigue limit of unpeened specimens (σ_{FL}) is inferior to that of shot peened specimen (σ_{FL}^{SP}) due to the absence of compressive residual stresses. Similar work has also been achieved on aluminum 7150-T651 by Curtis *et al.* (2003b).

The model has been used by de los Rios *et al.* (2000) to predict the fatigue life of aluminum 2024-T351 under peened and unpeened conditions, as shown in Figure 2.13(b). The predicted curves lie in the experimental points. Solis (2002) also successfully predicted fatigue life of shot peened aluminum 7150-T651.

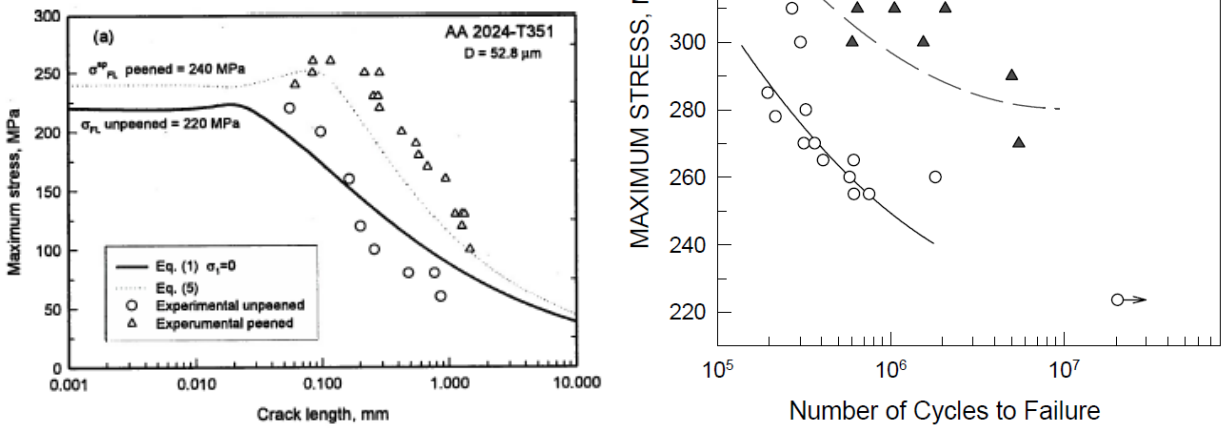

(a) (b)

Figure 2.13 Graphs showing the N-R model results. (a) Kitagawa-Takahashi diagram comparing N-R model and experimental results for peened (S110 cast steel shots at an intensity of 4 A for a 200 % coverage) and unpeened aluminum 2024-T351 (Solis *et al.*, 2009). (b) S-N curve comparing N-R model and experimental results on aluminum 2024-T351 (de los Rios *et al.*, 2000). The shot peening conditions were not specified

CHAPTER 3 LITERATURE ANALYSIS AND OBJECTIVES

3.1 Literature analysis

The literature review revealed that:

- Long crack propagation rates in Inconel 718 can be predicted using the Paris relation. However, the microstructurally and mechanically short crack propagation rates are challenging to predict. Crack initiation and short crack propagation represent most of the fatigue life of Inconel 718. A model that predicts crack propagation must account for the microstrutural dependent behavior of short cracks.

- An optimal shot peening process can improve Inconel 718 fatigue life by displacing the site of crack nucleation underneath the specimen's surface. Surface compressive residual stresses induced by shot peening mainly redistribute during the first fatigue cycle and can become tensile, which is a drawback to fatigue life, if the applied stress overcomes the yield strength. Residual stresses redistribution must thus be accounted for in the crack propagation model.

- The N-R model is an analytical model able to predict short and long crack propagation based on the physics of transgranular crack propagation. The N-R model assumes that a crack is inherently present in the material. This model is suitable to predict short and long crack propagation in bulk and shot peened metallic materials. Surface roughness, residual stresses and surface cold work induced by shot peening have already been accounted for. However, cold work and residual stresses redistribution have not been accounted for in the N-R model and the model has never been applied to Inconel 718.

- Non metallic inclusions located at the surface can crack during the first loading cycle or can be inherently damage during the machining process. They can be considered has cracks inherently present in Inconel 718.

- The number of cycles for crack initiation at PSB in Inconel 718 can be predicted using Chan's crack initiation model. However, this model does not account for residual stresses that would be induced by shot peening.

- Inconel 718 continuously softens when submitted to cyclic yielding. Chaboche's constitutive equations were successfully used to predict nickel-based superalloys stress-strain curves under cyclic yielding. However, continuous softening was not accounted for and

the physical parameters were not representative of the reality. Predicting Inconel 718 continuous softening under cyclic yielding would allow to take into account the crack's tip cyclic plastic zone in the N-R model.

- The effects of rolled edges on fatigue life are only summarily reported in the open literature. The effects of edge geometries (prior to shot peening) on the formation of rolled edges have not been studied in the open literature.

3.2 Research objectives

Based on the thesis objective outlined in the introduction and the literature analysis, the following specific objectives have been defined:

1. **Characterize and model Inconel 718 cyclic yielding behavior.**
   Inconel 718 cyclic yielding behavior will be studied and a model able to predict its continuous softening behavior will be developed. Such a model would allow to predict Inconel 718 mechanical behavior in LCF and to account for the crack's tip cyclic plastic zone in the N-R model.

2. **Study unpeened and shot peened Inconel 718 fatigue properties in HCF and LCF.**
   Surface characteristics, crack initiation mechanisms, crack propagation behavior, resulting fatigue life, cold work and residual stresses redistribution of bulk and shot peened Inconel 718 submitted to HCF and LCF will be studied. Meeting this objective will allow to experimentally obtain the data needed for the application and the improvement of the N-R model.

3. **Calibrate, improve and validate the N-R model for bulk and shot peened Inconel 718.**
   The N-R model will be encoded, calibrated and validated with the experimental results obtained during the fulfillment of the first and the second specific objective. It will also be improved by accounting for crack initiation and shot peening induced residual stresses and cold work redistribution that will have been experimentally studied in the second specific objective.

4. **Estimate rolled edges impact on fatigue life.**
   Different edge geometries will be shot peened and fatigue tested. The severity of the rolled edges formed during the shot peening process as well as the resulting fatigue lives will be experimentally studied. It will allow to draw guidelines concerning the shot peening conditions and initial edge geometries aiming at maximizing the fatigue life.

CHAPTER 4 SCIENTIFIC APPROACH

The specific objectives defined in Chapter 3 were addressed through 2 published and 2 submitted journal papers. The main ideas addressed in these papers are detailed in this Chapter.

4.1 Article 1: 1D cyclic yield model independent of load spectrum characteristics and its application to Inconel 718

This article characterizes Inconel 718 behavior under fully reversed plastic deformation cycles and presents Chaboche's constitutive equation modified to account for the continuous softening of Inconel 718. The analytical model developed in this paper is able to predict the stress-strain curves of Inconel 718 submitted to cyclic yielding. This article fulfills the first specific objective which is to characterize Inconel 718 cyclic yielding behavior.

This article was published in the journal "Mechanics of Materials", volume 109, pages 34–41 in June 2017. This journal "*is a forum for original scientific research on the flow, fracture, and general constitutive behavior of geophysical, geotechnical and technological materials*".

The mechanical tests were performed by Sébastien Blas. The specimens design, the development of the model and the redaction of the article were mainly performed by the author of the thesis.

4.2 Article 2: Surface characteristics and fatigue behavior of shot peened Inconel 718

This paper presents the effects of shot peening on Inconel 718, and their evolution under cyclic loading. The induced roughness, residual stresses and cold work were studied at a macro-scale down to their influence on the microstructure, in both HCF and LCF. These results provide the physical grounds to explain the different crack initiation locations and the dispersion in the fatigue results. This paper addresses the second specific objective since it characterizes the effects of shot peening on Inconel 718 and their influence on fatigue life. Moreover, it provides most of the data required to achieved the third specific objective which is the development of the fatigue life prediction model.

This paper was accepted for publication in the International Journal of Fatigue on January 6$^{\text{th}}$, 2018. This journal publishes advanced researches in the field of fatigue.

Residual stresses measurements and cold work determination were performed by Dorian Delbergue. The specimens design, preparation and testing as well as the writing were mainly performed by the author of this thesis.

4.3 Article 3: Analytical fatigue life prediction of shot peened Inconel 718

This article presents a model coupling the N-R crack propagation model and Chan's crack initiation model. The N-R model was modified to account for the residual stresses and cold work redistribution. The number of cycles for subsurface crack initiation was predicted with Chan's model modified to account for the residual stresses redistribution. The model was calibrated and validated with the second article's experimental results. It successfully predicted the fatigue life as well as the crack initiation location in bulk and shot peened Inconel 718 submitted to HCF and LCF. This paper completes the third specific objective.

This paper was submitted to the International Journal of Fatigue on January 4$^{\text{th}}$, 2018. This journal publishes advanced researches in the field of fatigue.

The finite element model used to predict residual stresses and cold work redistribution was developed by Hong Yan Miao. The demonstration of the $CTOD$ simplification was performed by Charles Bianchetti. The coupling of the modified N-R crack propagation and Chan's crack initiation models, the enhancement of both models as well as the redaction of the article are most entirely the work of the author of this thesis.

4.4 Article 4: Effects of rolled edges on the fatigue life of shot peened Inconel 718

This article presents the effects of different, unpeened and shot peened, edge geometries on the fatigue life of Inconel 718, in LCF and HCF. The three different edge preparations studied were: 1) polished rounded edges, 2) chamfered edges and 3) sharp edges. Crack initiation mechanisms were analyzed for the specimens tested in HCF and the different fatigue life results were discussed based on a statistical study of the number of cycles to failure. This paper fulfills the fourth specific objective.

This paper was submitted to the Journal of Materials and Processing Technology on February 13$^{\text{th}}$, 2018. This journal "*covers the processing techniques used in manufacturing components from metals and other materials. The journal aims to publish full research papers of original, significant and rigorous work and so to contribute to increased production efficiency and improved component performance*".

The specimens design, preparation and testing as well as the article redaction are most entirely the work of the author of this thesis.

CHAPTER 5 ARTICLE 1 : 1D CYCLIC YIELD MODEL INDEPENDENT OF LOAD SPECTRUM CHARACTERISTICS AND ITS APPLICATION TO INCONEL 718

T. Klotz, S. Blas, M. Lévesque and M. Brochu, (2017).
Mechanics of Materials, 109, pp. 34–41.

5.1 Abstract

At room temperature, nickel-based superalloy Inconel 718 softens under fully reversed plastic deformation cycles. Chaboche's unified constitutive equations have been previously used in the literature to predict nickel-based superalloy cyclic softening behavior. To better fit our results, the constitutive equations were modified to account for continuous softening. Moreover, applying the model to results gathered from two different loading spectrum indicates that the isotropic evolution is solely dependent on the accumulated plastic strain and can be applied to a variety of number of cycles and strain amplitudes combinations without adjusting the parameters. This new information is significant and has a considerable impact on material testing and modeling. It implies that a unique set of parameters extracted from any fully reversed strain controlled test can characterize the material flow stress evolution with accumulated plastic strain independently of the strain sequence, for $R_\varepsilon = -1$. This flexible prediction method could lead to significant experimental costs reductions.

5.2 Introduction

Inconel 718 hardens during the first cycles (Fournier and Pineau, 1977; Merrick, 1974) when tested under room temperature low cycle fatigue (LCF) conditions at a strain ratio $R_\varepsilon = -1$. However, Inconel 718 continuously softens after several strain cycles since second particles shearing occurs (Xiao *et al.*, 2008). At half its fatigue life, its yield strength can decrease as much as 40 % for a 1 % strain amplitude (Sudarshan Rao *et al.*, 2012).

The flow stress evolution of a metal under cyclic plastic deformation can be predicted using unified Chaboche's constitutive equations (Chaboche and Rousselier, 1983) that account for inelastic behaviors such as Bauschinger effect, ratcheting, cyclic hardening and creep (Lemaitre *et al.*, 2009). The elastic domain is commonly defined with the flow function f

expressed as (Chaboche *et al.*, 2012)

$$f = J(\sigma - \chi) - R - k \tag{5.1}$$

where χ is the back stress, k the initial yield strength and J is a stress space invariant function commonly chosen as the von Mises invariant J_2. In 1D, the von Mises stress space invariant is defined as

$$J_2(\sigma - \chi) = |\sigma - \chi| \tag{5.2}$$

The elastic domain is classically defined as $f < 0$ and the plastic domain as $f = 0$. R represents the isotropic hardening component (yield surface evolution) and is commonly defined as a function of the accumulated plastic strain p as

$$R(p) = Q\left(1 - e^{-qp}\right) \tag{5.3}$$

where Q and q represent respectively the saturation value and the hardening rate. This relation was successfully used on stainless steel 316 (Goodall *et al.*, 1981). The back stress χ is defined as a sum of independent variables χ_i. Each one governs a different domain of the plastic deformation. For a nickel-based superalloy, two such kinematic variables are sufficient (Zhao *et al.*, 2001) and can be expressed as a Armstrong and Frederick (Armstrong and Frederick, 1966) kinematic hardening rule as

$$\begin{aligned} \chi &= \chi_1 + \chi_2 \\ \chi_i &= a_i(1 - e^{-C_i\varepsilon_p}) \qquad i = 1, 2 \end{aligned} \tag{5.4}$$

where a_1, a_2, C_1 and C_2 are material constants and ε_p is the plastic strain within a half cycle.

Zhan and Tong (2007) and Tong *et al.* (2004) used Chaboche's constitutive model to predict nickel-based alloys behavior when submitted to constant $R_\varepsilon = 0$ cyclic strain amplitude and creep tests at 650 °C. They developed an algorithm based on a least square minimization to determine a set of parameters best fitting experimentally measured behavior. However, the validity of the fitting parameters could be questioned since the initial yield strength was identified as 150 MPa while it was of 1000 MPa in monotonous tensile tests.

A material's cyclic yield behavior can be characterized through three main testing procedures (Hales *et al.*, 2002). The single step test consists of performing fully reverse cyclic tests at constant strain amplitude. The incremental step test introduced by Landgraf *et al.* (1969) consists of loading blocks in which the strain amplitude is incremented every cycle to reach a maximum and then progressively decremented to its initial value. The multiple step test,

similar to the single step test, consists of increasing the strain amplitude after every chosen number of cycles. Polak and Hajek (1991) proved that a single incremental test on copper and low carbon steel can be used to approximate their cyclic stress-strain curves. This observation can lead to experimental costs reductions since one incremental tests could provide the same information as several constant amplitude tests. To the best of our knowledge, incremental test results have never been compared to constant strain amplitude tests results for Inconel 718.

This study aims at demonstrating that Inconel 718 behavior, when submitted to $R_\varepsilon = -1$ strain controlled LCF, can be fully characterized by the accumulated plastic strain independently of the strain spectrum characteristics. The paper is organized as follows: Section 5.3 presents the studied material and the experimental procedures used to extract Inconel 718 stress-strain curves under single step and incremental tests. The experimental results are analyzed in Section 5.4. Section 5.4 also compares the proposed model's predictions to experimentally measured behavior while Section 5.5 concludes this work.

5.3 Material and experimental procedure

5.3.1 Material

The material studied is a nickel-based superalloy Inconel 718 that underwent a solution and precipitation heat treatment. Its chemistry, measured by optical spectrometry, is given in Table 5.1. The microstructure consisted of an austenitic FCC matrix strenghened by γ' (Ni_3(Ti-Al)) and γ'' (Ni_3(Ti-Al)) particles (Alexandre *et al.*, 2004). The grain size was heterogeneous and mainly bi-modal with two median groups having mean diameters of 10 μm and 30 μm. It should be noted, however, that some grains could have diameters as large as 100 μm. The presence of NbC carbides, titanium carbo-nitride (TiCN) and δ phase (Ni_3Nb) particules located along the grain boundaries can be observed in Figure 5.1. Aluminum and magnesium oxides were often found in the TiCN particles, as can be seen in Figure 5.1. Monotonic tensile properties, measured according to ASTM E8M-13a standard (ASTM Standard E8M-13a, 2013), are presented in Table 5.2.

Table 5.1 Inconel 718 chemical composition obtained by optical spectrometry (weight %)

Elements	Ni	Cr	Nb	Mo	Ti	Al	Co	Si	Mn	Cu
Composition	Bal.	17.93	5.23	3.24	1.19	0.60	0.30	0.07	0.06	0.05

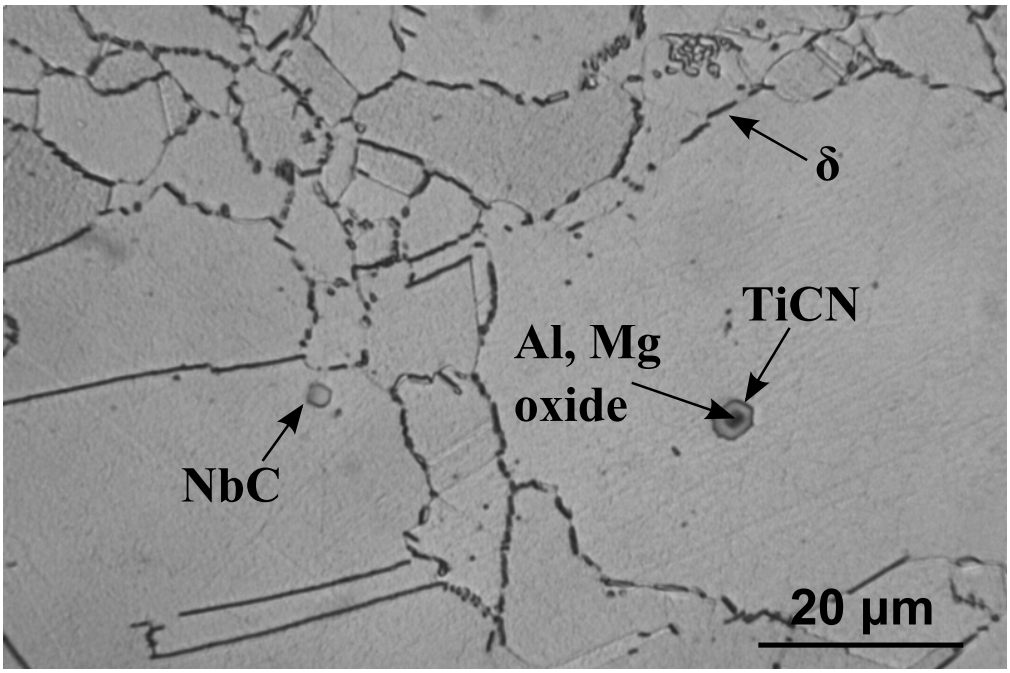

Figure 5.1 Micrograph showing Inconel 718 microstructure. Titanium carbo-nitride (TiCN) and NbC carbides are present within the grains. An Al, Mg oxide can be observed inside the TiCN particle. δ phase (Ni_3Nb) is located along the grain boundaries. The grain size's heterogeneity is visible

Table 5.2 Inconel 718 monotonic tensile properties following ASTM E8M-13a methodology

E (GPa)	ν	$\sigma_{y0.2\%}$ (MPa)	$\sigma_{y0.05\%}$ (MPa)	σ_u (MPa)	El (%)	AR (%)
205	0.32	1253	1125	1413	24	39

5.3.2 Cyclic tests

Specimens were extracted from the longitudinal direction of a 90 mm diameter bar. Samples had a dog bone shape with a 11.4 mm square reduced cross section and a 9 mm gage length. Specimens were designed in agreement with standards ASTM E9-09 (ASTM Standard E09-09, 2009) and E606M-12 (ASTM Standard E606M-12, 2012). Strain controlled tests were performed at room temperature on a MTS 318.25 equipped with a 250 kN MTS 661.22c-01 load cell with MTS 793 software and a FlexTest 60 (5.9A) controller. Tests were performed at a strain ratio $R_\varepsilon = -1$. The load path was triangular with a strain rate $\dot{\varepsilon} = 0.1$ %/s. Displacements were measured with a 8 mm gage length MTS 632.26C-20 extensometer.

Two types of cyclic yield tests were performed: four single step tests and one incremental test. A constant strain amplitude with a strain ratio $R_\varepsilon = -1$ was applied during single

step tests. An example of a single step test strain command can be seen on Figure 5.2(a). Four samples were tested at strain amplitudes $\Delta\varepsilon_{tot}/2 = 0.6$, 1.0, 1.6 and 2 %, respectively. The tests were performed until a qualitative sharp drop in the maximal stress was visually detected (see Figure 5.3(a)). The sample tested with 1 % strain amplitude was tested until failure.

Incremental tests consisted of a strain spectrum in which the initial strain amplitude of 0.4 % was increased by 0.2 % for each cycle until reaching an amplitude of 2 %. In the second half of the spectrum, the strain was decreased back to 0.4 % by steps of 0.2 %. This strain spectrum, also called block, was repeated 18 times. Two such strain blocks are shown on Figure 5.2(b).

5.4 Results and discussion

5.4.1 Softening

Figure 5.3(a) shows the maximum true stress as a function of the strain cycles. The figure shows that Inconel 718 hardens during the first cycles and then exhibits a constant softening. It can also be noted, as observed by Merrick (1974), that the higher the strain amplitude, the stronger the hardening is in the first cycles. Nevertheless, as was also observed by Xiao *et al.* (2005), the specimen submitted to a 0.6 % strain amplitude did not show initial hardening.

Figure 5.3(b) presents the maximum true stress as a function of the accumulated plastic

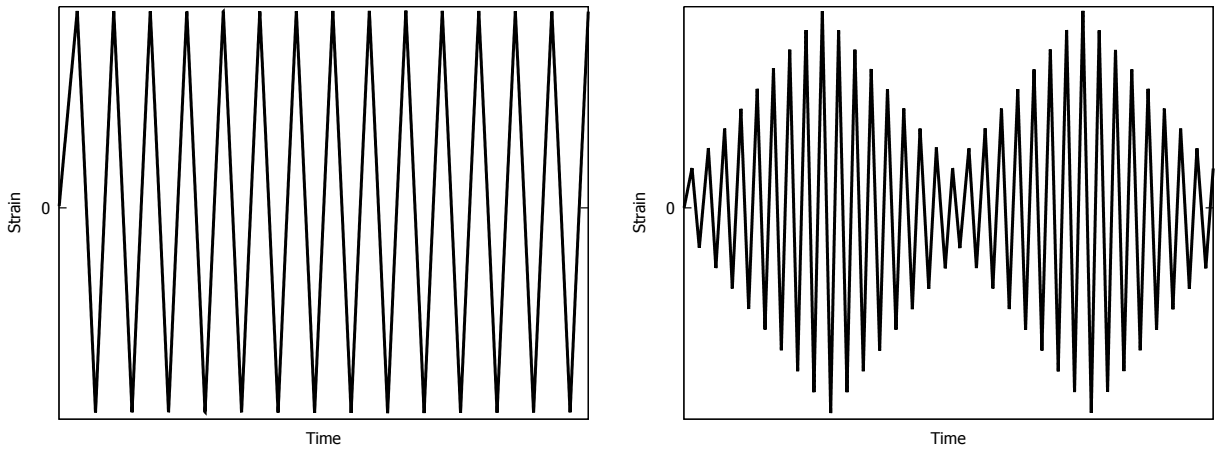

(a) (b)

Figure 5.2 Strain commands: (a) single step test, (b) incremental test (two blocks are represented)

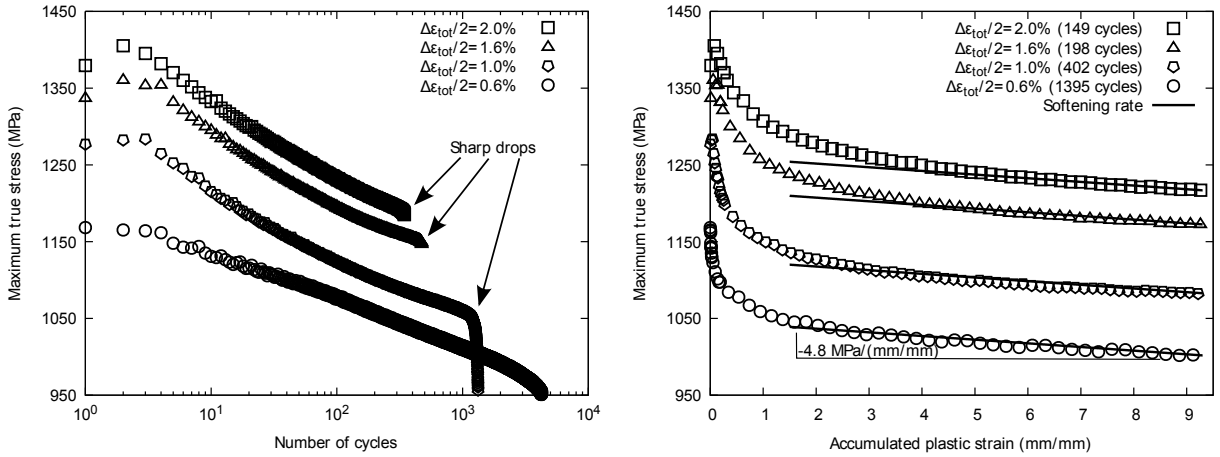

Figure 5.3 Maximum true stress depending on: (a) the number of cycles, (b) the accumulated plastic strain (until 9.3 mm/mm)

strain $p = \sum \mid \varepsilon_p \mid$ in order to establish an homogeneous comparison basis for all tests. ε_p, the plastic strain within a half cycle, was computed as the difference between the strain at maximum (or minimum in compression) stress and the strain at 0.05 % yield strength in a half cycle. The results are presented for up to 9.3 mm/mm, which correspond to the maximum accumulated plastic strain reached during the incremental test. Figure 5.3(b) shows a similar trend for all strain amplitudes above 0.6 %: hardening followed by rapid softening and then by a stage of steady state (constant) softening. In the last stage, the material softens at a rate of approximately -4.8 MPa/(mm/mm), independently of the strain amplitude. The figure shows that, the lower the strain amplitude, the faster is the transition to the stabilized softening behavior. Note that these comments only apply to samples tested at a strain range higher or equal to 0.6 % since Inconel 718 does not exhibit softening at a strain range of 0.4 % (Xiao *et al.*, 2008).

The transition between hardening, fast softening and steady state softening may be explained by an evolution of plastic deformation mechanisms. Fournier and Pineau (1977) showed that, at room temperature and during the first cycles, the plastic strain is homogeneously distributed in the material causing the hardening by dislocations pileups. Persistent slip bands (PSB) are subsequently formed after a certain level of plastic strain accumulation. PSB are responsible for second phase particles shearing causing softening.

Figure 5.4 shows a micrograph taken in the reduced section of a failed specimen tested in single step at 1 % strain amplitude. PSB are visible, confirming Fournier's observations. PSB were observed on all the samples surfaces. They are responsible for the constant softening of

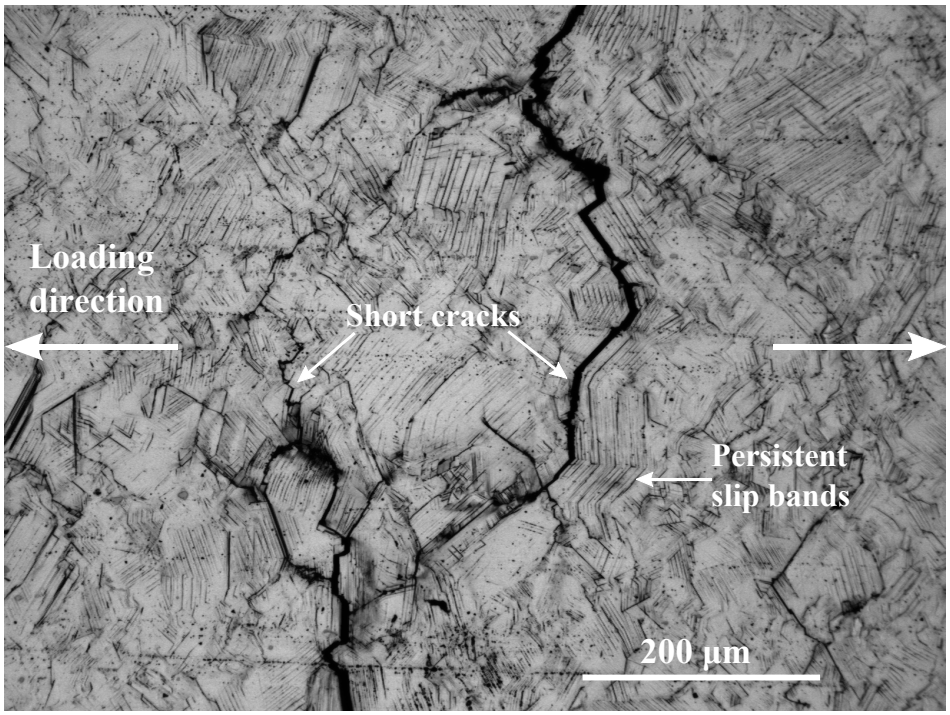

Figure 5.4 Post-test $\Delta\varepsilon_{tot}/2 = 1$ % reduced section's surface observation under optical microscope showing the presence of persistent slip bands and short cracks. Short cracks propagated along the persistent slip bands orientation

the material. Figure 5.4 clearly shows that the PSB have mainly an orientation of 45 ° with respect to the loading direction, which is the maximum shear stress orientation. Short cracks propagating along PSB are also present since the micrograph was taken after failure. The propagation of short cracks is responsible for the sharp drops observed on Figure 5.3. Short cracks initiation and propagation along slip bands are commonly observed in Inconel 718 (Maderbacher *et al.*, 2013) and more generally in FCC metallic materials (Sangid, 2013).

5.4.2 Yield surface evolution

Figure 5.5 plots the yield surface evolution (R) as a function of the total accumulated plastic strain (p) for every performed test. The yield surface evolution, here in 1D, is the difference between the yield surface at a given total accumulated plastic strain and the initial yield surface. The initial yield surface was approximated to twice the initial yield strength ($2k$). Moreover, the yield surface in a cycle was taken during the tensile loading phase as the difference between the yield strength and the minimum stress. Figure 5.5 shows that the yield surface evolution is function of the total accumulated plastic strain irrespectively of the performed test. This observation suggests that one test is sufficient to characterize the

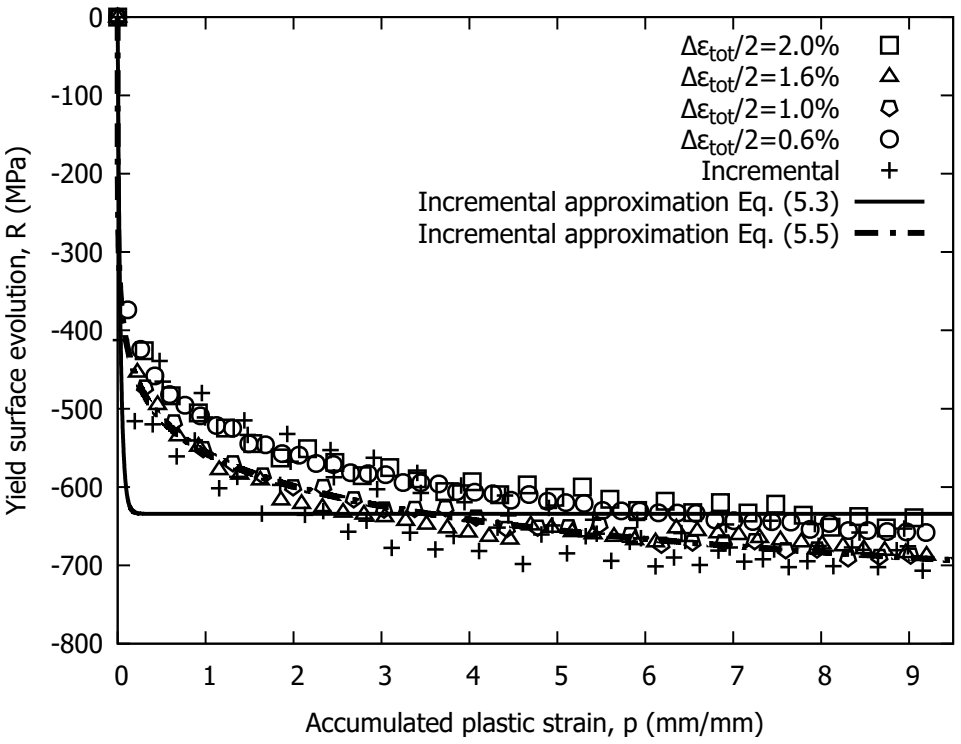

Figure 5.5 Yield surface evolution as a function of the accumulated plastic strain for different tests. The symbols represent experimental data while the lines represent model predictions

isotropic component of Inconel 718 softening behavior.

5.4.3 The proposed model

Chaboche's uni-axial constitutive equations (Equations (5.1) to (5.4)) were used to predict Inconel 718 stress response. Figure 5.5 shows that no stabilization was observed. Equation (5.3) is consequently not suitable to fit the yield surface evolution. A new yield surface evolution relation was proposed as

$$R(p) = \frac{-\gamma_2}{1 + p^{\gamma_1}} + \gamma_2 \tag{5.5}$$

where γ_1 and γ_2 are fitting constants. Figure 5.5 shows Equations (5.3) and (5.5) fitted on the incremental test results. The best fitting values for Equations (5.3) and (5.5) are presented in Table 5.3.

Table 5.3 Model parameters obtained for the single step tests and the incremental test

	γ_1	γ_2 (MPa)	k (MPa)	C_1	C_2	a_1 (MPa)	a_2 (MPa)
Single step tests	0.2651	-1039.02	1157	342.73	21.99	485.39	422.60
Incremental test	0.2241	-1112.05	1157	249.24	20.44	505.46	531.05
	Q (MPa)	q					
Incremental test	-634.18	30.71					

5.4.4 Modeling procedure

All the yield strengths were taken as 0.05 % strain offset yield according to the ASTM E8M-13a offset method (ASTM Standard E8M-13a, 2013) to ensure a consistent and stable measurement. The first tensile loading during the incremental test was performed until up to a strain deformation of 0.4 %. At this point, the 0.05 % offset yield strength was not reached and k, the initial yield strength, could not be extracted from the incremental test. Therefore, for all simulations, k was taken as the average of single step tests initial yield strengths.

Fitting parameters γ_1 and γ_2 (Equation (5.5)) were extracted from the curve $R(p)$ (Figure 5.5). Back stress parameters a_i and C_i (Equation (5.4)) were then calculated with a least square approximation where the cost function was defined as:

$$F = \sum_{i=1}^{N_{exp}} \frac{1}{N_{data,i}} \sum_{j=1}^{N_{data,i}} \left(\sigma_{exp}^{ij} - \sigma_{num}^{ij}\right)^2 \tag{5.6}$$

where N_{exp} is the total number of experiments ($N_{exp} = 4$ for the single step tests and $N_{exp} = 1$ for the incremental test), $N_{data,i}$ is the total number of data point of the i^{th} experiment, σ_{exp} and σ_{num} are respectively the experimental stress measured and the predicted stress obtained from Equation (5.1). Figure 5.6 shows contour plots of the cost function as a function of a_i values (Figure 5.6(a)) and C_i values (Figure 5.6(b)) for the incremental test, around the optimal values obtained. In other words, Figure 5.6(a) was obtained when the C_i values were fixed as their optimal values and Figure 5.6(b) was obtained for when the a_i values were fixed at their optimum values. The cost function was normalized so that it lied between 0 and 1. Figure 5.6(a) shows that the local minimum has an ellipse shape, which means that parameters a_1 and a_2 are correlated and several values could lead to a local optimum. However, Figure 5.6(b) has the shape of a circle, which means that C_1 and C_2 are independent

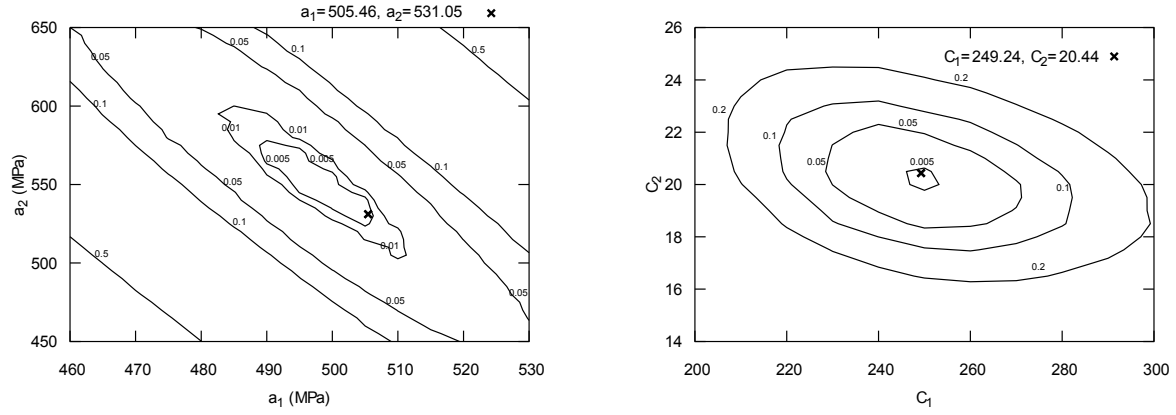

(a) (b)

Figure 5.6 Incremental test cost function contour plot as a function of (a) a_i and (b) C_i around the optimal values. Cost function F was normalized so that it lied between 0 and 1

of each other. Only one couple of values of C_1 and C_2 ensure to be at the local minimum. Similar contour plots of C_1 and C_2 for different a_1-a_2 couples lying in the 0.005 ellipse of Figure 5.6(a) revealed that the C_1 and C_2 optimal values were insensitive to the a_1-a_2 couple.

The incremental test stress response was first predicted with parameters extracted from the single step tests experimental results. Then, single step tests were predicted with material parameters extracted from the incremental test.

5.4.5 Model results

Figures 5.7 and 5.8 respectively show experimental and predicted stress-strain curves results for the incremental and the single step tests. The represented incremental test results were taken from the first half of each block.

Both predictions (Figures 5.7 and 5.8) fit the experimental data quite well, except for the very first cycles where a stress overestimation can be observed while the specimen is in plastic regime. This gap is likely to be due to the back stress estimation since the model's isotropic part (Equation (5.5)) was directly fitted on the experimental results. As discussed in Section 5.4.1, the yielding mechanism differs from the first cycles to the steady state softening. This suggests that the law used in Equation (5.4) is adapted to the steady state softening part under LCF conditions. A yield strength overestimation is also observed for all the cycles. This overestimation is due to the 0.05 % offset yield strength that was chosen as a criterion to determine the yield strength since it delivers a value higher than the yield

onset.

Based on parameters extracted from a complex loading data set, the model is capable of predicting stress-strain curves from simple loading conditions (single step tests). The stress-strain curves prediction under complex loading conditions (incremental test) was also successfully achieved with parameters extracted from simple loading data set results. Inconel 718 stress response under simple or complex loading conditions can be characterized, at $R_\varepsilon = -1$, with a different data set results coming from a test with a different $R_\varepsilon = -1$ strain spectrum.

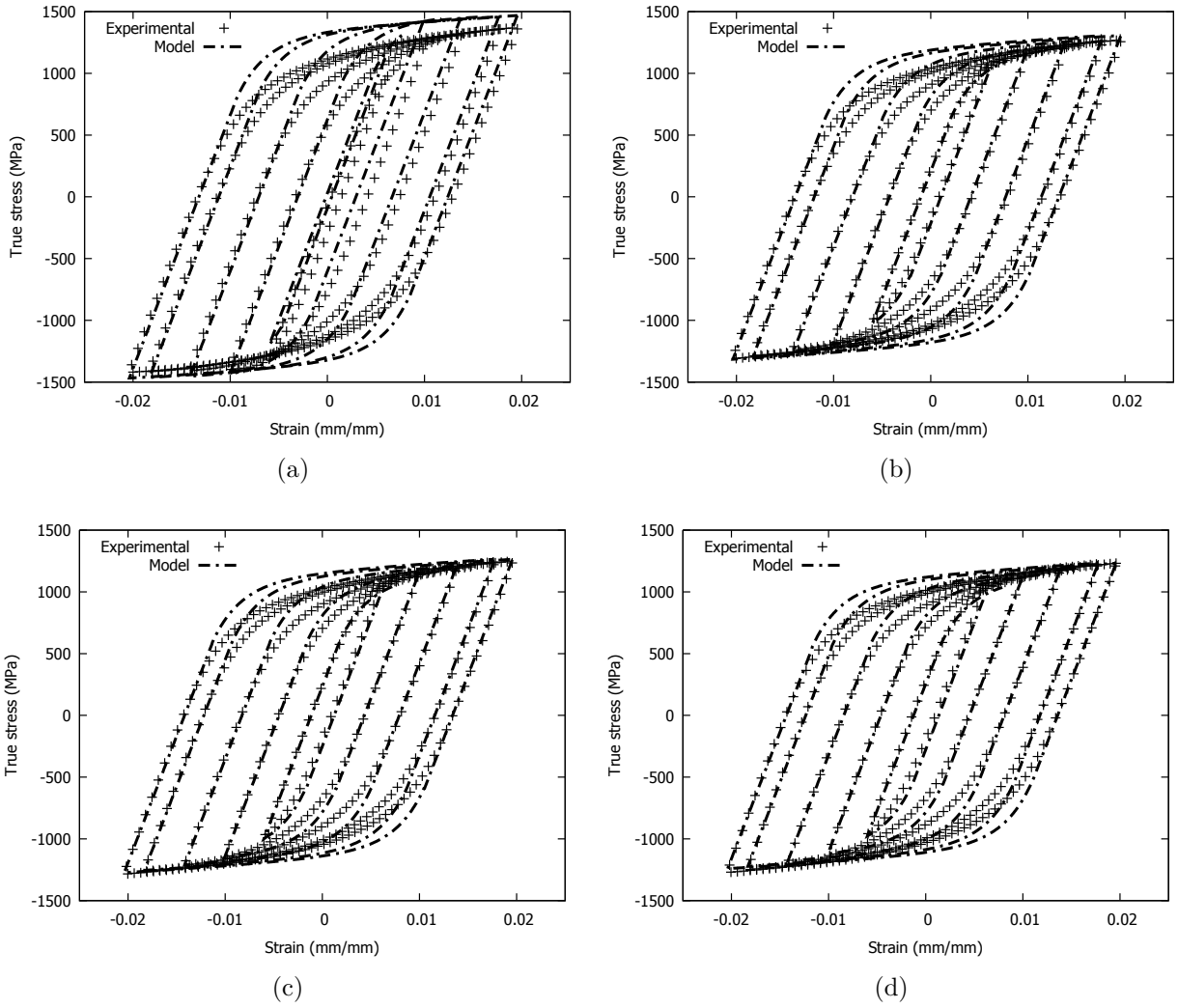

Figure 5.7 Simulated stress response of the incremental test compared to the experimental results for (a) 1$^{\text{st}}$ bloc, (b) 6$^{\text{th}}$ block, (c) 11$^{\text{th}}$ block, (d) 18$^{\text{th}}$ block. Crosses represent the experimental results while the dash line represents the model's prediction

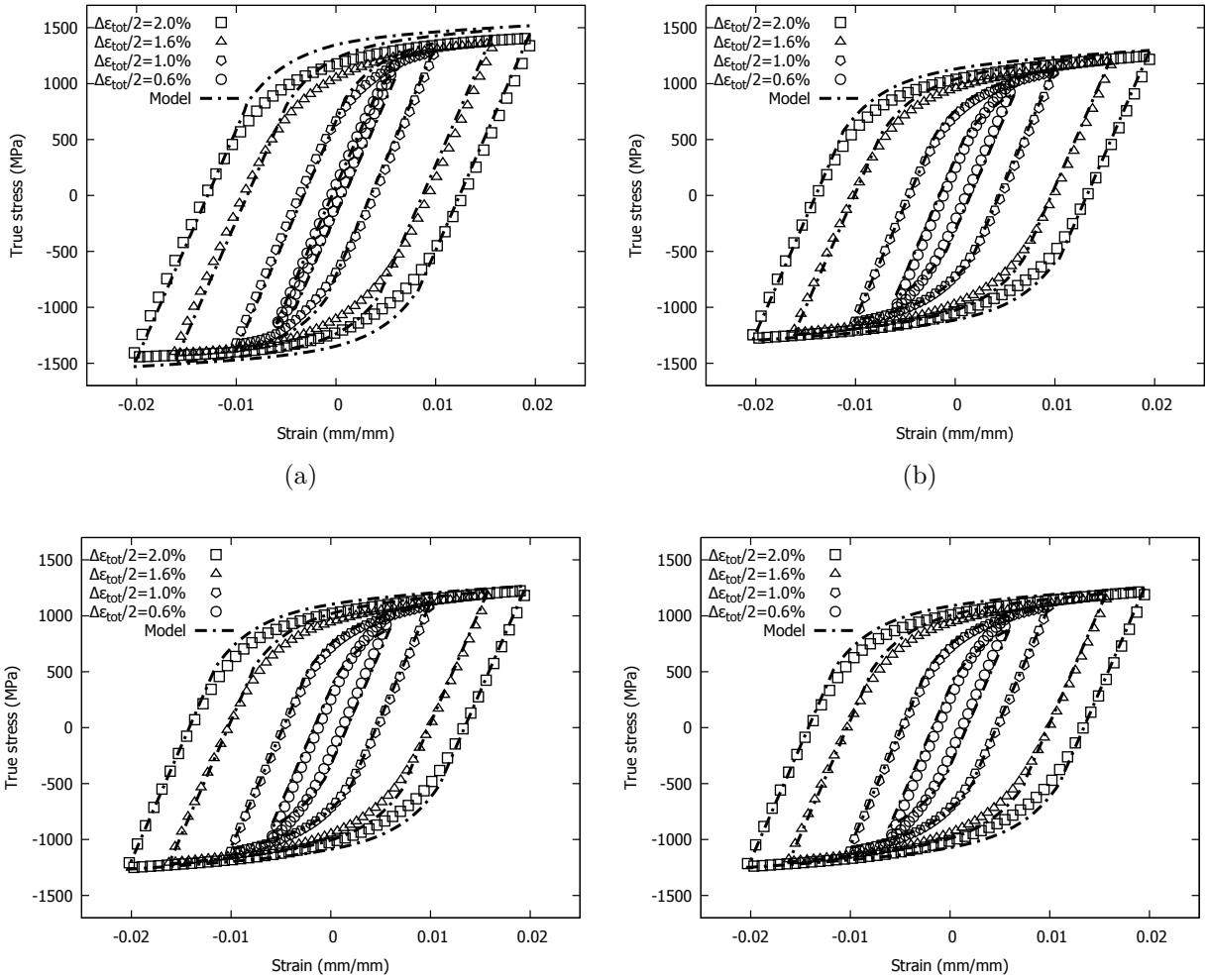

Figure 5.8 Simulated stress response of single step tests for (a) 1st cycle, (b) $p = 4$ mm/mm, (c) $p = 7$ mm/mm, (d) last cycle: $p = 9.3$ mm/mm. Symbols represent the experimental results while the dash line represents the model's prediction

5.4.6 Limitations of the model

The model is only valid for strain amplitudes higher than 0.5 %. For lower amplitudes Inconel 718 does not soften and the isotropic part of the model is obsolete.

The model's predictions were only validated for $R_\varepsilon = -1$. Other test campaigns for different values of R_ε should be carried out to further validate the model. However, it is worth noting that Cook (1985) showed that $\Delta\sigma/2$ and $\Delta\varepsilon_{tot}/2$ are R_ε independent at 566 °C for 0.2 % $\leq \Delta\varepsilon_{tot}/2 \leq$ 0.8 % and $-1 \leq R_\varepsilon \leq 0.4$ for the material studied in this work. The author has also found that the mean stress fully relaxed when the material was tested

at room temperature and for different R_ε ratios at strain ranges higher than 1 %. These observations suggest that Inconel 718 stress-strain behavior is R_ε independent (Cook, 1982) for strain ranges higher than 1 %.

It should also be noted that the mean stress evolution was not accounted for in the model and thus the model is limited to $R_\varepsilon = -1$. For other R_ε values and particularly when strain ranges are lower than 1 %, where the stress-strain behavior is not R_ε independent, the mean stress evolution has to be accounted for. The mean stress evolution could be empirically estimated for different R_ε and strain ranges values. This empirical relationship could be used to translate the results obtained for $\Delta\sigma/2$ and $\Delta\varepsilon_{tot}/2$ along the stress axis. It would also be of interest to investigate the possibility of establishing a common relationship for the mean stress relaxation between incremental and single step tests for $R_\varepsilon \neq -1$.

Chaboche's constitutive equations were adapted and developed in 1D in this work. Iyer and Lissenden (2003) showed that a model accounting for the second (J_2) and the third (J_3) principal invariants could describe the stress space of Inconel 718 tubular specimen submitted to bi-axial (torsional and uni-axial) tests at 650 °C. It was also observed that, at room temperature and for axial-torsional loads on tubular samples, Inconel 718 had a higher relative yield strength in compression than in tension (Iyer and Lissenden, 2000). Moreover, the second invariant J_2 alone was not sufficient to describe the inelastic flow. A combination of the three stress invariants (I_1, J_2 and J_3) seems to be required. Based on the above, extending the proposed model to 3D would require introducing more than one stress invariant in Equation (5.1). The stress invariant combinations proposed by Iyer and Lissenden (2003) and Iyer and Lissenden (2000) could be used and compared. Finally, Inconel 718 has a textured microstructure and if the grain size is isotropic, the mechanical behavior of the material should be the same in every direction.

5.5 Conclusion

The study showed the dependency of Inconel 718's softening on the accumulated plastic strain at room temperature. All the tests were performed at $R_\varepsilon = -1$ and at a constant strain rate. Stress response under incremental strain controlled loading was successfully simulated with a Chaboche's uni-axial constitutive model whose parameters were determined from single step tests. Single step tests stress responses were also predicted with parameters extracted from the incremental block test. The main conclusions are as follow:

- At $R_\varepsilon = -1$ and room temperature, Inconel 718 isotropic softening behavior is dependent on the accumulated plastic strain, irrespectively of the strain spectrum.

- Inconel 718 cyclic stress response during constant or complex strain controlled LCF loadings can be predicted using a data set obtained from a different fully reversed strain spectrum.
- Yield strength determination criterion can lead to a discrepancy between the predictions and the experimental results at the end of the elastic domain. Here, a 0.05 % strain offset criterion for the yield strength led to an overestimation of the yield onset.
- Predictions of the very first cycles show a stress response overestimation. This might be due to the difference in yielding mechanisms between the first cycles where hardening is observed and the rest of the fatigue life where continuous softening occurs.

Further work could consider the effect of the strain ratio R_ε and its adaptation in 3D. Such predictions could lead to an enrichment of fatigue life models considering the crack tip's plastic zone yield strength evolution.

5.6 Acknowledgements

This work was financially supported by the Consortium of Research and Innovation in Aerospace in Quebec, the Natural Sciences and Engineering Research Council of Canada, Mathematics of Information Technology and Complex systems, Pratt & Whitney Canada, Bell Helicopter Textron, L3-Communications MAS and Héroux-Devtek (grant number: RDC 435539-12).

5.7 Appendix

Computation of the isotropic parameters γ_1 and γ_2:

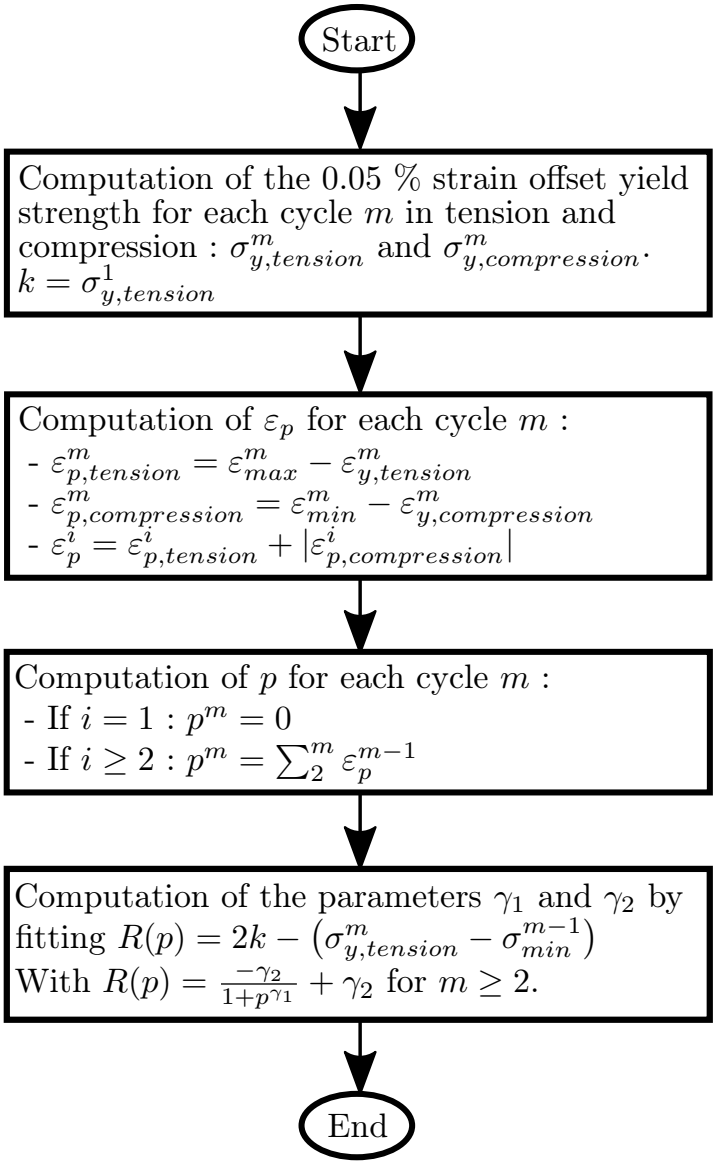

Computation of the numerical modeling stress σ_{num} value from the experimental strain data:

For each data point j: $f^j = |\sigma^j_{num} - \chi^j\left(a_i, C_i, \varepsilon^j_p\right)| - R(p) - k$.

Initialization: $\sigma^1_{num} = 0$ and $j = 1$.

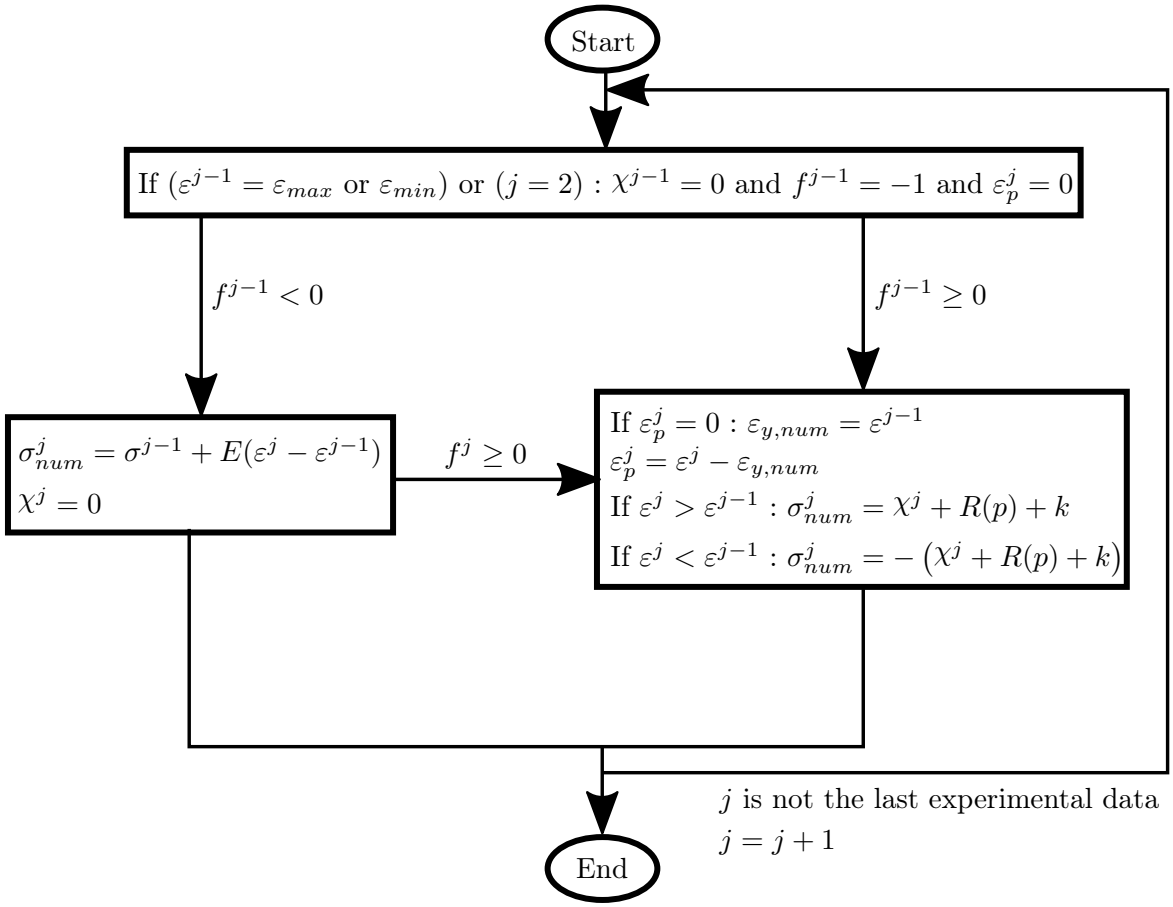

CHAPTER 6 LIMITATION OF THE CYCLIC YIELD MODEL

This Chapter explains why the results presented in the first article (Chapter 5) were not used in the fatigue life prediction model.

6.1 Different microstructures and mechanical properties

The specimens used for the cyclic yield tests presented in the first article were extracted from 90 mm diameters bars. For cost reduction purpose, the fatigue specimens that were used for the remaining experimental work were extracted from 25 mm diameter bars. This Chapter aims at showing the microstructural and mechanical differences between the two batches of raw material.

6.1.1 Different microstructures

Samples extracted from the two bars were polished and chemically etched in order to compare their microstructures. Optical micrographs presenting both microstructures are presented in Figure 6.1. The microstructure of the 90 mm diameter bars (Figure 6.1(a)) is characterized by a bi-modal grain size with two median groups having average diameters of 10 and 30 μm. Some grains have a grain size as large as 100 μm. On the other hand, the 25 mm diameter bars (Figure 6.1(b)) have a 13 μm grain size with grains ranging from 5 to 30 μm. Beside the difference in grain size, the materials are mainly composed of the same phases and non metallic inclusion.

6.1.2 Different chemical compositions

Chemical compositions of both microstructures are presented in Table 6.1. Both chemical compositions are similar except for niobium and molybdenum which are both lower in the 25 mm diameter bars. This difference in chemical composition may have an effect on the tensile mechanical properties, as presented in Section 6.1.3.

6.1.3 Different monotonic tensile mechanical properties

Monotonic tensile properties obtained following ASTM Standard E8M-13a (2013) testing procedure are presented in Table 6.2. For each bar, the results are the average of two

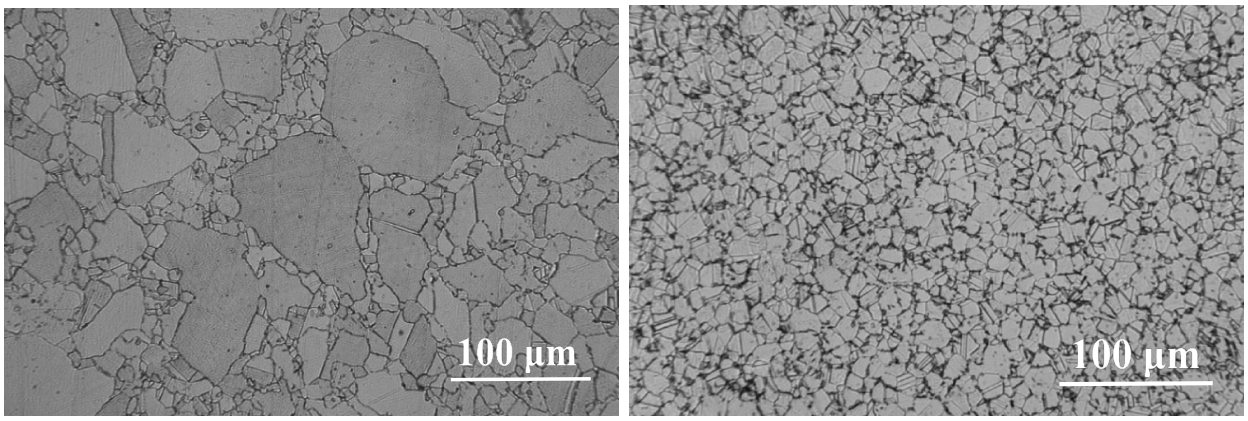

(a) (b)

Figure 6.1 (a) 90 and (b) 25 mm diameter bars optical micrographs. The chemical etching revealed the two different microstructure

Table 6.1 90 and 25 mm diameter bars chemical compositions (weight %). The results were obtained by optical spectrometry

	Ni	Fe	Cr	Nb	Mo	Ti	Al	Co	Si	Mn	Cu
90 mm	Bal.	18.38	17.93	5.23	3.24	1.19	0.60	0.30	0.07	0.06	0.05
25 mm	Bal.	19.53	17.84	5.04	3.07	1.16	0.64	0.35	0.06	0.16	0.06

monotonic tensile tests. The true stress as a function of the applied strain for each tensile test are presented in Figure 6.2.

As observed in Table 6.2 and in Figure 6.2, the yield strength of the specimens extracted from the 25 mm diameter bar is 100 MPa lower than the one of the specimens extracted from the 90 mm bars. This yield strength difference, in spite of the smaller grain size, might be explained by the lower amount of niobium present in the 25 mm diameter bars. Indeed, niobium is found in the γ'' ($Ni_3(Nb - Ti)$) precipitates which strengthen Inconel 718.

Despite their lower yield strength, the 25 mm diameter bar specimens show higher strain hardening rates and have a similar ultimate tensile strength than the 90 mm diameter bars specimens. The smaller grain size of the 25 mm diameter bar specimens might be responsible for the yielding resistance.

These differences in mechanical properties show that the parameters used in the cyclic yield model developed in the first article must be re-calibrated in order to predict cyclic yielding in the fatigue specimens which were extracted from the 25 mm diameter bars. It would require a new cyclic yielding experimental campaign to define and validate a new set of

Table 6.2 90 and 25 mm diameter bars monotonic tensile properties following ASTM E8M-13a methodology. The results are the average of 2 tests for each type of bar

	E (GPa)	$\sigma_{y0.2\%}$ (MPa)	σ_u (MPa)	El (%)	AR (%)
90 mm	205	1253	1413	24	39
25 mm	205	1156	1415	23	33

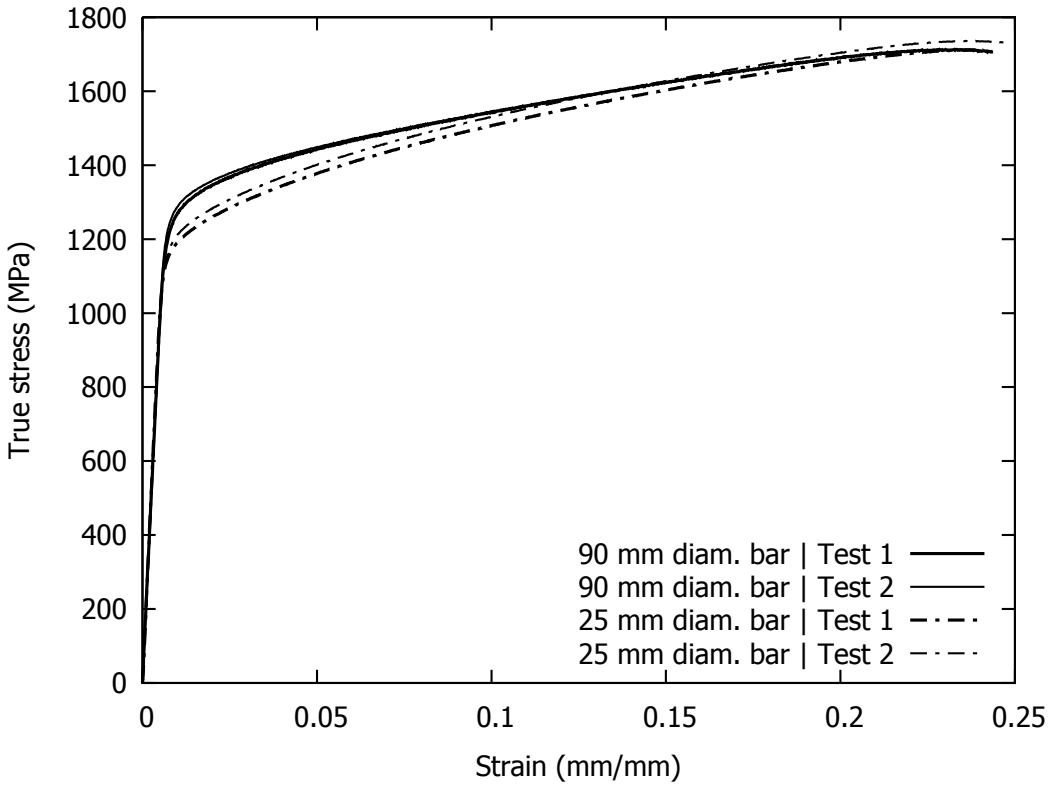

Figure 6.2 90 and 25 mm tensile test results

parameters. The experimental campaign required to re-calibrate the cyclic yield model was not initially planed in the doctoral project and was not performed due to budget limitation.

6.2 Strain ratio modeling

The cyclic plastic zone at the crack's tip is located within a larger monotonic plastic zone. The strain ratio (R_ε) is thus not constant in the cyclic plastic zone. R_ε evolves from 1 at the frontier with the monotonic plastic zone to a negative value at the crack's tip. The strain ratio will also depend on the applied loading and the crack geometry.

Further tests have to be performed to verify if the cyclic yield model proposed for $R_\varepsilon = -1$ is applicable to other R_ε. Moreover, since R_ε is not constant in the crack's tip plastic zone, another model should be used to determine exactly what is the load path seen by each location of the material encompassed by the cyclic plastic zone.

6.3 Microscopic scale

The yielding in the plastic zone at a short crack's tip will highly depends on the microstructure since the cyclic plastic zone will have the size of one or few grains. In this condition, the model developed in the first article should be modified to account for microstructural heterogeneity.

6.4 Conclusion

The cyclic yield model developed in the first article was not used to describe the behavior of the cyclic plastic zone at a crack's tip for the following reasons:

- The specimens used to calibrate the model have different microstructures and tensile mechanical properties than the specimens that were used for the fatigue tests.
- The model was only validated for $R_\varepsilon = -1$, which is not representative of the large range of R_ε at which the plastic zone can be submitted.
- The model was only validated at a macroscopic scale. It may have to be modified in order to account for the microstructural environment (grain sizes and grain orientations).

However, the first article is an important step for future work in the understanding and the simulation of the crack's tip plastic zone. It inquires on the cyclic yield behavior of Inconel 718 and gives the analytical tools to predict the cyclic stress-strain curves.

CHAPTER 7 ARTICLE 2 : SURFACE CHARACTERISTICS AND FATIGUE BEHAVIOR OF SHOT PEENED INCONEL 718

T. Klotz, D. Delbergue, P. Bocher, M. Lévesque and M. Brochu, (2018).
International Journal of Fatigue, 110, pp. 10–21.

7.1 Abstract

Shot peening is commonly used in the aerospace industry to improve mechanical components fatigue life. It introduces compressive residual stresses and cold work at the surface which tend to close short fatigue cracks and delay their propagation, respectively. However, shot peening also creates surface irregularities that can be detrimental to fatigue. The effect of different shot peening conditions on Inconel 718 tested in low and high cycle fatigue is presented in this study. An analysis of the fatigue life, crack initiation mechanisms, residual stress relaxation, process induced strain hardening and surface roughness showed that, in high cycle fatigue, shot peening can increase Inconel 718 fatigue life from 2 to 20 times, depending on the shot peening conditions. This observation suggests that careful selection of peening parameters is crucial. In low cycle fatigue, the roughness resulting from shot peening is to be considered while in high cycle fatigue, it is the presence of significant residual stresses.

7.2 Introduction

Inconel 718 is a nickel-based superalloy largely used in aerospace gas turbines components submitted to cyclic loads. Shot peening is a cold work process consisting in impinging hard particles at high velocity onto a ductile metallic surface. The process introduces compressive residual stresses and work hardening on the specimen's surface layer (de los Rios *et al.*, 1995), which improves its resistance to fatigue. Compressive residual stresses tend to close short cracks while work hardening improves the material resistance to plastic deformation, which enhances resistance to crack initiation and propagation. However, fatigue life is sensitive to shot peening intensity since deeper dimples are created on the specimen's surface as shot peening intensity increases, resulting in stress concentrating features (Li *et al.*, 1992). It has been reported that there is an optimal shot peening intensity, for each material, that maximizes fatigue life (Novovic *et al.*, 2004; Wagner, 1999).

Shot peening is specified by the type of media, the Almen intensity and the surface coverage. The Almen intensity is an indirect measure of the shot peening intensity and is

obtained by peening a flat standardized strip, called Almen strip, firmly fixed into an Almen holder by four bolts. Due to the presence of residual stresses, the strips progressively bend as the process progresses. The strip's arc height is measured throughout the process progression and the Almen intensity (A) is defined as the arc height (1 A = 25.4 μm) when doubling the peening time increases the arc height by 10 %. Coverage is the percentage of the shot peened surface covered by dimples. A coverage beyond 100 % corresponds to a multiple of the shot peening time required for reaching 98 % coverage. For example, 200 % coverage corresponds to twice the shot peening time required to reach 98 % coverage.

Compressive residual stresses in Inconel 718 shot peened at an Almen intensity of 8 A, with a coverage of 200 % can reach -1000 MPa and the plastic deformation responsible for the hardness increase, commonly called cold work, can be as high as 40 % (Prevéy, 2000) on the part's surface. Nakamura *et al.* (2011) showed that shot peened Inconel 718 can endure a strain range 1.3 times larger than polished specimens for the same 10^4 fatigue cycles at failure under strain controlled axial fatigue at a strain ratio of 0. Other authors (Cammett *et al.*, 2005) have found that cracks initiated beneath the surface and resulted in longer fatigue lives in shot peened Inconel 718 tested at 525 °C under a stress ratio of 0.1. For example, an electropolished specimen lasted 2.7×10^5 cycles for a maximum applied stress of 1240 MPa while it was around 9.0×10^6 cycles for a specimen shot peened at 9 A with a coverage of 100 %.

Fatigue crack initiations for unpeened Inconel 718 have mainly two sources (Maderbacher *et al.*, 2013): 1) initiation at a carbide located at, or beneath, the surface, 2) initiation within a large grain. Initiations from carbides are associated to carbide cracking (Ono *et al.*, 2004) which occurs during the first cycle (Alexandre *et al.*, 2004) or are inherently present in the material (Zhou *et al.*, 2012). Initiations in large grains are explained by the early formation of persistent slip bands. Slip bands are commonly observed in Inconel 718 following plastic deformation when a grain is favorably oriented in the direction of the maximum shear stress (Fournier and Pineau, 1977; Klotz *et al.*, 2017). It has been found that, in the nickel-based superalloy René 88DT (similar to Inconel 718), fatigue cracks were formed by localization of cyclic plastic deformation on {111} slip planes near twin boundaries in large grains with high Schmid factors (Miao *et al.*, 2009). Stinville *et al.* (2015) showed that local strains at favorably oriented twin boundaries can be 8 times higher than the macroscopically applied strain. In the case of twin boundaries parallel to a slip system, the dislocations can travel throughout the whole grain and their mobility is accentuated by the twin boundary's length (Miao *et al.*, 2012; Stinville *et al.*, 2016). Ideal shot peening conditions should prevent crack initiations at carbides and large grains located at the specimen's surface. To the best of our knowledge, fatigue crack initiation mechanism and nucleation depth controlled by shot

peening parameters commonly used in the industry is yet to be demonstrated. Making this demonstration would be of considerable interest for companies designing Inconel 718 shot peened parts.

In an attempt to fill this knowledge gap, this study aims to quantify the effects of several shot peening conditions commonly used in the aerospace industry on the fatigue life of Inconel 718 in low and high cycle fatigue (LCF and HCF) at room temperature. The paper is organized as follows: Section 7.3 presents the studied material, the experimental fatigue procedure, the measurements and observation methods, as well as the equipment used to identify crack initiation features. Experimental results such as surface roughness, residual stress relaxation and cold work redistribution are presented in Section 7.4, along with the fatigue results and their fractographies. The results are then discussed in Section 7.5 and Section 7.6 concludes this work.

7.3 Material and experimental procedure

7.3.1 Material

The studied nickel-based superalloy Inconel 718 underwent a solution and precipitation heat treatment as per AMS 5663M (SAE-Aerospace, 2009) to reach an hardness of 45 HRC. The hardness is mainly due to the formation of γ' and γ'' precipitates (Xiao *et al.*, 2008). The material's tensile properties and chemical composition are listed in Tables 7.1 and 7.2, respectively. The austenitic FCC matrix microstructure has a 13 μm average grain size with grains diameters ranging from 5 to 30 μm. The grain size was estimated by manually measuring the perimeter of 115 grains with ImageJ and approximated these as circles perimeters. Figure 7.1 shows that the microstructure consists of titanium carbo-nitride (TiCN), δ phase (Ni_3Nb) and NbC carbides. The NbC carbides sizes were measured with the same procedure as for the grain size. The NbC were ranging from 3 to 14 μm with a 9 μm average size. The δ phase is located along the grain and twin boundaries. Aluminum and magnesium oxides were also observed in some TiCN particles. Note that γ' and γ'' particles are not visible on the optical micrograph.

7.3.2 Fatigue tests

Two types of specimens were used to perform fatigue tests: 1) 9.5 mm diameter cylindrical samples designed in agreement with ASTM Standard E466-07 (2007) to study crack initiation and quantify fatigue life and 2) 3.56 mm $\times$ 10.16 mm rectangular cross section samples to study the evolution of residual stresses and cold work during interrupted fatigue tests. The

Table 7.1 Inconel 718 average tensile properties measured on two specimens in agreement with ASTM Standard E8M-13a (2013). E: Young's modulus, $\sigma_{y0.2\%}$: 0.2 % offset yield strength, σ_u: Ultimate strength, EL.: Elongation at failure and AR.: Area reduction at failure

E (GPa)	$\sigma_{y0.2\%}$ (MPa)	σ_u (MPa)	El. (%)	AR. (%)
205	1156	1415	23	33

Table 7.2 Inconel 718 chemical composition obtained by optical spectrometry (weight %)

Elements	Ni	Fe	Cr	Nb	Mo	Ti	Al	Co	Mn	Si
Composition	Bal.	19.53	17.84	5.02	3.07	1.16	0.64	0.35	0.16	0.06

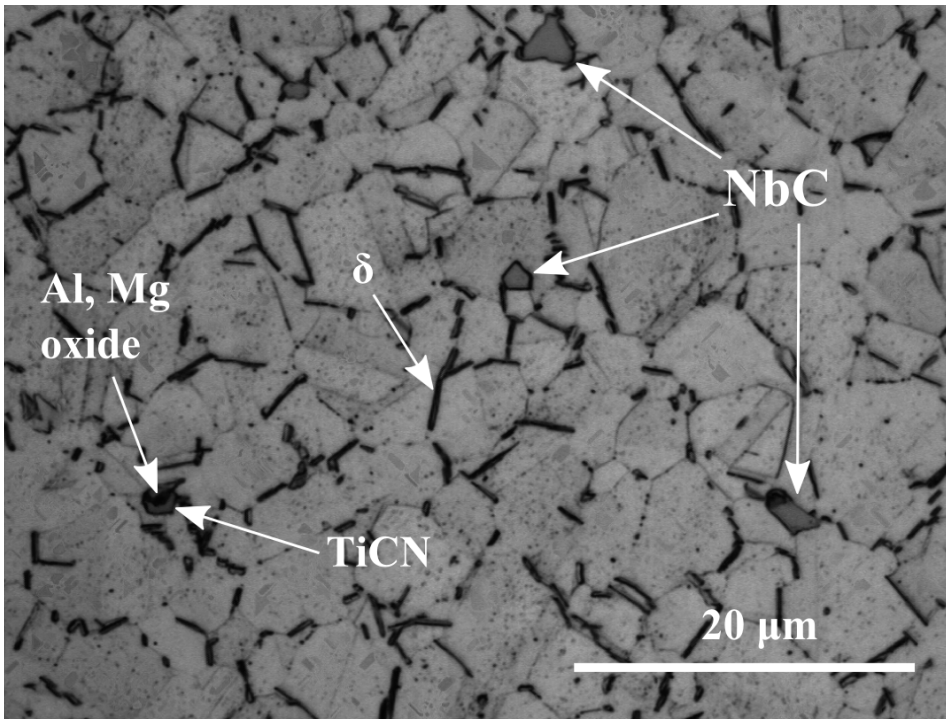

Figure 7.1 Inconel 718 optical micrograph. Niobium carbides (NbC) and titanium carbonitride (TiCN) are present at the grain boundaries and within the grains. δ phase (Ni_3Nb) can be observed along the grain boundaries. An Al-Mg oxide is present inside a TiCN particle

two geometries are presented in Figure 7.2. All specimens were extracted in the longitudinal direction of 25.4 mm diameter forged bars.

Tests were performed at room temperature under a 20 Hz constant stress amplitude on an MTS 318.10 hydraulic machine equipped with a 100 kN MTS 661.20e-03 load cell. A

stress ratio of $R_\sigma = \frac{\sigma_{min}}{\sigma_{max}} = 0.1$ with $\sigma_{max} = 1390$, 1380, 1370 and 1100 MPa was used under a sinusoidal load history. The stress level where $\sigma_{max} = 1100$ MPa is referred herein as HCF while the higher stress levels are referred as LCF since σ_{max} is above the material's yield strength (1156 MPa). Scanning electron microscope (SEM) observations of the rupture surfaces were performed with a JEOL JSM-7600F microscope. Energy dispersive X-ray

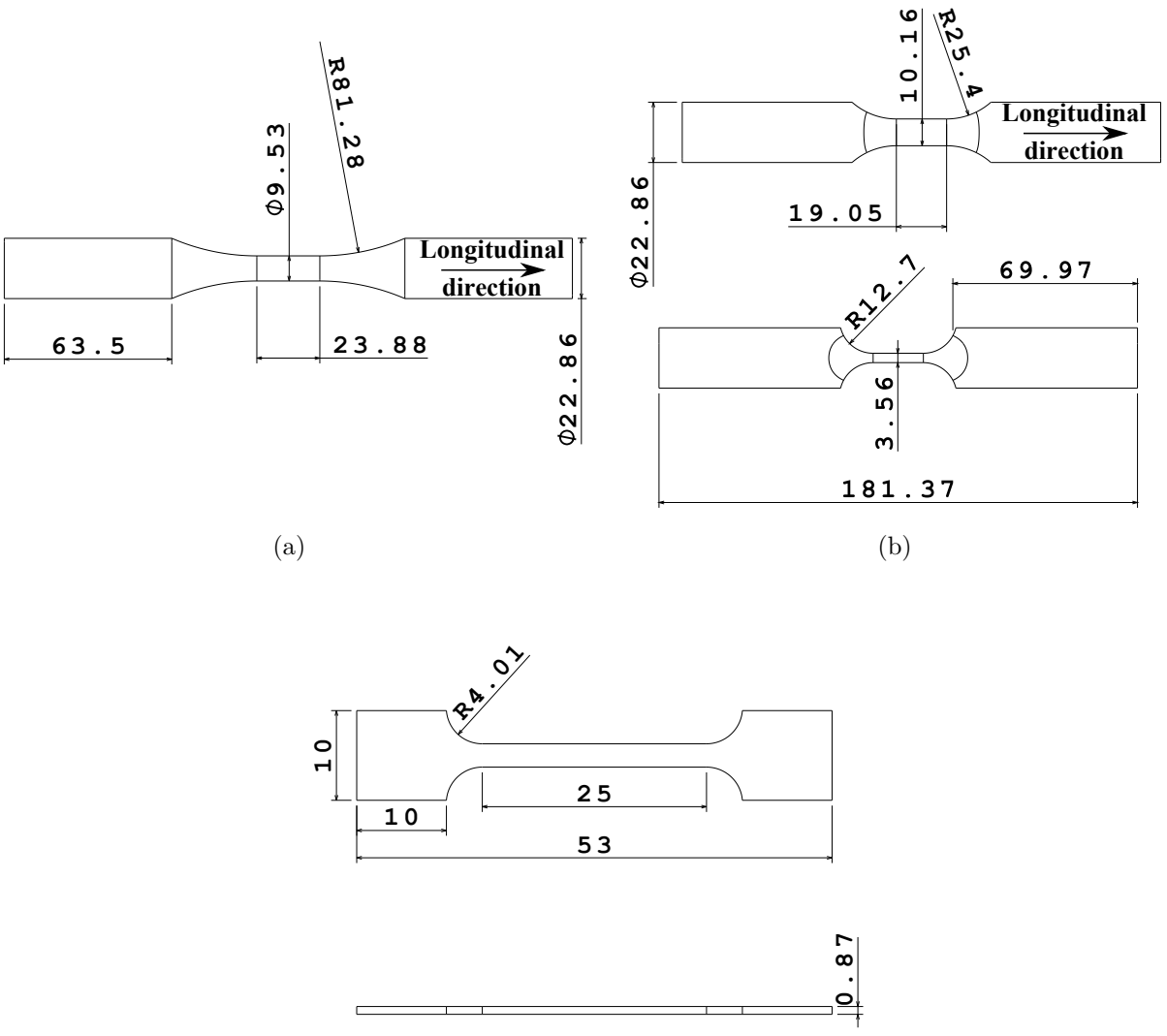

Figure 7.2 (a) Cylindrical and (b) rectangular specimens used for the fatigue tests and residual stresses relaxation measurements, respectively. (c) Micro-tensile specimen used for the X-ray elastic constant determination and the FWHM – ε_p relationship. Dimensions are in mm. The longitudinal direction is specified for the fatigue specimens

(EDX) spectroscopy was achieved with a silicon drift detector Oxford X-Max 80 to identify features present at crack initiation sites.

7.3.3 Surface conditions

Five different surface conditions were studied: 1) polished (down to 1 μm), 2) as machined, 3) shot peened with cast steel shots ASH 230 (S230) at an intensity of 4 A, 4) shot peened with conditioned carbon steel cut wire shots AWCR 14 (CW14) at an intensity of 4 A and 5) shot peened with CW14 at an intensity of 8 A, as summarized in Table 7.3. For the sake of clarity, shot peening conditions are designated in this paper by a type of media – Almen intensity couple. For example S230 4 A means a specimen shot peened with S230 media at an Almen intensity of 4 A.

Shot peening was performed with an air-pressured shot peening machine designed by Canablast and Genik. Shot peening was performed in agreement with SAE AMS2430T (2015) standard using a 6 axis M-20iA Fanuc robot and a rotating table mounted on a Fanuc 1-axis servo positioner. A 305 mm standoff distance and a 90° peening angle were used. The shots mass flow was controlled by MagnaValves provided by Electronics Inc. The average shots velocities were measured with a ShotMeter G3 from Progressive Technology and are presented in Table 7.3. 100 % coverage was reached for the three peening conditions.

Three longitudinal surface roughness profiles were measured per sample on specimens of each surface condition prior to fatigue testing. The roughness measurements on as machined specimens were performed on samples that were subsequently shot peened. The profiles were obtained using a profilometer Formtrace SV-C 3200 using a 8 mm cut-off wave length.

Table 7.3 The five surface conditions studied. The media diameter, velocity and the kinetic energy of a single shot are also presented. The kinetic energy is calculated as 0.5×media mass× velocity^2. The density of the shots was assumed to be of 7800 kg/m^3

	Surface	Media	Intensity (A)	Diameter (mm)	Velocity (m/s)	Kinetic energy (J)
1	Polished	-	-	-	-	-
2	As machined	-	-	-	-	-
3	Shot peened	S230	4	0.59	12	6.0×10^{-5}
4	Shot peened	CW14	4	0.36	34	2.2×10^{-4}
5	Shot peened	CW14	8	0.36	76	1.1×10^{-3}

Micro-hardness measurements were performed on a Akashi MVK-H0 microdurometer at 300 gf with a Vickers indenter, in agreement with ASTM Standard E384-11 (2011).

7.3.4 Residual stresses measurements

In-depth residual stress profiles were measured using X-ray diffraction (XRD). XRD measurements were performed on the {311} family of planes using the Kβ lines on a Pulstec μ-X360n apparatus equipped with a Cr-tube. Diffraction peaks were fit by the Lorentzian method (Noyan and Cohen, 2013). The cos α method (Sasaki *et al.*, 1997) was used to calculate the stresses. The X-ray elastic constant was previously determined for the {311} family of planes using a specimen, similar to that presented in Figure 7.2(c), having the same microstructure as the fatigue specimens and a Kammrath & Weiss GmbH micro-tensile machine, as described in the work of Delbergue *et al.* (2017). The parameters used for all residual stress measurements are summarized in Table 7.4. Thin layers of material were removed by electropolishing with a perchloric acid-based solution to extract a subsurface residual stress profile. The thickness of each removed layer was measured using an Olympus LEXT OLS4100 confocal microscope and a Mitutoyo SJ-400 profilometer. The Moore and Evans correction (Moore and Evans, 1958) was applied to correct stress redistribution caused by the layer-by-layer removal process, as the sample and electropolished pocket geometry agreed with the correction hypothesis. On average, the errors calculated for XRD measurements are roughly 80 MPa. The error is largely due to a combination of the K line used, the sample surface roughness and the inherent uncertainty associated to the layer removal method. Only the residual stress component parallel to the longitudinal direction (specified in Figures 7.2(a) and (b)) was measured as it is the direction in which most of the stress relaxation occurs in axial fatigue.

CW14 8 A rectangular specimens (Figure 7.2(b)) were used to measure the residual stress relaxation and/or redistribution that occurred during the cyclic loading. The same XRD settings, electrolytic solution and corrections as those used for the cylindrical specimens, were used.

7.3.5 Cold work measurement calibration

The XRD technique was also used to measure the extent of cold work caused by shot peening through diffraction peak broadening since this parameter is proportional to the dislocation dentsity (Warren, 1969). Prevéy (1987) has shown that the peak broadening is independent of the plastic deformation path and can be used as an independent measurement of the local strain in Inconel 718. Calibration was performed using an interrupted tensile test with the

Table 7.4 X-ray diffraction parameters used for residual stress measurements

Detector	Tube target	Aperture size	Diffraction plane
2D	Cr ($\lambda_{res} = 2.085$ Å)	1 mm	{311}

Bragg angle (2θ)	XEC ($\frac{1}{2}S_2$)	Nb of inclination	Exposure time
148.2°	7.41× 10^{-6} MPa^{-1}	1	90 s

Kammrath & Weiss GmbH micro-tensile machine paired up with the Pulstec μ-X360n apparatus used for residual stress measurements. A flat micro-tensile specimen, obtained from the same stock as the fatigue samples and whose geometry is presented in Figure 7.2(c), was prepared by grinding. A final layer of 10 μm was removed by electro-polishing to eliminate potential plastic deformation introduced by grinding. XRD measurements were performed up to 19 % of true strain, as the striction took place for higher strain values. The diffraction peaks were recorded and fit using the Lorentzian method (Noyan and Cohen, 2013) to extract peak width at half of the diffraction maximum intensity (Full Width at Half the Maximum (FWHM)). X-ray measurements were repeated 3 times.

7.4 Results

7.4.1 Surface characteristics prior to fatigue tests

Surface roughness

Surface roughness measurements and SEM observations of specimens surfaces are presented in Table 7.5 and Figure 7.3, respectively. The roughness parameters presented are the maximum peak to valley distance (R_t) and the mean width of roughness profile features (RSm) since the stress concentration induced by the dimples on a specimen's surface depends on their depth and width (Li *et al.*, 1992).

The average R_t of the as machined samples is 7.15 μm. As can be observed from Figure 7.3(b), the dimples created by the S230 media at an intensity of 4 A only partially erased the machining marks created by the turning process and slightly increased R_t to 8.65 μm. CW14 shot peening condition at the same intensity increased the R_t value up to 11.90 μm and the SEM observation (Figure 7.3(c)) still shows the presence of remaining machining marks. The surface appears to be more deformed than that obtained from the S230 4 A condition, which is consistent with the higher R_t measurements. The machining marks were

Table 7.5 Surface roughness prior to test for the studied surface conditions. Three longitudinal measurements were performed per sample

	As machined	S230 4 A	CW14 4 A	CW14 8 A
Nb of samples	15	6	6	6
R_t (μm) average (standard deviation)	7.15 (3.27)	8.65 (3.34)	11.90 (1.13)	25.38 (3.34)
RSm (μm) average (standard deviation)	246 (15)	362 (66)	328 (17)	405 (34)

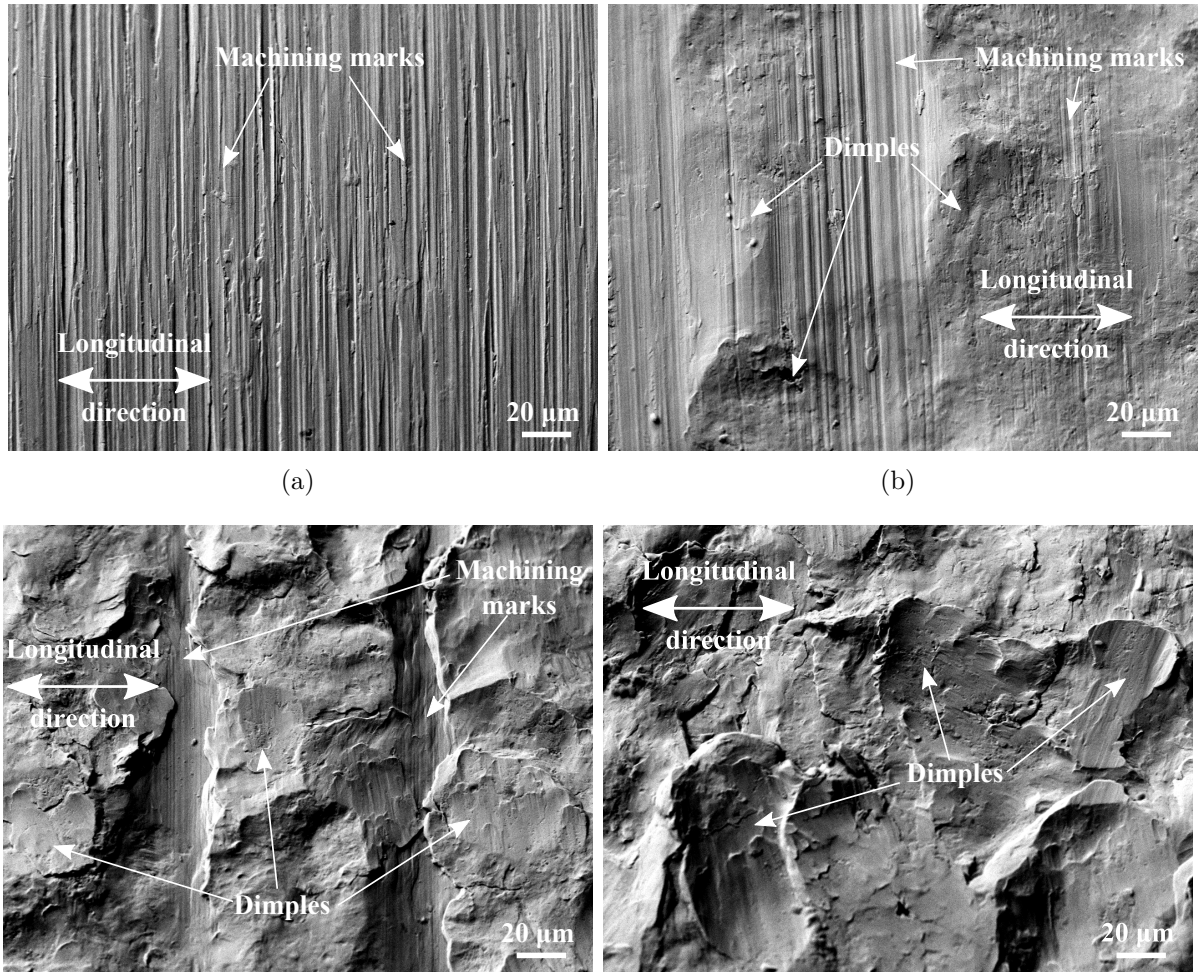

Figure 7.3 SEM picture of (a) as machined, (b) S230 4 A, (c) CW14 4 A, (d) CW14 8 A samples surface prior to fatigue testing. Machining marks are still present after S230 4 A and CW14 4 A shot peening

totally erased when peening with CW14 at an intensity of 8 A, as seen in Figure 7.3(d). Moreover, the surface's deformation appears to be more significant for this condition than for the others.

These results are consistent with the shot peening media size and the level of kinetic energies calculated in Table 7.3. In particular, S230 shot peening media is smaller and has less kinetic energy than the CW14 media for the same 4 A peening intensity. This situation results in smaller penetration for the S230 shot peening media, when compared to that of the CW14 media, and a lower average R_t is obtained.

All peening conditions increased the RSm. Peening with CW14 at an intensity of 8 A led to the highest RSm, in accordance with its higher shots kinetic energy.

Cross sections observations

Cross sections of as machined, S230 4 A, CW14 4 A and CW14 8 A samples were polished and etched to observe the effect of shot peening on the surface and subsurface microstructure. The micrographs are presented in Figure 7.4. Damaged NbC carbides were observed on the as machined specimen surfaces, as shown in Figure 7.4(a) inset. This observation is consistent with the works of Zhou *et al.* (2012) that showed that machining can damage surface carbides. No evidence of plastic deformation was observed on the as machined cross section (Figure 7.4(a)).

S230 4 A and CW14 8 A specimens present persistent slip bands in the first 10 and 25 μm below the surface (Figures 7.4(b) and (d)), respectively. Continuous bands of highly deformed material are visible at the surface of CW14 4 and 8 A specimens, as pointed out by the arrows in Figures 7.4(c) and (d). The qualitative amount of plastic deformation visually observed is consistent with the shots kinetic energy (Table 7.3): higher kinetic energy resulted in more plastic deformation.

Micro-hardness profiles were performed on the cross sections of shot peened specimens. The micro-harness profiles are presented in Figure 7.5. The base material had an hardness of 472 HV. Figure 7.5 shows that hardening is clearly observable for the CW14 8 A shot peening condition for which the hardness reached the maximum value of 524 HV at the surface and decreased until reaching the base material's hardness at a depth of roughly 125 μm. No evidence of hardening was detected near the surface for the S230 4 A and CW14 4 A shot peening conditions. It might be due to the fact that the measurements could not be performed sufficiently close to the shot peened surface.

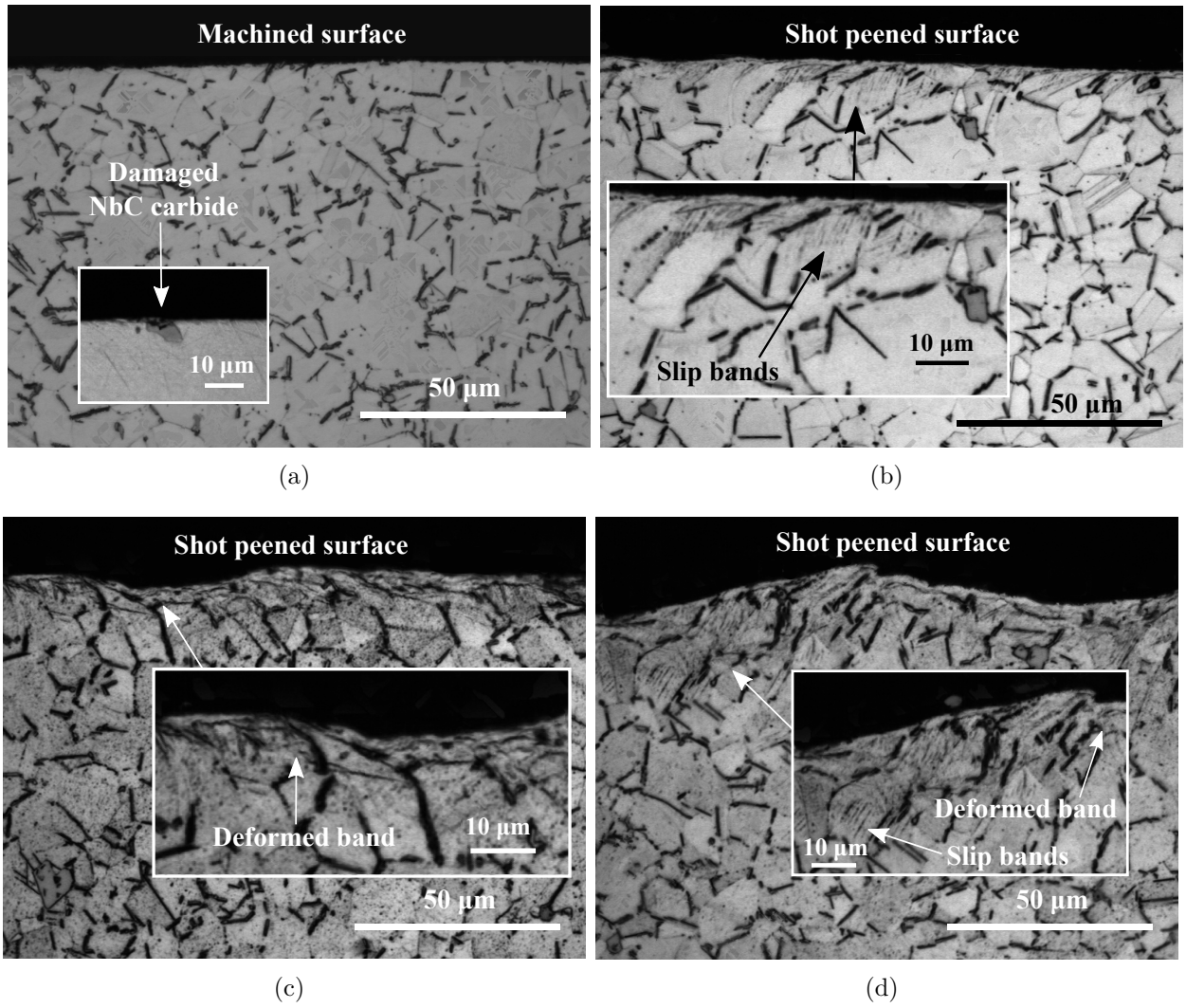

Figure 7.4 Pre-testing cross section optical micrographs of samples in the (a) as machined, (b) S230 4 A, (c) CW14 4 A and (d) CW14 8 A conditions. An optical micrograph of a damaged surface carbide taken on a non etched cross section of another as machined specimen is encapsulated in (a) to show that surface NbC carbides damaged by the machining process were found. Encapsulated zoom on persistent slip bands and deformed bands are also present in (b), (c) and (d)

Residual stress and cold work profiles

FWHM versus the plastic strain obtained on the micro-tensile specimen is plotted in Figure 7.6. As proposed in the work of Prevéy (1987), the relationship between FWHM and the plastic strain, ε_p, was approximated as

$$FWHM = P_1 \left[1 - e^{-P_2 \varepsilon_p}\right] + P_3 \varepsilon_p + P_4 \tag{7.1}$$

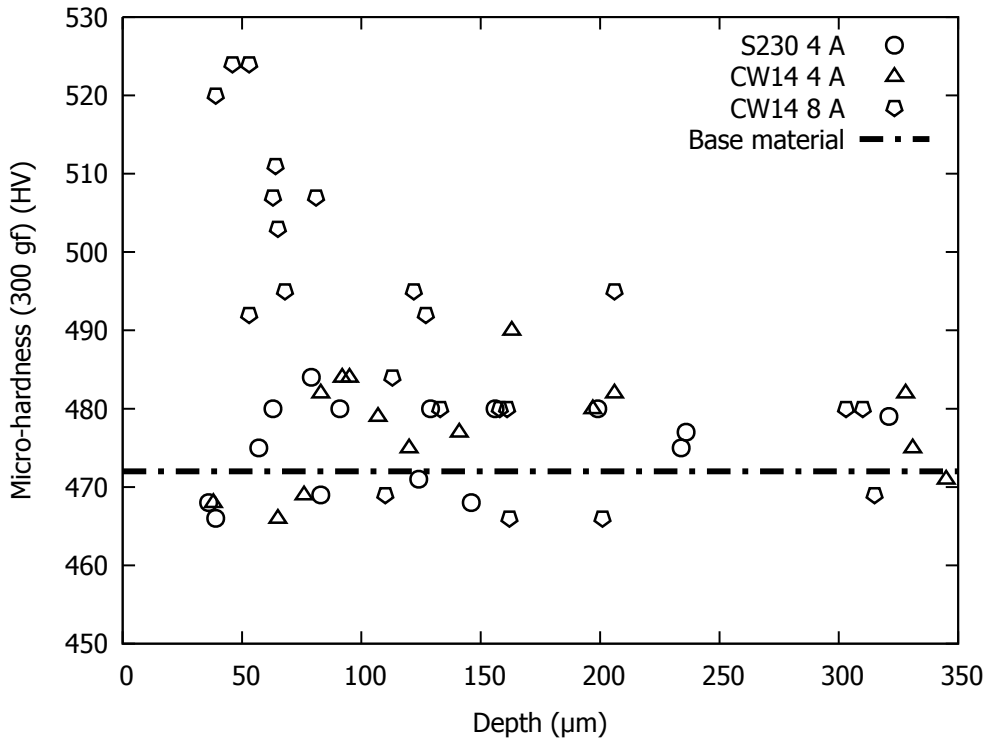

Figure 7.5 After shot peening micro-hardness profiles. The 472 HV base material hardness is also represented

where P_1, P_2, P_3 and P_4 are fitting constants determined by a least square regression. Table 7.6 lists the best fitting values, whose plot is also shown in Figure 7.6. The figure reveals that an excellent agreement was found and we believe that FWHM values for plastic strains above 20 % can be extrapolated from Equation (7.1). The depth of the cold work profile is defined herein as the depth at which the cold work value becomes lower than 0.2 %.

The residual stress and cold work profiles prior to fatigue testing are presented in Figure 7.7. Table 7.7 lists key residual stress measurements for comparison purposes.

The polished sample exhibited a compressive surface residual stress of -119 MPa decreasing to -40 MPa at 10 μm below the surface. The maximum compressive residual stress for the as machined specimen was -468 MPa at the surface and after the depth of 38 μm, the residual stresses are tensile staying in the range of $\pm$50 MPa.

The residual stresses profiles shapes for the shot peened specimens are similar to those commonly found in the literature. Surface residual stresses (σ_{surf}) and maximum compressive stresses depth ($d_{\sigma_{\text{comp,max}}}$) are not significantly affected by the shot peening intensity, nor by the type of media for the studied conditions. CW14 4 and 8 A shot peening led to comparable

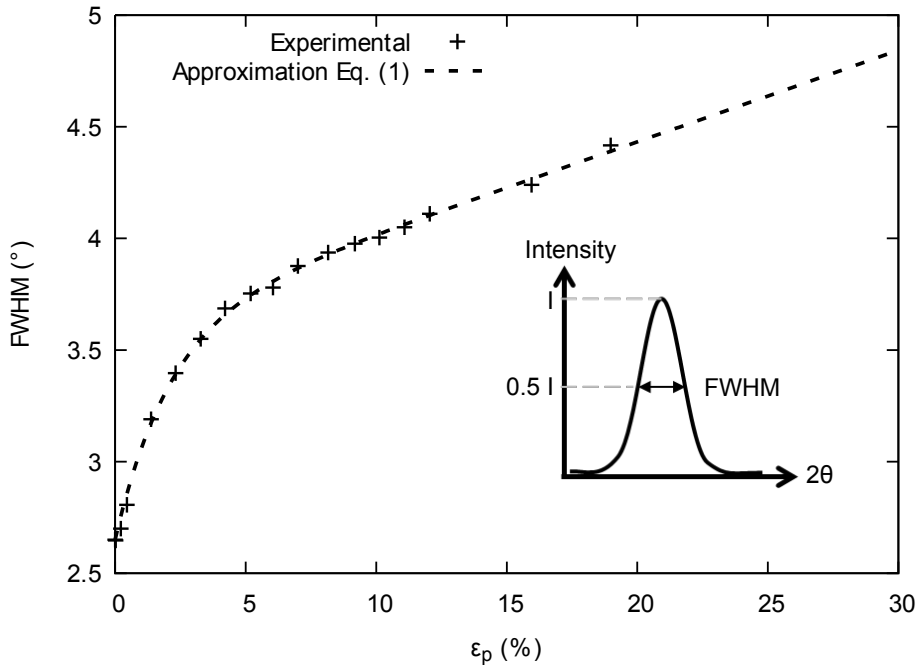

Figure 7.6 FWHM as a function of the plastic strain and its approximation by Equation (7.1). A schematic of the FWHM determination is encapsulated

Table 7.6 Fitting constants obtained for Equation (7.1)

P_1	P_2	P_3	P_4
0.9622	0.4808	0.0410	2.65

maximum compressive residual stresses ($\sigma_{\text{comp,max}}$), while peening with S230 4 A condition resulted in a lower value. The saturation value of maximum compressive residual stress is -1020 MPa, which corresponds to 88 % of $\sigma_{y0.2\%}$. Similar values were found by Gao *et al.* (2002) on shot peened 4340 steel samples with a saturation value of roughly 86 % of $\sigma_{y0.2\%}$. The depth at which the residual stresses becomes tensile ($d_{\sigma_{\text{comp}=0}}$) is the same for the two 4 A conditions ($\simeq$ 120 μm) and is deeper for the CW14 8 A specimen (210 μm). The CW14 8 A specimen exhibits a tensile residual residual stress peak of 157 MPa at a distance of 230 μm below the surface.

Figure 7.7(b) presents the in-depth cold work distribution. The polished specimen shows almost no cold work (0.72 % at the surface). The as machined specimen exhibits 5% of cold work at its surface and is free of cold work at a depth of 32 μm. The S230 4 A sample exhibits 36 % of cold work at the surface while this value increases to 51 % and 57 % when

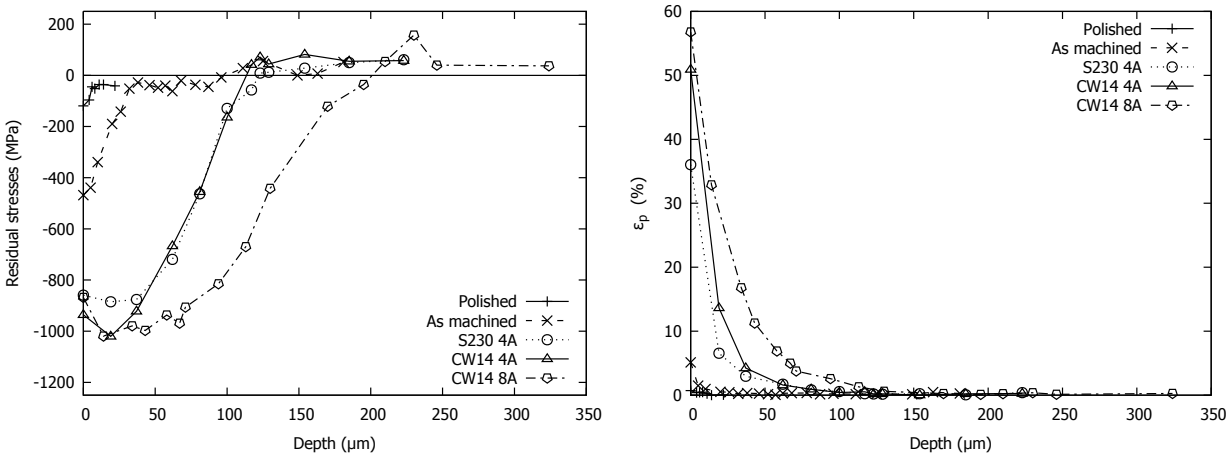

(a) (b)

Figure 7.7 Samples in-depth (a) residual stresses and (b) cold work profiles prior to test. Lines are displayed to ease the analysis but are not representative of physical phenomenon

Table 7.7 Summary of the results presented in Figure 7.7. σ_{surf}: Residual stress at the surface. $\sigma_{\text{comp,max}}$: maximum compressive residual stress. $d_{\sigma_{\text{comp,max}}}$: depth of the maximum compressive residual stress. $d_{\sigma_{\text{comp=0}}}$: depth at which the residual stresses become tensile

	Polished	As machined	S230 4 A	CW14 4 A	CW14 8 A
Residual stress profiles					
σ_{surf} (MPa)	-119	-468	-859	-936	-868
$\sigma_{\text{comp,max}}$ (MPa)	-119	-468	-885	-1020	-1019
$d_{\sigma_{\text{comp,max}}}$ (μm)	0	0	19	19	14
$d_{\sigma_{\text{comp=0}}}$ (μm)	-	38	123	117	210
Cold work profiles					
ε_p (%)	0.72	5	36	51	56
Profile depth (μm)	11	32	123	123	195

peening with CW14 4 A and 8 A, respectively. The shot peened specimens cold work profiles end ($\varepsilon_p < 0.2$ %) at a depth of 123 μm for S230 and CW14 4 A samples while this value is increased to 195 μm for the CW14 8 A specimen.

The surface cold work is consistent with the shots kinetic energy: The higher the shots

kinetic energy, the higher the surface cold work. The cold work profiles depths appear to be similar to the depth of the compressive residual stresses.

Note that no comparison between the hardness profiles presented in Figure 7.5 and the cold work profiles presented in Figure 7.7(b) can be clearly made.

7.4.2 Fatigue results

LCF results

The stress strain curve of the 100 first loading cycles of a cylindrical specimen tested in LCF are presented in Figure 7.8. The material exhibited nearly elastic behavior after 50 cycles since the hysteresis loops have a maximum width of roughly 2×10^{-4} mm/mm for a maximum strain of 0.123 mm/mm.

Fatigue results are presented in Figure 7.9. The fatigue results of the surface condition and stress level tested more than 3 times were fitted to a Weibull distribution. The average fatigue lives, the number of cycles leading to a failure probability of 50 % and the Weibull distributions shape and scale parameters are presented in Table 7.8. The lower bounds of the 95 % confidence interval for a failure probability of 50 % are also provided in Table 7.8 to inquire on the reliability of the Weibull distribution predictions. The 95 % confidence intervals were computed with a χ^2 test on the logarithm of the likelihood function (Bianchetti *et al.*, 2017; Abramovich and Ritov, 2013). The linearizations of the Weibull laws are presented in Figures 7.10(a) and (b). Typical rupture surfaces and SEM observations of the crack initiation sites are presented in Figures 7.11 and 7.12, respectively.

The fatigue lives obtained at $\sigma_{max} = 1380$ and 1390 MPa for the polished and as machined specimens, and at $\sigma_{max} = 1370$ MPa for the shot peened specimens are shown in Figure 7.9(a). The polished specimens present the longest average fatigue life ($\simeq 2 \times 10^4$ cycles) followed by 4 A shot peening conditions (1.59×10^4 and 1.57×10^4 cycles for S230 and CW14, respectively), as machined ($\simeq 1.30 \times 10^4$ cycles) and CW14 8 A (1.24×10^4 cycles). The shot peened specimens average fatigue lives are consistent with the specimens roughness presented in Table 7.5: The rougher the surface, the lower the fatigue life.

It was not possible to draw statistical conclusion from polished and as machined specimens since too few specimens were tested. However, the number of available data points enabled predicting the number of cycles for a 50 % probability of failure (median life) for the shot peened specimens with a Weibull distribution and acceptable regressions were found (Figure 7.10). The median lives follow the same trend as the average fatigue lives and provide, with the lower bounds of the 95 % confidence intervals, an assessment of fatigue life

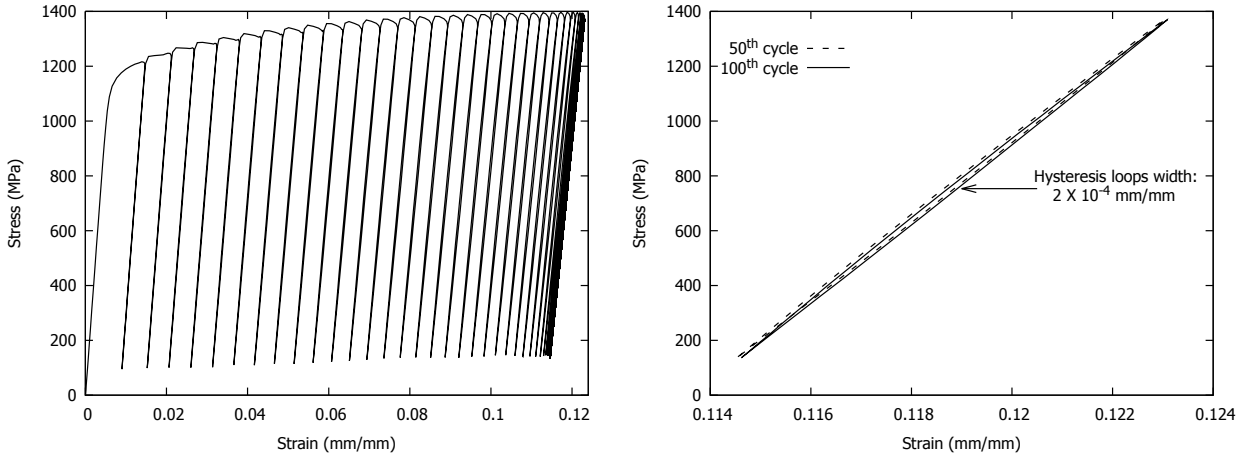

(a) (b)

Figure 7.8 Deformation versus stress for a sample tested at $\sigma_{max} = 1370$ MPa: (a) from the 1^{st} to the 100^{th} cycle and (b) the 50^{th} and the 100^{th} cycles. Plastic deformations in the form of 2×10^{-4} mm/mm width hysteresis loops are observed during the loading and unloading phases after 50 cycles

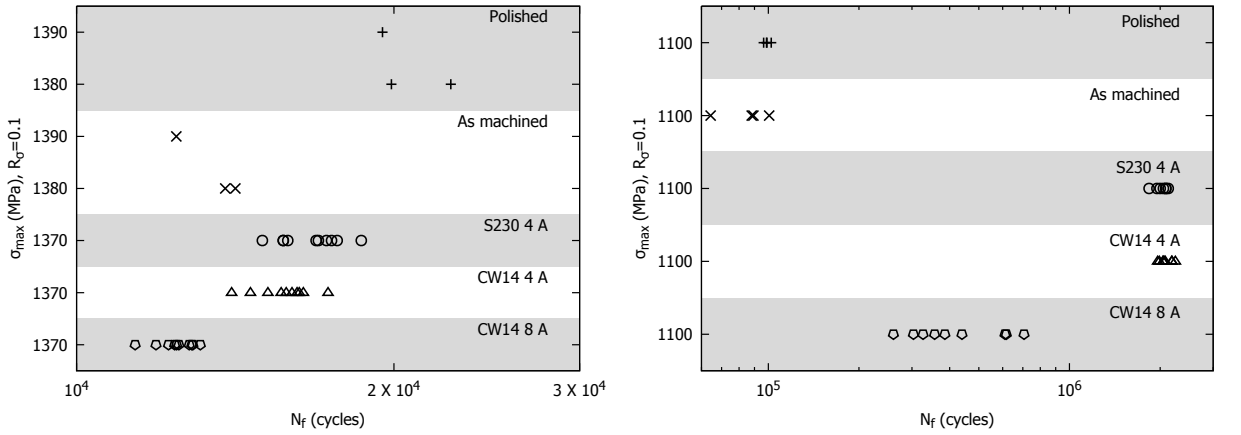

(a) (b)

Figure 7.9 SN curve results: (a) Fatigue results under LCF conditions, (b) Fatigue results under HCF conditions. Note that the surface conditions have been disposed one upon another for the sake of clarity and to allow for a better comparison. Each horizontal grey/white band represents one surface condition tested at the σ_{max} specified on the vertical axis

dispersion. The closer is the lower bound of the 95 % interval to the median life, the lower is the dispersion. All the shot peening parameters are robust in LCF since all the 95 % confidence interval lower bounds of the 50 % probability of failure are very close to the computed median fatigue life, with a difference of less than 2 % for each case.

All specimens tested in LCF presented similar rupture surfaces. A typical example is presented in Figure 7.11(a). The figure shows the main crack initiation zone containing ratchet marks, sign of several nucleation sites as pointed out by the arrows.

Table 7.9 summarizes the SEM observations and the corresponding fatigue lives. The fracture surfaces of one polished and one as machined specimens were observed after LCF testing. The shot peened specimen that had the longest fatigue life (1.86×10^4 cycles) and that having the shortest fatigue life (1.14×10^4) were also observed. All rupture surfaces observed under SEM show that cracks initiated either at a surface NbC carbide (Figure 7.12(a)) or at a stress concentration caused by surface irregularities such as machining marks (Figure 7.12(b)).

Table 7.8 Weibull statistical description of the fatigue tests results. Nb: number of specimens. Av. N_f: average fatigue life. Fatigue tests conditions for which the number of tested specimens was inferior to 3 were not considered. The shape (β_w) and scale (λ_w) parameters were determined with the linearization of the Weibull laws presented in Figure 7.10. The number of cycles for 50 % probability (prob.) of failure following the Weibull law are provided. The lower bounds (LB) of 95 % confidence (conf.) interval for 50 % probability of failure are also listed

Surface condition	Nb	Av. N_f (cycles)	Scale parameter λ_w	Shape parameter β_w	50 % prob. failure (cycles)	50 % LB 95 % conf. (cycles)
LCF: $\sigma_{max} = 1370$ MPa						
S230 4 A	10	1.65×10^4	1.72×10^4	16.2	1.68×10^4	1.66×10^4
CW14 4 A	10	1.57×10^4	1.61×10^4	18.2	1.58×10^4	1.56×10^4
CW14 8 A	10	1.24×10^4	1.27×10^4	25.8	1.25×10^4	1.23×10^4
HCF: $\sigma_{max} = 1100$ MPa						
Polished	4	9.91×10^4	1.00×10^5	39.4	9.94×10^4	9.82×10^4
As machined	4	8.56×10^4	9.29×10^4	5.0	8.64×10^4	7.68×10^4
S230 4 A	7	2.02×10^6	2.06×10^6	20.9	2.03×10^6	1.99×10^6
CW14 4 A	9	2.09×10^6	2.14×10^6	22.5	2.10×10^6	2.08×10^6
CW14 8 A	9	4.45×10^5	5.01×10^5	3.0	4.43×10^5	4.03×10^5

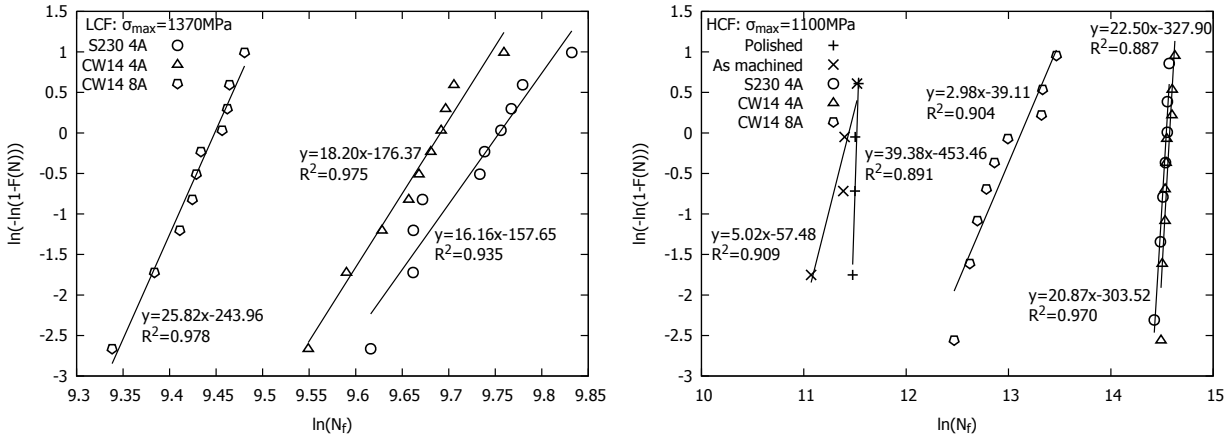

(a) (b)

Figure 7.10 Linearization of the Weibull law in (a) LCF and (b) HCF. The median ranks were estimated with the Bernard's approximation: $F(N) = (\text{n}^\circ - 0.3)/(\text{nb} + 0.4)$. n°: number of the specimen. nb: total number of specimens for one condition

Table 7.9 Summary of the initiation features observed under scanning electron microscope. NbC: initiation at a niobium carbide. Surf. conc.: initiation due to stress concentration along a surface defect (machining mark or shot peening dimple). Center: initiation in the center of the specimen. Subsurf.: initiation at roughly 210 μm underneath the surface. The fatigue lives (N_f) of the observed specimens are also presented

	Polished	As machined	S230 4 A	CW14 4 A	CW14 8 A
			LCF: $\sigma_{max} \geq 1370$ MPa		
Initiation	NbC	Surf. conc.	NbC	-	Surf. conc.
N_f (cycles)	2.24×10^4	1.38×10^4	1.86×10^4		1.14×10^4
			HCF: $\sigma_{max} = 1100$ MPa		
Initiation	NbC	NbC	Center	Center	Subsurf.
N_f (cycles)	1.02×10^5	1.01×10^5	1.84×10^6	2.19×10^6	6.17×10^5
Initiation	NbC	Surf. conc.	-	-	Subsurf.
N_f (cycles)	9.65×10^4	6.43×10^4			2.6×10^5

HCF results

HCF ($\sigma_{max} = 1100$ MPa) fatigue testing results are shown in Figure 7.9(b). When compared to as machined specimens average fatigue life (8.56×10^4 cycles), the average

fatigue life was increased by a factor of 4.5 for the CW14 8 A specimens (4.45×10^5 cycles) and by up to 20 for the S230 and CW14 4 A shot peening conditions (2.02 and 2.09×10^6 cycles, respectively).

The median fatigue lives follow the same trend as those for the average fatigue lives. Despite the fact that only 4 specimens were tested under the polished conditions, the dispersion in the results is very low since the lower bound of the 95 % confidence interval on the median life is only 1.2 % lower than the predicted median life. The as machined conditions shows a large dispersion in the results (Figure 7.9(a)) and the lower bound of the 95 % confidence

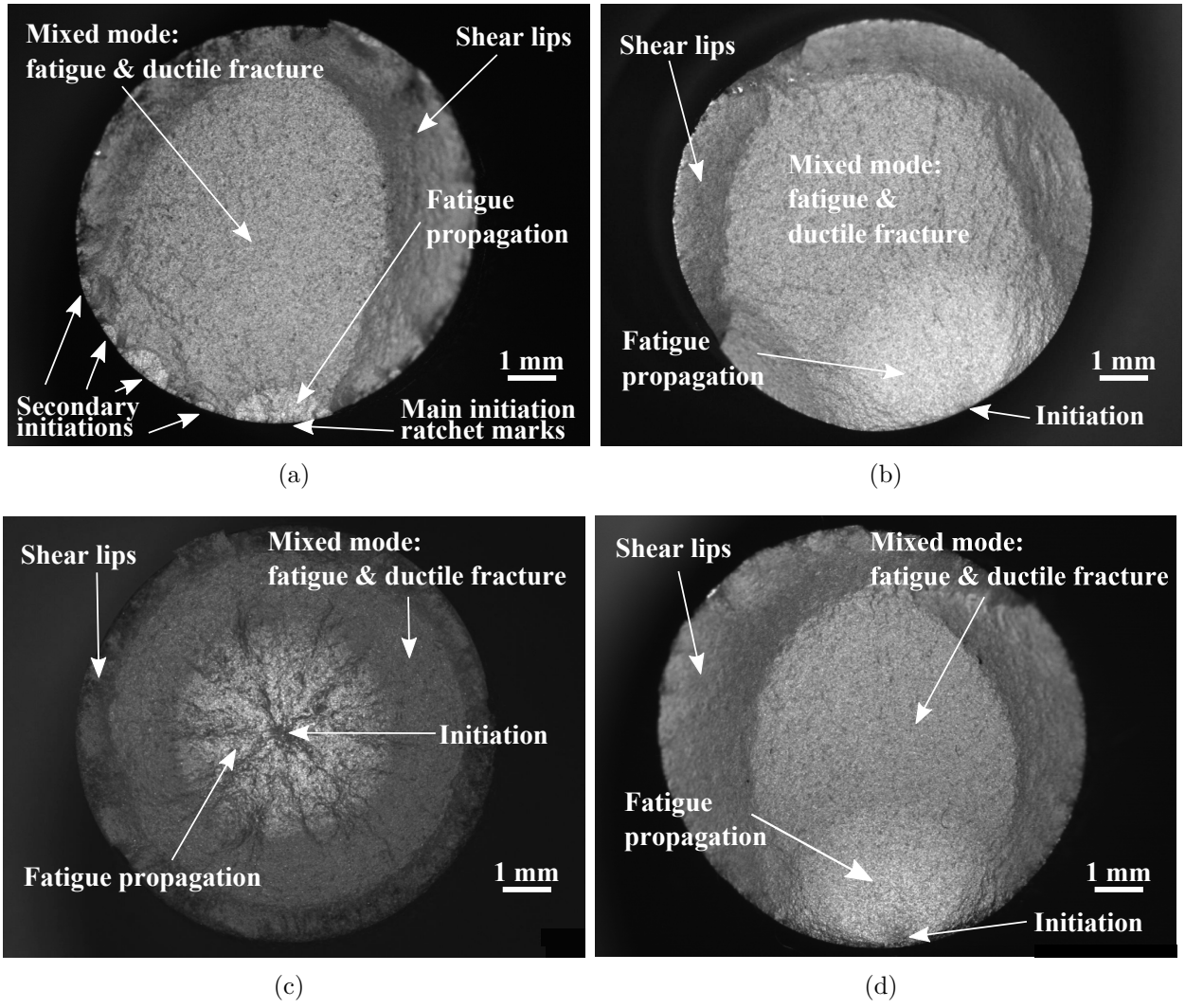

Figure 7.11 Rupture surfaces: (a) All surfaces conditions at $\sigma_{max} \geq 1370$ MPa (here a CW14 4 A specimen), (b) Polished and as machined samples at $\sigma_{max} = 1100$ MPa, (c) Shot peened CW14 4 A and S230 4 A at $\sigma_{max} = 1100$ MPa, (d) Shot peened CW14 8 A at $\sigma_{max} = 1100$ MPa

interval is 11 % lower than the median life. S230 and CW14 4 A fatigue lives are highly predictable in HCF since the lower bounds of the 95 % confidence interval of the median lives are less than 2 % lower than the computed median life. On the other hand, the lower bound of the 95 % confidence interval of the CW14 8 A median life is 9 % lower than the computed median life, corresponding to a wider dispersion in the results for this loading condition. S230 and CW14 4 A are thus the most robust shot peening conditions and those

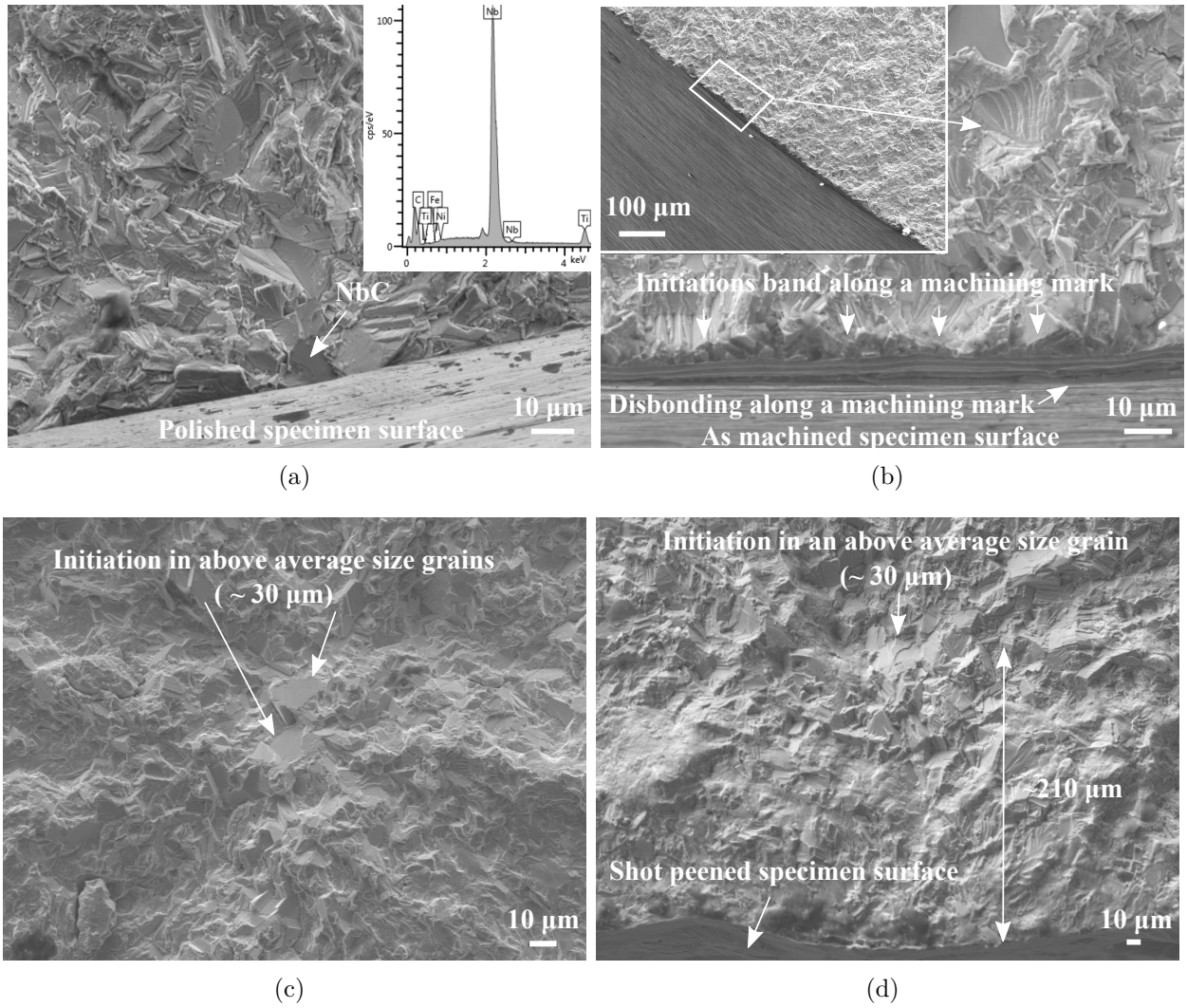

Figure 7.12 Various initiations observed under scanning electron microscope: (a) Initiation at a niobium carbide located at a polished specimen surface tested in HCF, the carbide EDX spectrum is inset, (b) Multiple initiations along a surface stress concentration feature on a machining mark. A machining mark disbonding can also be observed in this as machined sample tested in LCF, (c) Crack initiation at an above average size grain in the center of the center of a S230 4 A specimen tested in HCF, (d) Crack initiation in an above average size grain 210 μm underneath the surface in a CW14 8 A specimen tested in HCF

resulting in the longest fatigue lives in HCF.

Table 7.9 summarizes the SEM observations. For each surface condition, the specimens that had the longest and the shortest fatigue life were observed. S230 and CW14 4 A were not studied separately because their rupture surfaces and fatigue lives were similar. The experimental data resulting from these two peening conditions were pooled.

In HCF, polished and as machined rupture surfaces were characterized by one or two distinct surface crack initiation sites, as shown in Figure 7.11(b). Table 7.9 shows that all the crack initiations observed under SEM occurred at a surface NbC carbide for polished specimens, as illustrasted in Figure 7.12(a). The observed crack initiations for the as machined specimens were either located at a surface carbide or at a machining mark, as shown in Figure 7.12(b).

All the S230 and CW14 4 A specimens tested in HCF show crack initiations located at depth above 2 mm, as illustrated in Figure 7.11(c). SEM observations made on two specimens show that crack initiation occurred in a larger than average ($\simeq 30\mu$m) grain, as illustrated in Figure 7.12(c). All CW14 8 A specimens show crack initiations just beneath the surface, as shown in Figure 7.11(d). For this shot peening condition, the crack initiation occurred in a larger than average ($\simeq 30$ μm) grain at a depth of roughly 210 μm (Figure 7.12(d)) for the two specimen observed. This depth corresponds to the depth of the tensile residual stresses peak observed in Figure 7.7.

7.4.3 Residual stresses redistribution for CW14 8 A

Residual stress and cold work redistribution were measured in LCF ($\sigma_{\max} = 1370$ MPa) and HCF ($\sigma_{\max} = 1100$ MPa) on rectangular cross section specimens shot peened with CW14 8 A only. XRD measurements were performed before and after the first loading cycle, as well as at 80 % of the fatigue life previously determined for both fatigue conditions on cylindrical specimens. Each stress profile was obtained from a different specimen. Residual stress and cold work profiles are presented in Figures 7.13(a) and (b), respectively.

The initial profiles of residual stress are similar for both the rectangular and cylindrical samples. However, Figure 7.13(a) shows higher tensile residual stresses in the rectangular specimen (100 MPa instead of 40 MPa). This is mainly attributable to the difference in thickness between the two geometries and the smaller volume available to balance the compressive residual stresses. Indeed, the surface compressive residual stresses are balanced by nearly constant tensile residual stresses in the core material (Menig *et al.*, 2001) and thus the thicker the specimen, the lower the tensile residual stresses. The value of the tensile residual

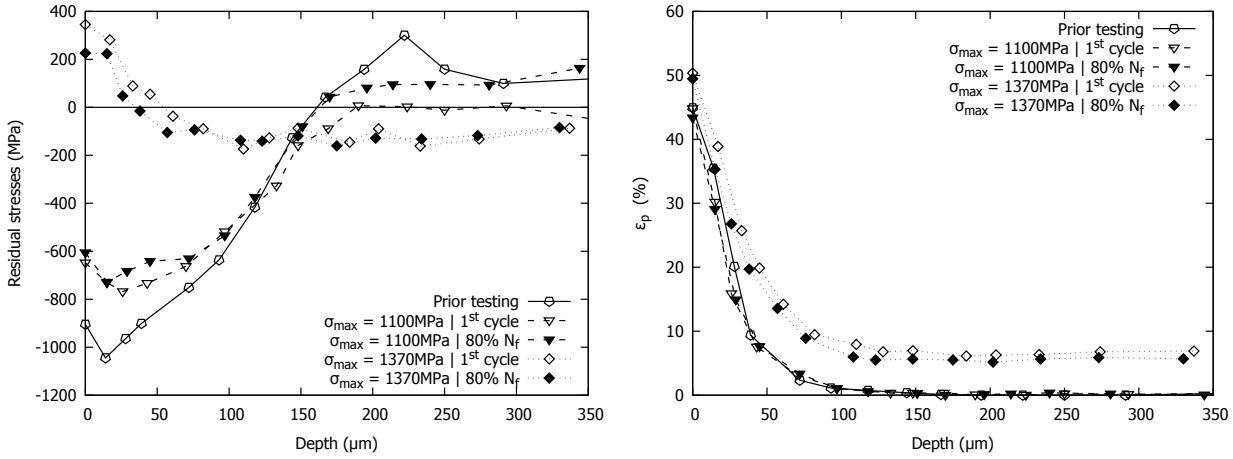

(a) (b)

Figure 7.13 (a) Residual stress and (b) cold work relaxation profiles for the CW14 8 A condition. Measurements were realized before testing, after the first cycle and at 80 % of the fatigue life (N_f). Lines are displayed for ease of the analysis but are not representative of physical phenomenon. Recall that the calculated average errors on XRD measurements is 80 MPa

stress peak is also higher (300 MPa instead of 157 MPa) but located at the same depth as that of the cylindrical specimen. On the other hand, the surface pre-testing cold work value of the flat specimen for CW14 8 A (45 %) is lower than that of the cylindrical samples (57 %).

As observed in Figure 7.13(a), most of the stress profiles evolution occurred in the first loading cycle as the difference between stresses characterizing the first cycle and 80 % of the fatigue life is in the range of the measurement errors ($\approx$ 80 MPa).

In LCF, due to the high level of applied stress, the compressive residual stresses become tensile at the surface (similar results were already reported in the literature (Kirk, 1987). The bulk of the material is plastically deformed. As surface layers have already been hardened by shot peening and are under a bi-axial residual compressive state, they are unlikely to undergo plastic deformation. The bulk material, which undergoes yielding during the first cycle, is permanently deformed and maintains the surface layers in tension when the axial stress is removed. This results in the formation of tensile residual stresses at the surface.

In HCF, after the first loading cycle, the compressive portions of the profile becomes less compressive. The maximum compressive stress value, which is initially at -1044 MPa, relaxes to -767 MPa after the first cycle and -728 MPa at 80 % of the fatigue life, which corresponds to a 27 and 30 % relaxation, respectively. The tensile residual stress peak vanishes after the first cycles, which suggests that local yielding occurs, leading to the relaxation of the residual

stresses. The residual stresses profile depth (150 μm) remains unaltered.

The associated cold work profiles, which are presented in Figure 7.13(b), remain stable during HCF. However, in LCF, the overall profile increases confirming that plasticity occurs during the first loading cycle throughout the material.

7.5 Discussion

LCF and HCF results are discussed separately to better emphasize the specific effect of shot peening on fatigue life and crack initiation mechanisms.

7.5.1 LCF

Three distinctive surface characteristics could influence the LCF of the shot peened specimens: roughness, residual stresses and cold work. In order to qualitatively determine the influence of the surface roughness, Figure 7.14(a) presents the fatigue life, at $\sigma_{max} = 1370$ MPa, for 14 shot peened samples plotted against the measured roughness parameters R_t. A correlation between the surface roughness and the fatigue life can be made: The higher the R_t, the lower the fatigue life. In this case, all crack initiated at the surface since no compressive residual stress could compensate the roughness induced stress concentration. Recall that the surface layer's residual stresses become tensile after the first cycle. Shot peening has a detrimental effect for the LCF conditions tested in this study.

Despite the surface tensile residual stresses and the increase in roughness resulting from shot peening, the average fatigue life of the shot peened specimens is not drastically lower than for the unpeened specimens. Apparently, the surface cold work can counterbalance the negative effects of roughness and tensile residual stresses by increasing the resistance to plastic deformation. Work hardening can delay crack nucleation on one hand, and on the other hand, the crack tip's plastic zone will be reduced resulting in lower short crack growth rate (de los Rios *et al.*, 1995; Miller, 1993). Figure 7.14(b) represents the fatigue life of the same 14 shot peened specimens against the surface cold work value. The figure shows that the cold work surface value did not improve the number of cycles to failure.

7.5.2 HCF

In HCF, only the compressive residual stresses under -700 MPa have relaxed somehow during the first cycle. The compressive residual stress profile introduced by shot peening remains effective so that for all shot peened specimens, crack initiation occurred underneath

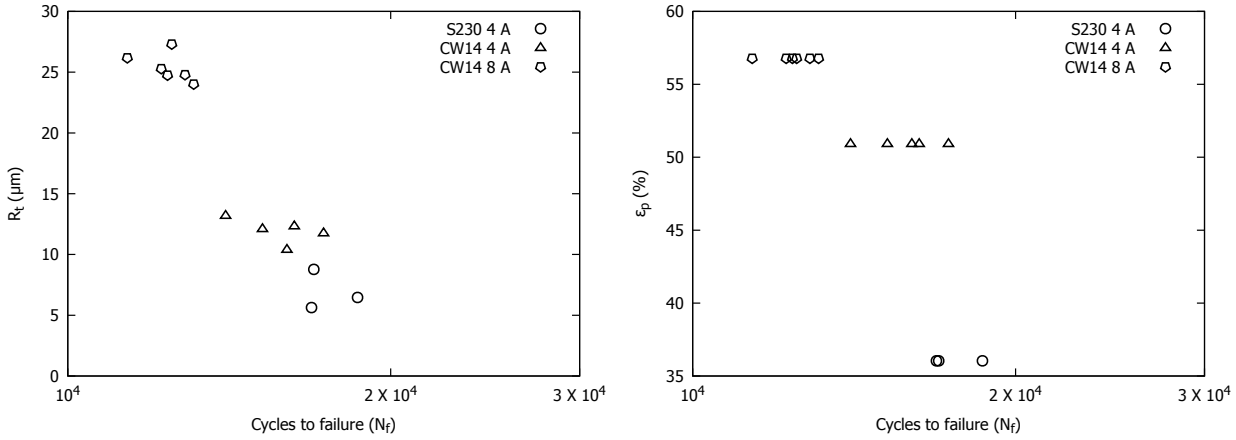

(a) (b)

Figure 7.14 Shot peened samples fatigue lives at $\sigma_{max} = 1370$ MPa versus (a) the surface roughness parameters R_t and (b) the surface cold work value. A correlation between R_t and the fatigue life under LCF condition can be observed: the lower the roughness, the better the fatigue life. A relation between the fatigue life and the surface cold work value cannot be clearly drawn

the surface. The predominant parameters for the site of crack nucleation are the size of grains and the position of an eventual tensile peak in the residual stress profile as introduced by shot peening, even if it seems to disappear after the first loading. Recall that the uncertainty on our residual stresses measurements was of ±80 MPa and that a tensile region must be present to balance the compressive residual stresses. Surface cold work and compressive residual stresses, which are the two benificial effects of shot peening, push the site of crack initiation underneath the surface, counterbalancing the detrimental effect of surface roughness.

In the case of S230 and CW14 4 A shot peening conditions, cracks initiated deep inside the material, in a large grain. Cracks initiated at depth above 2 mm where the residual stresses are negligible. The fatigue life dispersion of these samples is very low as the initial cracks are arising from a large volume of potential sites. The small scatter in the results suggests robust manufacturing parameters. Moreover, the average fatigue life is improved by a factor of 20, when compared to the polished specimens. With such improvement, 4 A shot peening conditions (S230 or CW14) illustrate the full potential of the material since the initiation occurred in a microstructural weakness regardless of surface defects (roughness, NbC carbides) and tensile residual stresses. The microstructural weakness becomes an above the average size grain and most likely a grain with twin boundaries, as suggested by Stinville *et al.* (2015). The local high strains are due to the resistance in slip transmission from a border of the twin boundary to the other one, resulting in slip bands parallel to the twin

boundary where crack will nucleate preferentially. The size of the grain is controlling the free distance of the dislocations and thus larger grains will also promote early crack nucleation. Miao *et al.* (2012) reported, in René 88DT, that initiation along twin boundary appeared in grains 3 times larger than average, as in this study. Stinville *et al.* (2016), as well as Miao *et al.* (2009), demonstrated that a large grain having a high Schmid factor and a twin boundary aligned with the slip systems are the criteria for crack initiations in plain materials.

The compressive residual stresses at the surface and beneath it for the CW14 8 A peening condition improved the fatigue life average by a factor of 4.5, when compared to polished specimens. When compared to the 4 A peening conditions, the samples seem to be "over peened" as the full potential of the process is not reached. As in the previous cases, crack initiations systematically occurred in a grain significantly larger than the average grain size. These crack initiations were found in a narrow region at roughly 210 μm below the surface. This position, 210 μm below the surface, corresponds to the tensile residual stress peak after peening. However, the tensile residual stress peak seems to disappear after the first cycle due to local yielding. This local yielding will lead to high strains along favorably oriented coherent twin boundaries in large grains (Stinville *et al.*, 2015) and thus will accelerate the accumulation of dislocations leading to early crack nucleation, when compared to randomly oriented grains. At this 210 μm depth, a relatively small number of grains are potential nucleation sites when compared to the S230 4 A and CW14 A conditions for which crack initiation occured at depths higher than 2 mm. This situation results in a wider results dispersion for the CW14 8A condition. Shot peening parameters should thus be chosen in order to avoid a subsurface tensile residual stress peak after peening.

7.6 Conclusions

Force controlled fatigue tests at $R_\sigma = 0.1$ were performed in HCF and LCF on polished, as machined, S230 4 A, CW14 4 and 8 A shot peened Inconel 718 samples. The initial surface roughness, surface microstructure alteration, initial and redistributed residual stresses profiles, cold work profiles and rupture surfaces were presented and analyzed. The analysis of the results led to 3 important conclusions:

1. Shot peening effects on fatigue life are different in LCF and HCF. In LCF, roughness seems to be the dominant parameter that controls fatigue life improvement while the presence of significant residual stresses is the controlling factor in HCF.

2. In LCF, residual stresses redistribute during the first loading cycle to become tensile and are detrimental to the fatigue life. Under this condition, a negative relation between

surface roughness and the logarithm of the fatigue life was shown. These two drawbacks are potentially counterbalanced by the surface cold work introduced by shot peening as the tensile residual stresses do not significantly reduce the fatigue life.

3. In HCF, all nucleation sites were located in subsurface grains three times larger than the average grain size. CW14 8 A shot peening led to an improvement of the average fatigue life by a factor of 4.5, but with a large scatter, and crack initiated systematically at the depth corresponding to the presence of the tensile peak in the residual stress profile after shot peening. Even if the tensile residual stress peak seemed to disappear from the first cycle due to local yielding, the accumulation of strain (dislocations) in the larger grains, in the yield region, seems to promote early crack initiation. S230 and CW14 4 A are optimal and robust shot peening parameters since no tensile residual stress peak is present in the surface layer and the fatigue lives were improved by a factor of 20 with low dispersion. Crack initiated in the material at microstructural weakness (large grains), regardless of the surface defects and residual stresses profile.

All in all, a too high shot peening intensity (8 A in this work) resulted in deeper compressive residual stress profiles but the resulting increased surface roughness and the presence of a tensile peak in the residual stress profile were found to be drawbacks in LCF and HCF, respectively. Larger media (S230 instead of CW14) and lower intensity (4 A instead of 8 A) will thus be preferred for the studied material in the range of the tested cases.

7.7 Acknowledgements

This work was financially supported by the Consortium of Research and Innovation in Aerospace in Quebec, the Natural Sciences and Engineering Research Council of Canada, Pratt & Whitney Canada, Bell Helicopter Textron, L3-Communications MAS, Héroux-Devtek and Mathematics of Information Technology and Complex Systems (grant number: RDC 435539-12).

CHAPTER 8 ARTICLE 3 : ANALYTICAL FATIGUE LIFE PREDICTION OF SHOT PEENED INCONEL 718

T. Klotz, H.Y. Miao, C. Bianchetti, M. Lévesque and M. Brochu.
Submitted to *International Journal of Fatigue* on January 4th, 2018.

8.1 Abstract

High and low cycle fatigue tests performed on shot peened Inconel 718 can result in different crack initiation locations and mechanisms as well as in a wide range of fatigue lives depending on shot peening parameters. A model coupling Navarro and de los Rios crack propagation with Chan's crack initiation models was developed and successfully used to predict crack initiation location and fatigue life of shot peened and unpeened Inconel 718 specimens tested in high and low cycle fatigue at room temperature. Redistributed residual stresses and cold work profiles were added in the propagation model while the crack initiation model was modified to account for the residual stresses. Such a model could lead to significant experimental cost reduction by avoiding the trial and error process required to define optimal shot peening parameters.

8.2 Introduction

Inconel 718 is a nickel-based superalloy commonly used in jet engines. Klotz *et al.* (2018a) observed that Inconel 718 room temperature high cycle fatigue (HCF) life can be improved by a factor of 20 when shot peened under optimal conditions. Depending on shot peening parameters, fatigue cracks can nucleate 210 μm beneath the surface, or deeper than 2 mm into the material, which leads to different fatigue lives. In low cycle fatigue (LCF), the relaxation of shot peening induced residual stresses can lead to tensile surface residual stresses (Klotz *et al.*, 2018a), after the first loading cycle. In that case, Klotz *et al.* (2018a) found that the fatigue life mainly depended on the surface roughness resulting from shots impacts. In these specific LCF cases, shot peening was detrimental to fatigue life.

Selecting optimal shot peening parameters for specific fatigue loadings is critical for industrial applications. In this context, accurate predictive models for the crack initiation site and fatigue life of shot peened components would be a considerable asset. This model could be used to optimize the shot peening process parameters and to reduce the usual costly experimental trials and errors.

Chen *et al.* (2000), as well as Morino *et al.* (2007), successfully used the short crack relation proposed by Nisitani (1981) that assumed that the short crack growth rate was proportional to the applied stress amplitude and the crack length. However, these relationships do not account for the several accelerations and decelerations that a short crack suffers due to its microstructurally dependent behavior (Miller, 1993). Hussain (1997) performed an extensive literature survey on analytical models predicting short cracks behavior. According to Hussain, Chan and Lankford (1983) model, relying on the concept of grain orientation and larger plastic strain at short crack's tips, is unable to predict short crack propagation rate decrease between two grains having the same crystallographic orientation. Also, short crack propagation models based on modifications of linear elastic fracture mechanics (LEFM), such as that of McEvily *et al.* (1991), are not suitable for predicting short crack propagation since the stress intensity factor range becomes a debatable notion in elastic plastic fracture mechanics (EPFM). Hobson (1982) developed a model that accounted for the short crack deceleration at the first grain boundary. However, this model was unable to account for the accelerations and decelerations of the short crack after it crossed the first grain boundary.

Navarro and de los Rios (1988d, 1987) developed a unified model (N-R model) that predicts short and long crack transgranular propagation based on Bilby *et al.* (1963, 1964) work on the dislocations distribution in a plastic zone. This model accounts for the microstructural barrier to crack propagation, as well as the different grain orientations. The model relies on the assumption that a crack is inherently present in the material. Many authors used and improved the N-R model to predict fatigue life. Navarro and Vallellano (Navarro *et al.*, 1999; Vallellano *et al.*, 2000a,b) added the stress concentration effect of a surface notch on the crack propagation. Curtis *et al.* (2003b), Solis (Solis, 2002; Solis *et al.*, 2009) and de los Rios *et al.* (2000) successfully predicted the fatigue lives and short crack behaviors of shot peened specimens by accounting for residual stresses, surface roughness and surface hardening.

To the best of the authors knowledge, residual stresses and cold work (amount of plastic deformation) redistribution have never been accounted for in the N-R model. McClung (2007) performed an extensive literature review on the redistribution of residual stresses under monotonic and cyclic mechanical loading, thermal exposure and crack extension. The study concluded that the relaxation of residual stresses should be taken into consideration for fatigue behavior and fatigue life prediction. Prevéy (2000) revealed that the amount of residual stresses relaxation depends strongly on the degree of cold work induced during surface treatment. Zhuang and Halford (2001) explained that cyclic relaxation is mainly influenced by: 1) Shot peening effects: initial residual stress and cold work profiles, 2) Loading conditions: fatigue stress amplitude, mean stress, stress ratio and number of cycles, and 3) Material properties: cyclic stress-strain response and degree of hardening/softening. The

authors developed analytical and numerical models to calculate residual stresses relaxation at the surface with respect to fatigue cycles, for different stress amplitudes at a stress ratio $R_\sigma = -1$. The model was not experimentally validated. Meguid and Maricic (2015) developed a finit element (FE) model incorporating the effect of shot peening process and predicting residual stress relaxation for an Inconel 718 turbine disk under mechanical and thermal loading. The FE simulation results showed that the thermomechanical loading was capable of fully relaxing the residual stresses within the first loading cycle. Buchanan and John (2014) developed a FE model to simulate the residual stress relaxation under a single thermomechanical loading in Inconel 100. Both experimental and simulated results showed that surface compressive residual stresses become tensile under an applied stress larger than the material's yield strength. This behavior has been experimentally observed in LCF in Inconel 718 by Klotz *et al.* (2018a).

Additionally, no crack initiation are accounted for in the N-R model since a crack is already assumed to be present in the material. The number of cycles (N_{init}) required to initiate a crack of length a_0 in Inconel 718 can be predicted (Ma *et al.*, 2010) using Chan's adaptation (Chan, 2003) of the Tanaka and Mura crack initiation model (Tanaka and Mura, 1981), defined as

$$N_{init} = \frac{8M^2G^2h^2\frac{a_0}{2}}{0.005\pi\left(1-\nu\right)D^3\left(\Delta\sigma - 2M\tau_f\right)^2} \tag{8.1}$$

where $\Delta\sigma$ is the stress range, M is the Taylor factor and τ_f is the frictional shear stress. The slip band width represented by h is usually used as a fitting constant (Chan, 2003) since it is quite challenging to measure. The model assumes that initiation occurs in a favorably oriented grain, which implies that $M = 2$. $2M\tau_f$ represents the applied stress range under which crack initiation does not occur (Chan, 2003).

This study aims at predicting crack initiation location and corresponding fatigue life experimentally obtained by Klotz *et al.* (2018a) on polished, as machined and shot peened Inconel 718 tested in high and low cycle fatigue. The proposed model builds on the N-R model and incorporates the relaxation of residual stresses, the number of cycles required for initiating a subsurface crack and cold work evolution.

This paper is organized as follows: The existing N-R model and previous experimental results are detailed in Section 8.3. Section 8.4 presents the material, the experimental procedure and sums up the experimental results obtained by Klotz *et al.* (2018a). Short crack monitored experimental results are presented in Section 8.5. Section 8.6 presents the proposed modeling strategy. The FE model developed to predict the redistributed residual stresses and cold work profiles used as input in the model is presented in Section 8.7.

Section 8.8 presents the model's parameters and its results are presented and discussed in Section 8.9. Finally, Section 8.10 concludes this work.

8.3 Background

8.3.1 Physical grounds of the N-R model

The N-R model is a 1D model that assumes that the crack propagation rate is proportional to the crack tip opening displacement ($CTOD$) as (Navarro and de los Rios, 1988d; Tanaka *et al.*, 1986)

$$\frac{\mathrm{d}a}{\mathrm{d}N} = A_2 CTOD^{m_2} \tag{8.2}$$

where a is the crack length, N is the number of cycles and A_2 and m_2 are fitting constants. The N-R model is based on the hypothesis that successive microstructural barriers (*i.e.,* grain boundaries) are blocking the plastic zone progression ahead of the crack tip (Navarro and de los Rios, 1988a; Tanaka *et al.*, 1986).

The model also assumes that a crack already exists in the material, which is idealized as a discontinuity contained within a half grain. The applied load then induces a plastic zone resulting from stress concentration at the crack tip. This plastic zone is confined by the closest grain boundary. The crack propagates through the plastic zone as cyclic loading progresses. While propagating through the plastic zone, the crack decelerates due to the increasing resistance to yielding at its tip. Next, it is assumed that a source of dislocations is present in the next grain. If the stress building at the crack's tip in the plastic zone is sufficient to activate this source of dislocations, the plastic zone expands to the next grain, causing the crack to accelerate and resume its propagation. However, if the stress intensity is not sufficient to trigger the dislocation source in an adjacent grain, the crack stops its propagation, resulting in a non propagating crack. This threshold is called the microstructural threshold. This sequence is repeated in each grain until brutal rupture occurs. Figure 8.1 schematizes the situation where the plastic zone has propagated through 3 half grains and is blocked at the second grain boundary. In Figure 8.1, axis x corresponds to the actual distance from a reference point located at the center of a grain, a represents the crack length, c the crack plus the plastic zone length and r_0 is the distance between the grain boundary at which the plastic zone is blocked and the source of dislocation in the next grain. i represents the number of half grains the plastic zone has propagated through ($i = 1, 3, 5...$). Assuming an uniform grain size of D yields $c = iD/2$. The N-R model relies on a normalized axis defined as $x/\left(c + r_0\right)$. In that normalized coordinate system, a is now related to n_1 as $n_1 = a/(c+r_0)$, c to $n_2 = c/(c + r_0)$ and the source of dislocations normalized coordinate becomes 1. For the

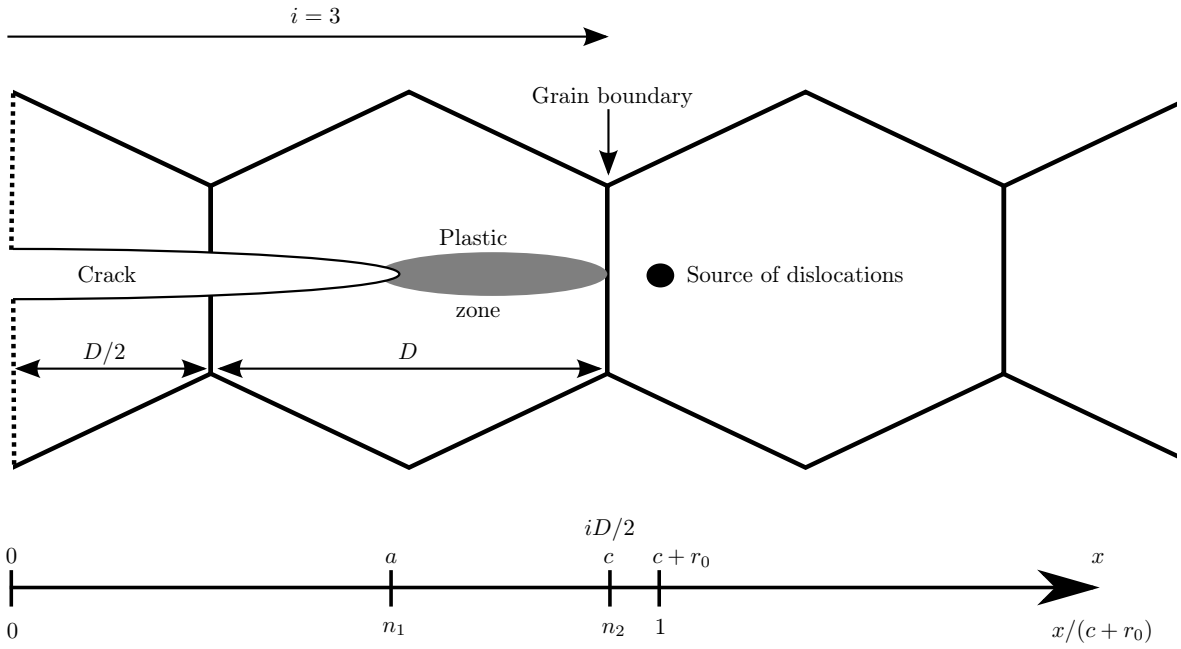

Figure 8.1 Schematization of the N-R model. The plastic zone has propagated through $i = 3$ half grains. D is the grain size. Two coordinate systems are represented: x and $x/(c + r_0)$. a and n_1 represent the position of the crack's tip, c and n_2 represent the crack plus plastic zone length and r_0 is the length between the grain boundary the plastic zone is stopped at and the source of dislocations in the next grain

sake of clarity, i is thereafter an exponent on a given variable to mark the number of half grains the plastic zone has expanded through (*i.e.,* a^i, c^i, n_1^i, n_2^i...). i is incremented each time the plastic zone expands to an adjacent grain and this consitute a new calculation step. Recall that i represents the number of half grain the plastic zone has propagated through and thus $i = 1, 3, 5....$

In the sequel, subscript s refers to crack's starting position within a grain either at the first computation or when the plastic zone has just spread into the next grain. Subscript c indicates that the plastic zone is just about to spread into the next grain. At the beginning of the computation ($i = 1$), or when the plastic zone has just expanded through the i^{th} half grain, the model is in the following state:

$$n_{1s}^i = \frac{a_s^i}{c + r_0} \tag{8.3a}$$

$$n_{2s}^i = \frac{c^i}{c + r_0} = \frac{\frac{iD}{2}}{c + r_0} \tag{8.3b}$$

During fatigue loading, the crack propagates until it reaches a length a_c^i. Then, the source of dislocations in the adjacent grain is triggered and the plastic zone c expands to the adjacent grain boundary, which leads to

$$n_{1s}^{i+2} = \frac{a_c^i}{c + r_0} = \frac{a_s^{i+2}}{c + r_0} \tag{8.4a}$$

$$n_{2s}^{i+2} = \frac{c^{i+2}}{c + r_0} = \frac{\frac{(i+2)D}{2}}{c + r_0} \tag{8.4b}$$

To overcome the i^{th} barrier, it is assumed that the applied stress σ has to be greater than σ_{arrest}^i, expressed as

$$\sigma_{arrest}^i = \frac{m^i}{m^{i=1}} \frac{\sigma_{FL} - \sigma_1^{i=1}}{\sqrt{i}} + \sigma_1^i \tag{8.5}$$

where σ_{FL} is the theoretical fatigue limit and σ_1^i is the crack closure stress. m^i represents the i^{th} grain orientation factor and $m^{i=1} = 1$ since crack initiation is assumed to occur in a grain where the shear stress is the greatest. Using a Kitagawa-Takahashi type diagram, de los Rios and Navarro (1990) proposed that the grain orientation factor evolves as

$$\frac{m^i}{m^{i=1}} = 1 + 0.5 \ln(i) \tag{8.6}$$

for mild steel until reaching the Taylor factor. Equation (8.6) was also succesfully used by de los Rios et al. on aluminum 2024-T351 de los Rios *et al.* (2000). If the applied stress σ is inferior to σ_{arrest}^i, the microstructural threshold is not overcome and the crack stops its propagation at the i^{th} microstructural barrier.

n_{1c}^i can be expressed as a function of σ_{arrest} and the yield strength σ_2 as (Navarro and de los Rios, 1988c)

$$n_{1c}^i = \cos\left(\frac{\pi}{2} \frac{\sigma - \sigma_{arrest}^i}{\sigma_2 - \sigma_1^i}\right). \tag{8.7}$$

The crack tip opening displacement ($CTOD$) is calculated based on the number of dislocations created in the plastic zone multiplied by the Burgers vector norm (b) as follows

(Navarro and de los Rios, 1988d, 1987; Vallellano, 1999)

$$CTOD^i = \frac{bc^i}{\pi^2 A}\Bigg\{2(\sigma_2 - \sigma_1^i)n_1^i \ln\left(\frac{1}{n_1^i}\right) + (\sigma_3^i - \sigma_2)\Bigg[(n_1^i + n_2^i)\cosh^{-1}\left(\left|\frac{1+n_2^i n_1^i}{n_2^i + n_1^i}\right|\right) + (n_2^i - n_1^i)\cosh^{-1}\left(\left|\frac{1-n_2^i n_1^i}{n_2^i - n_1^i}\right|\right)\Bigg]\Bigg\} \tag{8.8}$$

where $A = Gb/(2\pi(1-\nu))$ for edge dislocations and $A = Gb/(2\pi)$ for screw dislocations. G is the shear modulus, ν is the Poisson's ratio and σ_3^i is the stress applied to the dislocations source. r_0 is assumed to be negligible when compared to D (Navarro and de los Rios, 1988d), which implies that $n_2^i \simeq 1$. With this hypothesis, Equation (8.8) has been reduced to (see Appendix)

$$CTOD^i \simeq \frac{2b}{\pi^2 A}a^i(\sigma_2 - \sigma_1^i)\Bigg\{\ln\left(\frac{1}{n_1^i}\right) + \frac{\sqrt{1-(n_1^i)^2}}{n_1^i}\left[\arcsin\left(n_1^i\right) + \frac{\pi}{2}\left(\frac{\sigma - \sigma_2}{\sigma_2 - \sigma_1^i}\right)\right]\Bigg\} \tag{8.9}$$

The combination of Equation (8.2) and (8.9) yields the number of cycles to failure N_f expressed as

$$N_f = \frac{1}{A_2}\sum_i \int_{n_{1s}^i}^{n_{1c}^i} \frac{c^i \mathrm{d}n}{CTOD^{m_2}} \tag{8.10}$$

8.3.2 Incorporation of roughness effects in the N-R model

Klotz *et al.* (2018a) showed that surface roughness is driving the fatigue life of shot peened Inconel 718 tested in LCF. For cracks initiating at the surface of a shot peened specimen, Li *et al.* (1992) finite element simulation showed that the surface stress concentration factor K_{t0} can be expressed as

$$K_{t0} = 1 + 2.1\left(\frac{\alpha_d}{2\beta_d}\right) \qquad \text{for } \frac{\alpha_d}{2\beta_d} \leq 0.30 \tag{8.11a}$$

$$K_{t0} = 1 + 4.0\left(\frac{\alpha_d}{2\beta_d}\right)^{1.3} \qquad \text{for } \frac{\alpha_d}{2\beta_d} < 0.15 \tag{8.11b}$$

where α_d represents the dimples depth and β_d represents the dimples half width.

The effect of a notch on a dislocation source can be expressed with the Z parameter as

(Navarro *et al.*, 1999; Vallellano *et al.*, 2000a,b)

$$Z^i = \frac{\sqrt{i\frac{D}{2}}}{\alpha+\beta}\left[\frac{\beta}{\eta\left(i\frac{D}{2}\right)} + \frac{\alpha}{\sqrt{1+\eta\left(i\frac{D}{2}\right)^2}}\right]^{\frac{1}{2}} \tag{8.12a}$$

$$\eta(x) = \frac{1}{\alpha^2-\beta^2}\left[\alpha\sqrt{(\alpha+x)^2-\alpha^2+\beta^2} - \beta\,(\alpha+x)\right] \tag{8.12b}$$

where $Z \leq 1$, α represents the notch's depth and β its half width. The stress required to activate the next dislocations source when the plastic zone has propagated through i half grains is then expressed as (Navarro *et al.*, 1999; Vallellano *et al.*, 2000a,b)

$$\sigma^i_{arrest,Z} = \sigma^i_{arrest} Z^i. \tag{8.13}$$

Solis (2002) successfully approximated α_d and α by the roughness parameter R_t (height between the deepest valley and the highest peak) and β_d and β by $RSm/2$ (half of the mean width of the profile elements).

de los Rios *et al.* (1996) proposed that the stress concentration factor of a crack initiating at the root of a surface corrosion pit, which has its crack tip at a depth x_{depth}, is expressed as

$$K_t(a^i) = (K_{t0}-1)\left(\frac{R_t}{x_{\text{depth}}}\right)^2 + 1 \qquad \text{for } x_{\text{depth}} > R_t. \tag{8.14}$$

This relationship was successfully used by Solis (2002) on shot peened specimens.

8.3.3 Incorporation of residual stresses in the N-R model

The compressive residual stresses (σ_{RS}) introduced by shot peening typically result in a crack closure stress (σ_1). For a crack of length a^i, the crack closure stress can be expressed as (Curtis *et al.*, 2003a; Solis *et al.*, 2009)

$$\sigma^i_1 = -\frac{1}{a^i}\int_0^{a^i} \sigma_{RS}(x)\mathrm{d}x. \tag{8.15}$$

The fatigue limit of a shot peened specimen (σ^{SP}_{FL}) is assumed to be directly modified by the crack closure stress and is approximated by (Curtis *et al.*, 2003a)

$$\sigma^{SP}_{FL} = \sigma_{FL} + \sigma^{i=1}_1. \tag{8.16}$$

For a shot peened specimen, combining Equations (8.5) and (8.16) yields (Curtis *et al.*, 2003a)

$$\sigma^i_{arrest} = \frac{m^i}{m^1}\frac{\sigma_{FL}}{\sqrt{i}} + \sigma^i_1. \tag{8.17}$$

8.3.4 Brutal rupture conditions and prediction

The N-R model calculations must be stopped when brutal rupture occurs. Navarro and de los Rios (1992) listed the following stopping criteria:

1. The crack length needed to trigger yielding in the actual grain is longer than that needed to trigger the dislocations source in the next grain: $a^i_s > a^i_c$ (equivalent to $n^i_{1s} > n^i_{1c}$). This condition implies that the crack does not need to propagate anymore at each step to trigger plastification in the next grain. General yielding occurs and the crack continuously accelerates.

2. The excess of overall applied stress required to overcome the microstructural barrier is superior to the resistance to plastic deformation: $(\sigma - \sigma_{arrest,Z}) \geq (\sigma_2 - \sigma_1)$. This results in general yielding.

3. The stress required to trigger the dislocations source in the adjacent grain becomes negligible: $\sigma_{arrest,Z} \rightarrow 0$. The crack does not encounter any resistance to its propagation.

4. The crack reaches a predefined length, as proposed by Vallellano *et al.* (2009).

8.3.5 Previous experimental results

The studied material was the precipitation hardened nickel-based superalloy Inconel 718 tested by Klotz *et al.* (2018a). The microstructure was composed of equiaxed grains having diameters ranging from 5 to 30 μm. The average grain size was 13 μm. TiCN, NbC and aluminum and magnesium oxides particles were also present. Five surface conditions were studied: 1) Polished (down to 1 μm), 2) as machined, 3) shot peened with 0.59 mm diameter cast steel shots ASH 230 (S230) at an Almen intensity of 4 A, 4) shot peened with 0.36 mm diameter conditioned carbon steel cut wire shots AWCR 14 (CW14) at an intensity of 4 A and 5) shot peened with CW14 at an intensity of 8 A. For the shot peened specimens, full coverage was reached on the specimens reduced sections. The studied surface conditions are summarized in Table 8.1. For the sake of clarity, stress levels where the maximum stress (σ_{max}) was equal to 1100 MPa led to high cycle fatigue (HCF) and stress levels where

Table 8.1 The five surface conditions studied by Klotz *et al.* (2018a). The media diameter is also presented

	Surface	Media	Intensity (A)	Media diameter (mm)
1	Polished	-	-	-
2	As machined	-	-	-
3	Shot peened	S230	4	0.59
4	Shot peened	CW14	4	0.36
5	Shot peened	CW14	8	0.36

$\sigma_{max} \geq 1370$ MPa led to low cycle fatigue (LCF). The shot peening conditions are referred herein as the shot peening media – shot peening intensity couple. For example, CW14–8A condition means shot peened with the media CW14 at an intensity of 8 A.

Fatigue tests were performed on 9.5 mm diameter cylindrical specimens, at room temperature, at a stress ratio of $R_\sigma = 0.1$ and a frequency of 20 Hz. The results presented by Klotz *et al.* (2018a) are summarized in Table 8.2. Surface crack initiations occurred either

Table 8.2 Summary of the fatigue results published by Klotz *et al.* (2018a). Roughness parameters R_t, RSm and the number of cycles to failure N_f are averages. Center: crack initiation occurred deeper than 2 mm in the material. Subsurface: crack initiation occurred at the residual stress tensile peak at a depth of roughly 210 μm

Surface condition	Nb. of samples	σ_{max} (MPa)	R_t (μm)	RSm (μm)	N_f (cycles)	Initiation location
Polished	4 2	1100 1380	-	-	9.91×10^4 2.13×10^4	Surface
Machined	4 2	1100 1380	7.15	246.5	8.56×10^4 1.40×10^4	Surface
S230–4A	7 10	1100 1370	8.65	362.4	2.02×10^6 1.65×10^4	Center Surface
CW14–4A	9 10	1100 1370	11.90	328.2	2.09×10^6 1.57×10^4	Center Surface
CW14–8A	9 10	1100 1370	25.38	404.8	4.45×10^5 1.24×10^4	Subsurface Surface

at a stress concentration feature (due to machining or shot peening) or at a niobium carbide (NbC) emerging at the surface. Subsurface crack initiations occurred in larger than average grains; approximately 30 μm for all the observed rupture surfaces. Transgranular propagation was observed in all samples. Klotz *et al.* (2018a) experimentally observed that the rupture surface fatigue crack lengths, before any sign of ductile fracture, were in average 1.3 mm for all HCF surface conditions tested, 0.4 mm for a polished specimen in LCF and 0.2 mm for the other surface conditions tested in LCF.

8.4 Experimental procedure

Silicon elastomer replicas were taken at a specific number of load cycles to monitor the growth of short cracks on fatigue specimens, using the methodology of Brochu *et al.* (2010). Two polished 3.56 mm × 10.16 mm rectangular cross section specimens, whose geometry is shown in Figure 8.2(a), were axially fatigue tested at room temperature under a 20 Hz constant stress amplitude on an hydraulic MTS 318.10 frame equipped with an 100 kN MTS 661.20e-03 load cell at $R_\sigma = 0.1$. Two stress levels were used: $\sigma_{max} = 1100$ and 1370 MPa. Replicas were taken every 10,000 and 1,000 cycles for the stress levels $\sigma_{max} = 1100$ and 1370 MPa, respectively. The replicas were then observed under an optical microscope. All main cracks initiated from the specimen edges which was challenging for crack growth

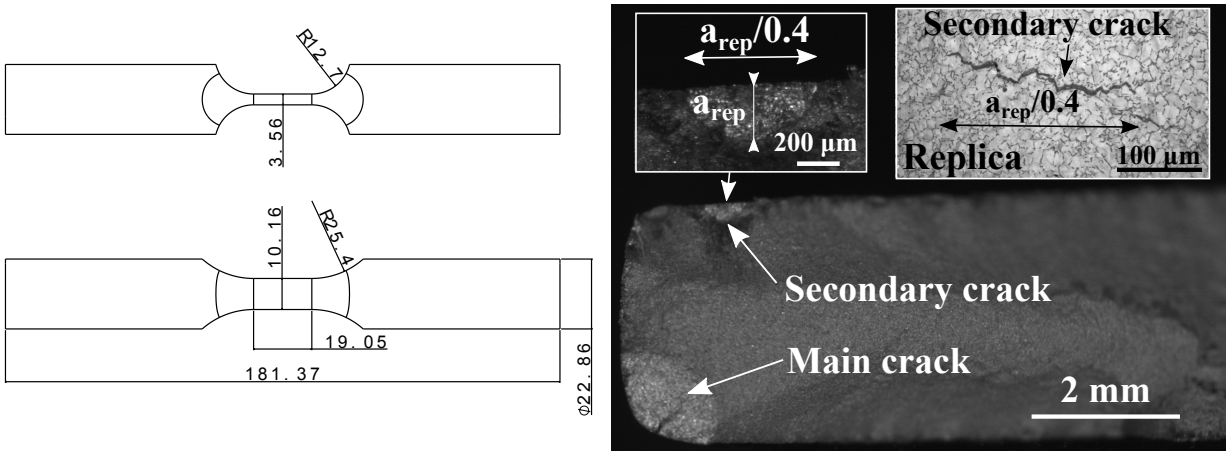

(a) (b)

Figure 8.2 (a) Geometry of the specimens used to monitor short crack behavior with replicas (dimensions are in mm). (b) Rupture surface of a specimen tested at $\sigma_{max} = 1370$ MPa. The main crack initiated in a corner. The secondary crack replica at 1.7×10^4 cycles is encapsulated. In average, the length of the crack in the material a_{rep} is 0.4 times the length of the crack on the surface of the specimen observed with the replica

monitoring. Therefore, secondary cracks found on the flat surfaces were used to gather the short crack propagation results, as shown in Figure 8.2(b). The observed surface cracks lengths were multiplied by 0.4 to obtain the corresponding depth, as shown in the encapsulated pictures of Figure 8.2(b). The crack growth rates ($\mathrm{d}a_{rep}/\mathrm{d}N$) were estimated by dividing the difference of crack depth by the difference in number of cycles for two consecutive crack width measurements.

8.5 Experimental results

Short crack monitoring results are presented in Figure 8.3 where the calculated crack propagation rate is plotted as a function of the crack depth. Each line represents one monitored crack.

Figure 8.3 shows that short crack propagation exhibits different rates for HCF and LCF regimes. In LCF, the cracks exhibit more acceleration and deceleration than in HCF. The short crack growth rates for the HCF and LCF conditions were fitted with power laws expressed as

$$\frac{\mathrm{d}a_{rep}}{\mathrm{d}N} = 1.138 \times 10^{-4} {a_{rep}}^{1.26} \qquad \text{for } \sigma_{max} = 1100 \text{ MPa} \tag{8.18a}$$

$$\frac{\mathrm{d}a_{rep}}{\mathrm{d}N} = 1.559 \times 10^{-4} {a_{rep}}^{0.92} \qquad \text{for } \sigma_{max} = 1370 \text{ MPa}. \tag{8.18b}$$

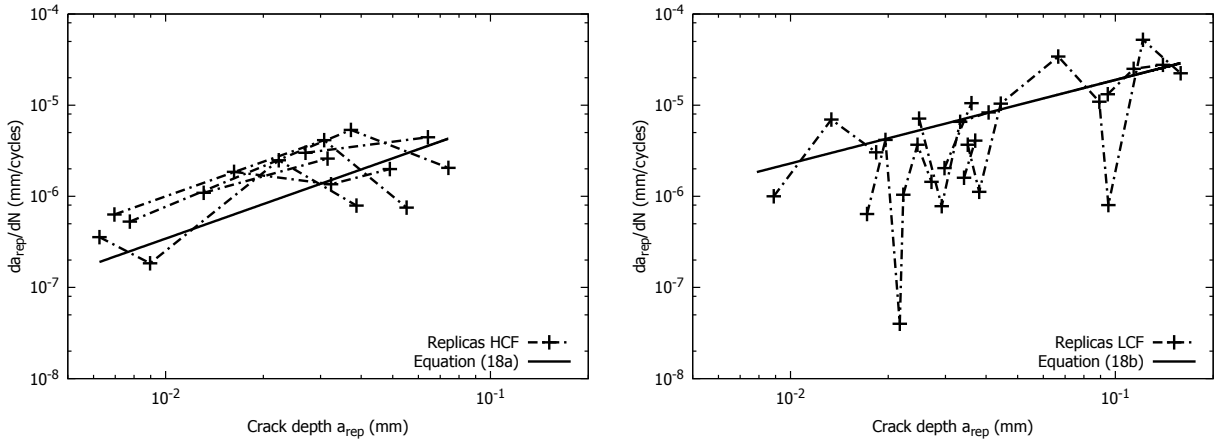

(a) (b)

Figure 8.3 Replicas results in (a) HCF and (b) LCF. Each dotted line represents a monitored crack. Approximations with Equation (8.18a) and (8.18b) are also represented

The power law approximations of Equation (8.18) suggest that the short crack propagation rates are roughly 10 times higher in LCF than in HCF. This result was expected since the crack growth rate increases with the applied stress.

8.6 Modeling strategy

The overall modeling strategy consists in predicting the number of cycles to failure for specific crack initiation simulated points through the thickness as a function of the redistributed residual stress and cold work profiles, the surface roughness and the microstructural features such as damaged surface carbides and larger than average size grains. The simulated crack initiation depth yielding the lowest fatigue life was assumed to be the weakest location in term of fatigue life, as well as the predicted crack initiation site.

Redistributed residual stresses and cold work were accounted for in the modeling process. Klotz *et al.* (2018a) showed that most of the redistribution occurred during the first cycle. A FE model was calibrated with the experimental results on rectangular specimens (Figure 8.2(a)) and used to predict the residual stresses and cold work redistribution during the first loading cycle applied on the cylindrical specimens used by Klotz *et al.* (2018a). The redistributed residual stress and cold work profiles, converted into a yield strength profile using the true stress - strain tensile curve, were used in the model.

Recall that the N-R model assumes the presence of an existing crack. The hypothesis of a crack inherently present in the material is not validated in the case of subsurface crack initiations. For this reason, surface and subsurface crack initiations had to be considered separately.

For a surface crack, Klotz *et al.* (2018a) experimentally observed that surface niobium carbides were inherently damaged due to the machining process. Thus, a crack having for initial length the average size of a niobium carbide (9 μm) was considered. This 9 μm crack was supposed to be located at the bottom of a dimple where the stress concentration is maximum. The N-R model was also stopped by one of the criteria listed in Section 8.3.4. The crack lengths before brutal rupture were chosen as that experimentally observed by Klotz *et al.* (2018a).

In the case of subsurface crack initiation, a modified version of Chan's model, that accounts for the redistributed residual stresses, was used to predict the number of cycles required to initiate a crack having the length of a grain (N_{init}) in the material. The N-R model was then used to predict the number of cycles until brutal rupture. Finally the fatigue life (N_f) was considered as the sum of N_{init} and N_{NR}, the number of cycle to failure calculated with

the N-R model.

For both surface and subsurface crack initiations, if the microstructural threshold was not reached while computing the N-R model, or if the applied stress range was under the fatigue limit stress range predicted by Chan's model, the fatigue life was considered as infinite.

The N-R model and the overall model strategy algorithms are presented in Figure 8.4 and Figure 8.5, respectively.

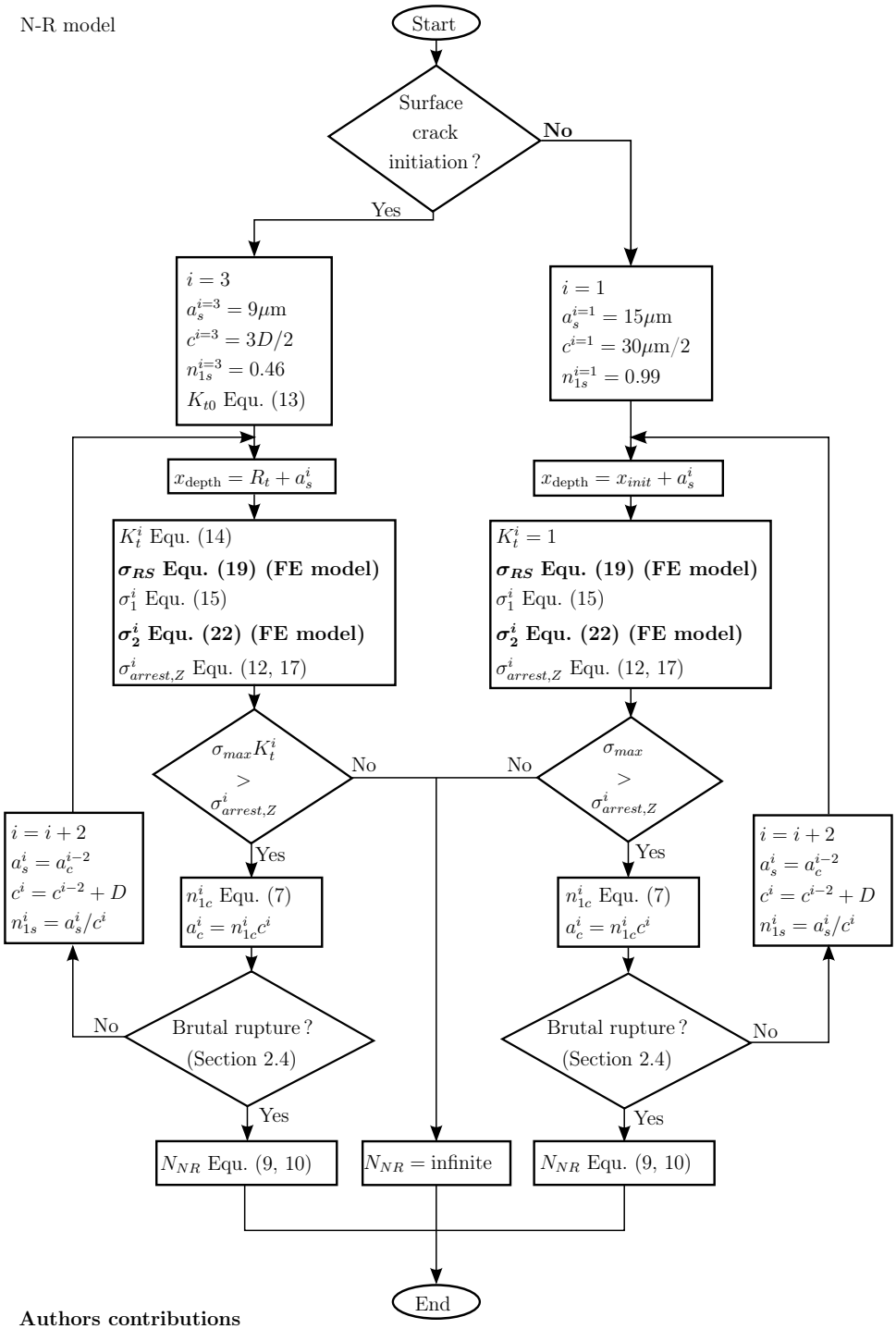

Figure 8.4 N-R model algorithm. The authors contributions are in bold

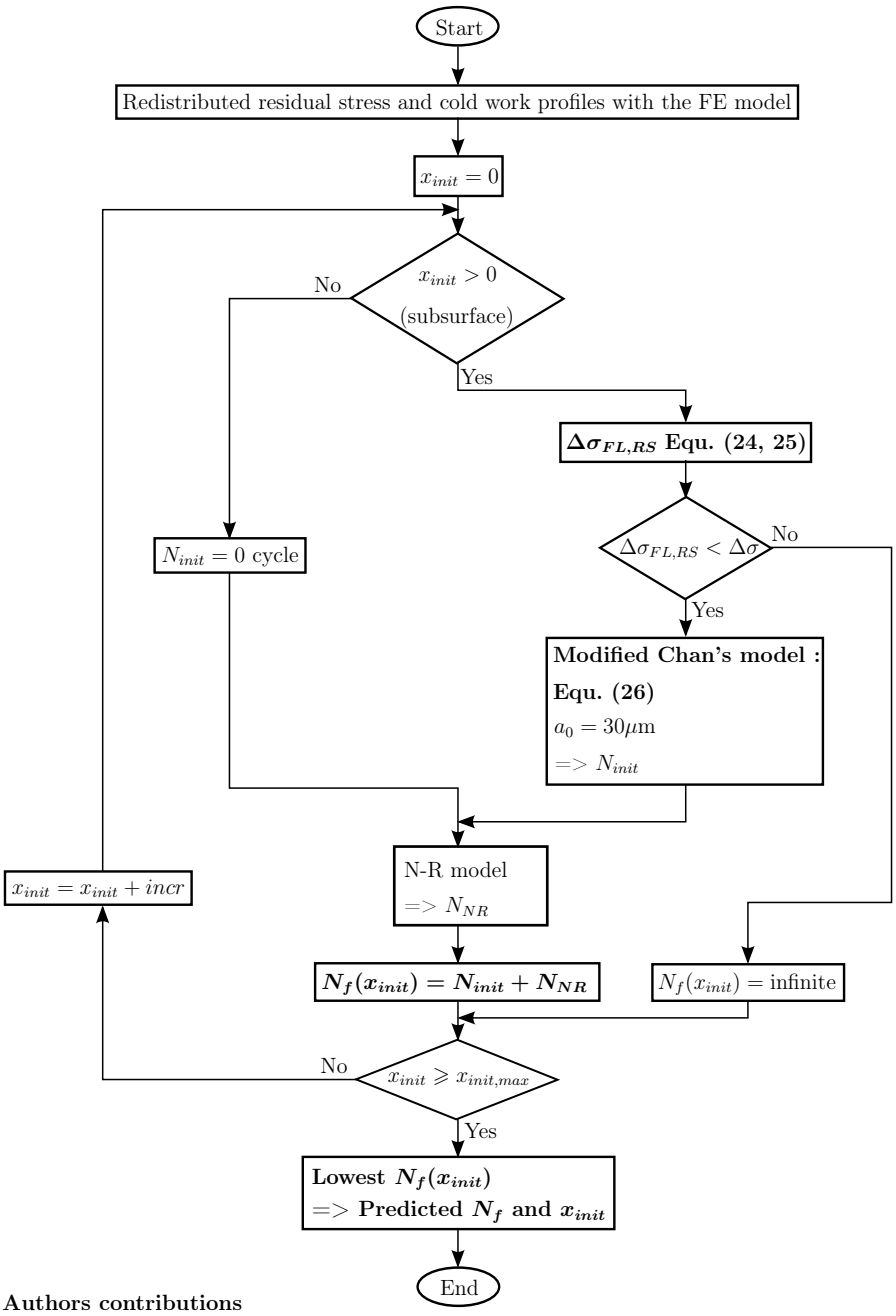

Figure 8.5 Overall proposed model. The authors contributions are in bold

8.7 Residual stresses redistribution modeling

A FE model developed using ANSYS was used to predict residual stress and cold work redistribution during fatigue loading. The FE model was validated with the residual stress and cold work redistribution obtained by Klotz *et al.* (2018a) on rectangular CW14–8A specimens similar to that presented in Figure 8.2(a). The validated model was then used to predict the residual stresses and cold work redistribution on cylindrical specimens.

8.7.1 FE model validation

To simulate the rectangular specimens, one eighth of the reduced section was modeled in ANSYS using symmetric boundary conditions and hexahedral 3D linear solid elements SOLID185. The FE model is presented in Figure 8.6(a). Residual stress and cold work profiles obtained from experimental measurements on untested rectangular samples were input into the FE model as initial state in the surface layer using the following fitting equation

$$\sigma_{RS}(x) = B_1 e^{\frac{-2(x-x_d)^2}{B_2^2}} + B_3 + B_4 e^{\frac{-(x-x_e)^2}{2B_5}} \tag{8.19}$$

for the residual stress profile and the fitting equation

$$\varepsilon_p(x) = b_1 e^{b_2 x} \tag{8.20}$$

for the cold work profile. In these equations, x represents the depth, x_d is the depth of the highest compressive or tensile value of the profile, x_e is the depth of an eventual secondary tensile or compressive peak, B_3 is the residual stress value in the bulk material, b_1 is the surface cold work value and B_1, B_2, B_4, B_5 and b_2 are fitting constants obtained with a least square approximation. The initial experimental measurements along with the model's input values are shown in Figure 8.7(a) and (b) for the residual stress and cold work profiles, respectively. The obtained parameters are listed in Table 8.3.

The elements size from the surface to a depth of 445 μm was set to a characteristic length of 5.5 μm to capture the residual stress and cold work gradients in the shot peened layer. The true stress versus plastic strain curve were obtained using Chaboche's constitutive equation (Chaboche and Rousselier, 1983; Lemaitre *et al.*, 2009)

$$\sigma_{true}(\varepsilon_p) = a_1 \left(1 - e^{-C_1 \varepsilon_p}\right) + a_2 \left(1 - e^{-C_2 \varepsilon_p}\right) + \sigma_{y0.05\%} \tag{8.21}$$

which was successfully used in the literature to describe Inconel 718 behavior in the plastic

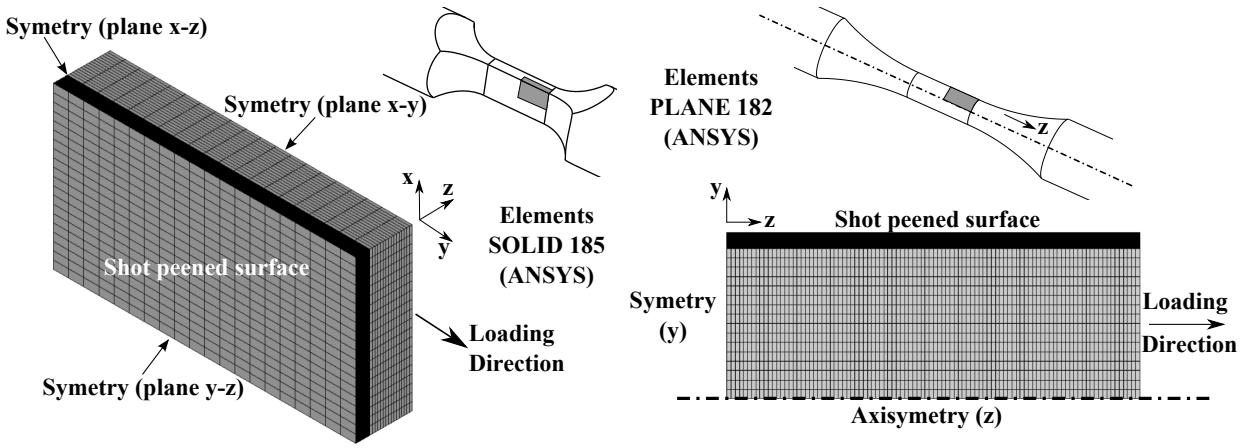

(a) (b)

Figure 8.6 Finite element models used for the redistribution of the residual stress and cold work profiles: (a) one-eighth of the rectangular specimen's reduced section is simulated with solid elements and (b) a half of the cylindrical specimen reduced section is simulated with axisymetric solid elements

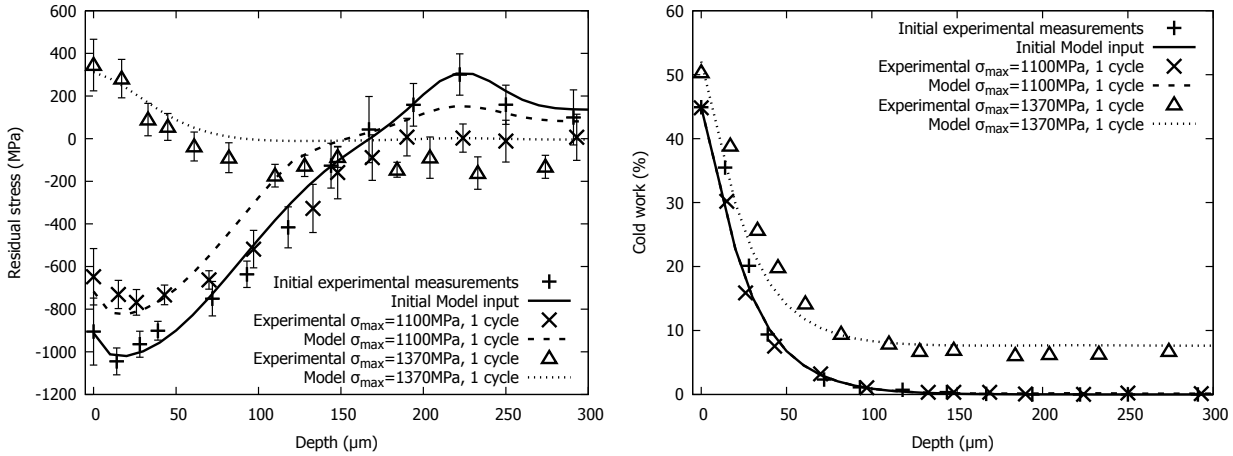

(a) (b)

Figure 8.7 FE (a) residual stress and (b) cold work redistribution model results compared to experimental results (Klotz *et al.*, 2018a) on rectangular specimens. The error bars on the residual stress profiles represent the average error for each measurement

regime (Klotz *et al.*, 2017). To input Inconel 718 plastic behavior in ANSYS, the ANSYS APDL command TB with the options of non-linear plasticity (PLAS) and isotropic hardening (MISO) was used. 120 nonlinear true stress - plastic strain data curve points, in agreement with Equation (8.21), were manually input using the ANSYS APDL function TBPT. a_1, a_2, C_1 and C_2 are fitting constants listed in Table 8.4. $\sigma_{y0.05\%} = 1074$ MPa is the 0.05 %

Table 8.3 CW14–8A rectangular specimen prior to test residual stress and cold work profiles fitting constants

B_1 (MPa)	x_d (μm)	B_2 (μm)	B_3 (MPa)	B_4 (MPa)	x_e (μm^2)	B_5 (μm)	b_1 (%)	b_2 (μm^{-1})
-1161.05	14	151.30	116.21	201.02	222	517.17	0.45	0.040

offset yield strength which was preferred to the commonly used 0.2 % offset yield strength ($\sigma_{y0.2\%} = 1156$ MPa) to better capture residual stress redistribution at $\sigma_{max} = 1100$ MPa. The experimental true stress - plastic strain (ε_p) curve and the fitting obtained with Equation (8.21) are shown in Figure 8.8. During the tensile test, striction occurred at $\varepsilon_p = 22$ %.

Table 8.4 Equation (8.21) fitting constants and 0.05% offset yield strength

a_1 (MPa)	C_1	a_2 (MPa)	C_2	$\sigma_{y0.05\%}$ (MPa)
147.50	324.28	652.00	6.49	1074

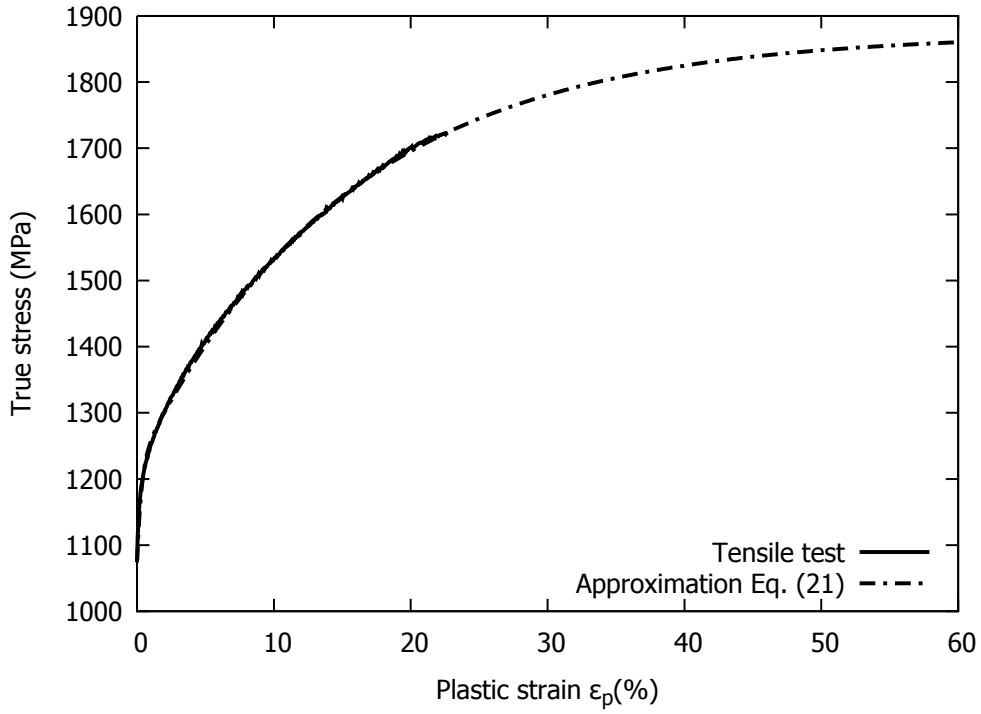

Figure 8.8 Fitting of Equation (8.21) on a tensile test

Therefore, Equation (8.21) could not be validated for plastic deformations above 22 %. Nevertheless, it was assumed that the true stress - strain curve could be extrapolated for higher strain values, as proposed by Prevéy (1987), since plastic deformation up to 50 % were recorded. Equation (8.21) was then also used for plastic strains higher than 22 %.

Klotz *et al.* (2018a) experimental results, using X-ray diffraction, showed that the residual stress and cold work profiles were mainly redistributed during the first fatigue cycle. Therefore, the simulation of residual stresses relaxation was limited to one cycle. The simulation was performed for the two studied loading conditions (σ_{max} = 1100 and 1370 MPa). Figure 8.7 compares the FE simulation results with the experimental X-ray diffraction measurements presented by Klotz *et al.* (2018a). It can be seen that the simulated residual stress and cold work redistribution for both loading conditions are consistent with the experimental measurements. Therefore, the developed FE model predicts reasonably well the residual stress and cold work redistribution after one single cycle of fatigue loading at both stress amplitude.

8.7.2 FE model on the cylindrical specimens

The FE model validated on rectangular cross section specimens was then used to estimate the residual stresses and cold work redistribution of the cylindrical specimens tested by Klotz *et al.* (2018a). The same simulation procedure was used except that axisymmetric 2D linear rectangular PLANE182 elements were used to model half of the cylindrical specimen's reduced section as presented in Figure 8.6(b).

8.8 Fatigue life prediction model's parameters

8.8.1 Redistributed residual stresses and cold work

Redistributed residual stresses were extracted from the FE model on the cylindrical specimens and inputed in the N-R and Chan models through Equation (8.19), which represents the residual stresses as a function of the depth ($\sigma_{RS}\left(x_{\text{depth}}\right)$).

The redistributed cold work profiles obtained from the FE model were converted into yield strength profiles using the tensile stress – strain curve (Figure 8.8) approximated with Equation (8.21), where the cold work represents the plastic strain (ε_p). Yield strength profiles were input in the N-R model, through the parameter σ_2, using the following fitting equation

$$\sigma_2(x_{\text{depth}}) = Y_1 e^{\frac{-2x_{\text{depth}}^2}{Y_2^2}} + \sigma_{y0.2\%} \tag{8.22}$$

where Y_1 and Y_2 are fitting constants.

The obtained residual stresses and yield strength profiles of the studied specimens are presented in Figure 8.9. The fitting parameters of Equations (8.19) and (8.22) are listed in Table 8.5.

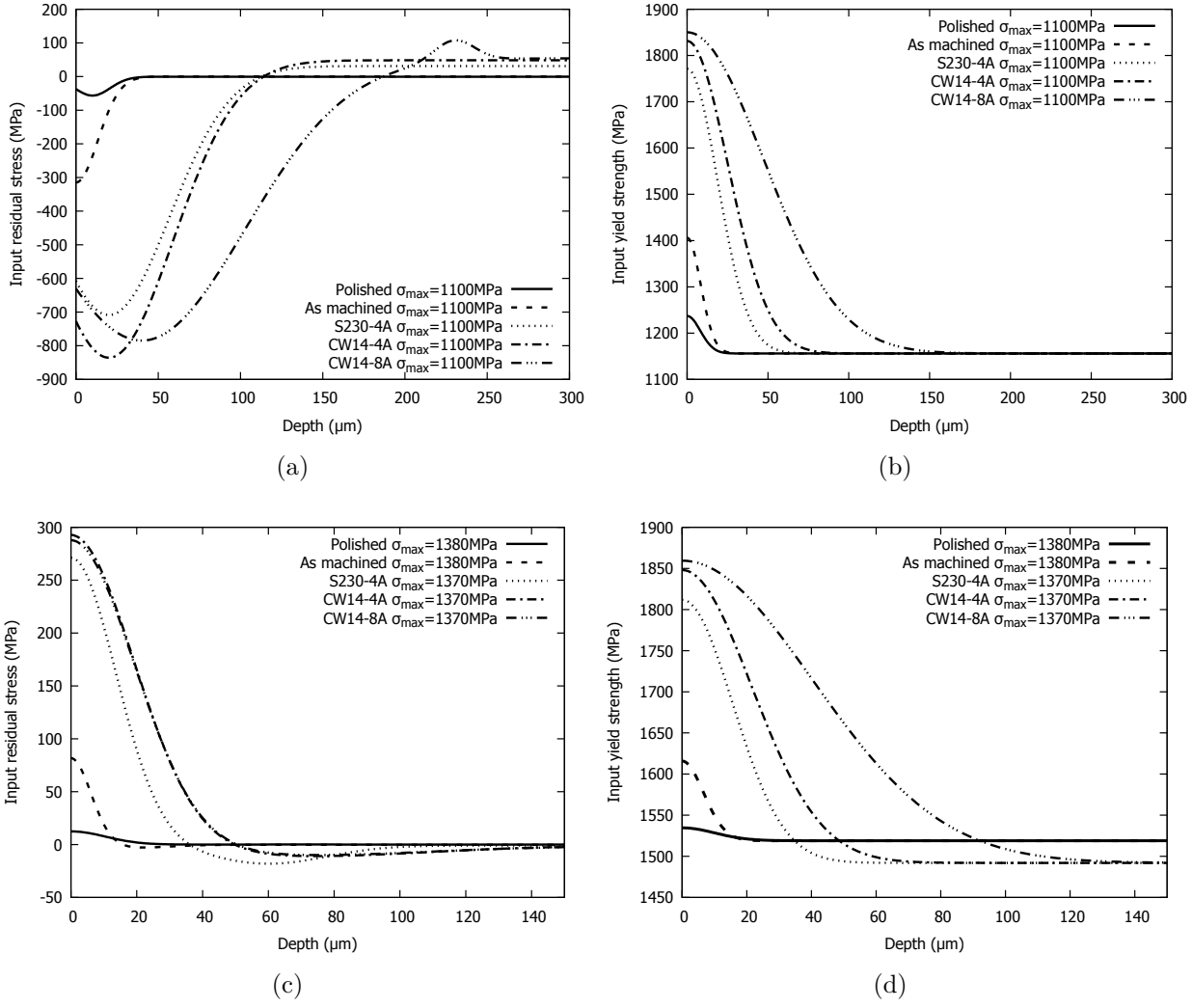

Figure 8.9 N-R and Chan models input redistributed residual stresses as a function of depth in (a) HCF and (c) LCF. Yield strength profiles input in the N-R model as a function of the depth in (b) HCF and (d) LCF

Table 8.5 Equations (8.19) and (8.22) N-R model input constants

σ_{max} (MPa)	B_1 (MPa)	x_d (μm)	B_2 (μm)	B_3 (MPa)	B_4 (MPa)	x_e (μm^2)	B_5 (μm)	Y_1 (MPa)	Y_2 (μm)
				Polished					
1100	-56.02	10	21.58	-0.54	0	0	1	80.99	16.37
1380	12.50	0	20.87	-0.07	0.13	70	2019.31	15.62	20.14
				Machined					
1100	-314.47	0	26.52	0	0	0	1	249.88	16.61
1380	82.41	0	12.08	-0.22	-2.70	20	103.22	96.83	13.19
				S230–4A					
1100	-739.81	20	73.76	31.08	0	0	1	615.2	37.77
1370	272.12	0	27.14	-0.86	-17.24	60	318.97	319.88	31.28
				CW14–4A					
1100	-883.74	20	78.12	48.27	0	0	1	675.19	50.34
1370	295.75	0	38.17	-1.02	-10.02	70	1472.32	355.97	42.78
				CW14–8A					
1100	-838.81	40	125.48	54.15	61.98	230	145.63	694.08	94.43
1370	320.18	0	69.57	-4.47	-10.88	130	717.96	367.37	80.58

8.8.2 N-R model's physical parameters

The basic model's parameters are the following (Table 8.6):

- E, ν and $\sigma_{y0.02\%}$ were measured by Klotz *et al.* (2018a).
- The applied stress σ was computed as the maximum applied true stress ($\sigma_{max,true}$).
- Inconel 718 fatigue endurance, in term of σ_{max} at 10^8 cycles under rotating bending fatigue ($\sigma_{FL,R_\sigma=-1}$) (Gale and Totemeier, 2003), was converted to σ_{FL} (at $R_\sigma = 0.1$) using the Goodman relationship (Goodman, 1918; Smith, 1942).
- D was taken as the average grain size measured by Klotz *et al.* (2018a).
- Only edge dislocations were considered in Equation (8.9) since rupture mode I (long

cracks) and mode II (short cracks) both trigger edge dislocations (Chowdhury *et al.*, 2014).

- To be conservative, the initial crack length for surface crack was considered to be equal to the length of the average niobium carbide size. The initial state was therefore set to $i = 3$ ($9\ \mu\text{m} > D/2$) and $n_s^{i=3} = 9\ \mu\text{m}/(3D/2) = 0.46$. The parameter x_{depth} was considered as $x_{\text{depth}} = 9\ \mu\text{m} + R_t$ to account for the dimples depth.

- In case of a subsurface crack initiation, the initial crack length was 30 μm above the average grain size in which subsurface crack initiations were experimentally observed (Klotz *et al.*, 2018a). Thus, a_0 was set to 30 μm in Chan's model and in the N-R model, $n_{1s}^{i=1}$ was set to 0.99 (the closest value to 1) to simulate the fact that the pre-existent crack tip was at the first grain boundary and to respect the, even negligible, r_0 parameter in Equation 8.3(a).

- α, α_d and β, β_d were set equal to the measured roughness parameter R_t and $RSm/2$, respectively.

8.8.3 N-R model's fitting constants A_2 and m_2

Parameters A_2 and m_2 of Equation (8.2) were fitted on the short crack growth behavior presented in Figure 8.3. Since, in LCF, the material's yield strength is influenced by the maximum applied stress, A_2 - m_2 were independently fitted on HCF and LCF results, resulting in two sets of parameters A_2 - m_2. n_{1s}^1 was arbitrarily set to 0.2, which is smaller than the shortest crack observed on the replicas. Residual stresses were assumed to be negligible and the yield strength profile was assumed to be constant since the rectangular specimens were polished and not shot peened. A least square optimization was performed to best fit the crack propagation rate as a function of the crack length in HCF and LCF, respectively. The cost function F was defined as

$$F = \sum_{j=1}^{Nb(a_{NR})} \left(\frac{\mathrm{d}a_{NR}^j}{\mathrm{d}N} - \frac{\mathrm{d}a_{rep}\left(a_{NR}^j\right)}{\mathrm{d}N} \right)^2 \tag{8.23}$$

where $Nb(a_{NR})$ represents the number of times the plastic zone was about to spread in the next grain and in which the corresponding crack length calculated with the model, a_{NR}, was in the range of the a_{rep} experimentally observed (Figure 8.3). Each of these crack lengths was numbered from $j = 1$ to $j = Nb(a_{NR})$. $\mathrm{d}a_{rep}\left(a_{NR}^j\right)/\mathrm{d}N$ represents the replicas crack propagation rate calculated with Equation (8.18a) in HCF and Equation (8.18b) in LCF.

Table 8.6 Model parameters

σ_{max}	1100 MPa	1370 MPa	1380 MPa
$\sigma_{max,true}$	1100 MPa	1492 MPa	1519 MPa
$\sigma_{y0.02\%}$	1156 MPa	1492 MPa	1519 MPa
A_2	1.795×10^{-2}	2.335×10^{-4}	
m_2	1.108	0.742	
$\sigma_2(x_{\text{depth}})$	Equation (8.22), Table 8.5		
$\sigma_{RS}(x)$	Equation (8.19), Table 8.5		
σ_u	1415 MPa		
G	78 GPa		
ν	0.32		
D	13 μm		
σ_{FL}	900 MPa		
$\sigma_{FL,R_{\sigma=-1}}$	620 MPa Gale and Totemeier (2003)		
a_0	30 μm		
D_{init}	30 μm		
h	2.82 μm		
M	2		
n_{1s}^3 surface	0.46		
n_{1s}^1 subsurface	0.99		
α, α_d	R_t, Table 8.2		
β, β_d	$RSm/2$, Table 8.2		

Figure 8.10 shows the contour plot of $\log_{10}(F)$ as a function of the parameters A_2 and m_2. $\log_{10}(F)$ was normalized so it lied between 0 and 1. Both contour plots exhibit the presence of several local minima, which implies that the set of parameters $A_2 - m_2$ is not unique. The chosen parameters for both stress levels are represented in Figure 8.10 with a cross. It can be concluded that the cost function is slightly sensitive to parameter A_2 while it is highly affected by the parameter m_2 when its values are inferior to the local minima. Figure 8.11 presents

the N-R model predicted crack propagation rates obtained with the optimized parameters A_2 - m_2, along with the replicas results.

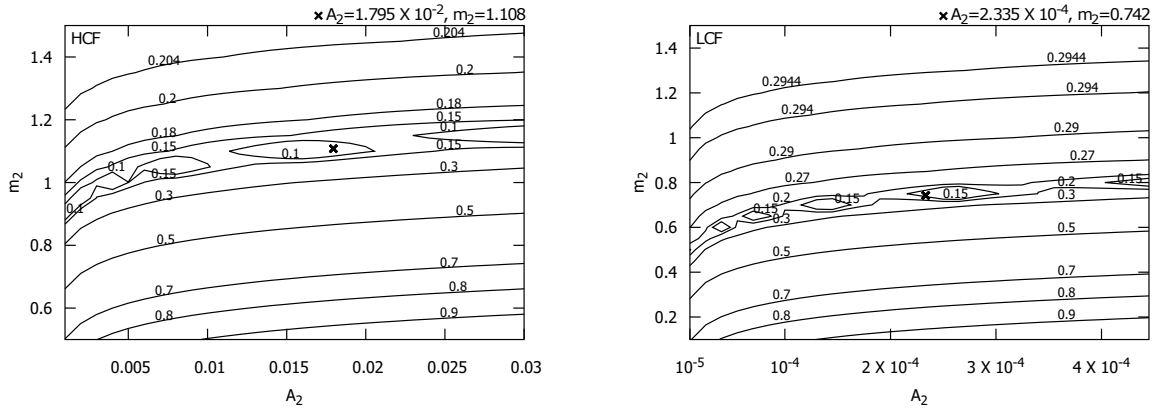

(a) (b)

Figure 8.10 Contour plot of the cost function $\log_{10}(F)$ used to determine the fitting constants A_2 and m_2 in the N-R model. The cost function was normalized so that it lied between 0 and 1. Several minima were found in both (a) HCF and (b) LCF. The chosen parameters A_2 and m_2 are represented with a cross

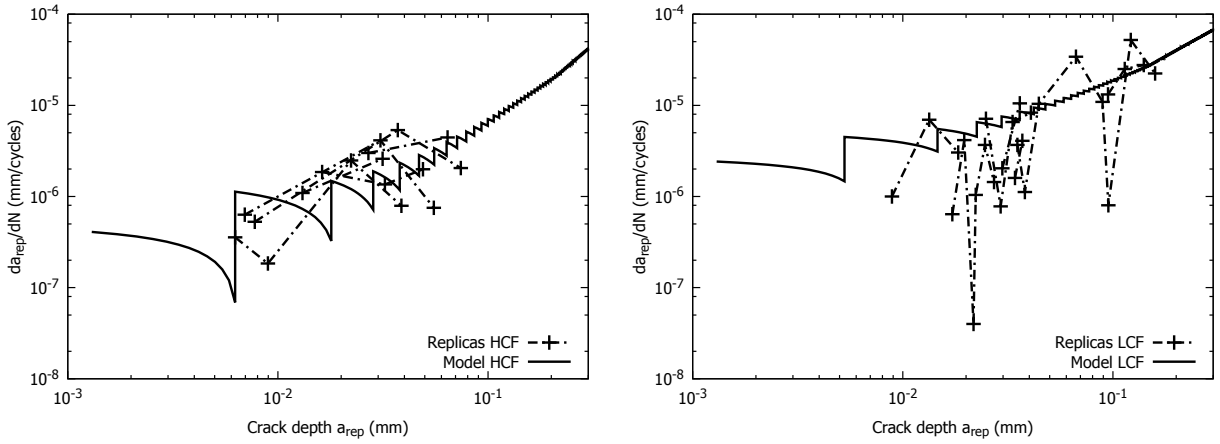

(a) (b)

Figure 8.11 (a) HCF and (b) LCF N-R model's crack propagation rates with the optimized parameters $A_2 - m_2$ presented along with the replicas results

8.8.4 Subsurface crack initiation parameters

The number of cycles to initiate a crack in a 30 μm grain (N_{init}), as predicted by Equation (8.1), was modified to account for the residual stresses. The underlying assumption was that the residual stresses increased the average cyclic stress without modifying its amplitude. The stress ratio (R_σ) at a depth x_{init} changed to:

$$R_{\sigma,RS}(x_{init}) = \frac{\sigma_{min} + \sigma_{RS}(x_{init})}{\sigma_{max} + \sigma_{RS}(x_{init})}. \tag{8.24}$$

The fatigue endurance stress range at 10^8 cycles was then obtained by solving the Goodman relation

$$\frac{\sigma_{FL,RS}(x_{init})(1 - R_{\sigma,RS}(x_{init}))}{2\sigma_{FL,R_\sigma=-1}} + \frac{\sigma_{FL,RS}(x_{init})(1 + R_{\sigma,RS}(x_{init}))}{2\sigma_u} = 1 \tag{8.25}$$

where σ_u is the ultimate strength (1415 MPa (Klotz *et al.*, 2018a)) and $\sigma_{FL,RS}(x_{init})$, which is the maximum fatigue endurance stress at 10^8 cycles under the stress ratio $R_{\sigma,RS}$, is the unknown. Then, $\Delta\sigma_{FL,RS}(x) = \sigma_{FL,RS}(x)(1 - R_{\sigma,RS}(x))$ was computed and Equation (8.1) becomes

$$N_{init}(x_{init}) = \frac{8M^2G^2h^2\frac{a_0}{2}}{0.005\pi\,(1-\nu)\,D_{init}^3\,(\Delta\sigma - \Delta\sigma_{FL,RS}(x_{init}))^2} \tag{8.26}$$

where D_{init} is the size of the larger than average grain in which the crack initiates and x_{init} is the depth of the grain in which the crack initiation was simulated. M, the Taylor factor, was set to 2 since the crack initiation was assumed to occur in a favorably oriented grain. The crack length at initiation, a_0, was set equal to 30 μm since it was experimentally observed by Klotz *et al.* (2018a) that regular stage I propagation occurred after the first grain.

The slip band width h was estimated from the average fatigue lives of the S230–4A and CW14–4A specimens, $N_{fav,4A} = 2.06 \times 10^6$ cycles, using a depth of crack initiation $x_{init} = 3$ mm to be in the stable tensile part of the profile where crack initiations were experimentally observed (Klotz *et al.*, 2018a). The best fitting value was $h = 2.82$ μm, which is of the same order of magnitude of the roughly 2 μm slip bands width observed by Klotz *et al.* (2017) in Inconel 718. The evolution of $N_{fav,4A}$ as a function of h is presented in Figure 8.12(a).

The evolution of N_{init} as a function of the residual stress at $\sigma_{max} = 1100$ MPa is presented in Figure 8.12(b). It can be observed that, for compressive residual stresses lower than -320 MPa, the condition $\Delta\sigma < \Delta\sigma_{FL,RS}$ is met and thus infinite fatigue life is predicted.

Note that it was not possible to determine the parameter h value with LCF results since

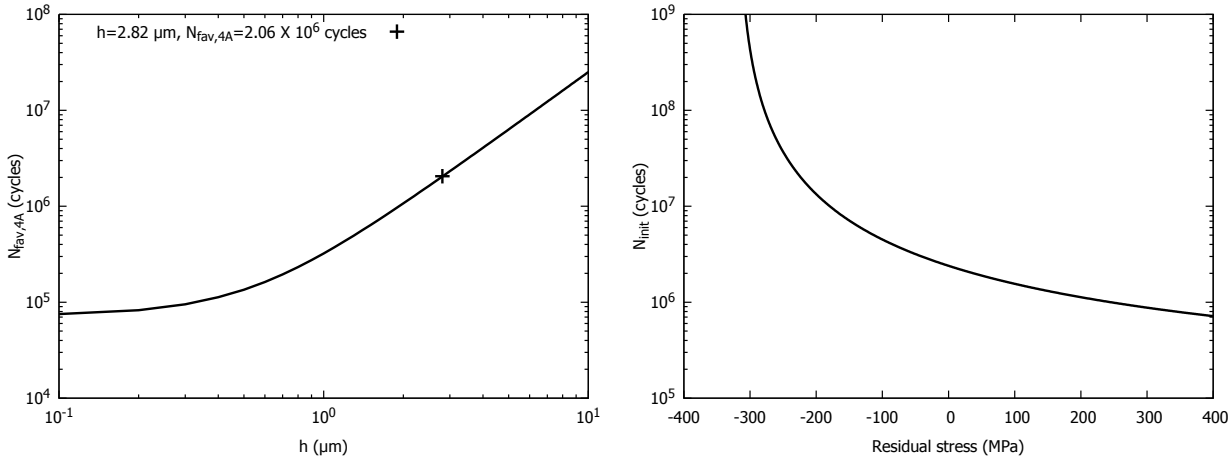

(a) (b)

Figure 8.12 (a) Evolution of $N_{fav,4A}$ as a function of h. The best fitting value of h is represented with a cross. (b) Number of cycles to initiate in a 30 μm diameter grain (N_{init}) as a function of the residual stress at $\sigma_{max} = 1100$ MPa according to Equation (8.26)

LCF experimental fatigue lives were all resulting from surface crack initiation due to damaged NbC or stress concentration features.

8.9 Results and discussion

8.9.1 Crack initiation depth predictions

Predicted fatigue lives as a function of the simulated crack initiation depth are presented in Figure 8.13. Depth steps of 10 μm were used to find the location leading to the shortest predicted fatigue life. The absence of marker means that infinite fatigue life was predicted. The depth resulting in the shortest predicted fatigue life is assumed to be the depth at which an actual crack initiation occurs.

Results at $\sigma_{max} = 1100$ MPa are presented in Figure 8.13(a). The model predicts surface crack initiations for polished and as machined conditions. The microstructural threshold was not surpassed for the as machined condition, in the case of simulated crack initiations at depths of 10 and 20 μm because of the local compressive residual stresses (Figure 8.9(a)). This condition held up to a depth of 100 μm for S230–4A and CW14–4A specimens, and up to 160 μm for the CW14–8A condition. The model predicts that initiation occurs at a depth of 230 μm, corresponding to the input residual stress tensile peak depth (Figure 8.9(a)), for the CW14–8A condition. The fatigue life predictions for S230–4A and CW14–4A conditions are the same from a depth of 150 μm to the middle of the cross section. This indicates

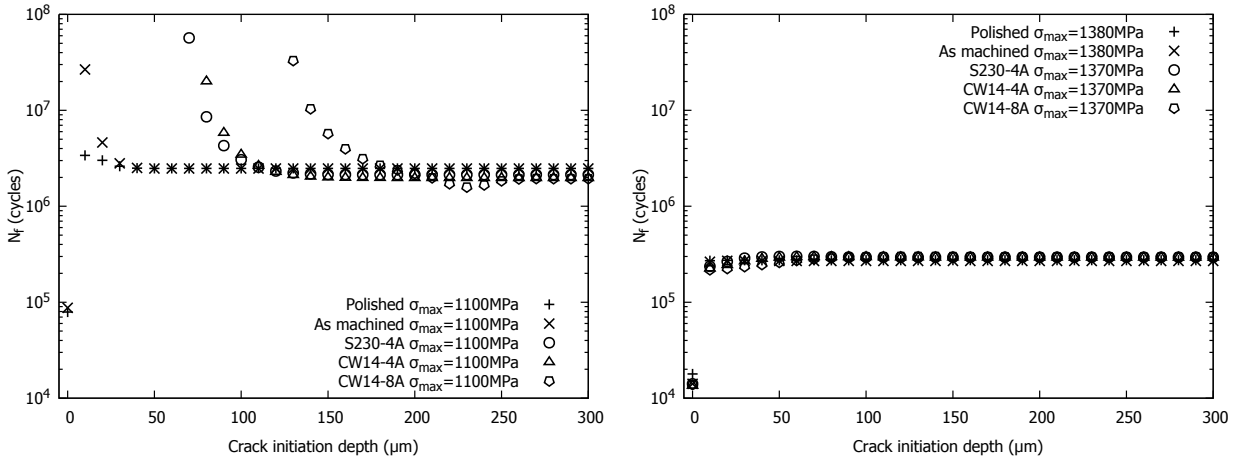

(a) (b)

Figure 8.13 Proposed model fatigue life predictions as a function of the crack initiation depth in (a) HCF and (b) LCF. Fatigue life was predicted for surface and subsurface crack initiations with a depth increment of 10 μm. Missing data points correspond to infinite fatigue life prediction

that the initiation will occur in the weakest grain (combination of largest size and favorable orientation) located at a depth equal or above 150 μm. Note that Klotz *et al.* (2018a) observed that, for the S230-4A and CW14-4A conditions tested in HCF, crack initiations occurred at a depth superior or equal to 2 mm. This suggests that crack initiation depth depended on the location of the weakest link in the microstructure (largest favorably oriented grain). Thus, if more specimens would have been tested, initiations at depth inferior to 2 mm could have been found.

In LCF, as it can be seen from Figure 8.13(b), the model predicts that all crack initiations occur at the surface.

Crack initiation depth predictions are summed up in Table 8.7 along with Klotz *et al.* (2018a) experimental observations. The predicted crack initiation depths are in good agreement with the experimental observations, for all the tested conditions.

N_{init}, the number of cycles to initiate a crack in a subsurface large grain, predicted with Equation (8.26), are also presented in Table 8.7. In HCF, in the case of subsurface crack initiations, N_{init} represents more than 95 % of the total number of cycles to failure (N_f). Since N_{init} represents at least 95 % of the fatigue life for the predicted subsurface crack initiations, and considering that Figure 8.12(b) shows the negative relationship between N_{init} and $\sigma_{RS}(x_{init})$, the predicted fatigue life resulting from a subsurface crack initiation is highly influenced by the input residual stresses profile. For this reason, all the conditions

Table 8.7 Proposed model crack initiation (init.) depth, subsurface predicted number of cycles to initiation (N_{init}) and fatigue life (N_f) predictions (pred.) compared with experimental (exp.) results. The error is based on the average experimental fatigue lives presented in Table 8.2. Note that h was chosen to fit the S230–4A and CW14–4A conditions in HCF

Surface condition	σ_{max} (MPa)	Crack init. pred. depth (μm)	Exp. crack init. depth (μm)	N_{init} (cycles)	N_f (cycles)	Error (%)
Polished	1100	0	0	-	7.91×10^4	-20
	1380	0	0	-	1.79×10^4	-15
Machined	1100	0	0	-	8.74×10^4	+2
	1380	0	0	-	1.41×10^4	+1
S230–4A	1100	>150	>2 mm	2.06×10^6	2.14×10^6	+6
	1370	0	0	-	1.41×10^4	-15
CW14–4A	1100	>150	>2 mm	1.91×10^6	1.98×10^6	-5
	1370	0	0	-	1.39×10^4	-12
CW14–8A	1100	230	$\simeq 210$	1.51×10^6	1.58×10^6	+255
	1370	0	0	-	1.36×10^4	+9

exhibited constant fatigue life (Figure 8.13) when crack initiation was sufficiently deep to be in the constant residual stresses portion of the input profiles (Figures 8.9(a) and (c)). For the same reasons, the prediction of a 230 μm deep crack initiation is solely due to the residual stress tensile peak present at this exact depth as observed in Figure 8.9(a). However, it was experimentally observed that the tensile residual stress peak disappeared after the first loading cycle (Figure 8.7(a)) due to local damage accumulation at twin boundaries in the largest favorably oriented grains (Klotz *et al.*, 2018a). This damage mechanism is not accounted for in the proposed model.

As mentionned previously, the parameter h was fitted on the S230–4A and CW14–4A HCF results. It was not possible to determine its value in LCF since all cracks initiated at surface damaged NbC and/or at a surface stress concentration feature. Predicted fatigue lives for subsurface crack initiation in LCF can thus be questioned. However, in LCF, the surface is the most critical location for crack initiation due to the presence of tensile residual stresses and roughness. The fatigue life prediction of a crack initiating at a surface damaged carbide located at the bottom of a dimple would still be shorter, in LCF, than that of a subsurface crack initiation in a grain submitted to tensile residual stresses. Indeed, the number of cycles to crack initiation (more than 90 % of the fatigue life) plus the number of cycles to propagate the crack have to be considered. For example, the fatigue life prediction with the N-R model

of a subsurface crack having an initial length of 30 μm and propagating in a constant 287 MPa tensile residual stress field is 1.20×10^4 cycles. This simulation is highly conservative since 287 MPa tensile residual stresses are only present at the surface and reach 0 at roughly 60 μm below the surface for the CW14–8A specimens. The result is close to the 1.36×10^4 cycles predicted for a surface crack initiation. Since the number of cycles to initiate a crack having the size of a grain has to be added, we can safely assume that another value of h would not have affected the crack initiation location prediction in LCF.

8.9.2 Fatigue life predictions

Table 8.7 compares the N-R model fatigue life predictions with the experimental results obtained by Klotz *et al.* (2018a). Model predictions are also plotted along with Klotz *et al.* (2018a) experimental results in Figure 8.14. Fatigue lives for the S230–4A and CW14–4A conditions cannot be considered as predictions since the parameter h was adjusted to best fit their average experimental results. Except for the polished and CW14–8A condition in HCF, fatigue lives were predicted with a ± 15 % error, when compared to the average experimental results.

In HCF, the fatigue life is nevertheless over-estimated for the CW14–8A condition. Indeed, as observed by Klotz *et al.* (2018a), the tensile residual stress peak seems to disappear after the first loading cycle (Figure 8.7(a)). Klotz *et al.* (2018a) suggested that it might be

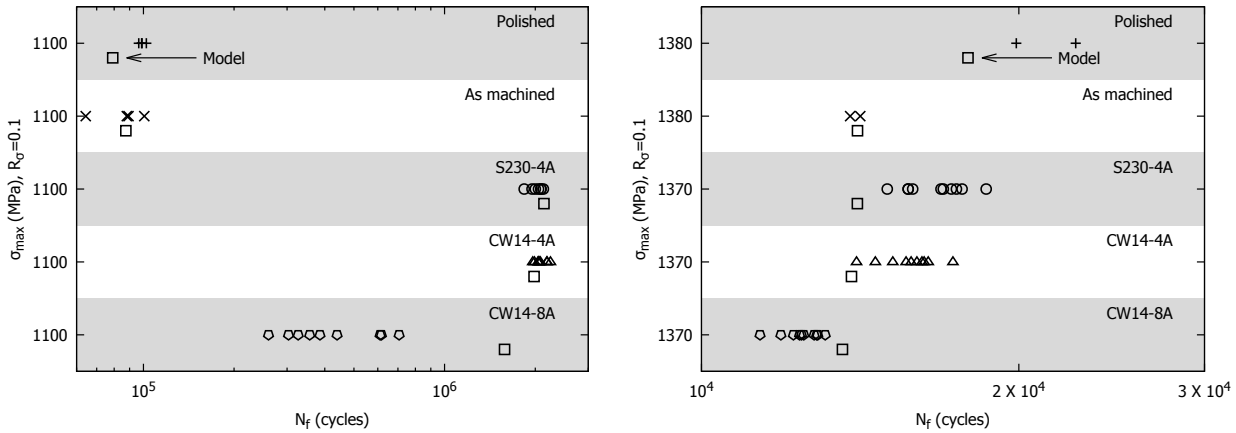

(a) (b)

Figure 8.14 Proposed model fatigue life predictions plotted along with the experimental results (Klotz *et al.*, 2018a) in (a) HCF and (b) LCF. The squares represent the model predictions

due to local yielding leading to local damage (dislocations) accumulation. However this local damage accumulation is not accounted for in Equation (8.26) and only the relaxed value predicted by the FE model (108 MPa) was accounted for.

In LCF, the S230–4A and CW14–4A shot peening conditions predicted fatigue lives are under-estimated, when compared to experimental results. On the other hand, it is over-estimated for the CW14–8A condition. These prediction errors might be explained by the form of Equation (8.11) which accounts for the surface stress concentration. Indeed, Li *et al.* (1992) established Equation (8.11) using a finite element model applied to round shaped dimples. However, Klotz *et al.* (2018a) observed that the specimen's surface was highly altered after CW14–8A shot peening and thus the hypothesis of round shaped dimples underlying in Equation (8.11) might not be valid anymore. For the CW14–8A condition, $K_{t0} = 1.11$ when calculated with Equation (8.11). Simulations with the stress concentration factor K_{t0} evolving from 1 to 2 were performed to evaluate the impact of K_{t0} on the predicted LCF fatigue life of the CW14–8A specimens. The results are presented in Figure 8.15(a). The model predicted brutal rupture at the first cycle for $K_{t0} \geq 1.80$ due to general yielding at the crack tip. The predicted fatigue life is sensitive to K_{t0} and thus a better estimation of this parameter could improve fatigue life predictions. A 3D map with an optical microscope could be performed on a shot peened specimen and reproduced in a FE model. A loading FE simulation would provide stress concentrations factor closer to reality than the idealized

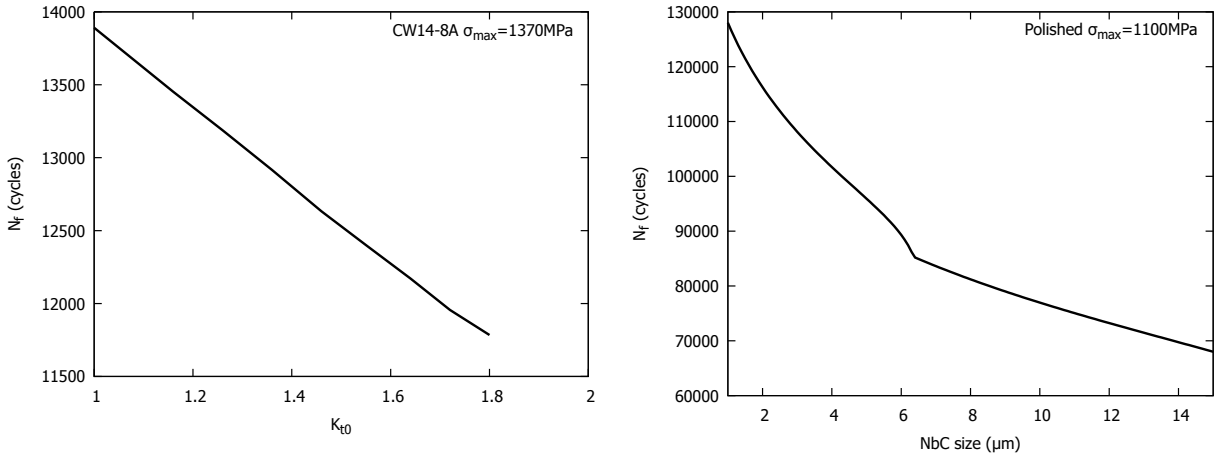

(a) (b)

Figure 8.15 (a) Predicted fatigue life of a CW14–8A specimen at $\sigma_{max} = 1370$ MPa as a function of the parameter K_{t0}. Brutal rupture at the first cycle was predicted for $K_{t0} > 1.8$. (b) Predicted fatigue life of a polished speciment at $\sigma_{max} = 1100$ MPa as a function of the inherently damaged NbC size. The inflection is due to the transition from $i = 1$ to $i = 3$

case simulated by Li *et al.* (1992).

In HCF and LCF, polished specimens fatigue lives are under-estimated, as well as these in LCF for the S230–4A and CW14–4A conditions. The inherently damage niobium carbide size was taken as the average carbide size observed by Klotz *et al.* (2018a) in the plain material microstructure. This choice might be conservative since the carbides intersecting with the specimens surface were cut during the machining process and might be smaller than the carbides average size in the plain material. The predicted fatigue life of polished specimens tested in HCF for different inherently damaged niobium carbides size are plotted in Figure 8.15(b). The predicted fatigue life is very sensitive to the inherently damaged NbC size. A statistical study on the surface inherently damaged carbides size should be undertaken and by changing the initial NbC size in the model, the predictions could be enhanced.

8.10 Conclusion

Fatigue lives and crack initiation locations were predicted for polished, as machined and shot peened cylindrical Inconel 718 specimens fatigue tested under axial controlled force at $R_\sigma = -1$. Crack propagation was predicted using the Navarro and de los Rios crack propagation model which we enhanced by accounting for the redistributed residual stress and cold work profile estimated using a finite element model. Subsurface crack initiations were predicted using Chan's crack initiation model modified to account for the residual stresses.

Surface crack initiations were assumed to occur at a carbide that cracked during the first cycle or was inherently altered during sample manufacturing. The Navarro and de los Rios model accounting for the redistributed residual stress and cold work profile was used for the fatigue life predictions. Subsurface crack initiations were assumed to occur in 3 times larger than average grains (as experimentally observed (Klotz *et al.*, 2018a)) and the modified Chan's crack initiation model was used to predict the number of cycles to initiate in a grain. The modified Navarro and de los Rios model was then used to predict the number of cycles for crack propagation.

Crack initiation location was determined by successively simulated crack initiations at the specimen surface and at different depths. The crack initiation location resulting in the lowest predicted fatigue life was considered as the specimen's weakest link. Crack initiation locations were successfully predicted for all the tested conditions.

Fatigue lives were predicted with a ± 15 % error, when compared to the average experimental results. The exceptions were 1) the condition at which a tensile residual stress peak led to local yielding (CW14–8A in HCF), not accounted for in the modified Chan's

model, 2) the polished condition in HCF for which fatigue life prediction is highly sensitive to the damaged carbide size and 3) for the S230–4A and CW14–4A conditions, which were used as fitting conditions to obtain the parameter h and thus they cannot be considered as predictions.

For future work, the proposed enhancements on the model, which will have a direct impact on the predicted fatigue life, could be performed to better predict the fatigue life: 1) Better estimate the surface stress concentrations factors, 2) better estimate the surface inherently damage niobium carbides size and 3) account for local damage accumulation due to yielding at residual stress profile tensile peak.

8.11 Acknowledgements

This work was financially supported by Pratt & Whitney Canada, Bell Helicopter Textron, L3-Communications MAS, Héroux-Devtek, the Consortium of Research and Innovation in Aerospace in Quebec, the Natural Sciences and Engineering Research Council of Canada and Mathematics of Information Technology and Complex Systems (grant number: RDC 435539-12).

8.12 Appendix

This Appendix aims to present how Equation (8.8) was simplified to Equation (8.9). The method is similar to that used by Vallellano (1999) except that herein $\sigma_1 \neq 0$.

The equation to simplify is

$$CTOD = \frac{bc^i}{\pi^2 A}\left\{2(\sigma_2^i - \sigma_1^i)n_1^i \ln\left(\frac{1}{n_1^i}\right) + (\sigma_3^i - \sigma_2^i)\left[(n_1^i + n_2^i)\cosh^{-1}\left(\left|\frac{1+n_2^i n_1^i}{n_2^i + n_1^i}\right|\right) + (n_2^i - n_1^i)\cosh^{-1}\left(\left|\frac{1-n_2^i n_1^i}{n_2^i - n_1^i}\right|\right)\right]\right\}. \tag{8.27}$$

Since $\cosh^{-1}(x) = \ln\left(x + \sqrt{x^2-1}\right)$, the two $\cosh^{-1}$ functions, renamed P_1 and P_2 can be expressed as

$$P_1 = \cosh^{-1}\left(\left|\frac{1+n_2^i n_1^i}{n_2^i + n_1^i}\right|\right) = \ln\left(\left|\frac{1+n_2^i n_1^i}{n_2^i + n_1^i}\right| + \sqrt{\left(\left|\frac{1+n_2^i n_1^i}{n_2^i + n_1^i}\right|\right)^2 - 1}\right) \tag{8.28a}$$

and

$$P_2 = \cosh^{-1}\left(\left|\frac{1-n_2^i n_1^i}{n_2^i - n_1^i}\right|\right) = \ln\left(\left|\frac{1-n_2^i n_1^i}{n_2^i - n_1^i}\right| + \sqrt{\left(\left|\frac{1-n_2^i n_1^i}{n_2^i - n_1^i}\right|\right)^2 - 1}\right). \tag{8.28b}$$

In the N-R model: $0 < n_1^i < n_2^i < 1$ and thus P_1 and P_2 can be expressed as

$$P_1 = \ln\left(\left|\frac{1+n_2^i n_1^i}{n_2^i + n_1^i}\right| + \sqrt{\frac{1+\left(n_2^i n_1^i\right)^2 - (n_2^i)^2 - (n_1^i)^2}{\left(n_2^i + n_1^i\right)^2}}\right) \tag{8.29a}$$

and

$$P_2 = \ln\left(\left|\frac{1-n_2^i n_1^i}{n_2^i - n_1^i}\right| + \sqrt{\frac{1+\left(n_2^i n_1^i\right)^2 - (n_2^i)^2 - (n_1^i)^2}{\left(n_2^i - n_1^i\right)^2}}\right). \tag{8.29b}$$

It is assumed that r_0 is negligible in front of the grain size which implies that $n_2^i \simeq 1$ and since $\ln(1+x) \simeq x$ for $x \to 0$, P_1 and P_2 can be expressed as

$$P_1 \simeq \sqrt{\frac{1+\left(n_2^i n_1^i\right)^2 - (n_2^i)^2 - (n_1^i)^2}{\left(n_2^i + n_1^i\right)^2}} \tag{8.30a}$$

and

$$P_2 \simeq \sqrt{\frac{1+\left(n_2^i n_1^i\right)^2 - (n_2^i)^2 - (n_1^i)^2}{\left(n_2^i - n_1^i\right)^2}}. \tag{8.30b}$$

If we refer to P_3 as the common part in P_1 and P_2, then

$$P_3 = 1 + \left(n_2^i n_1^i\right)^2 - (n_2^i)^2 - (n_1^i)^2 \tag{8.31}$$

and since $n_2^i = c^i/(c^i + r_0)$,

$$P_3 = 1 + \left(\frac{c^i}{c^i + r_0}\right)^2 \left(n_1^i\right)^2 - \left(\frac{c^i}{c^i + r_0}\right)^2 - \left(n_1^i\right)^2. \tag{8.32}$$

Which can be reformulated as

$$P_3 = 1 + \frac{\left(n_1^i\right)^2}{\left(1 + \frac{r_0}{c^i}\right)^2} - \frac{1}{\left(1 + \frac{r_0}{c^i}\right)^2} - \left(n_1^i\right)^2. \tag{8.33}$$

r_0 is negligible in front of c^i and since $1/(1+x)^2 \simeq 1-2x$ for $x \to 0$, P_3 becomes

$$P_3 \simeq 1 + \left(n_1^i\right)^2 \left(1 - \frac{2r_0}{c^i}\right) - \left(1 - \frac{2r_0}{c^i}\right) - \left(n_1^i\right)^2, \tag{8.34}$$

which can be simplified to

$$P_3 \simeq \frac{2r_0}{c^i}\left(1 - \left(n_1^i\right)^2\right). \tag{8.35}$$

Injecting back P_3 in P_1 and P_2 leads to

$$P_1 \simeq \sqrt{\frac{\frac{2r_0}{c^i}\left(1-\left(n_1^i\right)^2\right)}{\left(n_2^i + n_1^i\right)^2}} \tag{8.36a}$$

and

$$P_2 \simeq \sqrt{\frac{\frac{2r_0}{c^i}\left(1-\left(n_1^i\right)^2\right)}{\left(n_2^i - n_1^i\right)^2}}. \tag{8.36b}$$

Then, injecting back P_1 and P_2 in the CTOD formula results in

$$CTOD \simeq \frac{bc^i}{\pi^2 A}\left\{2(\sigma_2^i - \sigma_1^i)n_1^i \ln\left(\frac{1}{n_1^i}\right) + (\sigma_3^i - \sigma_2^i)\left[2\sqrt{\frac{2r_0}{c^i}\left(1-\left(n_1^i\right)^2\right)}\right]\right\}. \tag{8.37}$$

The equilibrium condition imposes (Navarro and de los Rios, 1992) that

$$\sigma_3^i = \frac{1}{\arccos\left(n_2^i\right)}\left[\left(\sigma_2^i - \sigma_1^i\right)\arcsin\left(n_1^i\right) - \sigma_2^i \arcsin\left(n_2^i\right) + \frac{\pi}{2}\sigma\right], \tag{8.38}$$

which can also be written as

$$\sigma_3^i - \sigma_2^i = \frac{\left(\sigma_2^i - \sigma_1^i\right)\arcsin\left(n_1^i\right) - \sigma_2^i \arcsin\left(n_2^i\right) + \frac{\pi}{2}\sigma - \sigma_2^i \arccos\left(n_2^i\right)}{\arccos\left(n_2^i\right)}. \tag{8.39}$$

Since $n_2^i \simeq 1$, $\arcsin\left(n_2^i\right) \simeq \pi/2$ and $\arccos\left(n_2^i\right) \simeq 0$ we have

$$\sigma_3^i - \sigma_2^i \simeq \frac{\left(\sigma_2^i - \sigma_1^i\right)\arcsin\left(n_1^i\right) + \frac{\pi}{2}\left(\sigma - \sigma_2^i\right)}{\arccos\left(n_2^i\right)}. \tag{8.40}$$

The $CTOD$ then becomes

$$CTOD \simeq \frac{bc^i}{\pi^2 A}\Bigg\{2(\sigma_2^i-\sigma_1^i)n_1^i \ln\left(\frac{1}{n_1^i}\right) + 2\sqrt{\frac{2r_0}{c^i}}\frac{(\sigma_2^i-\sigma_1^i)\arcsin\left(n_1^i\right)+\frac{\pi}{2}\left(\sigma-\sigma_2^i\right)}{\arccos\left(n_2^i\right)}\sqrt{1-\left(n_1^i\right)^2}\Bigg\}. \tag{8.41}$$

We know that $n_2^i = c^i/(c^i+r_0) = 1/(1+r_0/c^i)$, that r_0 is negligible in front of c^i and that $\arccos(1/(1+x)) \simeq \sqrt{2x}$ for $x \to 0$. And thus

$$CTOD \simeq \frac{bc^i}{\pi^2 A}\Bigg\{2(\sigma_2^i-\sigma_1^i)n_1^i \ln\left(\frac{1}{n_1^i}\right) + \left[2\left(\sigma_2^i-\sigma_1^i\right)\arcsin\left(n_1^i\right)+\frac{\pi}{2}\left(\sigma-\sigma_2^i\right)\right]\sqrt{1-\left(n_1^i\right)^2}\Bigg\}, \tag{8.42}$$

which can be rewritten as

$$CTOD \simeq \frac{2bc^i n_1^i}{\pi^2 A}(\sigma_2^i-\sigma_1^i)\Bigg\{\ln\left(\frac{1}{n_1^i}\right)+\frac{\sqrt{1-\left(n_1^i\right)^2}}{n_1^i}\left[\arcsin\left(n_1^i\right)+\frac{\pi}{2}\frac{\sigma-\sigma_2^i}{\sigma_2^i-\sigma_1^i}\right]\Bigg\}. \tag{8.43}$$

And finally, $c^i n_1^i = a^i$ which results in

$$CTOD \simeq \frac{2b}{\pi^2 A}a^i(\sigma_2^i-\sigma_1^i)\Bigg\{\ln\left(\frac{1}{n_1^i}\right)+\frac{\sqrt{1-\left(n_1^i\right)^2}}{n_1^i}\left[\arcsin\left(n_1^i\right)+\frac{\pi}{2}\frac{\sigma-\sigma_2^i}{\sigma_2^i-\sigma_1^i}\right]\Bigg\} \tag{8.44}$$

CHAPTER 9 ARTICLE 4 : EFFECTS OF ROLLED EDGES ON THE FATIGUE LIFE OF SHOT PEENED INCONEL 718

T. Klotz, M. Lévesque and M. Brochu.
Submitted to the *Journal of Materials Processing Technology* on February 13th, 2018.

9.1 Abstract

Shot peening on part edges is a critical operation in aerospace manufacturing. Edges are plastically deformed by the shot peening media, which can create stress concentration features known as "rolled edges". The detrimental impact of rolled edges on fatigue life has already been observed in the literature. However, the effects of the geometries of the unpeened edges on rolled edge formation and on the resulting fatigue life have never been published in the open literature. This study presents the effects of different shot peened edge geometries on the fatigue life of Inconel 718, in high and low cycle fatigue. Chamfered, sharp and rounded edges were prepared, shot peened, and fatigue tested. An analysis of crack initiation mechanisms and fatigue lives showed that shot peened sharp edges represent the worst configuration tested in terms of fatigue life and that shot peened rounded edges do not improve the fatigue life when compared to chamfered shot peened edges.

9.2 Introduction

Nickel-based superalloy Inconel 718 is commonly used in gas turbine components. Some gas turbine components can be shot peened to increase their fatigue lives. The shot peening process consists of projecting hard particles, called shot, at high velocity onto the part's surface. The process introduces surface work hardening (cold work) and compressive residual stresses that were found by de los Rios *et al.* (1995) to delay both crack initiation and propagation. Klotz *et al.* (2018a) have shown that in high cycle fatigue (HCF) on cylindrical specimens of Inconel 718, compressive residual stresses and work hardening at the surface can push crack nucleation beneath the specimen's surface and can yield a twenty-fold fatigue life improvement under some testing conditions. However, dimples created by shot peening on the part's surface are stress concentrating features that can decrease the effectiveness of the process. Bagherifard and Guagliano (2012) showed that surface roughness increased with shot peening intensity on a low-alloy steel. Klotz *et al.* (2018a) observed that in low cycle fatigue (LCF), the fatigue performances of shot peened specimens were governed by

the surface roughness and that the shot peened specimens peened at an intensity of 8 A had shorter fatigue life than unpeened samples.

Previous studies on the fatigue behavior of shot peened Inconel 718, such as that of Cammett *et al.* (2005), in HCF at room and high temperature, the work of Nakamura *et al.* (2011) in LCF at room and high temperature, and the study of Klotz *et al.* (2018a) in both LCF and HCF at room temperature focused on cylindrical specimens to avoid stress concentrations. Klotz *et al.* (2018b) found that, in HCF and LCF, polished rectangular specimens on which the edges were rounded and polished showed crack initiation at their edges. Most industrial parts include edges that are critical locations for the formation of discontinuities during the manufacturing process. For example, Lara *et al.* (2013) showed that the fatigue life of high strength steel sheets cut by shearing or by laser was mainly dependent on the defects created on the cut edges. Pessoa *et al.* (2016) attributed the fatigue life reduction of laser-cut stainless steel to the formation of melted drops at the cut edges.

Edges are also delicate to handle during shot peening. They can be plastically deformed in the shape of a fold. You *et al.* (2017) observed that this feature, commonly called "rolled edge" or "shot peened lip", was detrimental to fatigue life on a shot peened, tempered martensitic steel. He *et al.* (2013) showed that rolled edges had no significant effects on fatigue life in LCF and that their detrimental effects on fatigue life increased when load decreased. The authors tested martensitic steel samples, submitted to room temperature bending fatigue at a load ratio of 0.1 and shot peened with 0.58 mm diameter shot at an Almen intensity of 13 A and 200 % coverage, at multiple strain ranges. With and without rolled edges, the specimens had the same fatigue lives as unpeened specimens at an applied strain range of 1 %, indicating that rolled edges had not significant effects on fatigue life in LCF. At an applied strain range of 0.7 %, the fatigue lives were 6×10^4 cycles for unpeened specimens, 10^5 cycles for shot peened specimens with rolled edges, and 2×10^5 cycles for shot peened samples on which the rolled edges were removed. For an applied strain range of 0.55 %, these fatigue lives became 10^5, 3×10^5 and 10^7 cycles, respectively. The results published by He *et al.* (2013) suggest that shot peening on edges can provide fatigue life improvement in HCF, even in the presence of rolled edges, although the gain can be about 30 times greater if the rolled edges are removed.

Edges are commonly chamfered before shot peening in order to minimize the formation of rolled edges. To the best of the authors' knowledge, the effects of the unpeened edge's geometry on the resulting rolled edges and fatigue lives have not been published in the open literature. This work examines the effects of different edge preparations on the formation of

rolled edges during shot peening of Inconel 718 and the resulting effects on fatigue lives and crack initiation mechanisms in both HCF and LCF.

The paper is organized as follows: Section 9.3 presents the material, the specimen's geometry, the shot peening parameters, the fatigue procedures and the observations methods. Fatigue results and fractographs are presented and discussed in Section 9.4. Section 9.5 concludes the work.

9.3 Material and experimental procedure

9.3.1 Material

The precipitation-hardened superalloy Inconel 718 was the same as that tested by Klotz *et al.* (2018a). Tables 9.1 and 9.2 list the mechanical properties and chemical composition. The microstructure is presented in Figure 9.1. Oxides, NbC, TiCN, and δ (Ni_3Nb) particles are present in the microstructure. Hardening precipitates γ' and γ'' are not visible in Figure 9.1. The average grain size is 13 μm.

9.3.2 Edge preparation

Specimens with a rectangular reduced section similar to that presented in Figure 9.2(a) were used. Three types of edge preparations were studied: 0.6 mm chamfers at 45° (Figure 9.2(b)) obtained by wire electrical discharge machining; sharp edges as obtained after machining the reduced section (Figure 9.2(c)); and edges rounded by polishing down to 1 μm (Figure 9.2(d)). The rounded edges had a radius of approximately 0.9 mm.

Table 9.1 Tensile properties of Inconel 718 (Klotz *et al.*, 2018a)

E (GPa)	$\sigma_{y0.2\%}$ (MPa)	σ_u (MPa)	El. (%)	AR. (%)
205	1156	1415	23	33

Table 9.2 Chemical composition of Inconel 718 obtained by optical spectrometry (weight %) (Klotz *et al.*, 2018a)

Elements	Ni	Fe	Cr	Nb	Mo	Ti	Al	Co	Mn	Si
Composition	Bal.	19.53	17.84	5.02	3.07	1.16	0.64	0.35	0.16	0.06

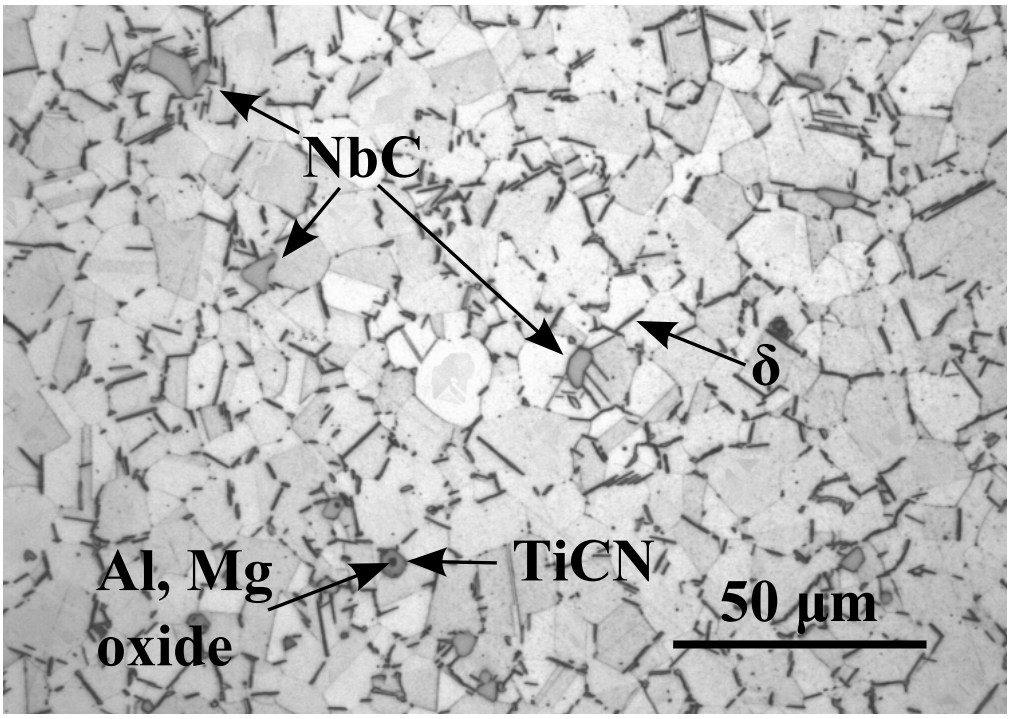

Figure 9.1 Inconel 718 microstructure micrograph. NbC (niobium carbides), titanium carbonitride (TiCN), aluminum and magnesium oxides and δ phase (Ni_3Nb) can be observed

9.3.3 Surface preparation

The reduced sections of the rounded edges specimens were polished down to 1 μm during the edge preparation. The other specimens were left as machined for shot peening.

Specimens were shot peened with 0.36 mm conditioned, carbon steel cut wire shot AWCR14 (CW14) at the intensities of 4 and 8 A. Full coverage was obtained on the reduced section. Shot peening was performed, in agreement with SAE AMS2430T (2015) standard, with an air-pressured machine designed by Genik and Canablast. The machine was equipped with a rotating table mounted on a Fanuc 1-axis servo positioner and with a 6-axis M-20i Fanuc robot. MagnaValves, provided by Electronics Inc., were used to control the shot mass flow. The shot peening setup is schematized in Figure 9.3. The table rotated at 22 rpm and the nozzle, positioned at a 205 mm standoff distance, moved vertically at 22 mm/s.

9.3.4 Fatigue tests

Fatigue tests were performed with a 20 Hz sinusoidal loading scheme with a constant stress amplitude and with stress ratio $R_\sigma = \sigma_{max}/\sigma_{min} = 0.1$, at room temperature. A hydraulic MTS 318.10 machine equipped with a 100 kN MTS 661.20e-03 load cell was used. Two

stress levels were used: 1) $\sigma_{max} = 1100$ MPa ($< \sigma_{y0.2\%}$) for HCF and 2) $\sigma_{max} = 1370$ MPa ($> \sigma_{y0.2\%}$) for LCF. The edge preparations and shot peening conditions that were fatigue-tested are presented in Table 9.3.

Rupture surfaces were examined by scanning electron microscope (SEM) using a JEOL JSM-7600F. An Oxford X-Max 80 was used to perform energy dispersive X-ray spectroscopy.

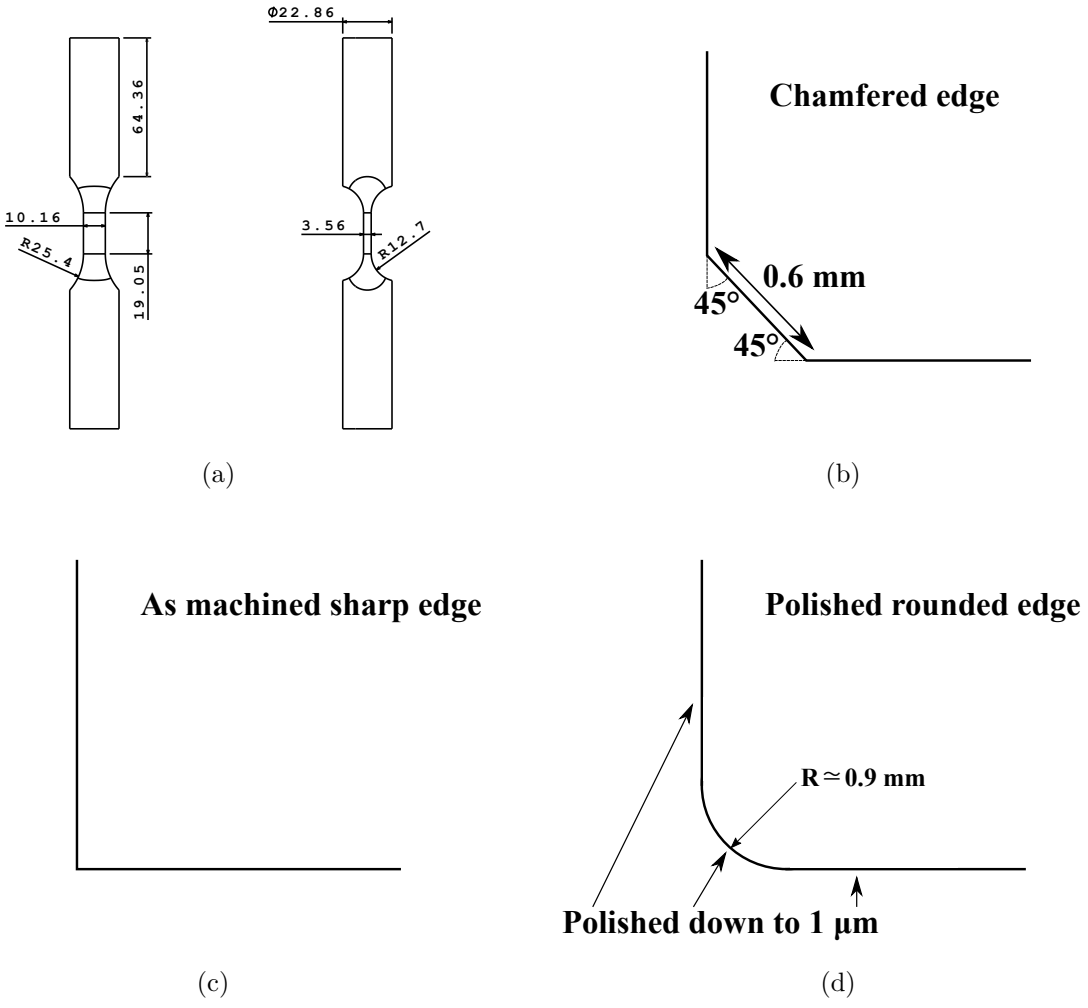

Figure 9.2 (a) Rectangular specimen's geometry. The dimensions are in mm. Schematize of the three edge preparations: (b) chamfered edge, (c) as machined sharp edge and (d) rounded edge

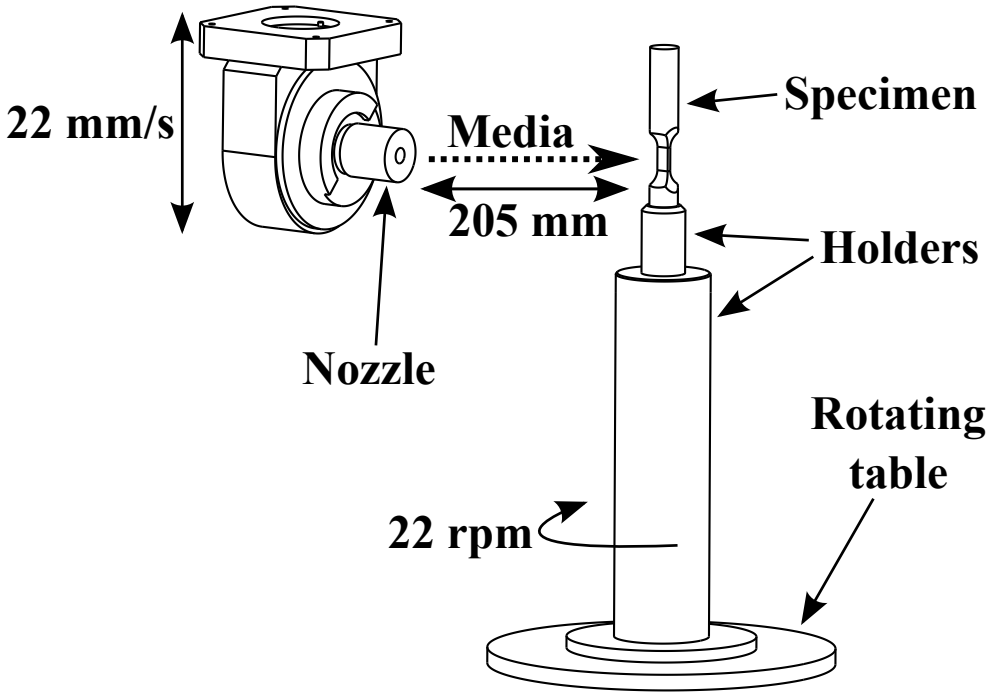

Figure 9.3 Diagram of the shot peening setup

Table 9.3 Edge preparations and shot peening conditions tested in high and low cycle fatigue. "X" means that the condition was tested

	Chamfer	Sharp	Rounded
Unpeened	X		X
CW14 4 A	X		
CW14 8 A	X	X	X

9.4 Results and discussion

9.4.1 Effects of shot peening on the edge characteristics

The faces of the shot peened specimens were polished and etched to observe the effects of shot peening on the edges prior to fatigue testing. The micrographs obtained are presented in Figure 9.4. Dimples on the specimens' surfaces due to the shots impacts can be observed on all micrographs.

Figures 9.4(a) and (b) show the effects of shot peening on a chamfered edge at the intensities of 4 and 8 A, respectively. Figure 9.4(b) shows that the microstructure at the

chamfered edge shot peened at an intensity of 8 A is highly altered by plastic deformations, upto a depth of about 40 μm.

Figure 9.4(c) shows a sharp corner morphology after shot peening at an intensity of 8 A. Two rolled edges can clearly be observed (see in the inlet). The material is highly deformed near the rolled edge, from the surface to a depth of roughly 40 μm.

Figure 9.4(d) shows the cross section of a polished rounded edge that was submitted to a peening intensity of 8 A. Except for the dimples, no specific features can be observed.

The approximate initial shapes of the shot peened edges presented in Figure 9.4 are schematized in Figure 9.5. It can be observed that the deformed regions observed in Fig-

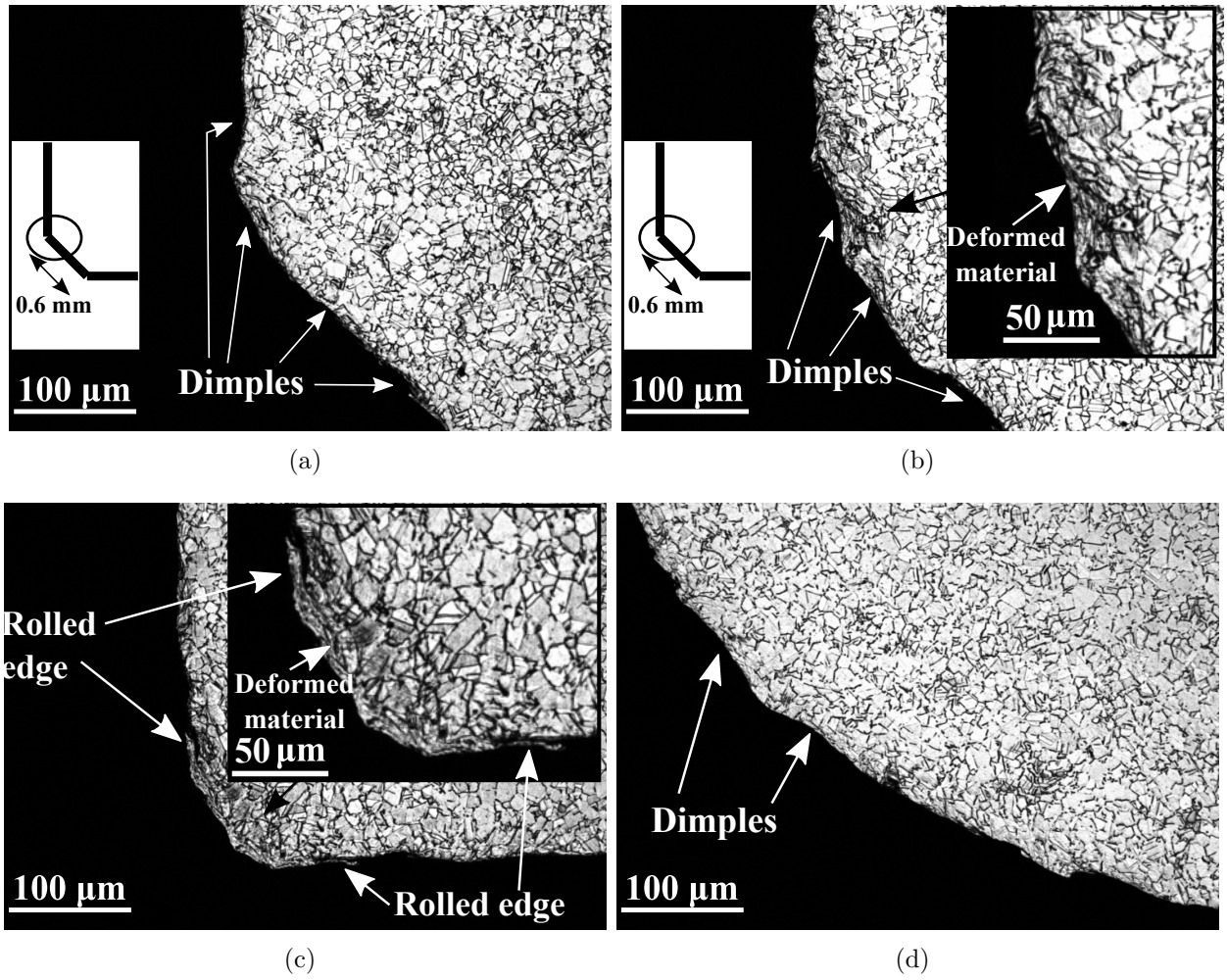

Figure 9.4 Micrographs prior to fatigue tests performed on (a) chamfered specimen shot peened at 4 A, (b) chamfered specimen shot peened at 8 A, (c) sharp edge specimen shot peened at 8 A and (d) polished rounded specimen shot peened at 8 A. Two rolled edges are visible on the sharp edge specimen

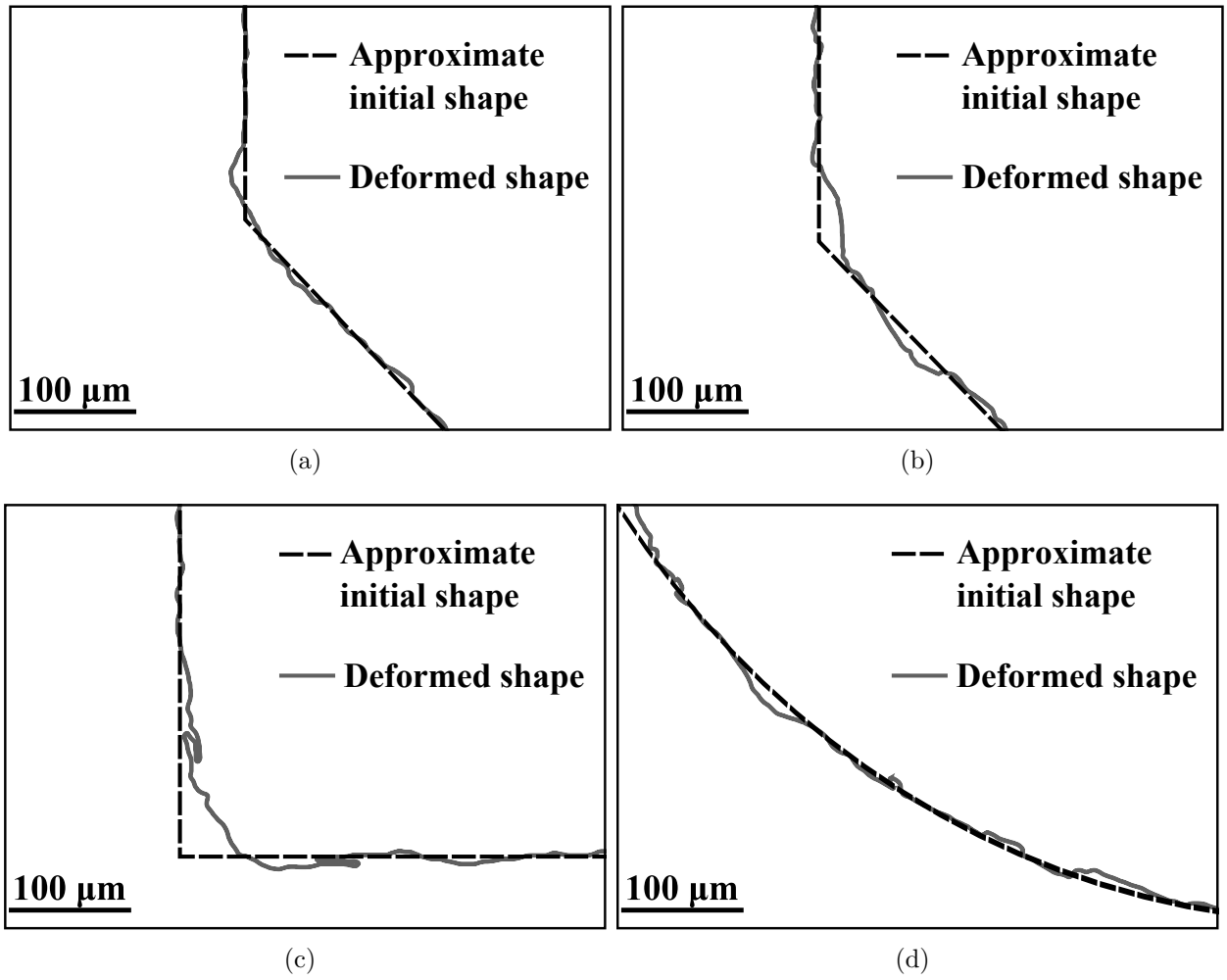

Figure 9.5 Approximate initial shape compared to that shot peened for (a) chamfered specimen shot peened at 4 A, (b) chamfered specimen shot peened at 8 A, (c) sharp edge specimen shot peened at 8 A and (d) polished rounded specimen shot peened at 8 A. The shapes deformed by shot peening were extracted from Figure 9.4

ure 9.4(b) and (d) correspond to the tapered part of the edges that have been impacted by the shots. Note that such material deformations were not observed on the chamfer shot peened at an intensity of 4 A (Figure 9.4(a) and Figure 9.5(a)).

Figures 9.6 shows SEM pictures of a sharp edge surface and a polished rounded edge one that were each peened at an intensity of 8 A. The pronounced plastic deformation of a sharp edge in the form of rolled edges can be clearly observed in Figure 9.6(a). Figure 9.6(b) shows that material folds were also present on the rounded specimens edges.

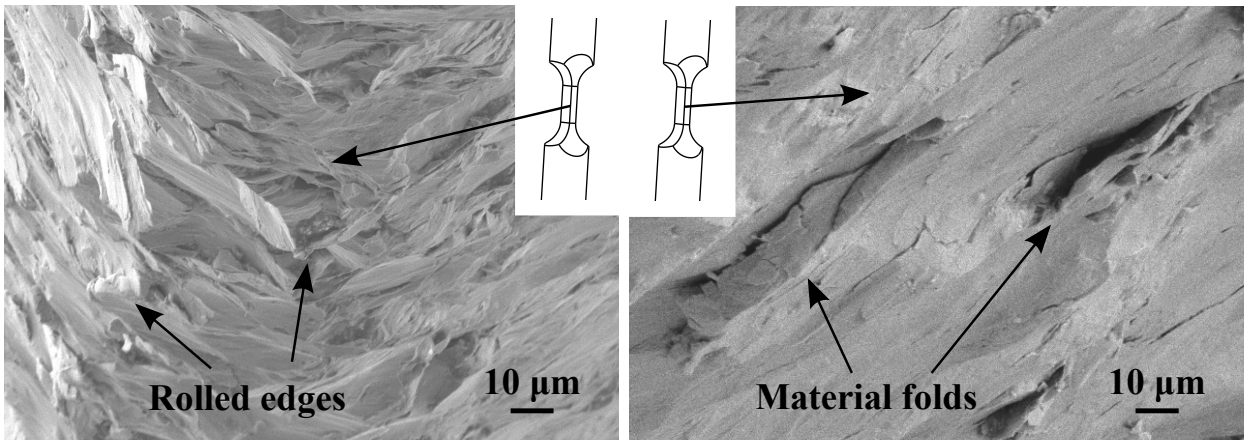

(a) (b)

Figure 9.6 Prior-testing SEM pictures of (a) sharp edge shot peened at 8 A and (b) polished round edge shot peened at 8 A. Rolled edges are observed on the sharp edge while on the polished rounded edge, the presence of material folds is observed

9.4.2 Fatigue results

LCF and HCF fatigue results are presented in Figures 9.7(a) and (b), respectively. A Weibull distribution was used to fit the fatigue results for the conditions tested at least three times. The statistical results are presented in Table 9.4. The Weibull distributions' scale parameters λ_w and shape parameters β_w were obtained with the `MATLAB` function `wblfit`.

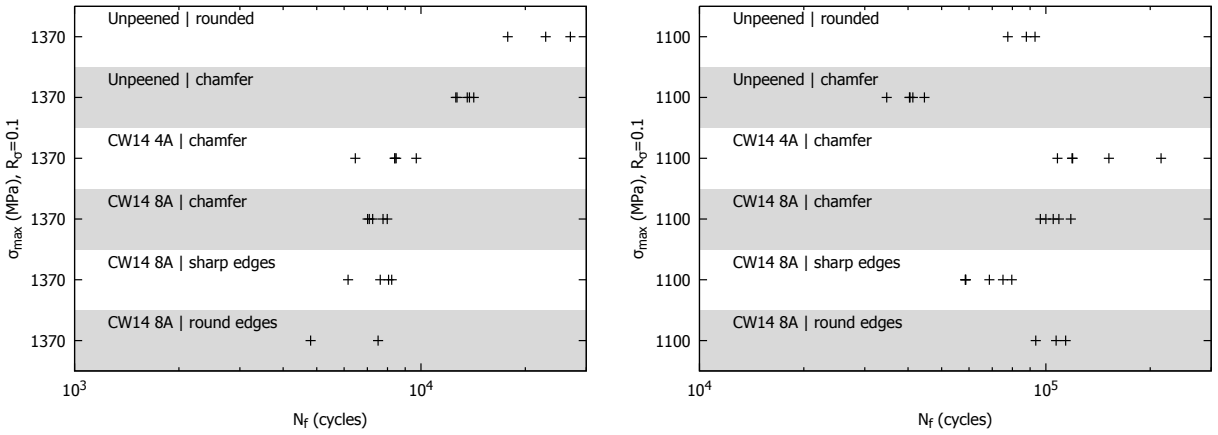

(a) (b)

Figure 9.7 Fatigue results in (a) LCF and (b) HCF. The logarithmic abscissa represents the fatigue life and the vertical axis represents the maximum applied stress (σ_{max}). The different edge geometries were put one upon another to allow better comparisons

As in Bianchetti *et al.* (2017), the coefficient of determination R^2 was used as a goodness-of-fit test and was computed for each tested condition as

$$R^2 = 1 - \frac{\sum_{j=1}^{\mathrm{Nb}} \left(D_{exp,j} - D_{theo,j}\right)^2}{\sum_{j=1}^{\mathrm{Nb}} \left(D_{exp,j} - \bar{D}_{theo}\right)^2} \tag{9.1}$$

where Nb is the number of specimens tested and $\bar{D}_{theo}$ is the theoretical deciles average. $D_{exp,j}$ and $D_{theo,j}$ are the deciles determined from the j^{th} experimental data and the theoretical

Table 9.4 Statistics of the fatigue test results using a Weibull distribution. Nb: number of specimens. Av. N_f: average fatigue life. The Weibull distribution's scale (λ_w) and shape (β_w) parameters were determined with the `MATLAB` function `wblfit`. R^2: coefficient of determination calculated with Equation (9.1). 50 % prob. failure: number of cycles for 50 % probability of failure. 50 % LB 95 %: lower bound of 95 % confidence interval for 50 % probability of failure. Note that, at $\sigma_{max} = 1370$ MPa, only 2 rounded shot peened specimens were tested and thus no statistical analysis was performed

Specimens	Nb	Av. N_f (cycles)	λ_w	β_w	R^2	50 % prob. failure (cycles)	50 % LB 95 % conf. (cycles)
			$\sigma_{max} = 1370$ MPa				
Polished rounded	3	2.26×10^4	2.42×10^4	7.1	0.97	2.30×10^4	2.13×10^4
Machined chamfer	5	1.34×10^4	1.37×10^4	25.3	0.92	1.35×10^4	1.33×10^4
4 A chamfer	5	8.29×10^3	8.73×10^3	9.9	0.82	8.41×10^3	8.09×10^3
8 A chamfer	5	7.42×10^3	7.61×10^3	20.4	0.86	7.48×10^3	7.34×10^3
8 A sharp	4	7.52×10^3	7.86×10^3	13.6	0.88	7.65×10^3	7.40×10^3
8 A rounded	2	6.16×10^3	-	-	-	-	-
			$\sigma_{max} = 1100$ MPa				
Polished rounded	3	8.61×10^4	8.90×10^4	17.0	0.96	8.71×10^4	8.45×10^4
Machined chamfer	5	4.03×10^4	4.17×10^4	15.6	0.89	4.07×10^4	3.97×10^4
4 A chamfer	5	1.43×10^5	1.58×10^5	3.8	0.82	1.43×10^5	1.29×10^5
8 A chamfer	5	1.06×10^5	1.09×10^5	14.5	0.95	1.07×10^5	1.04×10^5
8 A sharp	6	6.66×10^4	7.05×10^4	8.4	0.85	6.75×10^4	6.47×10^4
8 A rounded	3	1.05×10^5	1.09×10^5	15.6	0.96	1.06×10^5	1.03×10^5

deciles from the Weibull distribution, respectively. For all the tested conditions, R^2 was superior or equal to 0.85, except for the chamfer specimens shot peened at an intensity of 4 A and tested in both LCF and HCF. It suggests that the Weibull distribution might not be suitable for these two latter conditions. The number of cycles for a 50 % probability of failure are also presented in Table 9.4. The lower bounds of the 95 % confidence interval for a 50 % failure probability, determined with a χ^2 test on the logarithm of the likelihood function as described by Abramovich and Ritov (2013), are also presented to express the spread of the results. In Table 9.5, the average fatigue lives of the shot peened specimens are qualitatively compared to those of the unpeened specimens. This qualitative comparison shows that the effect of edge preparation on fatigue life is stress or strain dependent. This behavior will be further analyzed in parallel with fractographic observations.

SEM observations were carried out on the specimens tested in HCF. For each specimen's surface condition, the specimen that had the longest fatigue life and the specimen with the shortest fatigue life were examined. Typical SEM observations are shown in Figure 9.8. Table 9.6 summarizes the observations.

LCF results

All crack initiations, without exception, occurred at edges for the specimens tested in LCF.

In LCF (Figure 9.7(a)), the unpeened, polished, rounded edge specimens had the longest fatigue lives, with an average of 2.26×10^4 cycles. This average fatigue life is comparable to the 2×10^4 cycles obtained by Klotz *et al.* (2018a) on polished cylindrical specimens tested at

Table 9.5 Qualitative comparison of the average fatigue lives of the shot peened and unpeened specimens. Av. N_f: average fatigue life. +, −: longer or shorter average fatigue life for the peened samples, when compared to those of the unpeened samples

	$\sigma_{max} = 1370$ MPa		$\sigma_{max} = 1100$ MPa	
Condition	Av. N_f polished	Av. N_f as machined	Av. N_f polished	Av. N_f as machined
Av. N_f 4 A chamfer	–	–	+	+
Av. N_f 8 A chamfer	–	–	+	+
Av. N_f 8 A sharp	–	–	–	+
Av. N_f 8 A rounded	–	–	+	+

$\sigma_{max} = 1380$ MPa and $R_\sigma = 0.1$. It suggests that unpeened polished specimens with rounded edges behave as cylindrical polished specimens in LCF. There must be a critical radius size below which this similarity does not hold, but this conclusion was not investigated in this work.

On the other hand, the unpeened chamfered specimens had an average fatigue life of 1.34×10^4 cycles, which is shorter than the 1.4×10^4 cycles for as machined cylindrical specimens tested at $\sigma_{max} = 1380$ MPa and $R_\sigma = 0.1$ by Klotz *et al.* (2018a). Chamfered edges with the studied geometry were thus detrimental to fatigue life at $\sigma_{max} = 1370$ MPa.

For all shot peening conditions tested at $\sigma_{max} = 1370$ MPa, the resulting average fatigue lives were shorter than those of the unpeened chamfered and unpeened rounded edge specimens indicating that shot peening can be a drawback in LCF, in terms of fatigue life. This detrimental effect could be explained by the presence of rolled edges and surface tensile residual stresses. Indeed, Klotz *et al.* (2018a) showed that, on identical specimens shot peened with CW14 at an intensity of 8 A and tested under the same LCF loadings ($\sigma_{max} = 1370$ MPa), the shot peening induced surface residual stresses redistributed from -900 MPa before testing to +350 MPa after the first fatigue cycle. Meanwhile, the surface cold work increased from 45 % after shot peening to 50 % after a single cycle due to general yielding ($\sigma_{max} = 1370$ MPa $> \sigma_{y0.2\%}$). Both residual stresses and cold work redistributions were negligible between the first fatigue cycle and 80 % of the fatigue life. The presence of both stresses induced by stress concentrating features and surface tensile residual stresses at the edges can explain the shot peened specimens' shorter fatigue lives. On the other hand, the surface cold work counterbalances the negative effects of surface tensile residual stresses and rolled edges, and prevents a drastic decrease of the shot peened specimens' fatigue lives.

The average fatigue lives of all the shot peened specimens are in the same range, around 8×10^3 cycles, as shown in Table 9.4. The only exception is for the shot peened specimens with rounded edges, for which the average fatigue life is 6.16×10^3 cycles. Note that, for this latter condition, only two specimens were fatigue tested and thus the average fatigue life is not reliable. Moreover, the differences between the number of cycles for a 50 % probability of failure and the lower bound of the number of cycles to failure for the same probability of failure with a confidence of 95 % are less than 4 % for all the shot peened conditions. This indicates low dispersion in the fatigue results. The only exception is for the specimens with chamfered edges shot peened at an intensity of 4 A which had a difference of 8 % and for which the Weibull distribution might not be suitable due to the low R^2 value. This indicates that the edge preparation has no significant effect on the fatigue life of shot peened specimens in LCF. These results are in agreement with those of He *et al.* (2013).

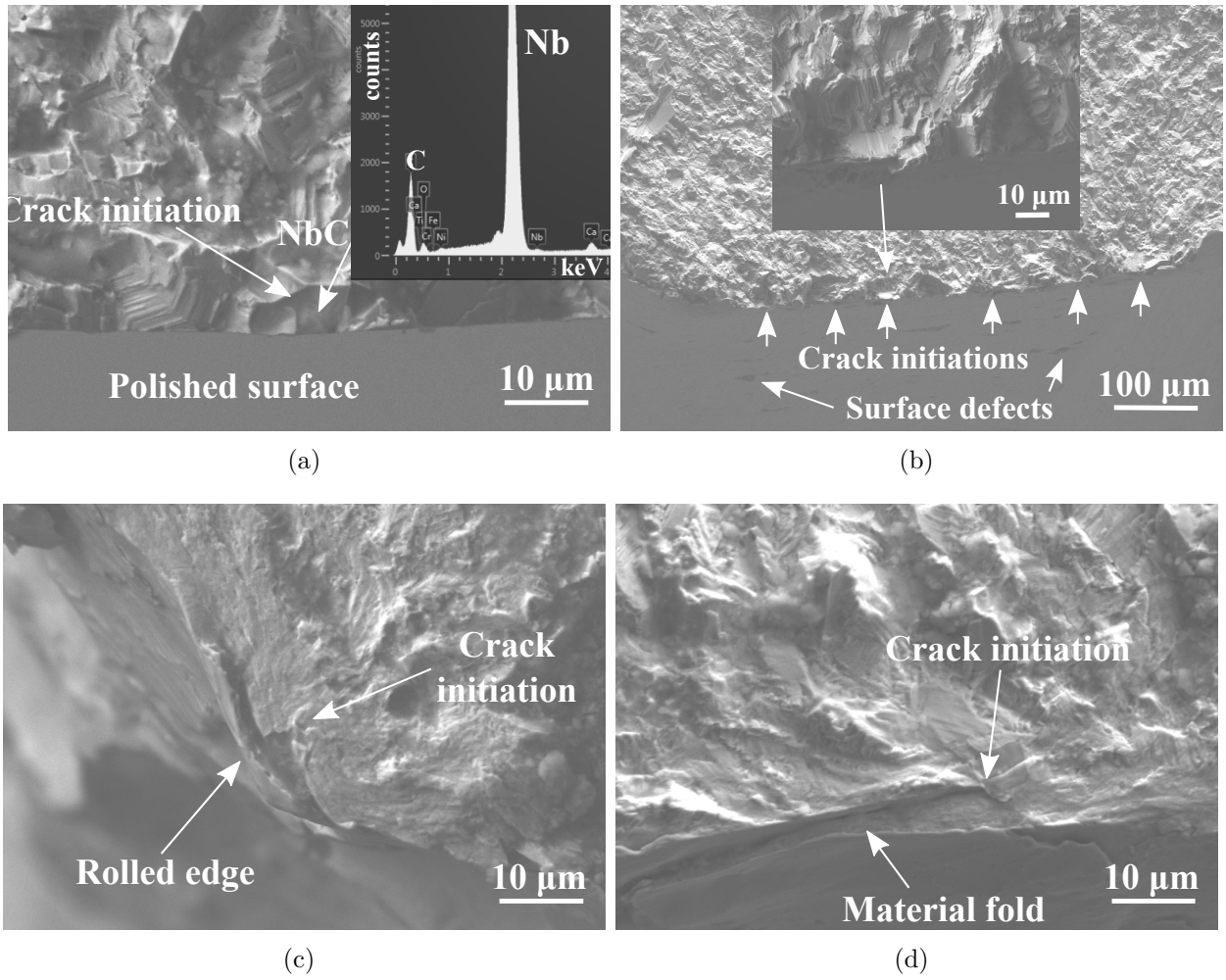

Figure 9.8 SEM observations on specimens tested in HCF: (a) crack initiation at a surface NbC on an unpeened rounded edge polished specimen, (b) crack initiations on surface defects on an as machined chamfered specimen, (c) crack initiation at a rolled edge created in a specimen having chamfers and peened at an intensity of 8 A and (d) crack initiation at a material fold on a rounded edge polished specimen shot peened at an intensity of 8 A

Since the edge preparation had no significant effect on the fatigue lives of shot peened specimens and because the fatigue lives of the shot peened specimens were shorter than those of unpeened specimens, the fracture surfaces were not further studied.

HCF results

All crack initiations occurred at edges for the specimens tested in HCF ($\sigma_{max} = 1100$ MPa).

Table 9.4 shows that unpeened specimens with rounded edges had a longer average fatigue life (8.61×10^4 cycles) than the unpeened chamfered specimens (4.03×10^4 cycles). This

Table 9.6 Summary of the crack initiation observations under scanning electron microscope. $N_{f,min}$ and $N_{f,max}$: minimum and maximum fatigue life of a specific surface condition. NbC: crack initiation at a surface niobium carbide. Stress conc.: crack initiation at a surface stress concentration feature. Rolled edge: crack initiation at a rolled edge. Material fold: crack initiation at a material fold

Specimens	$N_{f,min}$ (cycles)	$N_{f,min}$ Crack initiation	$N_{f,max}$ (cycles)	$N_{f,max}$ Crack initiation
		$\sigma_{max} = 1100$ MPa		
Polished rounded	7.76×10^4	NbC	9.30×10^4	NbC
As machined chamfer	3.47×10^4	Stress conc.	4.46×10^4	Stress conc.
4 A chamfer	1.08×10^5	Rolled edge	2.15×10^5	Rolled edge
8 A chamfer	9.64×10^4	Rolled edge	1.18×10^5	Rolled edge
8 A sharp	5.85×10^4	Rolled edge	7.97×10^4	Rolled edge
8 A rounded	9.35×10^4	Material fold	1.14×10^5	Material fold

indicates that the edges' rounding is beneficial to fatigue life on unpeened specimens in HCF. Figure 9.8(a) and Table 9.6 show that, for this condition, crack initiations occurred at surface NbC located at the edges. Klotz *et al.* (2018a) observed the same crack initiation mechanism on polished cylindrical specimens tested under the same loading conditions. However, the average fatigue life of the unpeened specimens with rounded edges (8.61×10^4 cycles) is shorter than the 9.91×10^4 cycles obtained by Klotz *et al.* (2018a) for the cylindrical polished specimens. It indicates that, in HCF, the presence of 0.9 mm radius rounded edges on polished specimens is a drawback in term of fatigue life. There might be a radius size past which the fatigue life results of the rectangular specimens would be comparable to those of the polished cylindrical specimens.

The average fatigue life of unpeened chamfered edge specimens (4.03×10^4 cycles) is shorter than the average fatigue life of all the other tested conditions (Table 9.5), without exception. Figure 9.8(a) and Table 9.6 reveal that several crack initiations occurred on the chamfer surfaces due to defects left during edge preparation.

Shot peening on rectangular specimens had a beneficial effect on fatigue life when tested at $\sigma_{max} = 1100$ MPa. The qualitative comparisons of Table 9.5 show that all the shot peening conditions resulted in longer average fatigue lives than for the unpeened chamfered specimens. This beneficial effect of shot peening, despite the stress concentration features formed at the

edges during shot peening (Figure 9.6), can be explained by the surface compressive residual stresses and cold work induced by the shot peening process. Indeed, Klotz *et al.* (2018a) showed that, with specimens having the same geometry, shot peened with CW14 at an intensity of 8 A and tested under the same HCF loading conditions, shot peening induced surface residual stresses redistributed from -900 MPa before loading to -606 MPa at 80 % of the fatigue life. The authors have also observed that 45 % cold work deformation was produced on the specimen surface by shot peening, and remained at the same value at 80 % of the fatigue life. Nevertheless, the increase of fatigue life for shot peened rectangular specimens is only a portion of the gain that can be expected on cylindrical specimens. In fact, Klotz *et al.* (2018a) observed a potential twenty-fold improvement in the fatigue life for cylindrical specimens shot peened with CW14 at an intensity of 4 A and tested under the same HCF conditions.

The crack initiation mechanisms were different from one shot peening condition to another in HCF. Rolled edges were responsible for crack initiation in the shot peened specimens with chamfered and sharp edges, as shown in Figure 9.8(c) and in Table 9.6. The material folds observed in Figure 9.6(b) appear to have been responsible for crack initiation in the shot peened specimens with rounded edges, as shown in Figure 9.8(d). It suggests that for all the edge geometries tested, surface compressive residual stresses induced by shot peening did not counterbalance the stress concentrations due to rolled edges or material folds. Crack initiations were not constrained below the specimens' surface, as they were for the cylindrical samples tested by Klotz *et al.* (2018a). Shot peening did not significantly improve the fatigue life when compared with the unpeened rounded specimens.

The severity of the stress concentration features induced by shot peening on the specimens' edges had a direct impact on the resulting fatigue life. Indeed, sharp edges were highly susceptible to rolled edge formation during the shot peening process, as shown in Figures 9.4(c) and 9.6(a). They were also the shot peened specimens with the shortest average fatigue lives. Sharp edges are therefore to be avoided on specimens submitted to shot peening due to the formation of severe rolled edges. On the other hand, chamfered specimens shot peened at an intensity of 4 A, which had least plastic deformation at the edges (Figure 9.4(a)), had the longest average fatigue lives. The chamfered specimen shot peened at an intensity of 4 A that had the shortest fatigue life endured 1.5×10^4 more cycles than the unpeened sample with polished rounded edges having the longest fatigue life. Shot peening at an intensity of 4 A, on chamfered specimens, is thus clearly beneficial in term of fatigue life in comparison with unpeened polished specimens with rounded edges.

It must be noted that the chamfered specimens shot peened at an intensity of 4 A and

tested in HCF suffered a wide dispersion in the fatigue results, when compared with the same specimen geometry shot peened at an intensity of 8 A. Further studies on the geometries of the created rolled edges on specimens having chamfered corners shot peened at an intensity of 4 A might provide explanations for the wide dispersion of the fatigue results. Indeed, the repeatability of the rolled edge geometry might be lower at a peening intensity of 4 A than at 8 A. It suggests that a lower shot peening intensity should be more beneficial to fatigue life due to smaller plastic deformations at the edges.

In HCF, chamfered and rounded edges are equivalent in term of fatigue life when shot peened at an intensity of 8 A. Indeed, the conditions have differences in average fatigue life, number of cycles for 50 % probability of failure, and lower bounds of the 95 % confidence interval for a 50 % probability of failure equal to 10^3 cycles. This means that the two edge conditions can, from a statistical point of view, be considered as the same condition. It indicates that the material folds created by the CW14 shot at an intensity of 8 A on the 0.9 mm radius rounded edges result in stress concentration features equivalent to the rolled edges on the chamfered specimens.

The rounded edges had a radius of about 0.9 mm, which is 5 times larger than the 0.18 mm CW14 shot radius. We can assume that there is a threshold radius value for the rounded edges, larger than 0.9 mm, past which material folds will not be formed on the rounded edges during the shot peening process. Indeed, Klotz *et al.* (2018a) did not observe such stress concentration features on 4.8 mm radius cylindrical specimens shot peened with CW14 at an intensity of 8 A. Crack initiation could thus be, theoretically, restricted to below the rounded edge surfaces. The fatigue life would, consequently, be significantly improved, as it was on the cylindrical specimens tested by Klotz *et al.* (2018a) under the same loading and shot peening conditions.

9.5 Conclusion

Room temperature force-controlled fatigue tests were performed on Inconel 718 specimens with rectangular reduced section in HCF and LCF at $R_\sigma = 0.1$. The objective was to study the effects of shot peening on different edge geometries upon fatigue life. Unpeened chamfered and polished rounded edge specimens, as well as shot peened samples having sharp, chamfered, and rounded edges, were fatigue tested. HCF rupture surfaces were studied under SEM. Crack initiations, without exception, occurred at specimen edges.

In LCF, for all the tested edge geometries and shot peening conditions, shot peening is a drawback in terms of fatigue life when compared with the fatigue lives obtained for

unpeened rounded or chamfered edge specimens. The fatigue lives of shot peened specimens were independent of the shot peening conditions and edge geometries. The association of rolled edges and tensile residual stresses after the first loading cycle is responsible for the decrease in fatigue life when compared to unpeened specimens with the same geometry. On the other hand, the surface cold work prevents a drastic decrease of the fatigue life.

In HCF, cracks initiated at surface NbC in the unpeened specimens having round edges. These occurred at surface defects on the chamfers for the as machined specimens, at rolled edges for the chamfered shot peened specimens, and at material folds for the shot peened specimens having polished rounded edges. For all the tested shot peening conditions and edge geometries, The HCF fatigue lives of shot peened specimens were longer than those of as machined chamfered specimens. The severity of the stress concentration features formed at edges during the shot peening process had a direct negative impact on the fatigue lives. Samples having polished rounded corners and shot peened at an intensity of 8 A did not have longer fatigue lives than chamfered specimens shot peened at the same intensity due to the presence of material folds induced by shot peening. Chamfered specimens shot peened at an intensity of 4 A had the longest fatigue lives due to reduced plastic deformation at the edges. Lower shot peening intensities might result in longer fatigue lives.

The radius of the rounded edges was five times larger than the shot radius. The authors assume that rounded edges with larger radius will prevent the formation of material folds at the edges during the shot peening process and will lead to significant fatigue life improvements in HCF.

All in all, this study provides evidence that shot peening is to be avoided for parts with edges submitted to LCF loading conditions. In HCF, shot peening with CW14 media is beneficial to fatigue life when compared with unpeened chamfered specimens. 4 A shot peening intensity should be preferred to 8 A and chamfered or rounded edges should be preferred to sharp edges. Larger rounded edge radius might maximize the fatigue life improvement.

Future works could study the effects of lower shot peening intensities on the same edge geometries. Also, the ratio of the radius of the rounded corners and the shot peening media radius might be an important parameter to study. The threshold value past which material folds are not created on the rounded edge surfaces (depending on the shot diameter and the shot peening intensity) might be a major parameter to improve the fatigue lives of shot peened industrial components.

9.6 Acknowledgements

This work was financially supported by the Consortium of Research and Innovation in Aerospace in Quebec, the Natural Sciences and Engineering Research Council of Canada, Pratt & Whitney Canada, Bell Helicopter Textron, L3-Communications MAS, Héroux-Devtek and Mathematics of Information Technology and Complex systems.

CHAPTER 10 GENERAL DISCUSSION

Key findings of this thesis are summarized in Section 10.1 and an extended discussion is provided in Section 10.2. The findings are only valid for Inconel 718 under the tested loading conditions, the tested shot peening conditions and at room temperature.

10.1 Key findings

10.1.1 Finding 1: Inconel 718 softening rate under cyclic yielding is solely dependent on the accumulated plastic strain

As it was experimentally showed in the first article, under fully reversed applied strain ($R_\varepsilon = -1$) for $0.6\ \% \leq \varepsilon_{max} \leq 2\ \%$, the softening rate of Inconel 718 was solely dependent on the total accumulated plastic strain. This result allowed to predict the 1D cyclic stress-strain curves of complex uniaxial LCF loadings, at $R_\varepsilon = -1$, using data obtained from a unique LCF single step test performed at the same strain ratio. This prediction method is very flexible and could lead to significant experimental costs reductions.

As discussed in Chapter 6, the cyclic yield model developed in the first article was not suitable to predict the softening at a crack's tip cyclic plastic zone due the different tensile mechanical properties between the specimens used in the first article and those used for the fatigue tests.

10.1.2 Finding 2: Shot peening is detrimental to the fatigue life in LCF

All the LCF results obtained during the experimental campaign are summarized in Figure 10.1.

As it was shown in the second article, shot peening on cylindrical specimens is detrimental to the fatigue life in LCF. The surface residual stresses redistributed during the first loading cycle and became tensile. The surface roughness was then the main driving parameter in terms of fatigue life, as cracks initiated at the specimen surfaces.

It was also shown, in the fourth article, that shot peening on rectangular specimens reduced the fatigue life in LCF when compared to unpeened specimens. Crack initiations occurred at the specimen edges and more precisely at rolled edges.

10.1.3 Finding 3: Shot peening improves the fatigue life in HCF

All the HCF results obtained during the experimental campaign are presented in Figure 10.2.

It was shown in the second article that shot peening on cylindrical specimens resulted in crack initiations beneath the surface and improved the fatigue life by a factor ranging from 2 to 20 in HCF. Nevertheless, high shot peening intensity (8 A) induced a tensile peak in the residual stress profile that led to local yielding which promoted crack nucleation. This situation resulted in large dispersion in the fatigue results due to a small potential volume of crack initiation sites. For a lower shot peening intensity (4 A), which resulted in the absence of such a tensile peak, the fatigue life was the highest observed. It was also characterized by a low dispersion in the fatigue results.

To the best of the author's knowledge, it was the first time that it was shown that shot peening can displace the site of crack nucleation at a depth higher than 2 mm in the specimen and that the fatigue life can be improved up to 20 times.

For rectangular specimens, as showed in the fourth article, shot peening also improved fatigue life when compared to as machined specimens. The lowest shot peening intensity (4 A) was also the most beneficial. Crack initiations occurred at the edge surfaces.

10.1.4 Finding 4: Residual stresses and cold work redistribution can be predicted and accounted for in both Chan's crack initiation and N-R models

Residual stresses and cold work mainly redistributed during the first loading cycle. Their redistribution was negligible between the first cycle and 80 % of the fatigue life. A simple finite element model was successfully developed to predict both redistribution during the first loading cycle. The redistributed residual stresses were directly accounted for in the N-R model and were input in Chan's crack initiation model through their effects on the fatigue limit stress range. The redistributed cold work profile was implemented in the N-R model using the yield strength profile. Indeed, the cold work (plastic strain) was converted in a yield strength using the tensile test stress-strain curve.

To the best of the author's knowledge, the redistributed residual stress and cold work profiles were never accounted for in Chan's crack initiation model and in the N-R model. Their redistribution had a direct impact on the fatigue life, especially in LCF where the cold work increased due to general yielding and where the initial surface compressive residual stresses became tensile.

10.1.5 Finding 5: Crack initiation location can be predicted using an analytical model

The proposed model predictions are presented in Figures 10.1 and 10.2.

Coupling both enhanced Chan's crack initiation and N-R models allowed to accurately predict the crack initiation location for each shot peening and loading condition tested. Indeed, crack initiation was simulated at different depth which allowed to plot a graph of the predicted fatigue life depending on the simulated crack initiation depth. The depth resulting in the lowest predicted fatigue life was assumed to be the weakest link in the specimen in terms of fatigue life, and thus the location where crack initiation occurred.

To the best of the author's knowledge it is the first time that the crack initiation location can be predicted.

10.1.6 Finding 6: Shot peened rounded edges do not improve fatigue life when compared to chamfered ones

Shot peening on polished rounded edges did not improve the fatigue life, when compared to chamfered peened specimens. Indeed, material folds were created during the shot peening process on the polished rounded edges. These features were the source of crack initiations due to stress concentration and led to the same fatigue lives as for the specimens with chamfered edges. Rounded edges with larger radius might prevent material folds formation and could lead to significant fatigue life improvement. The idea that there is a threshold ratio between the shots diameter and the edge radius below which material folds would not be formed was also developed.

To the best of the author's knowledge, it was the first time that the effects of the edge geometries on the formation of rolled edges during shot peening were studied in the open literature.

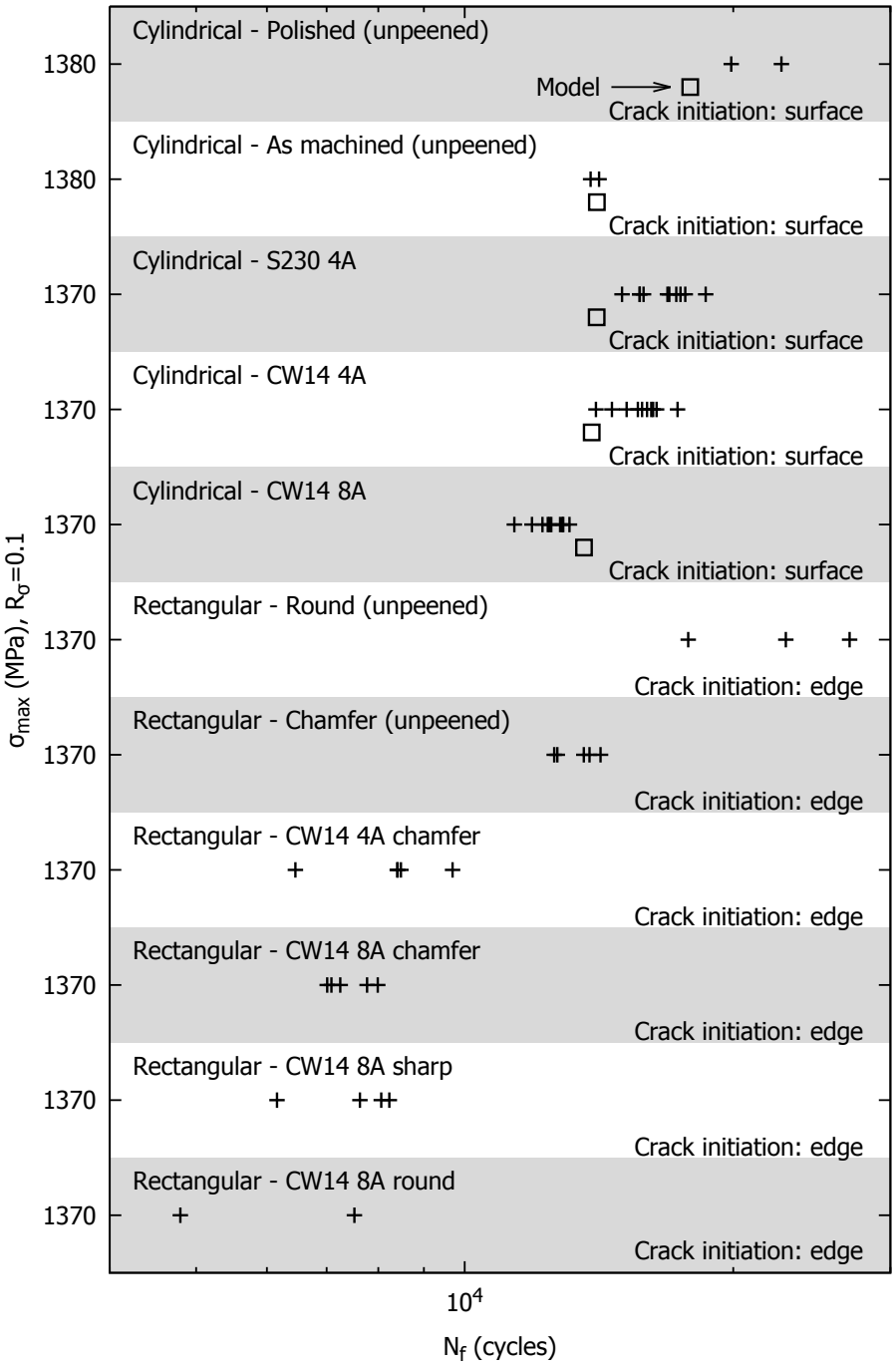

Figure 10.1 LCF results. The crosses represent the experimental results and the squares represent the model predictions. Note that the different surface conditions and specimen geometries have been disposed one upon another for the sake of clarity and to allow for a better comparison. Each horizontal grey/white band represents one surface condition tested at the maximum applied stress specified on the vertical axis. The crack initiation location is also presented

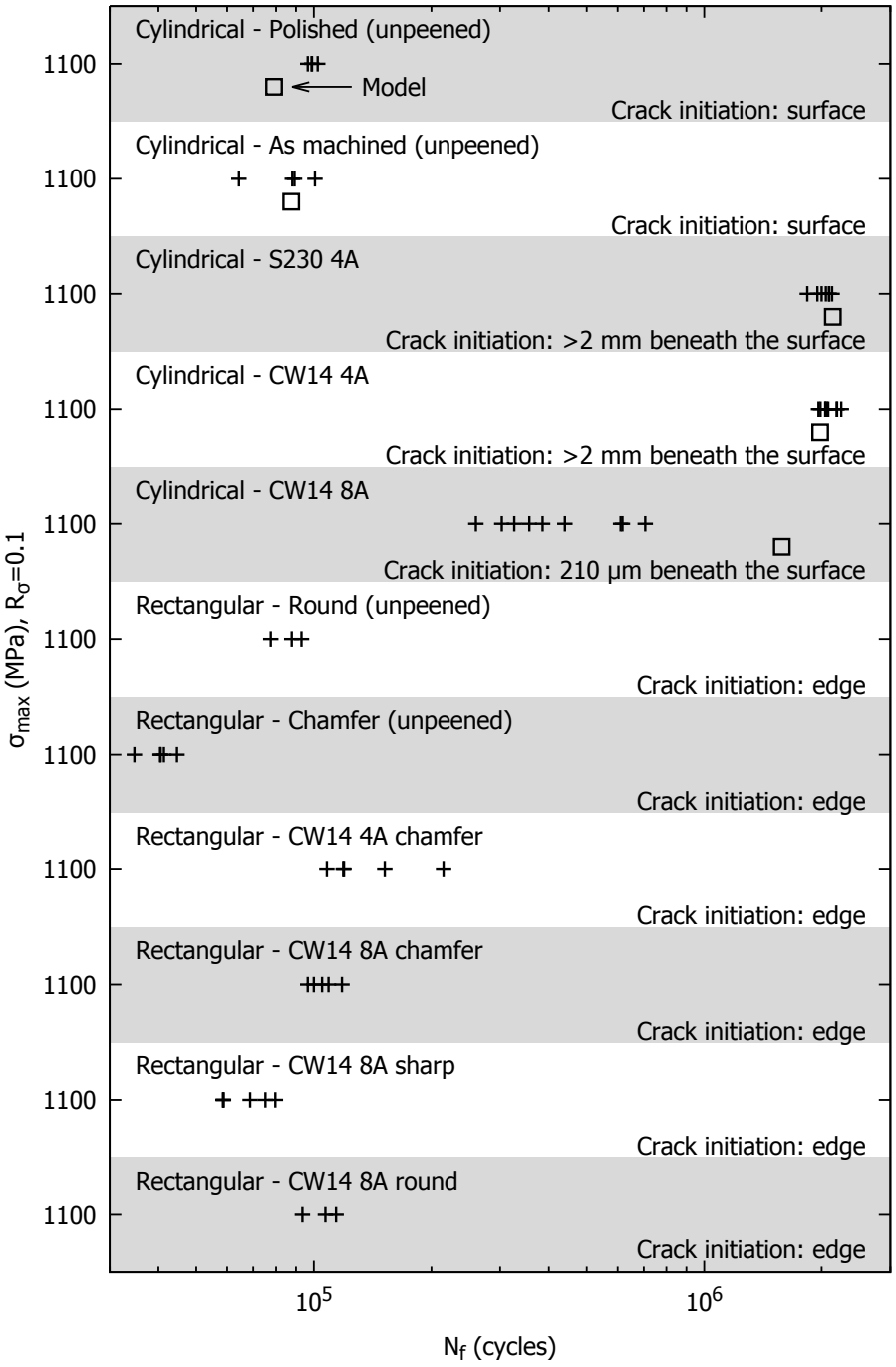

Figure 10.2 HCF results. The crosses represent the experimental results and the squares represent the model predictions. The CW14 4A and S230 4A experimental results were used to calibrate the model. The model predictions for these two conditions cannot be considered as predictions. Note that the different surface conditions and specimen's geometries have been disposed one upon another for the sake of clarity and to allow for a better comparison. Each horizontal grey/white band represents one surface condition tested at the maximum applied stress specified on the vertical axis. The crack initiation location is also presented

10.2 Extended discussion

10.2.1 Optimization of shot peening parameters

In LCF, lower shot peening intensity resulted in a lower surface roughness and yielded a better fatigue life on cylindrical specimens, when compared to higher shot peening intensity with similar shot peening media. On the other hand, no direct effect of the shot peening intensity was found in LCF on rectangular specimens.

In HCF shot peening at an intensity of 8 A resulted in lower fatigue lives, when compared to those resulting from shot peening at an intensity of 4 A for both cylindrical and rectangular specimens.

The presence of a residual stress tensile peak induced by shot peening at an intensity of 8 A resulted in local yielding during the first cycle in HCF. This local damage accumulation promoted crack initiation in cylindrical specimens. On the other hand, shot peening cylindrical specimens at an intensity of 4 A pushed the fatigue life to the maximum potential of the material in HCF.

Lower shot peening intensity resulted in longer fatigue life due to lower plastic deformation at rectangular specimen edges submitted to HCF.

Larger shot peening media (S230 versus CW14 in this study) resulted in better surface roughness due to the shallower penetration, for a peening intensity of 4 A.

These observations suggest that the following guidelines should be followed to maximize the fatigue life of shot peened parts:

1. The shot peening intensity must be sufficiently low to avoid the presence of a tensile peak in the residual stress profile.

2. The shot peening intensity must be as low as possible to minimize the resulting surface roughness.

3. The shot peening intensity must be as low as possible to minimize the plastic deformation on the part edges.

4. The shot peening intensity must be sufficiently high to introduce surface compressive residual stresses that will remain compressive during service life. This situation should repel crack nucleation underneath the surface in the absence of edges.

5. The shot peening media must be as large as possible to reduce the surface roughness.

According to the first criterion, the shot peening intensity should always be below a given threshold. In this project, this particular value was between 4 and 8 A. Shot peening intensity should be as low as possible, but sufficiently high to meet the fourth criterion. The shot peening media is also important in the shot peening process optimization. An ideal shot peening intensity – shot peening media couple would result in sufficiently small plastic deformation at the specimen edges and sufficiently high surface cold work and compressive residual stresses to prevent crack initiation from occurring at the edge surfaces.

10.2.2 Model's potential in shot peening parameters optimization

Crack initiation location can be predicted with the model developed in this thesis. The model could thus be used to reduce experimental fatigue test campaign expenses. Indeed, having an estimation of the crack initiation mechanism and the fatigue life of shot peened specimens would reduce the costs of specimens machining and testing. The model's input parameters that depend on the shot peening parameters are 1) the roughness and 2) the redistributed cold work and residual stress profiles. The redistributed cold work and residual stress profiles can be determined from residual stresses measurements performed after shot peening with the finite element model developed and validated in the third article.

Surface roughness can be measured at low cost after shot peening with a profilometer as it was performed in the second article. On the other hand, residual stresses measurements are expensive. Thus, to determine optimal shot peening parameters using the developed model would still be expensive due to the residual stresses measurements required for each tested shot peening condition.

However, it has been recently shown by Tu *et al.* (2017) that the surface roughness and the residual stresses induced by shot peening parameters on Inconel 718 could be predicted by coupling a discrete element model with a finite element model. This model accounts for shot peening parameters such as the shot peening media size and mechanical properties, the shot peening media mass flow and velocity, the shot-shot interaction, the peening angle and the distance between the nozzle and the specimen. Inconel 718 softening due to the several yielding sequences occurring at the specimen's surface under the shots impact is also accounted for in Tu *et al.* (2017) model based on the experimental results of the first article presented in this thesis.

Tu *et al.* (2017) model could be used to predict the surface roughness and the residual stress and cold work profiles after shot peening with a set of shot peening parameters (shot peening media, shots velocity, shots mass flow, peening angle, the nozzle standoff distance and the specimen geometry). The predicted cold work and residual stress profiles could then be

used in the finite elements model developed in the third article to predict their redistribution due to the fatigue loadings. Finally, the model developed in this thesis would predict the fatigue life as well as the crack initiation location.

This simulation sequence could be repeated iteratively to find shot peening parameters that fill the criteria presented in Section 10.2.1 and that are worth to be experimentally tested. Note that rolled edges creation during shot peening and their effects on fatigue life have not been yet modeled in the open literature.

10.2.3 Generalization of the model to other loading conditions

The model developed in this thesis is only valid at room temperature under $R_\sigma = 0.1$ uniaxial loading. One can wonder how a different stress ratio or loading type could be accounted for in the model and what additional experimental tests would be necessary.

Adaptation of the model to different stress ratios

The stress ratio has an effect on the redistribution of the residual stresses, especially for $R_\sigma < 0$. Indeed, the surface layer of the material affected by shot peening will suffer yielding at a lower (absolute value) compressive applied stress than the bulk material due to the presence of the compressive residual stresses. When the applied stress will increase, the bulk material will then maintain the surface layer affected by shot peening into tension which will result in surface tensile residual stresses. The surface layer will then suffer yielding under a tensile applied stress lower then the bulk material. When the applied stress will decrease, the bulk material will maintain the surface layer in compression. This sequence will be repeated during each cycle. Zhuang and Halford (2001) showed that the surface residual stresses in shot peened Inconel 718 remained tensile after 20 cycles for $\sigma_{max} = 0.8\sigma_{y0.2\%}$, at $R_\sigma = -1$.

The effect of different stress ratios on the residual stresses redistribution could theoretically be predicted by the finite element model developed in the third article. However, for $R_\sigma < 0$, the simulation of one loading cycle might not be enough to characterized the residual stresses redistribution. An experimental campaign should be performed to study the residual stresses redistribution under different applied stress ratios. It would allow to further validate the finite element residual stresses redistribution model.

The crack propagation rates will also depend on the applied stress ratio. Short crack monitoring tests or long crack propagation tests should be performed at different stress ratios to obtain a relationship between the parameters A_2, m_2 and the applied load ratio. For experimental cost reduction purpose, the parameters A_2 and m_2 could also be adjusted by

fitting the model fatigue life prediction with fatigue experimental results obtained at different load ratios.

Adaptation of the model to different loading types

The applied loading type will have an effect on the residual stresses redistribution to the local stress ratio seen by the material. The residual stress relaxation could theoretically be predicted by the finite element model developed in the third article.

Bending and fully reverse bending fatigue would also have an influence on the crack initiation location and the fatigue life. Indeed, shot peening would not provide a 20 time improvement of the fatigue life since the crack initiation location would occur near or at the surface due to the through thickness applied stress gradient. The applied stress gradient could be simulated by changing the value of the applied stress, depending on the crack's tip depth, at each computation increment of the model. The parameters A_2 and m_2 should also be evolving depending on the local applied stress ratio.

CHAPTER 11 CONCLUSION AND RECOMMENDATIONS

In order to reduce the costs associated with the error and trial experimental campaigns performed to find optimal shot peening conditions, an analytical model that predicts the fatigue life and the crack initiation location in shot peened Inconel 718 was developed in this thesis. Its calibration and validation were based on experimental results obtained during an extensive experimental campaign.

The first step was to characterize Inconel 718 mechanical properties and behavior under fatigue loading. A large multi-scale experimental campaign was performed for this purpose. Unpeened and shot peened specimens crack initiation mechanisms, short crack propagation rates, fatigue lives and the effects of different edge geometries on the fatigue life were studied in both HCF and LCF. Cyclic yield tests were also performed to characterize the macroscopic mechanical behavior of Inconel 718 in strain controlled LCF. The main conclusions of this experimental campaign are:

- For the first time, it was shown that shot peening can increase the fatigue life up to twenty times in HCF on Inconel 718 cylindrical specimens tested under $R_\sigma = 0.1$ uniaxial loading conditions. In LCF, shot peening is detrimental or with no significant effects on fatigue life

- The shot peening intensity must be as low as possible to avoid the presence of a residual stress tensile peak and to minimize the surface roughness. However, it should be high enough to induce compressive residual stresses that will repel crack initiation below the specimen's surface in HCF. For the loading conditions and shot peening media used in this work, the ideal shot peening intensity might be below 4 A.

- Sharp edges are to be avoided on shot peened parts due to severe rolled edge formation during the shot peening process.

- Chamfered edges are equivalent to rounded ones, in terms of fatigue life, when shot peened. Rounded edges with larger radius than those used in the experimental campaign might prevent crack initiation from occurring at the edge surfaces and improve the fatigue life.

- For the first time, it was shown that the softening rate of Inconel 718 is solely dependent on the total accumulated plastic strain for 0.6 %$\leq \varepsilon_{max} \leq$ 2 % at $R_\varepsilon = -1$. It allows

to predict the cyclic stress-strain curves of a complex test using the data from a test performed at a constant strain amplitude.

The experimental results allowed to develop an analytical tool able to predict shot peened Inconel 718 fatigue life. For this purpose, the N-R propagation model and Chan's crack initiation model were coupled to allow fatigue life prediction in case of surface and subsurface crack initiations. Indeed, the underlying hypothesis of the N-R model is that a crack is inherently present in the material. However, in case of subsurface crack initiation this hypothesis is not validated. Chan's crack initiation model was, in this case, used to calculate the number of cycles to initiate a crack in a subsurface grain as it was the subsurface crack initiation mechanism experimentally observed. The N-R model could have then be used to predict the number of cycles to failure. For each loading and shot peening condition, different crack initiation depth were simulated. The crack initiation depth resulting in the shortest fatigue life was considered to be the weakest link in the material and thus the predicted crack initiation location. The N-R model was enhanced to account for the redistribution of the cold work and the residual stresses. Chan's crack initiation model was also modified to account for the redistributed residual stresses. The model developed in this thesis allowed, for the first time, to predict with accuracy the crack initiation location. The fatigue life predictions were in good agreement with the experimental results.

All in all, in addition to the extensive experimental campaign results, this thesis provides an analytical model able to predict the location of crack initiation and the fatigue life in unpeened and shot peened Inconel 718. The model can be used to optimize the shot peening process.

Recommendations for future studies

- **Extend the validity of the cyclic yield model to different strain ratios.**
  It would be interesting to perform cyclic yield tests at $R_\varepsilon \neq -1$ to enhance the cyclic yield model developed in this thesis and it could be used to simulate the material softening at the crack's tip. However, the simulation of the softening behavior at the crack's tip plastic zone will be highly challenging because the strain ratio is not constant in the plastic zone. Moreover, the softening would occur at a microstructural scale and the local strain in a grain will depend on its orientation, its size, the orientation of the surrounding grains and the distance from the crack's tip.

- **Model damage accumulation at twin boundaries.**
  The model developed in this thesis did not accurately predict the HCF fatigue life for the shot peening condition resulting in a residual stress tensile peak. This prediction could be enhanced by accounting for the local damage accumulation at twin boundaries due to the tensile residual stress peak relaxation during the first loading cycle.

- **More realistic approach on the stress concentration due to roughness.**
  Instead of assuming that the dimples have perfect rounded shapes, it would be interesting to develop a model able to predict the real surface stress concentration factors. One could, for example, perform a 3D mapping of the shot peened surface and reproduce it in a finite element model to extract the stress concentration factor.

- **Include rolled edge effects in the model.**
  The fatigue life prediction model could be improved by including the effects of the rolled edges. One could simulate the rolled edges with a finite element model and extract a stress concentration factor value.

- **Couple the model with a coupled discrete-finite element model.**
  The shot peening process and the fatigue test campaign could be simulated in its entirety by coupling the analytical model developed in this thesis with the discrete-finite element model developed by Tu *et al.* (2017).

- **Adapt the model to other loading condition.**
  As discussed in Section 10.2.3, the model could be adapted for other loading conditions. A residual stresses redistribution experimental campaign will be required at different applied stress ratio to further validate the residual stresses redistribution finite element model. The evolution of the parameters A_2 and m_2 depending on the applied load ratio should also be determined.

- **Adapt the model to high temperatures.**
  A major improvement of the model would be to adapt it to the high temperatures at which Inconel 718 parts are usually submitted. For this purpose, the model would have to be largely modified. Indeed, the crack initiation mechanisms would change (Connolley *et al.*, 2000), the short crack propagation rates would be decreased by the oxidation (Kawagoishi *et al.*, 2000) and the long crack propagation mechanism would be either transgranular, intragranular or mixed, depending on the loading frequency (Antunes *et al.*, 2000). The temperature would also have to be taken in account in the residual stresses redistribution model (Hoffmeister *et al.*, 2012).

- **Adapt the model to other materials.**
  The model developed in this thesis could be adapted to other materials. The crack initiation part of the model might have to be modified if different subsurface crack initiation mechanisms were at stake.

REFERENCES

Abramovich, F and Ritov, Y (2013). *Statistical theory: a concise introduction*. CRC Press.

Alexandre, F and Deyber, S and Pineau, A (2004). Modelling the optimum grain size on the low cycle fatigue life of a Ni based superalloy in the presence of two possible crack initiation sites. *Scripta materialia*, *50*(1), 25–30.

Antunes, FV and Ferreira, JM and Branco, CM (2000). High temperature fatigue crack growth in Inconel 718. *Materials at High Temperatures*, *17*(4), 439–448.

Armstrong, PJ and Frederick, CO (1966). *A mathematical representation of the multiaxial Bauschinger effect*. Central Electricity Generating Board and Berkeley Nuclear Laboratories, Research & Development Department.

ASTM Standard E09-09 (2009). Compression testing of metallic materials at room temperature.

ASTM Standard E384-11 (2011). Standard test method for Knoop and vickers hardness of materials.

ASTM Standard E466-07 (2007). Standard practice for conducting force controlled constant amplitude axial fatigue tests of metallic materials.

ASTM Standard E606M-12 (2012). Standard test method for strain-controlled fatigue testing.

ASTM Standard E647-13 (2013). Standard test measurement of fatigue crack growth rates.

ASTM Standard E8M-13a (2013). Standard test methods for tension testing of metallic materials.

Bagherifard, S and Fernandez-Pariente, I and Ghelichi, R and Guagliano, M (2014). Effect of severe shot peening on microstructure and fatigue strength of cast iron. *International Journal of Fatigue*, *65*, 64–70.

Bagherifard, S and Guagliano, M (2012). Fatigue behavior of a low-alloy steel with nanostructured surface obtained by severe shot peening. *Engineering Fracture Mechanics*, *81*, 56–68.

Bianchetti, C and Lévesque, M and Brochu, M (2017). Probabilistic analysis of the effect of shot peening on the high and low cycle fatigue behaviors of AA 7050-T7451. *Submitted to International Journal of Fatigue (November 2017)*.

Bilby, BA and Cottrell, AH and Smith, E and Swinden, KH (1964). Plastic yielding from sharp notches. *Proceedings of the Royal Society of London A: Mathematical, Physical and Engineering Sciences*. The Royal Society, vol. 279, 1–9.

Bilby, BA and Cottrell, AH and Swinden, KH (1963). The spread of plastic yield from a notch. *Proceedings of the Royal Society of London A: Mathematical, Physical and Engineering Sciences*. The Royal Society, vol. 272, 304–314.

Brochu, M and Verreman, Y and Ajersch, F and Bouchard, D (2010). High cycle fatigue strength of permanent mold and rheocast aluminum 357 alloy. *International Journal of Fatigue*, *32*(8), 1233–1242.

Buchanan, DJ and John, R (2014). Residual stress redistribution in shot peened samples subject to mechanical loading. *Materials Science and Engineering: A*, *615*, 70–78.

Cammett, JT and Prevéy, PS and Jayaraman, N (2005). The effect of shot peening coverage on residual stress, cold work, and fatigue in a nickel-base superalloy. Rapport technique, DTIC Document.

Chaboche, JL and Kanoute, P and Azzouz, F (2012). Cyclic inelastic constitutive equations and their impact on the fatigue life predictions. *International Journal of Plasticity*, *35*, 44–66.

Chaboche, JL and Rousselier, G (1983). On the plastic and viscoplastic constitutive equations - part I: Rules developed with internal variable concept. *Journal of Pressure Vessel Technology*, *105*(2), 153–158.

Chan, KS (2003). A microstructure-based fatigue-crack-initiation model. *Metallurgical and Materials Transactions A*, *34*(1), 43–58.

Chan, KS and Lankford, J (1983). A crack-tip strain model for the growth of small fatigue cracks. *Scripta Metallurgica*, *17*(4), 529–532.

Chen, Q and Kawagoishi, N and Nisitani, H (2000). Evaluation of fatigue crack growth rate and life prediction of Inconel 718 at room and elevated temperatures. *Materials Science and Engineering: A*, *277*(1), 250–257.

Chowdhury, PB and Sehitoglu, H and Rateick, RG (2014). Predicting fatigue resistance of nano-twinned materials: Part II–effective threshold stress intensity factor range. *International Journal of Fatigue*, *68*, 292–301.

Connolley, T and Starink, M and Reed, PAS (2000). Effect of oxidation on high temperature fatigue crack initiation and short crack growth in Inconel 718. *Superalloys*, 435–444.

Cook, TS (1982). Stress-strain behavior of Inconel 718 during low cycle fatigue. *Journal of Engineering Materials and Technology*, *104*(3), 186–191.

Cook, TS (1985). Effect of R_ϵ on cyclic stress-strain behavior of Inconel 718. *Journal of Testing and Evaluation*, *13*(6), 434–440.

Curtis, S and de los Rios, ER and Rodopoulos, CA and Levers, A (2003a). Analysis of the effects of controlled shot peening on fatigue damage of high strength aluminium alloys. *International journal of Fatigue*, *25*(1), 59–66.

Curtis, SA and Romero, J Solis and de los Rios, ER and Rodopoulos, CA and Levers, A (2003b). Predicting the interfaces between fatigue crack growth regimes in 7150-T651 aluminium alloy using the fatigue damage map. *Materials Science and Engineering: A*, *344*(1), 79–85.

de los Rios, ER and Navarro, A (1990). Considerations of grain orientation and work hardening on short-fatigue-crack modelling. *Philosophical Magazine A*, *61*(3), 435–449.

de los Rios, ER and Trull, M and Levers, A (2000). Modelling fatigue crack growth in shot-peened components of Al 2024-T351. *Fatigue & Fracture of Engineering Materials & Structures*, *23*(8), 709–716.

de los Rios, ER and Walley, A and Milan, MT and Hammersley, G (1995). Fatigue crack initiation and propagation on shot-peened surfaces in A316 stainless steel. *International Journal of Fatigue*, *17*(7), 493–499.

de los Rios, ER and Wu, XD and Miller, KJ (1996). A micro-mechanics model of corrosion-fatigue crack growth in steels. *Fatigue & Fracture of Engineering Materials & Structures*, *19*(11), 1383–1400.

Delbergue, D and Texier, D and Lévesque, M and Bocher, P (2017). Comparison of two X-ray residual stress measurement methods: Sin2 ψ and cos α, through the determination of a martensitic steel X-ray elastic constant. *Materials Research Proceedings*, *2*.

Dowling, NE (1977). Crack growth during low-cycle fatigue of smooth axial specimens. *Cyclic stress-strain and plastic deformation aspects of fatigue crack growth*, ASTM International.

Dowling, NE (2013). *Mechanical behavior of materials (4^{th}Edition): Engineering methods for deformation, fracture, and fatigue*. Pearson.

El Haddad, MH and Smith, KN and Topper, TH (1979). A strain based intensity factor solution for short fatigue cracks initiating from notches. *Fracture Mechanics: Proceedings of the Eleventh National Symposium on Fracture Mechanics: Part I*. ASTM International.

Fournier, D and Pineau, A (1977). Low cycle fatigue behavior of Inconel 718 at 298 K and 823 K. *Metallurgical Transactions A*, *8*(7), 1095–1105.

Gale, WF and Totemeier, TC (2003). *Smithells metals reference book (8^{th} edition)*. Butterworth-Heinemann.

Gao, YK and Wu, XR (2011). Experimental investigation and fatigue life prediction for 7475-T7351 aluminum alloy with and without shot peening-induced residual stresses. *Acta Materialia*, *59*(9), 3737–3747.

Gao, YK and Yao, M and Li, JK (2002). An analysis of residual stress fields caused by shot peening. *Metallurgical and Materials Transactions A*, *33*(6), 1775–1778.

Goodall, IW and Hales, R and Walters, DJ (1981). *On constitutive relations and failure criteria of an austenitic steel under cyclic loading at elevated temperature*. Springer.

Goodman, J (1918). *Mechanics applied to engineering*. Longmans, Green.

Hales, R and Holdsworth, SR and O'Donnell, MP and Perrin, IJ and Skelton, RP (2002). A code of practice for the determination of cyclic stress-strain data. *Materials at high temperatures*, *19*(4), 165–185.

He, BY and Soady, KA and Mellor, BG and Morris, A and Reed, PAS (2013). Effects of shot peening on short crack growth rate and resulting low cycle fatigue behaviour in low pressure turbine blade material. *Materials Science and Technology*, *29*(7), 788–796.

Hobson, PD (1982). The formulation of a crack growth equation for short cracks. *Fatigue & Fracture of Engineering Materials & Structures*, *5*(4), 323–327.

Hoffmeister, J and Schulze, V and Hessert, R and Koenig, G (2012). Residual stresses under quasi-static and cyclic loading in shot peened Inconel 718. *International Journal of Materials Research*, *103*(1), 66–72.

Hussain, K (1997). Short fatigue crack behaviour and analytical models: a review. *Engineering Fracture Mechanics*, *58*(4), 327–354.

Irwin, GR (1957). Analysis of stresses and strains near the end of a crack traversing a plate. *Journal of applied mechanics*, *24*(3), 361–364.

Iyer, SK and Lissenden, CJ (2000). Inelastic anisotropy of Inconel 718: Experiments and mathematical representation. *Journal of engineering materials and technology*, *122*(3), 321–326.

Iyer, SK and Lissenden, CJ (2003). Multiaxial constitutive model accounting for the strength-differential in Inconel 718. *International Journal of Plasticity*, *19*(12), 2055–2081.

Kawagoishi, N and Chen, Q and Nisitani, H (2000). Fatigue strength of Inconel 718 at elevated temperatures. *Fatigue and Fracture of Engineering Materials and Structures*, *23*(3), 209–216.

Keller, R and Zielinski, W and Gerberich, WW (1989). On the onset of low-energy dislocation substructures in fatigue: grain size effects. *Materials Science and Engineering: A*, *113*, 267–280.

Kirk, D (1987). Effects of plastic straining on residual stresses induced by shot-peening. *Shot Peening: Science, Technology*, 213–220.

Klotz, T and Blas, S and Lévesque, M and Brochu, M (2017). 1D cyclic yield model independent of load spectrum characteristics and its application to Inconel 718. *Mechanics of Materials*, *109*, 34–41.

Klotz, T and Delbergue, D and Bocher, P and Lévesque, M and Brochu, M (2018a). Surface characteristics and fatigue behavior of shot peened Inconel 718. *International Journal of Fatigue*, *110*, 10–21.

Klotz, T and Miao, HY and Bianchetti, C and Lévesque, M and Brochu, M (2018b). Analytical fatigue life prediction of shot peened Inconel 718. *Submitted to International Journal of Fatigue (January 2018)*.

Landgraf, RW and Morrow, JD and Endo, T (1969). Determination of the cyclic stress-strain curve. *J MATER*, *4*(1), 176–188.

Lara, A and Picas, I and Casellas, D (2013). Effect of the cutting process on the fatigue behaviour of press hardened and high strength dual phase steels. *Journal of Materials Processing Technology*, *213*(11), 1908–1919.

Lemaitre, J and Chaboche, JL and Benallal, A and Desmorat, R (2009). *Mécanique des matériaux solides*. Dunod.

Li, JK and Mei, Y and Duo, W and Renzhi, W (1992). An analysis of stress concentrations caused by shot peening and its application in predicting fatigue strength. *Fatigue & Fracture of Engineering Materials & Structures*, *15*(12), 1271–1279.

Liu, JL and Umemoto, M and Todaka, Y and Tsuchiya, K (2007). Formation of a nanocrystalline surface layer on steels by air blast shot peening. *Journal of materials science*, *42*(18), 7716–7720.

Ma, XF and Duan, Z and Shi, HJ and Murai, R and Yanagisawa, E (2010). Fatigue and fracture behavior of nickel-based superalloy Inconel 718 up to the very high cycle regime. *Journal of Zhejiang University-Science A*, *11*(10), 727–737.

Madariaga, A and Esnaola, JA and Arrazola, PJ and Ruiz-Hervias, J and Muñoz, P and Ostolaza, K (2015). Stability of machining induced residual stresses in Inconel 718 under quasi-static loading at room temperature. *Materials Science and Engineering: A*, *620*, 129–139.

Maderbacher, H and Oberwinkler, B and Gänser, HP and Tan, W and Rollett, M and Stoschka, M (2013). The influence of microstructure and operating temperature on the fatigue endurance of hot forged *Inconel*® 718 components. *Materials Science and Engineering: A*, *585*, 123–131.

McClung, RC (2007). A literature survey on the stability and significance of residual stresses during fatigue. *Fatigue & Fracture of Engineering Materials & Structures*, *30*(3), 173–205.

McEvily, AJ and Eifler, D and Macherauch, E (1991). An analysis of the growth of short fatigue cracks. *Engineering Fracture Mechanics*, *40*(3), 571–584.

Meguid, SA and Maricic, LA (2015). Finite element modeling of shot peening residual stress relaxation in turbine disk assemblies. *Journal of Engineering Materials and Technology*, *137*(3), 031003.

Menig, R and Pintschovius, L and Schulze, V and Vöhringer, O (2001). Depth profiles of macro residual stresses in thin shot peened steel plates determined by X-ray and neutron diffraction. *Scripta Materialia*, *45*(8), 977–983.

Merrick, HF (1974). The low cycle fatigue of three wrought nickel-base alloys. *Metallurgical Transactions*, *5*(4), 891–897.

Miao, J and Pollock, TM and Jones, JW (2009). Crystallographic fatigue crack initiation in nickel-based superalloy rené 88DT at elevated temperature. *Acta Materialia*, *57*(20), 5964–5974.

Miao, J and Pollock, TM and Jones, JW (2012). Microstructural extremes and the transition from fatigue crack initiation to small crack growth in a polycrystalline nickel-base superalloy. *Acta Materialia*, *60*(6), 2840–2854.

Miller, KJ (1993). Materials science perspective of metal fatigue resistance. *Materials Science and Technology*, *9*(6), 453–462.

Mills, WL and Brown, CM (2001). Fatigue fracture surface morphology for alloy 718. *Superalloys*, *718*, 625–706.

Moore, M.G and Evans, W.P (1958). Mathematical correction for stress in removed layers in X-ray diffraction residual stress analysis. Rapport technique, SAE Technical Paper.

Morino, K and Kawagoishi, N and Chen, Q and Matsuyama, Y and Nakamura, Y (2007). Fatigue crack growth resistance in ni-base super alloy. *Key Engineering Materials*. Trans Tech Publ, vol. 348, 541–544.

Nakamura, H and Takanashi, M and Itabashi, Y and Kuroki, H and Ueda, Y (2011). Shot peening effect on low cycle fatigue properties of Ti-6Al-4V and Inconel 718. *ASME 2011 Turbo Expo: Turbine Technical Conference and Exposition*. American Society of Mechanical Engineers, 791–797.

Navarro, A and de los Rios, ER (1987). A model for short fatigue crack propagation with an interpretation of the short-long crack transition. *Fatigue & Fracture of Engineering Materials & Structures*, *10*(2), 169–186.

Navarro, A and de los Rios, ER (1988a). An alternative model of the blocking of dislocations at grain boundaries. *Philosophical Magazine A*, *57*(1), 37–42.

Navarro, A and de los Rios, ER (1988b). Compact solution for a multizone BCS crack model with bounded or unbounded end conditions. *Philosophical Magazine A*, *57*(1), 43–50.

Navarro, A and de los Rios, ER (1988c). A microstructurally-short fatigue crack growth equation. *Fatigue & Fracture of Engineering Materials & Structures*, *11*(5), 383–396.

Navarro, A and de los Rios, ER (1988d). Short and long fatigue crack growth: a unified model. *Philosophical Magazine A*, *57*(1), 15–36.

Navarro, A and de los Rios, ER (1992). Fatigue crack growth modelling by successive blocking of dislocations. *Proceedings of the Royal Society of London A: Mathematical, Physical and Engineering Sciences*. The Royal Society, vol. 437, 375–390.

Navarro, A and Vallellano, C and de los Rios, ER and Xin, XJ (1999). Notch sensitivity and size effects described by a short crack propagation model. *Engineering against fatigue*, 63–72.

Nisitani, H (1981). Unifying treatment of fatigue crack growth laws in small, large and non-propagating cracks. *Mechanics of Fatigue, ASME AMD (Edited by T. Mura)*, *47*, 151–166.

Novovic, D and Dewes, R.C and Aspinwall, D.K and Voice, W and Bowen, P (2004). The effect of machined topography and integrity on fatigue life. *International Journal of Machine Tools and Manufacture*, *44*(2), 125–134.

Noyan, IC and Cohen, JB (2013). *Residual stress: measurement by diffraction and interpretation*. Springer.

Ono, Y and Yuri, T and Sumiyoshi, H and Takeuchi, E and Matsuoka, S and Ogata, T (2004). High-cycle fatigue properties at cryogenic temperatures in INCONEL 718 nickel-based superalloy. *Materials Transactions*, *45*(2), 342–345.

Paris, P and Erdogan, F (1963). A critical analysis of crack propagation laws. *Journal of basic engineering*, *85*(4), 528–533.

Pessoa, D and Grigorescu, A and Herwig, P and Wetzig, A and Zimmermann, M (2016). Influence of notch effects created by laser cutting process on fatigue behavior of metastable austenitic stainless steel. *Procedia Engineering*, *160*, 175–182.

Polak, J and Hajek, M (1991). Cyclic stress-strain curve evaluation using incremental step test procedure. *International journal of Fatigue*, *13*(3), 216–222.

Prevéy, PS (1987). The measurement of subsurface residual stress and cold work distributions in nickel base alloys. *Residual Stress in Design, Process and Materials Selection, WB Young, ed., ASME, Metals Park, OH*, 11–19.

Prevéy, PS (2000). The effect of cold work on the thermal stability of residual compression in surface enhanced IN718. Rapport technique, DTIC Document.

Riemelmoser, FO and Pippan, R (2002). Consideration of the mechanical behaviour of small fatigue cracks. *International journal of fracture*, *118*(3), 251–270.

Ritchie, RO and Lankford, J (1986). Small fatigue cracks: a statement of the problem and potential solutions. *Materials Science and Engineering*, *84*, 11–16.

SAE-Aerospace (2009). Nickel alloy, corrosion and heat-resistant, bars, forgings, and rings 52.5Ni-19Cr-3.0Mo-5.1Cb(Nb)-0.90Ti-0.50Al-18Fe consumable electrode or vacuum induction melted 1775°F (968°C) solution and precipitation heat treated.

SAE AMS2430T (2015). Shot peening, automatic.

Sangid, MD (2013). The physics of fatigue crack initiation. *International journal of Fatigue*, *57*, 58–72.

Sasaki, T and Hirose, Y and Sasaki, K and Yasukawa, S (1997). Influence of image processing conditions of debye scherrer ring images in x-ray stress measurement using an imaging plate. *Adv X-ray Anal*, *40*, 588–594.

Sato, M and Tsuji, N and Minamino, Y and Koizumi, Y (2004). Formation of nanocrystalline surface layers in various metallic materials by near surface severe plastic deformation. *Science and Technology of Advanced Materials*, *5*(1-2), 145–152.

Smith, James Ohrea (1942). The effect of range of stress on the fatigue strength of metals. Rapport technique, University of Illinois at Urbana Champaign, College of Engineering. Engineering Experiment Station.

Solis, JR (2002). *Optimisation of the shot peening process in terms of fatigue resistance*. Thèse de doctorat, University of Sheffield.

Solis, J and Oseguera-Peña, J and Betancourt, I (2009). Short crack propagation model applied to shot peened aluminium alloys. *Advanced Materials Research*. Trans Tech Publ, vol. 65, 53–61.

Stinville, JC and Lenthe, WC and Miao, J and Pollock, TM (2016). A combined grain scale elastic–plastic criterion for identification of fatigue crack initiation sites in a twin containing polycrystalline nickel-base superalloy. *Acta Materialia*, *103*, 461–473.

Stinville, JC and Vanderesse, N and Bridier, F and Bocher, P and Pollock, TM (2015). High resolution mapping of strain localization near twin boundaries in a nickel-based superalloy. *Acta Materialia*, *98*, 29–42.

Sudarshan Rao, G and Sharma, VMJ and Thomas Tharian, K and Ramesh Narayanan, P and Sreekumar, K and Sinha, Parameshwar Prasad (2012). Study of LCF behavior of

IN718 superalloy at room temperature. *Materials Science Forum*. Trans Tech Publ, vol. 710, 445–450.

Suresh, SO and Ritchie, RO (1984). Propagation of short fatigue cracks. *International Metals Reviews*, *29*(1), 445–475.

Tanaka, K and Akiniwa, Y and Nakai, Y and Wei, RP (1986). Modelling of small fatigue crack growth interacting with grain boundary. *Engineering Fracture Mechanics*, *24*(6), 803–819.

Tanaka, K and Mura, T (1981). A dislocation model for fatigue crack initiation. *Journal of Applied Mechanics(Transactions of the ASME)*, *48*(1), 97–103.

Texier, D and Cormier, J and Villechaise, P and Stinville, JC and Torbet, CJ and Pierret, S and Pollock, TM (2016). Crack initiation sensitivity of wrought direct aged alloy 718 in the very high cycle fatigue regime: the role of non-metallic inclusions. *Materials Science and Engineering: A*, *678*, 122–136.

Tong, J and Zhan, ZL and Vermeulen, B (2004). Modelling of cyclic plasticity and viscoplasticity of a nickel-based alloy using chaboche constitutive equations. *International journal of Fatigue*, *26*(8), 829–837.

Tu, F and Delbergue, D and Miao, HY and Klotz, T and Brochu, M and Bocher, P and Levesque, M (2017). A sequential DEM–FEM coupling method for shot peening simulation. *Surface and Coatings Technology*, *319*, 200–212.

Vallellano, C (1999). *Crecimiento de grietas pequeñas por fatiga en componentes con concentradores de tensión*. Thèse de doctorat, PhD thesis, University of Seville.

Vallellano, C and Navarro, A and Dominguez, J (2000a). Fatigue crack growth threshold conditions at notches. part i: theory. *Fatigue and Fracture of Engineering Materials and Structures*, *23*(2), 113–122.

Vallellano, C and Navarro, A and Dominguez, J (2000b). Fatigue crack growth threshold conditions at notches. part ii: generalization and application to experimental results. *Fatigue and Fracture of Engineering Materials and Structures*, *23*(2), 123–128.

Vallellano, C and Navarro, A and Dominguez, J (2013). Two-parameter fatigue crack growth driving force: Successive blocking of the monotonic and cyclic plastic zones at microstructural barriers. *International Journal of Fatigue*, *46*, 27–34.

Vallellano, C and Vazquez, J and Navarro, A and Dominguez, J (2009). A micromechanical model for small fatigue crack growth: an approach based on two threshold conditions. *Fatigue & Fracture of Engineering Materials & Structures*, *32*(6), 515–524.

Wagner, L (1999). Mechanical surface treatments on titanium, aluminum and magnesium alloys. *Materials Science and Engineering: A*, *263*(2), 210–216.

Warren, BE (1969). X-ray diffraction. *Courier Corporation*.

Xiao, L and Chaturvedi, MC and Chen, DL (2005). Low-cycle fatigue behavior of INCONEL 718 superalloy with different concentrations of boron at room temperature. *Metallurgical and materials Transactions A*, *36*(10), 2671–2684.

Xiao, L and Chen, DL and Chaturvedi, MC (2008). Cyclic deformation mechanisms of precipitation-hardened Inconel 718 superalloy. *Materials Science and Engineering: A*, *483*, 369–372.

Xin, XJ and de los Rios, ER and Navarro, A (1990). Modelling strain hardening at short fatigue cracks. *Short Fatigue Cracks*, 369–389.

You, Chao and Achintha, Mithila and Soady, KA and Reed, PAS (2017). Low cycle fatigue life prediction in shot-peened components of different geometries–part II: life prediction. *Fatigue & Fracture of Engineering Materials & Structures*, *40*(5), 749–760.

Zaleski, K and Skoczylas, A and Brzozowska, M (2017). The effect of the conditions of shot peening the Inconel 718 nickel alloy on the geometrical structure of the surface. *Advances in Science and Technology Research Journal*, *11*(2), 205–211.

Zhan, ZL and Tong, J (2007). A study of cyclic plasticity and viscoplasticity in a new nickel-based superalloy using unified constitutive equations. Part I: Evaluation and determination of material parameters. *Mechanics of materials*, *39*(1), 64–72.

Zhao, LG and Tong, J and Vermeulen, B and Byrne, J (2001). On the uniaxial mechanical behaviour of an advanced nickel base superalloy at high temperature. *Mechanics of materials*, *33*(10), 593–600.

Zhou, JM and Bushlya, V and Stahl, JE (2012). An investigation of surface damage in the high speed turning of Inconel 718 with use of whisker reinforced ceramic tools. *Journal of Materials Processing Technology*, *212*(2), 372–384.

Zhuang, WZ and Halford, GR (2001). Investigation of residual stress relaxation under cyclic load. *International Journal of Fatigue*, *23*, 31–37.

APPENDIX A AUTHOR'S CONTRIBUTIONS

A.1 Published papers

Klotz, T., Blas S., Lévesque, M. and Brochu, M. *1D cyclic yield model independent of load spectrum and its application to Inconel 718.* Mechanics of Materials, 2017.

Tu, F., Delbergue, D., Miao, H.Y., Klotz, T., Brochu, M., Bocher, P. and Lévesque, M. *A sequential DEM-FEM coupling method for shot peening simulation.* Surface and Coatings Technology, 2017.

Klotz, T., Delbergue, D., Bocher, P., Lévesque, M. and Brochu, M. *Surface characteristics and fatigue behavior of shot peened Inconel 718.* International Journal of Fatigue, 2018.

A.2 Submitted papers

Fubin, T., Delbergue, D., Klotz, T., Bag, A., Bianchetti, C., Brochu, M., Bocher, P. and Lévesque, M. *Discrete element-periodic cell coupling model and investigations on shot stream expansion, Almen intensities and target materials.* Submitted to International Journal of Mechanical Sciences on November 8$^{\text{th}}$, 2017.

Klotz, T., Miao, H.Y., Bianchetti., C., Lévesque, M. and Brochu, M. *Analytical fatigue life prediction of shot peened Inconel 718.* Submitted to the International Journal of Fatigue on January 4$^{\text{th}}$, 2018.

Klotz, T., Lévesque, M. and Brochu, M. *Effects of rolled edges on the fatigue life of shot peened Inconel 718.* Submitted to the Journal of Materials Processing Technology on February 13$^{\text{th}}$, 2018.

A.3 To be submitted papers

Tu, F., Zheng, R., Klotz, T., Castro Moreno, A., Miao, H.Y. and Lévesque, M. *Rolled edge prediction for shot peening on non-flat IN718 parts.*

Castro Moreno, A., Zheng, R., Gao, J., Klotz, T., Bocher, P., Chromik, R. and Lévesque, M. *On the crystal plasticity identification: From low to high strain rate using different length scales tests.*

A.4 Conference papers

Klotz, T., Delbergue, D., Bocher, P., Lévesque M. and Brochu M. *Analytical fatigue life prediction of shot peened Inconel 718.* Proceedings, 13th International Conference on Shot Peening, 2017.

Miao, H.Y., Tu, F., Delbergue, D., Bianchetti, C., Klotz, T., Bag, A. and Lévesque, M. *Shot peening DEM-FEM simulation considering shot stream expansion, peening intensity and target materials.* Proceedings, 13th International Conference on Shot Peening, 2017.

Miao, H.Y., Klotz, T., Delbergue, D. and Lévesque M. *Finite element simulation of shot peened residual stress relaxation under low and high cycle fatigue loadings.* Proceedings, 13th International Conference on Shot Peening, 2017.

A.5 Conference poster

Klotz, T., Blas, S., Lévesque, M. and Brochu, M. *Modelling of Inconel 718 crack tip's plastic zone softening during crack propagation.* Conference of Metallurgists, 2015.

A.6 Awards

Best student scientific poster, Conference of Metallurgists, 2015.

Best student paper and oral presentation, 13th International Conference on Shot Peening, 2017.

APPENDIX B LONG CRACK GROWTH RATES MEASUREMENTS

Measurements of fatigue long crack growth rates in rupture mode I were achieved in agreement with ASTM Standard E647-13 (2013). Two compact test (CT) specimens similar to that presented in Figure C.5 were used (CT 1 and CT 2). The CT specimens were machined from a 90 mm diameter bar. The crack size was estimated with the compliance method. The tests were performed at $R_\sigma = 0.1$.

As it can be observed in Figure B.1, the Paris relation can be expressed as

$$\frac{\mathrm{d}a}{\mathrm{d}N} = 3.45 \times 10^{-12} \Delta K^{3.12} \tag{B.1}$$

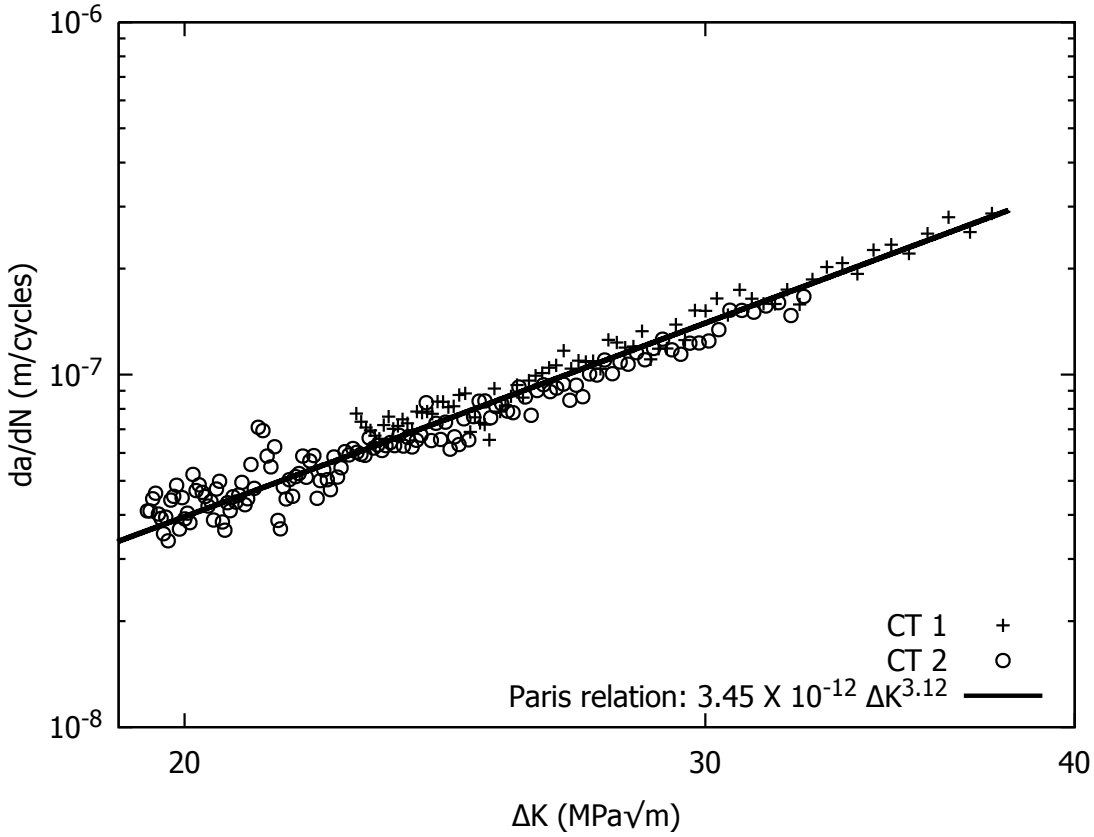

Figure B.1 Long crack growth rate measurements on two CT specimens

APPENDIX C TECHNICAL DRAWINGS

This appendix presents the technical drawings of the specimens used in the project. These technical drawings were sent to Pratt & Whitney Canada for machining.

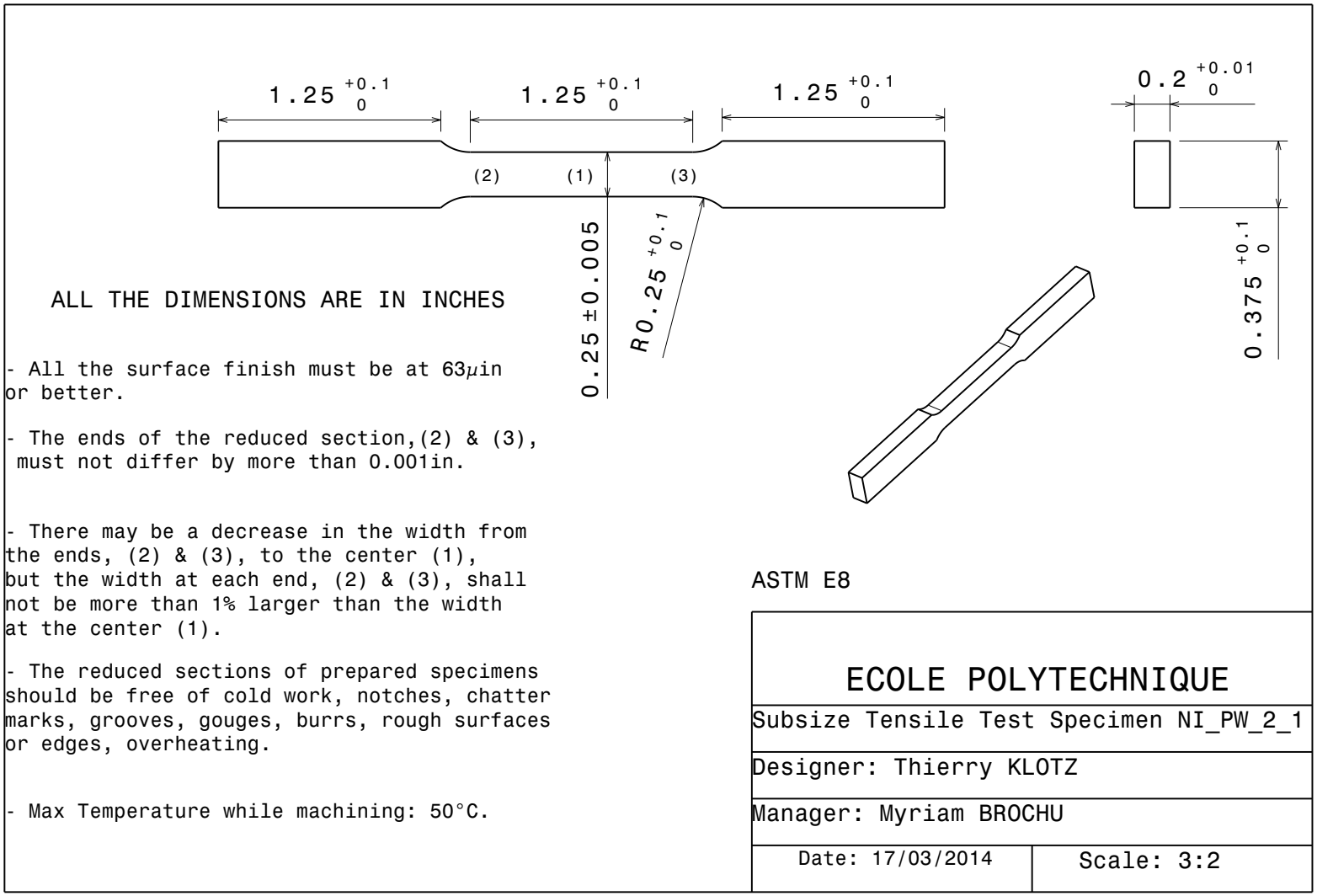

Figure C.1 Tensile test specimen

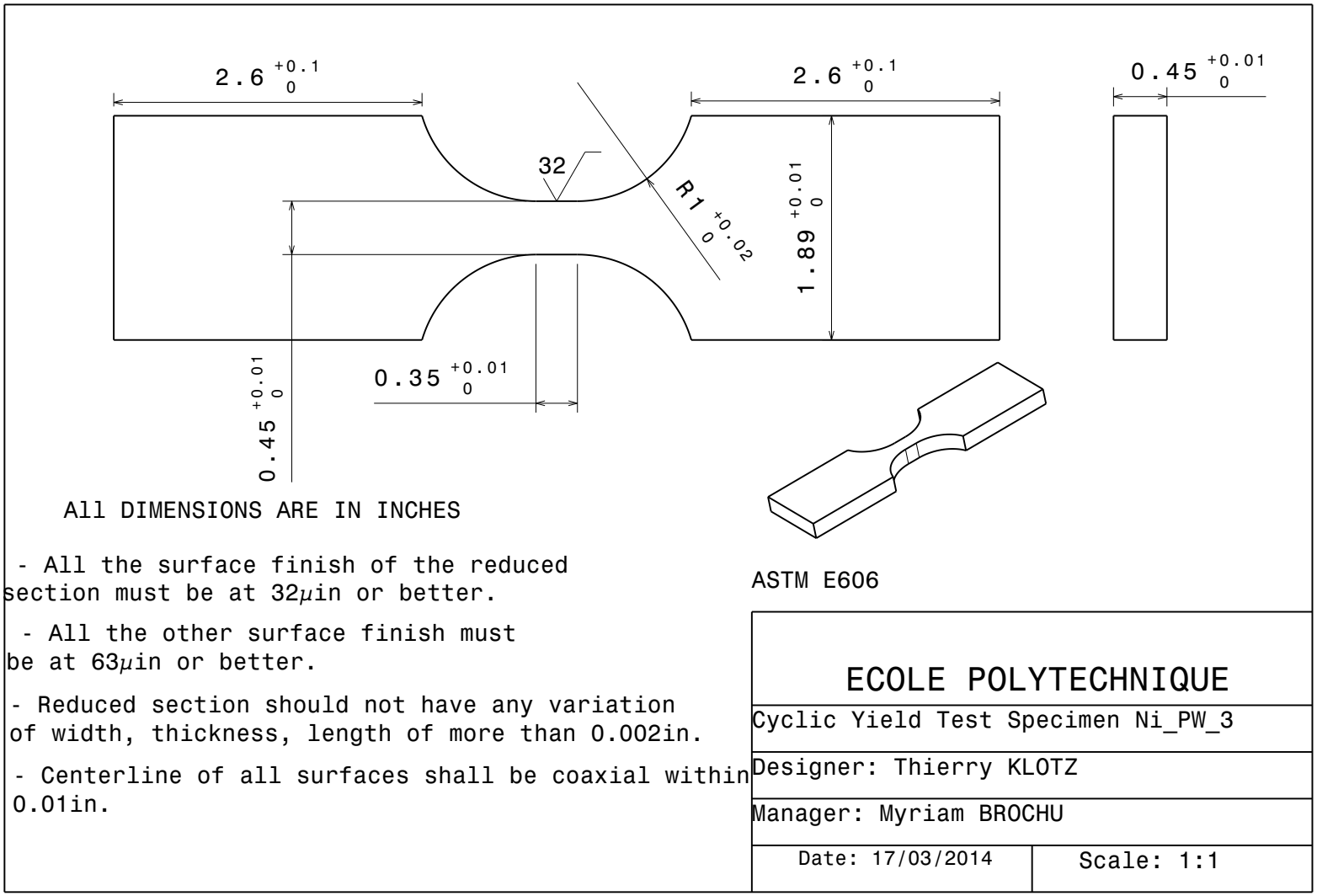

Figure C.2 Cyclic yield specimen

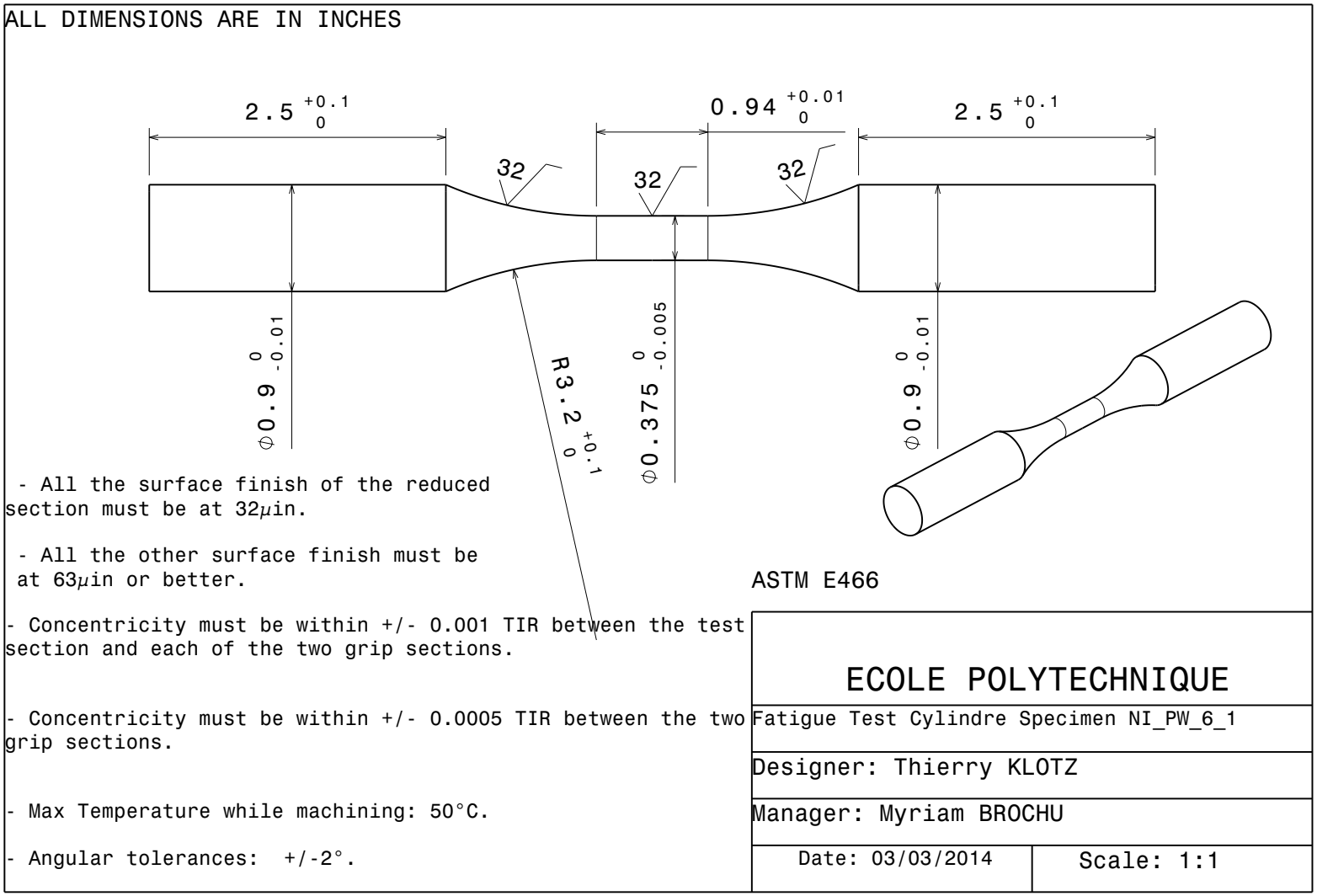

Figure C.3 Cylindrical fatigue specimen

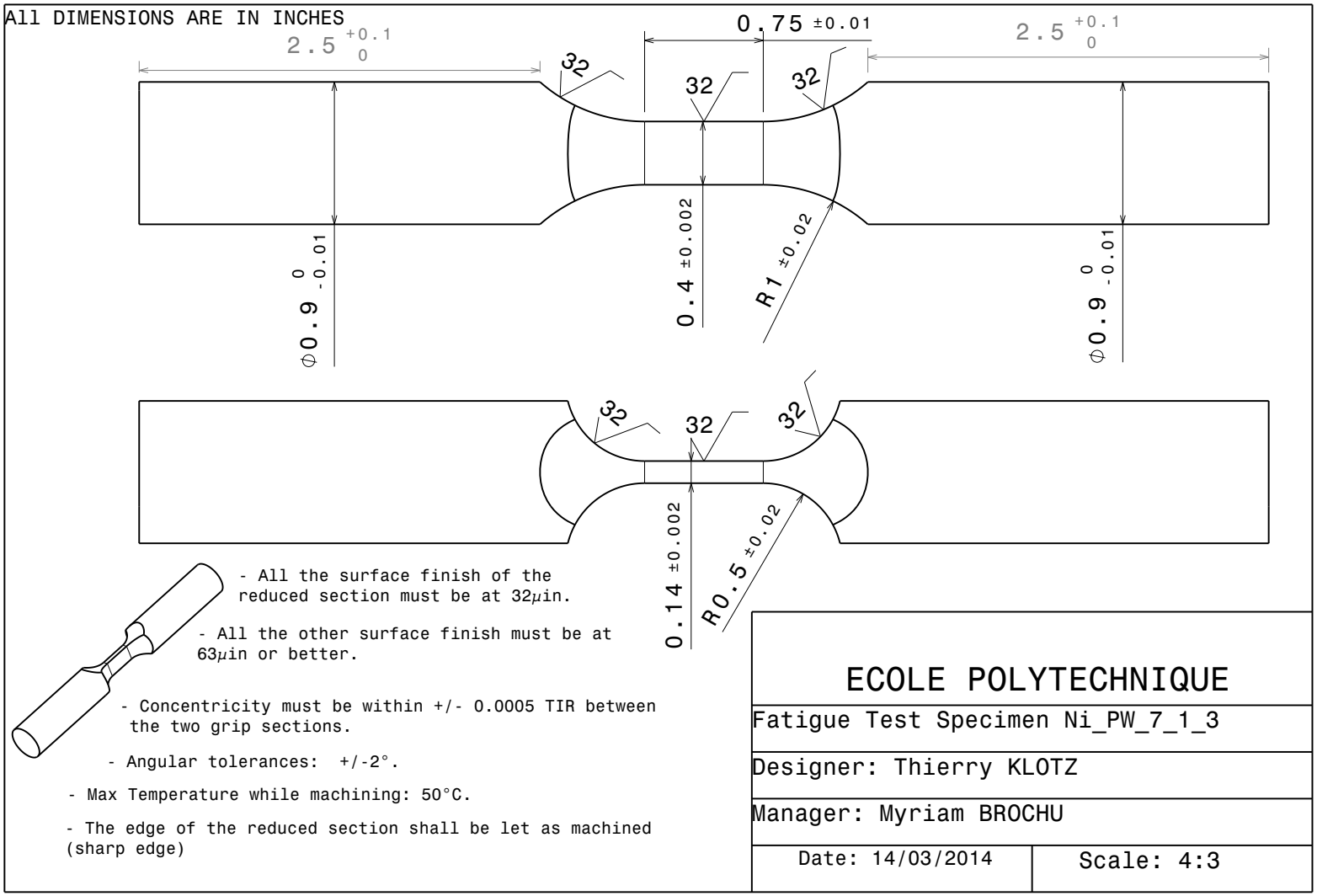

Figure C.4 Rectangular fatigue specimen

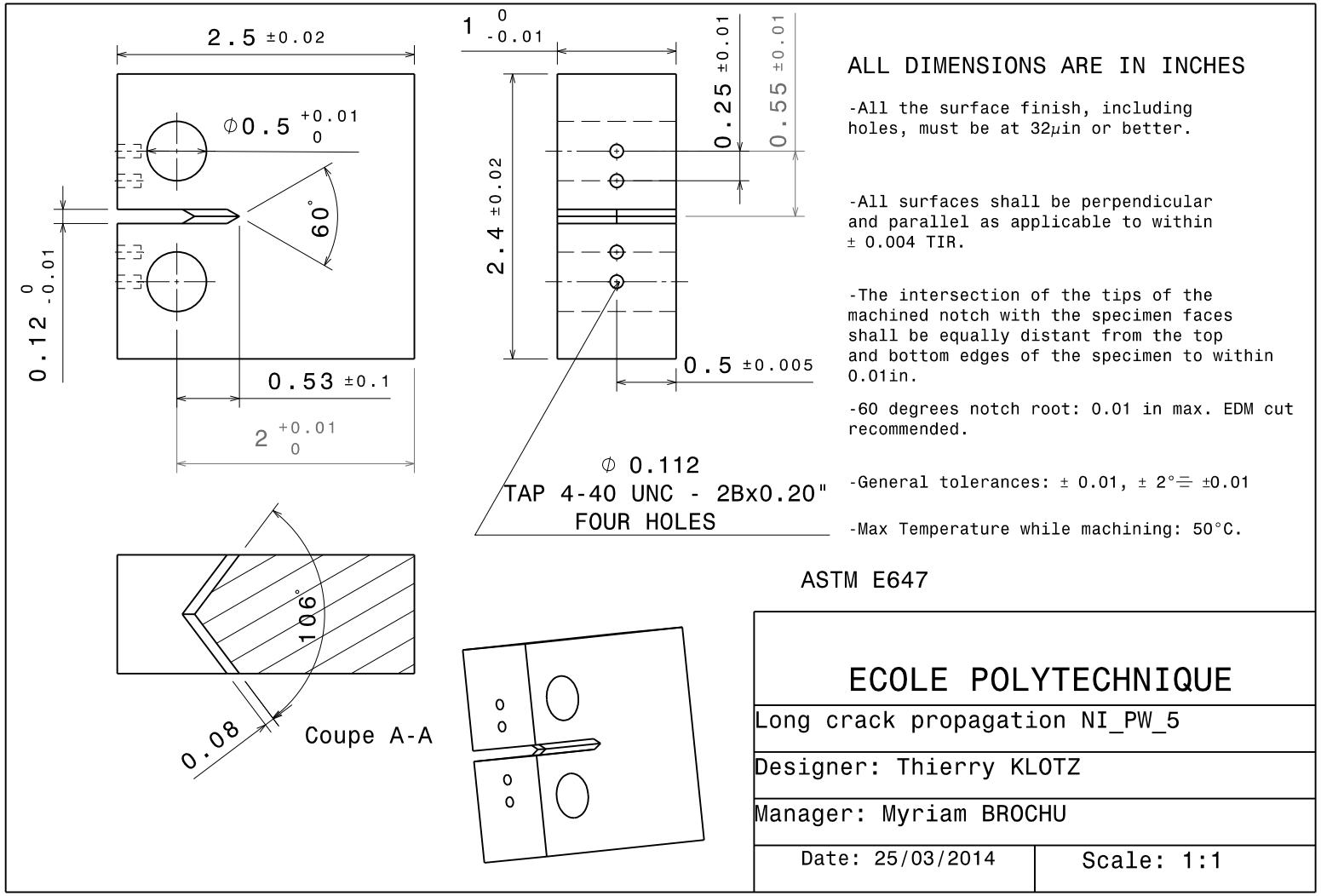

Figure C.5 Compact test (CT) specimen

APPENDIX D SHOT PEENING PROCEDURE

This is the shot peening procedure developed by the author of the thesis in agreement with AMS2430T standard. The guidance of John Quinn from Bell Helicopter was very helpful. This exact procedure was the one used on the cylindrical specimens shot peened with the S230 shot peening media at an Almen intensity of 4 A.

MANU508 F-Ni

École Polytechnique de Montréal

Shot peening: Inconel 718 cylindrical fatigue samples

Process parameters sheet following AMS2430T

Media: S230

Intensity: 4 A

Coverage: 98 %

Thierry KLOTZ

September 26, 2015

D.1 Peening parameters

D.1.1 Shot peening machine

The shot peening machine is located at:

Centre technologique en aérospatiale (CTA)
5555, place de la Savane
Saint-Hubert J3Y 8Y9 Québec, Canada
(450) 678-2001
cta@cegepmontpetit.ca

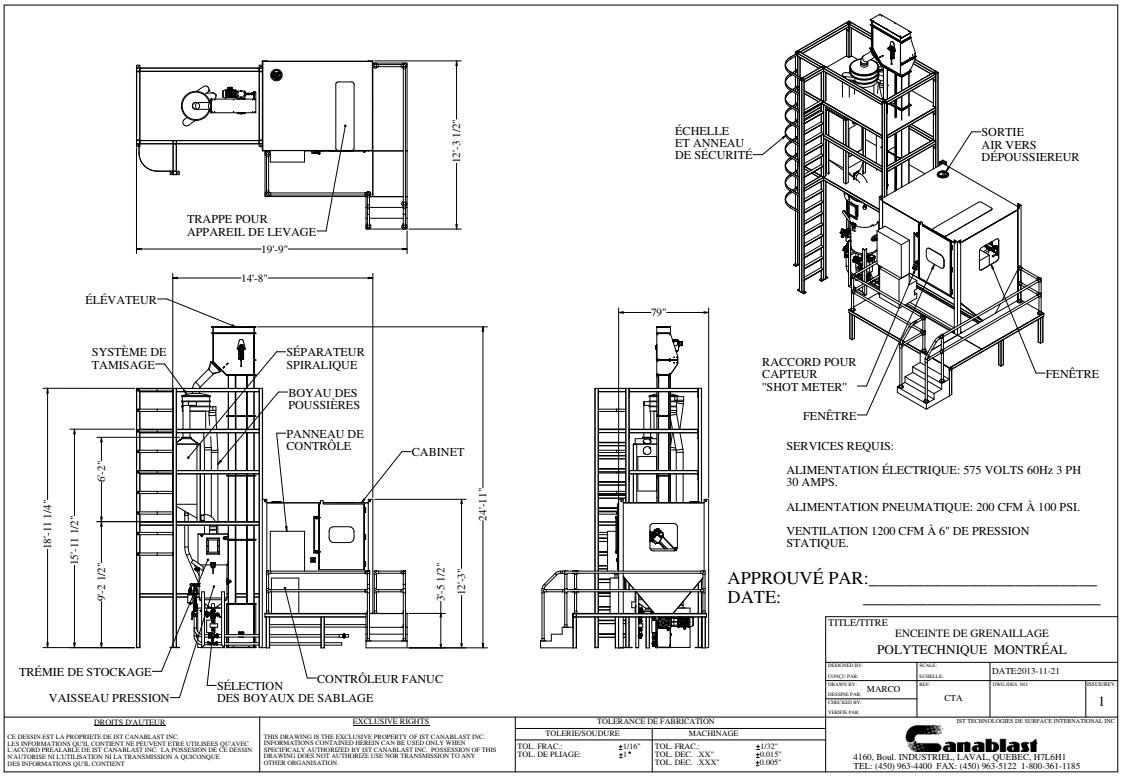

Figure D.1 Overall view of the shot peening machine

Table D.1 Shot peening machine description

Model	Serial number	Type
Peening machine CANABLAST		
Enceinte de grenaillage Polytechnique Montréal	2693	-
Robot FANUC		
M-20iA	R12Y01306	A05B-1222-B202
Controller		
R-30iB	E12Y30008	A05B-2611-B322
Rotating table		
FANUC 1-axis Servo Positioner	R13110359	A05B-1220-J103
Holders		
General holder	PF-444066	-
Almen holder	PA1-7529	-
Samples holder	-	-
Shotmeter (Calibration: 2013-12-20 (12 measured points) ±1.5%)		
SM-HEAD-G3	0060	-
SM-CONTROLLER-G3	0060	-
Almen gage		
TSP-3 Rev. B	4394	-
Almen gage numerical indicator		
2032440	1412550	-
RoTap machine		
RX-29	10-4931	-

D.1.2 Shot peening parameters

Table D.2 Shot peening parameters

Parameter	Value
Media	S230 (AMS2431/2E)
Strips	A
Intensity	4 A
Coverage	98 %
Stand-off distance	12 in
Pressure	8.1 psi
Massflow	30 lb/min
Table rotation speed	22 rpm
Robot speed	22 mm/s
Nozzle type	Straight-Bore
Nozzle diameter	0.5 in
Nozzle length	3.25 in
Almen intensity program	X_ALMEN_12IN
Samples peening program	X_CTM
Shot meter program	X_SHOTMETER_12IN

D.1.3 Samples

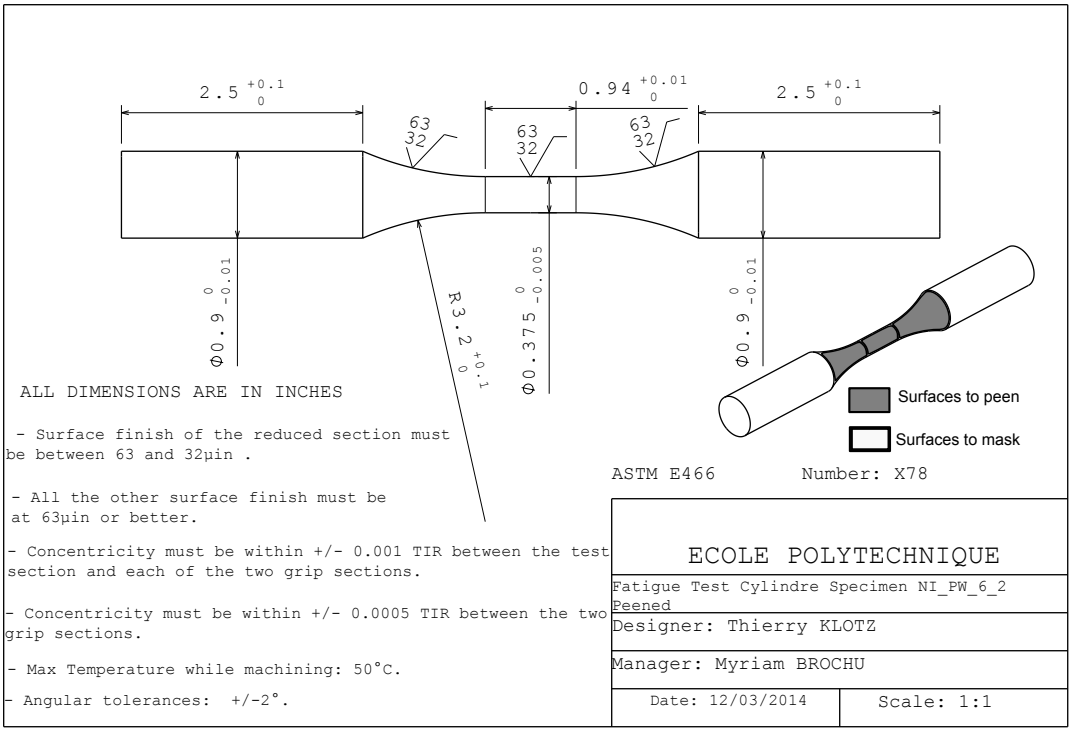

Figure D.2 Samples to peen

Table D.3 Samples properties

Material	Inconel 718
Tensile strength	1410 MPa
Yield strength	1150 MPa
Hardness	43 HRC

D.1.4 Peening trajectory

Intensity measurement trajectory

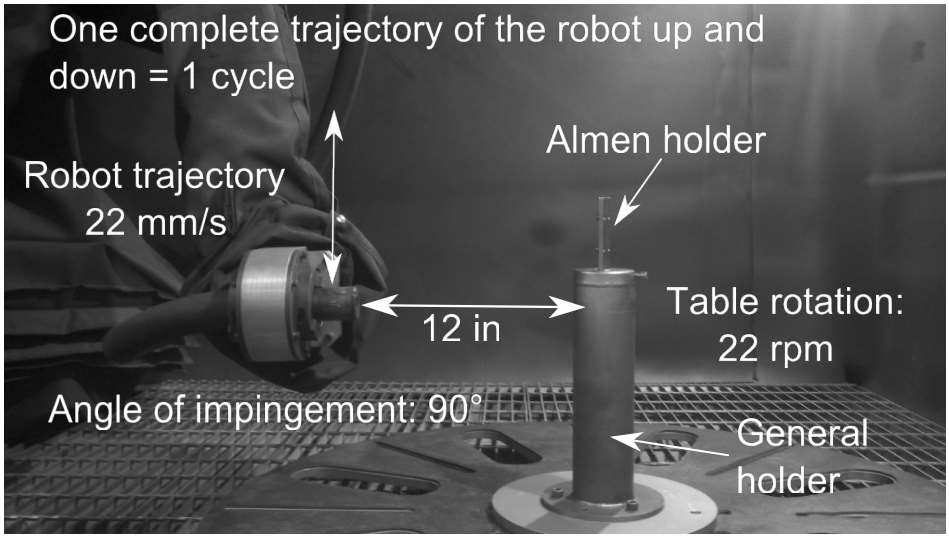

Figure D.3 Intensity measurement trajectory

Samples peening trajectory

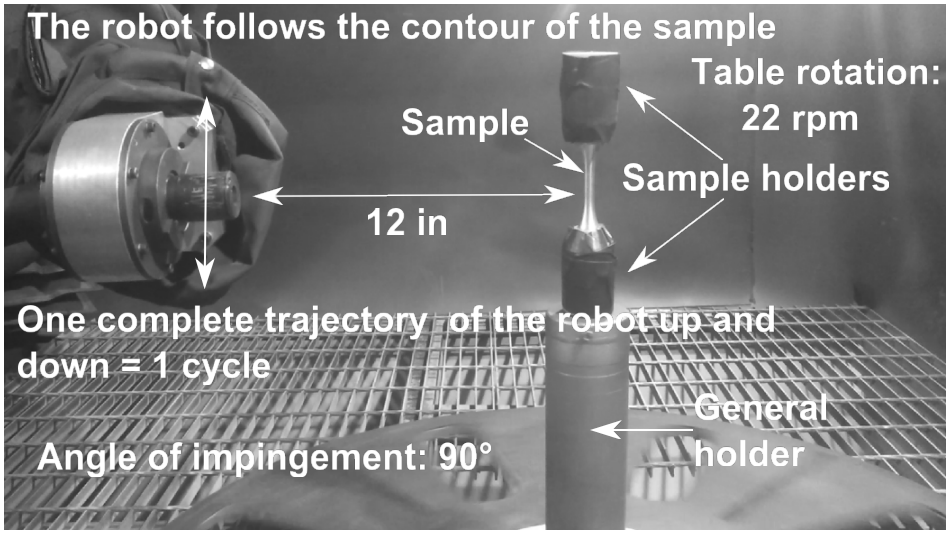

Figure D.4 Intensity measurement trajectory

D.2 Media inspection

D.2.1 Size inpection

The media was taken from the nozzle the 21st September 2015 at 11:00am.

In-process S230 media.

Table D.4 Running time of the RoTap machine

Required AMS2430T	5 min ± 5 s
Executed	5 min 0 s

Table D.5 Size inspection test results

	Retained by sieve 18	**Passing sieve 30**
Required AMS2430T	< 0.5 %	< 20 %
Results	0 %	2 %

D.2.2 Shape inspection

The media was taken from the nozzle the 21th September 2015 at 11:00am.

Table D.6 Shape inspection sample size

	Sample size
Required AMS2430T	1/2 in × 1/2 in
Used	1/2 in × 1/2 in

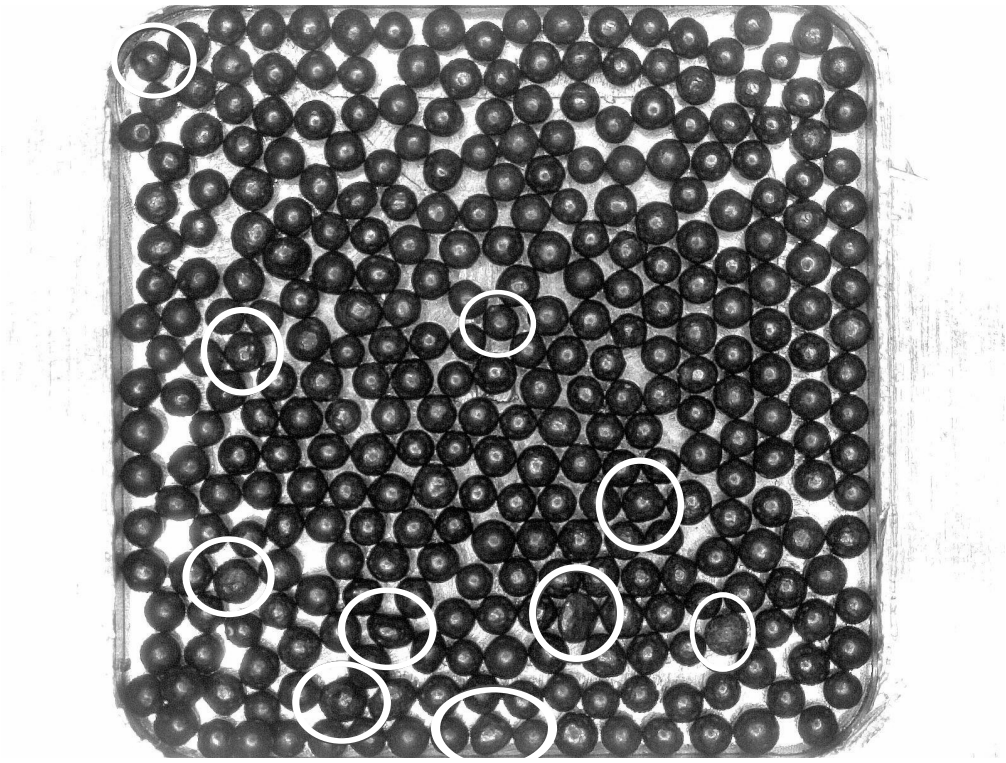

Figure D.5 Media shape inspection

Table D.7 Shape inspection results

	Number of unacceptable shots
Max. allowed AMS2430T	14
Found	10

D.3 Intensity measurement

D.3.1 Intensity prior to coverage measurement

The saturation curve was made prior to coverage measurement the 21th September 2015 at 3:00pm.

The shots velocity was measured immediately after the saturation curve with a 194 mm focal length.

The arc heights used to find the intensity are equal to the arc heights measured minus the pre-bows.

Table D.8 Saturation curve prior to coverage measurement

Peening time	**Pre-bow (10^{-3} in)**	**Arc height (10^{-3} in)**
1 cycle	0.15	2.3
2 cycles	0.15	3.5
4 cycles	0.1	4.2
8 cycles	0.15	4.8

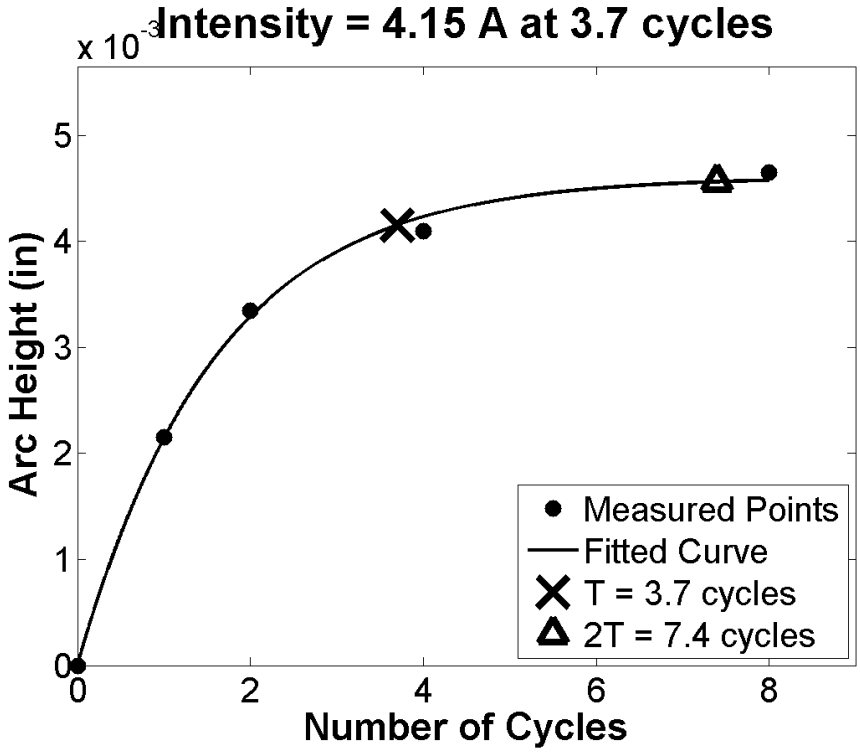

Figure D.6 Saturation curve prior to coverage measurement

Table D.9 Intensity prior to coverage measurement

Tolerance AMS2430T	4 A -0/+30%
Measured	4.15 A
Number of cycles	3.7 cycles
Shots velocity	12.5 m/s
% identified shots*	65 %

* Percentage of shots on which the shotmeter managed to measure the velocity. The manufacturer requires a minimum of 60%.

D.3.2 Intensity prior to samples peening

The saturation curve was made prior to samples peening the 25th September 2015 at 11:00am.

The shots velocity was measured immediately after the saturation curve with a 194 mm focal length.

The arc heights used to find the intensity are equal to the arc heights measured minus the pre-bows.

Table D.10 Saturation curve prior to samples peening

Peening time	**Pre-bow (10^{-3} in)**	**Arc height (10^{-3} in)**
1 cycle	0.0	2.40
2 cycles	0.2	3.60
4 cycles	0.0	4.4
8 cycles	0.2	5.10

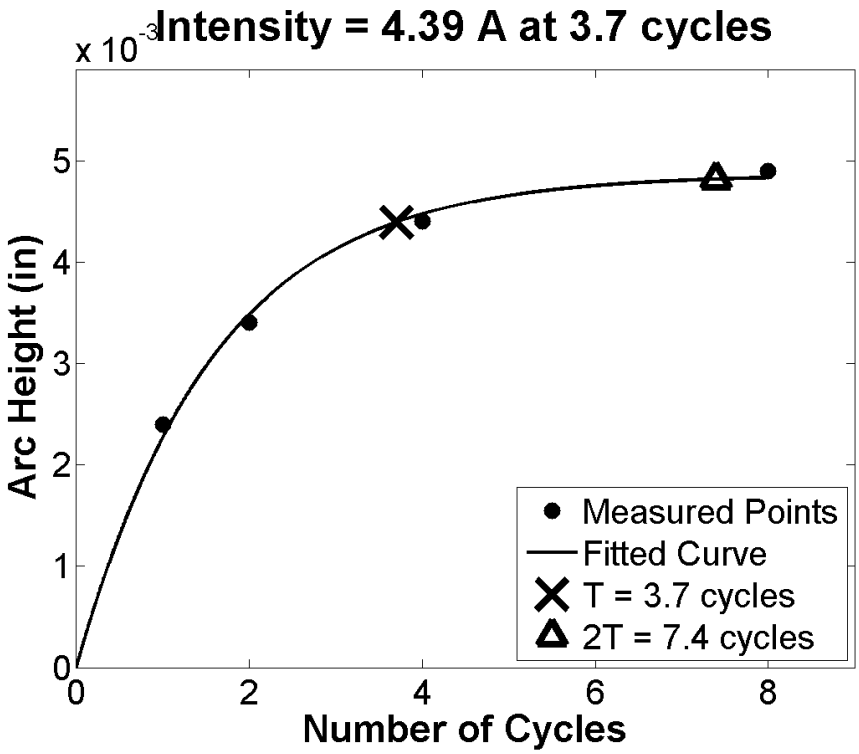

Figure D.7 Saturation curve prior to samples peening

Table D.11 Intensity prior to samples peening

Tolerance AMS2430T	4 A -0/+30%
Measured	4.39 A
Number of cycles	3.7 cycles
Shots velocity	12 m/s
% identified shots*	73 %

* Percentage of shots on which the shotmeter managed to measure the velocity. The manufacturer requires a minimum of 60%.

D.3.3 Intensity after samples peening

The saturation curve was made after samples peening the 25th September 2015 at 11:00am.

The shots velocity was measured immediately after the saturation curve with a 194 mm focal length.

The arc heights used to find the intensity are equal to the arc heights measured minus the pre-bows.

Table D.12 Saturation curve prior to samples peening

Peening time	**Pre-bow (10^{-3} in)**	**Arc height (10^{-3} in)**
1 cycle	0.3	2.55
2 cycles	0.2	3.55
4 cycles	0.25	4.20
8 cycles	0.3	4.85

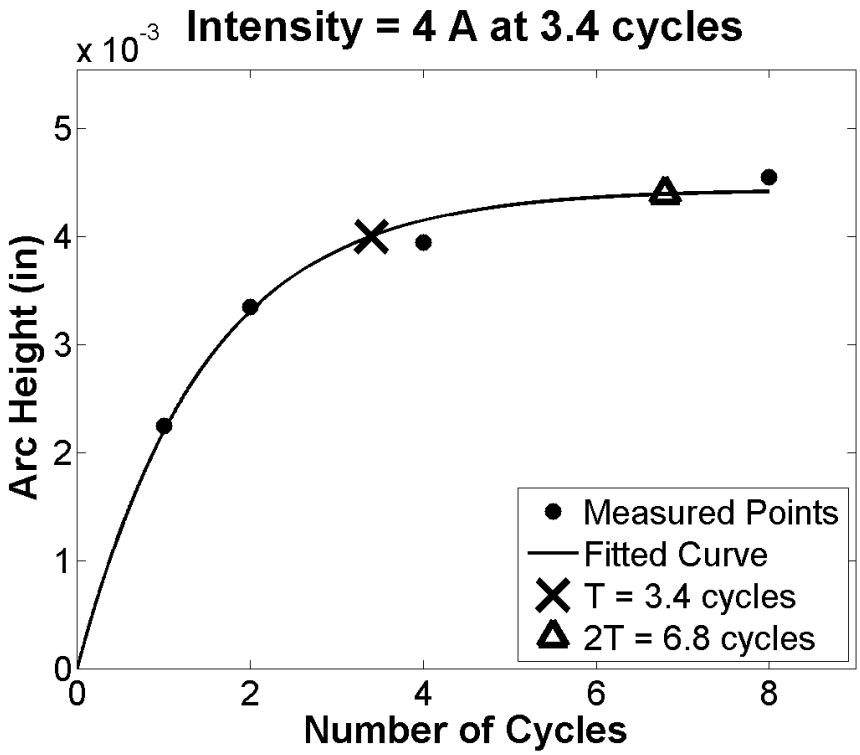

Figure D.8 Saturation curve after samples peening

Table D.13 Intensity after samples peening

Tolerance AMS2430T	4 A -0/+30%
Measured	4.0 A
Number of cycles	3.4 cycles
Shots velocity	12 m/s
% identified shots*	72 %

* Percentage of shots on which the shotmeter managed to measure the velocity. The manufacturer requires a minimum of 60%.

D.4 Coverage measurement

The coverage measurement peening was performed the 21th September 2015 at 3:00pm. The coverage was measured visualy with a X50 magnification.

Table D.14 Coverage measurement results

Target	98 %
Obtained	98 %
Number of cycles executed	7

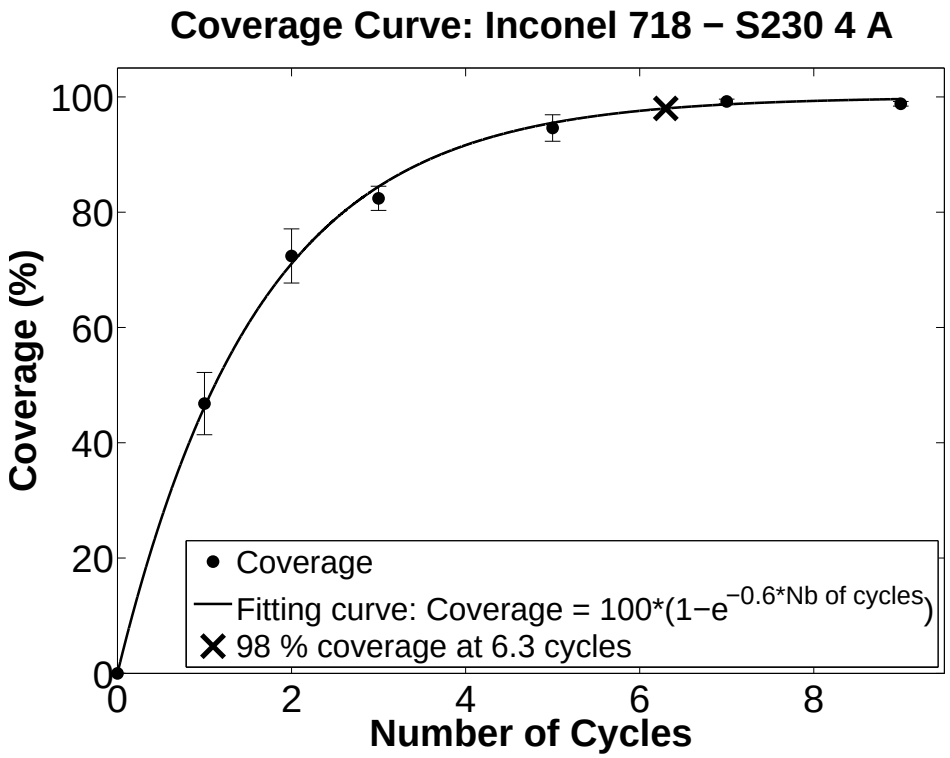

Figure D.9 Coverage curve

D.5 Samples shot peening

The samples were shot peened on the 25th September 2015. The peening number of cycles is 7.

Table D.15 Samples shot peening

Samples	**Peening time**	**Comments**
CP18	12:20pm	-
CP3	12:30pm	-
CP10	12:33pm	-
CP23	12:36pm	-
CP14	12:40pm	-
CP13	1:15pm	-
CP24	1:18pm	-
CP2	1:23pm	-
CP6	1:26pm	-
CP1	1:29pm	-
CP7	1:40pm	-
CP22	1:44pm	-
CP16	1:49pm	-
CP4	1:53pm	-
CP9	2:33pm	Stopped after 2 cycles because of a lack of media. 5 cycles were done 1h15 after.
CP8	3:18pm	-
CP11	3:22pm	-
CP15	3:32pm	-
CP17	3:36pm	-
CP19	3:40pm	-
CP5	3:44pm	-
CP21	3:49pm	-
CP12	3:53pm	-